



Chia, Wei Ming (Dan) (2025) *Real-time recursive risk assessment for autonomous vehicles*. PhD thesis.

<https://theses.gla.ac.uk/84978/>

Copyright and moral rights for this work are retained by the author

A copy can be downloaded for personal non-commercial research or study, without prior permission or charge

This work cannot be reproduced or quoted extensively from without first obtaining permission from the author

The content must not be changed in any way or sold commercially in any format or medium without the formal permission of the author

When referring to this work, full bibliographic details including the author, title, awarding institution and date of the thesis must be given

Enlighten: Theses

<https://theses.gla.ac.uk/>  
[research-enlighten@glasgow.ac.uk](mailto:research-enlighten@glasgow.ac.uk)



University  
of Glasgow

# Real-time Recursive Risk Assessment For Autonomous Vehicles

Thesis submitted in partial fulfilment  
of the requirements for the degree of  
DOCTOR OF PHILOSOPHY

by  
Wei Ming, (Dan) Chia

School of Computing Science

College of Science and Engineering  
University of Glasgow

February 2025

© 2025 Wei Ming (Dan) Chia

## Abstract

The existing risk assessment coverage for Autonomous Vehicle (AV) deployment is insufficient for AV operations. The existing risk assessment is based on static processes, such as Hazard Analysis and Risk Assessment (HARA), which are performed during AV development. The hazard identification is based on prior lessons learned and know-how. The current risk assessment primarily focuses on vehicular malfunctions and does not assess AV's safety actions when hazards are detected during real-time operations. The static risk assessment is unable to measure AV control actions when a hazardous event is detected during AV operations. These planned control actions can also pose risks during AV operations without real-world testing.

This thesis proposes a real-time risk assessment for AV operations, comprising a Real-time Risk Assessment Framework (ReRAF) within the AV and a Real-time Risk Assessment for Cooperative mode (ReRAC) within the infrastructure. The real-time risk assessment operates in a continuous and recursive loop for safety improvement.

In ReRAF, a novel Dynamic Acquired Risk Assessment (DARA) algorithm is designed, developed and verified to provide a Predicted Risk Number (*PRN*) for the AV to assess the risk of its ability to mitigate hazards through its control actions. The *PRN* is derived using the scenarios' risk tag figures and the AV control tag figures. The risk tag figures are achieved by object detection, scene segmentation and probabilistic modelling, while control tag figures are derived from the AV's parametric controls. The resulting *PRN* is a quantitative outcome of ReRAF in an objective end-to-end approach, without any human intervention within the AV. The DARA algorithm was tested in real-world AV operations with unregulated traffic scenarios that consist of vehicles and pedestrians. The accumulative *PRN* results over time can be used to identify potential hotspots and improve AV's path planning. The DARA algorithm demonstrated the ability to use a single *PRN* to represent the real-time risk assessment of an AV by measuring the risk mitigation of the AV control parameters based on the detected risk from its camera.

For ReRAC, a novel Spatial-Temporal Risk Estimation Ensemble Technique (STREET) algorithm is designed, developed and verified to provide remote advanced risk warnings to the AV. STREET compute the environment's risk tag figure and provides hazard identifications and warnings from the infrastructure viewpoint to the AV. Risk tag figures are obtained by first performing a risk zoning of the environment, followed by probabilistic modelling to convert the scene into a risk matrix. Object detection is then used to map the detected object onto the risk matrix to provide risk tag figures for the scene. ReRAC can also derive the time to collide, while hazard identifications and warnings are obtained by detecting pedestrians and/or vehicles in proximity within an intersection or road section of the scene. STREET provides an objective end-to-end approach without human intervention and was tested in unregulated traffic scenarios that provide advanced AV warnings using cooperative mode. STREET results demonstrated the ability to perform real-time conversion from qualitative image to quantitative risk tag figures from the infrastructure's environment scene and time to collision to act as AV's preemptive warning purposes. In addition, the STREET algorithm also illustrated the ability to detect hazard identifications and warnings with roads and intersections, such as vehicle-to-vehicle and vehicle-to-pedestrian hazards, as well as pedestrian warnings and vehicle warnings for intersections. These hazard identifications and warnings are potential risks when the AV arrives at the infrastructure location. They can also detect potential accidents and road congestions if the detection persists.

The combination of ReRAC and ReRAF provides complete coverage of safety enhancements for AV operations in real time, within and beyond the AV. With ReRAC operating as remote advanced warnings, the AV's resultant actions can be safer as it moves towards the ReRAC location. In parallel, the ReRAF continuously monitors and assesses the AV's real-time risk assessment and acts as a trigger if further improvements for safer actions are required for subsequent routes.

## **Acknowledgement**

The acknowledgement for this thesis goes out to my family, who have accompanied me throughout this six-year PhD journey, especially my wife, who has supported me throughout this process. Special thanks to my supervisors (Professor Cindy Goh and Associate Professor Keoh Sye Loong), who guided and supported me during my PhD journey.

## **Declaration**

I hereby declare that except where specific reference is made to the work of others, the contents of this dissertation are original and have not been submitted in whole or in part for consideration for any other degree or qualification in this, or any other University.

This dissertation is the result of my own work, under the supervision of Dr. Keoh Sye Loong and Professor Cindy Goh.

Wei Ming (Dan) Chia

Nov, 2024

# Table of Content

Abstract .....	ii
Acknowledgement .....	iv
Declaration .....	v
Table of Content .....	vi
List of Tables .....	ix
List of Figures .....	xii
List of Publication and Research Grants .....	xv
Definitions/Abbreviations .....	xvi
1 Introduction.....	1
1.1 Safety Standards of AV risk assessment .....	2
1.2 Motivation.....	3
1.3 Thesis statement.....	6
1.4 Contribution .....	6
1.5 Thesis structure & scope .....	7
2 Critical review of existing AV risk assessment .....	9
2.1 Category, methodologies and areas of focus for AV risk assessment.....	9
2.2 Evolution of AV risk assessment .....	11
2.3 Static risk assessment.....	12
2.3.1 Process-based risk assessment .....	12
2.3.2 Model-based risk assessment .....	16
2.3.3 Probabilistic-based risk assessment .....	19
2.3.4 Probabilistic and model-based risk assessment.....	20
2.4 Real-time Risk Assessment .....	23
2.4.1 Process-based real-time risk assessment .....	23
2.4.2 Model-based real-time risk assessment .....	25
2.4.3 Probabilistic-based real-time risk assessment .....	26
2.4.4 Probabilistic and model-based .....	28
2.4.5 AI, Neural Network-based real-time risk assessment.....	29
2.4.6 Cooperative mode .....	35
2.5 Identified gaps in existing works and selection of topics for research approaches.....	40

2.6	Summary .....	43
3	Real-time risk assessment framework and cooperative mode.....	45
3.1	Adaptation of key requirements.....	46
3.2	Overview of Real-time Risk Assessment Framework (ReRAF) and Real-time Risk Assessment Cooperative mode (ReRAC).....	48
3.3	Real-time Risk Assessment Framework (ReRAF) .....	49
3.3.1	AV ReRAF design concept .....	50
3.3.2	ReRAF methodologies and its algorithm .....	51
3.3.3	Scenarios for ReRAF .....	57
3.3.4	ReRAF database and datatype information .....	58
3.4	Real-time risk assessment with cooperative mode (ReRAC) .....	59
3.4.1	AV ReRAC design concept .....	60
3.4.2	ReRAC methodologies and its algorithm .....	61
3.4.3	Scenarios for ReRAC.....	66
3.4.4	ReRAC database and datatype information .....	69
3.5	Summary .....	70
4	Real-time risk assessment with cooperative mode .....	71
4.1	Spatial-Temporal Risk Evaluation Ensemble Technique (STREET) algorithm.....	72
4.1.1	Risk zoning of the environment .....	73
4.1.2	Risk detection matrix with probabilistic models .....	76
4.1.3	Object detection process .....	84
4.1.4	Risk Tag (RT) Matrix and Risk Tag (RT) figure .....	86
4.1.5	Occurrence .....	88
4.1.6	Road Side Unit Time To Collide (RSU-TTC) .....	90
4.1.7	Hazard identifications and warning .....	92
4.2	STREET Risk tagging process and results.....	93
4.2.1	Risk zoning matrix.....	94
4.2.2	Risk detection matrix with probabilistic model .....	97
4.2.3	Object detection matrix.....	100
4.2.4	Risk Tag (RT) figure and results .....	104
4.2.5	Occurrence data and results visualisation.....	112
4.2.6	Road Side Unit Time to collide matrix and results.....	114
4.2.7	Real-world events with RT figures and RSU-TTC .....	116
4.2.8	Comparison of LID, CED, AED and Time to collision findings .....	132
4.2.9	Hazard identifications and warnings results .....	135



4.3	Summary .....	139
5	Real-time risk assessment framework for AV.....	142
5.1	Dynamic Acquired Risk Assessment (DARA) algorithm .....	143
5.1.1	Image Risk Tagging and Mapping.....	144
5.1.2	Control Tagging of the AV .....	151
5.1.3	Predicted Risk Number ( <i>PRN</i> ).....	154
5.1.4	Occurrence and visualisation with regional <i>PRN</i> .....	157
5.2	DARA evaluation process and results .....	158
5.2.1	Scenarios for the AV test.....	160
5.2.2	Image risk tagging and mapping.....	161
5.2.3	Control Tagging of the AV .....	169
5.2.4	Predicted Risk Number ( <i>PRN</i> ).....	173
5.2.5	Occurrence with regional <i>PRN</i> visualisation.....	175
5.3	Verification of DARA with real-world test routes.....	177
5.3.1	Determination of <i>PRN</i> ratings through statistical methods .....	181
5.3.2	Scenario A, first loop with rated high <i>PRN</i> .....	183
5.3.3	Scenario B, first loop with rated middle <i>PRN</i> .....	186
5.3.4	Scenario C, first loop with rated low <i>PRN</i> .....	187
5.3.5	Scenario D, second loop with rated high <i>PRN</i> .....	188
5.3.6	Scenario E, second loop with rated middle <i>PRN</i> .....	190
5.3.7	Scenario F, second loop with rated low <i>PRN</i> .....	192
5.3.8	Scenario G, third loop with rated high <i>PRN</i> .....	194
5.3.9	Scenario H, third loop with rated middle <i>PRN</i> .....	196
5.3.10	Scenario I, third loop with rated low <i>PRN</i> .....	200
5.3.11	Verification summary for all scenarios.....	202
5.4	Summary .....	204
6	Conclusion and further work .....	206
6.1	Conclusion .....	206
6.2	Key benefits .....	210
6.3	Recommendation for future works.....	213
7	List of reference .....	215
7.1	References .....	215

## List of Tables

Table 1.1 SAE Levels, fallback responsibility and risk assessment.....	2
Table 2.1 Static risk assessment using process-based methodology.....	13
Table 2.2 HARA ASIL classification table (QM indicates that no further action is required) .....	14
Table 2.3 Static risk assessment using model-based methodology .....	17
Table 2.4 Static risk assessment using probabilistic-based methodology.....	19
Table 2.5 Static risk assessment using probabilistic and model-based methodology.....	21
Table 2.6 Real-time risk assessment coverage using process-based methodology .....	23
Table 2.7 Real-time risk assessment coverage using model-based methodology	25
Table 2.8 Real-time risk assessment coverage using probabilistic-based methodology.....	26
Table 2.9 neural network for computer vision used within AV.....	30
Table 2.10 Real-time risk assessment coverage using neural network-based methodology.....	33
Table 2.11 Real-time risk assessment coverage cooperative mode methodology	37
Table 3.1 ReRAF scenarios to be tested .....	57
Table 3.2 Sample of database information from ReRAF.....	58
Table 3.3 Parameters and its datatype for ReRAF .....	59
Table 3.4 Hazard Detection Classification.....	64
Table 3.5 ReRAC scenarios to be tested for RT figures.....	67
Table 3.6 ReRAC hazard identifications and warnings to be tested .....	68
Table 3.7 Sample of database information from ReRAC.....	69
Table 4.1 Weight for different risk zonal areas.....	76
Table 4.2 Comparison of model and utility.....	84
Table 4.3 Comparison of YOLO variants on mAP.....	85
Table 4.4 Comparison of YOLO variants on Precision, Recall and F1 score .....	85
Table 4.5 STREET hazard detection features .....	92
Table 4.6 Hazard identifications and warnings conditions.....	93
Table 4.7 LID risk detection matrix derivation .....	97
Table 4.8 Inter-zonal probability distribution for LID risk detection matrix.....	98
Table 4.9 CED risk detection matrix derivation .....	99
Table 4.10 AED risk detection matrix derivation .....	99

Table 4.11 Comparison of YOLOv3 vs YOLOv5s .....	101
Table 4.12 Illustrated scenes (A), (B) and (C) for <i>TTCvalue</i> .....	128
Table 4.13 Summary of LID, CED or AED with <i>TTCvalue</i> at corner scenario for different events.....	133
Table 4.14 Summary of models with <i>TTCvalue</i> to identify high or low risk scenario .....	134
Table 5.1 Simulated scenes of <i>PRN</i> .....	156
Table 5.2 <i>PRN</i> rating guideline.....	156
Table 5.3 The determination of <i>PRTsum</i> based on scenario 1 .....	164
Table 5.4 The determination of <i>VRTsum</i> based on scenario 2 .....	166
Table 5.5 The determination of <i>PRTsum</i> based on scenario 3 .....	168
Table 5.6 The determination of <i>VRTsum</i> based on scenario 3 .....	169
Table 5.7 Scenario 1, scene one, <i>AV Ctrl</i> .....	170
Table 5.8 Scenario 1, scene two, <i>AV Ctrl</i> .....	170
Table 5.9 Scenario 2, scene one, <i>AV Ctrl</i> .....	171
Table 5.10 Scenario 2, scene two, <i>AV Ctrl</i> .....	171
Table 5.11 Scenario 3, scene one, <i>AV Ctrl</i> .....	172
Table 5.12 Scenario 3, scene two, <i>AV Ctrl</i> .....	173
Table 5.13 Parameters for <i>PRN</i> in Scenarios 1, 2 and 3.....	173
Table 5.14 Data statistics for three loops of DARA real-world testing.....	180
Table 5.15 <i>PRN</i> rating thresholds.....	182
Table 5.16 Scenario A first loop with high <i>PRN</i> rating .....	183
Table 5.17 Simulated safety actions for DARA in scenario A .....	185
Table 5.18 Scenario B, first loop with rated middle <i>PRN</i> .....	186
Table 5.19 Simulated safety actions for DARA in scenario B .....	187
Table 5.20 Scenario C, first loop with rated low <i>PRN</i> .....	188
Table 5.21 Scenario D, second loop with rated high <i>PRN</i> .....	189
Table 5.22 Simulated safety actions for DARA in scenario D .....	190
Table 5.23 Scenario E, second loop with rated middle <i>PRN</i> .....	190
Table 5.24 Simulated safety actions for DARA in scenario E.....	192
Table 5.25 Scenario F, second loop with rated low <i>PRN</i> .....	193
Table 5.26 Scenario G, third loop with rated high <i>PRN</i> .....	195
Table 5.27 Simulated safety actions for DARA in scenario G .....	196
Table 5.28 Scenario H, third loop with rated middle <i>PRN</i> .....	197
Table 5.29 “Red box” scene for scenario H .....	199

Table 5.30 Simulated safety actions for DARA in “red box” scenario H .....	200
Table 5.31 Scenario H, third loop with rated low <i>PRN</i> .....	200
Table 5.32 Summary of <i>PRN</i> vs ground truth across the nine scenarios .....	202
Table 5.33 AV’s risk assessment outcome with improvements to inherent safety actions .....	203

## List of Figures

Figure 1.1 Risk assessment coverage from development to deployment .....	4
Figure 2.1 AV risk assessment category, methodologies and areas of focus .....	10
Figure 2.2 Timeline of risk assessment for AV .....	11
Figure 2.3 Skill graph of an AV categorised into different components or skills .	15
Figure 2.4 Comparison of YOLOv5, v6, v7 and v8 performance .....	32
Figure 3.1 Overview of ReRAF and ReRAC .....	49
Figure 3.2 Overview of ReRAF .....	50
Figure 3.3 ReRAF's methodologies and algorithm that links to the corresponding outcomes .....	52
Figure 3.4 Example of probabilistic modelling for risk tagging and mapping .....	54
Figure 3.5 ReRAC design concept .....	60
Figure 3.6 ReRAC's methodologies and algorithm that links to the corresponding outcomes .....	61
Figure 3.7 Time to collision parameters .....	65
Figure 4.1 Block diagram of STREET algorithm within the RSU .....	72
Figure 4.2 LID, CED and AED coverages .....	78
Figure 4.3 Illustration of zonal and inter-zonal probability distribution.....	78
Figure 4.4 Object detection process.....	84
Figure 4.5 Reference location for detecting object bounding box .....	86
Figure 4.6 An example of a 2D risk zoning matrix, risk detection matrix and object detection matrix .....	87
Figure 4.7 STREET testing scenario for cornering .....	94
Figure 4.8 Example one: three persons detected and mapped to object detection matrix.....	102
Figure 4.9 Example two: three persons detected and mapped to object detection matrix.....	102
Figure 4.10 Rule 1: YOLOv5 + Mapping .....	103
Figure 4.11 Rule 2: YOLOv5 + Mapping .....	103
Figure 4.12 LID RT figures illustrations and result .....	106
Figure 4.13 CED RT figures illustration and result.....	107
Figure 4.14 AED RT figures illustration and result.....	108
Figure 4.15 Normalised LID RT figures illustration and result .....	110
Figure 4.16 Normalised CED RT figures illustration and result .....	111
Figure 4.17 Normalised AED RT figures illustration and result .....	112

Figure 4.18 Heatmap of overall pedestrian occurrence .....	113
Figure 4.19 Probability of pedestrian occurrence in front, middle and rear rows of the AOI .....	114
Figure 4.20 Relationship between <i>TTCvalue</i> , and normalised LID RT and LID RT figure .....	115
Figure 4.21 Images of pedestrians crossing from both sides for event 1 .....	117
Figure 4.22 LID RT figures vs LID RT ground truth for event 1 .....	118
Figure 4.23 Comparison of LID, CED and AED RT figures for event 1.....	119
Figure 4.24 Verify <i>TTCvalue</i> and compare LID and normalise LID RT figures for event 1 .....	120
Figure 4.25 Images of pedestrian diagonal crossing for event 2 .....	121
Figure 4.26 LID RT figures vs LID RT ground truth for event 2 .....	122
Figure 4.27 Comparison of LID, CED and AED RT figures for event 2.....	123
Figure 4.28 Comparing LID RT figure, normalised LID RT figure and <i>TTCvalue</i> for event 2 .....	124
Figure 4.29 Images of pedestrians' movement from rear to front for event 3 .	125
Figure 4.30 LID RT figures, ground truth and normalised RT figure for event 3	126
Figure 4.31 Comparison of LID, CED and AED RT figures for event 3.....	127
Figure 4.32 Comparing LID RT figure, normalised LID RT figure and <i>TTCvalue</i> for event 3 .....	128
Figure 4.33 Images of pedestrian occluded by moving vehicle for event 4 .....	129
Figure 4.34 LID RT figures vs LID RT ground truth for event 4 .....	130
Figure 4.35 Comparison of LID, CED and AED RT figures for event 4.....	131
Figure 4.36 Comparing LID RT figure, LID RT ground truth and <i>TTCvalue</i> for event 4 .....	132
Figure 4.37 Hazard identifications and warnings tested at T-junction .....	135
Figure 4.38 Real-world T-junction with zoning .....	136
Figure 4.39 Scene A, vehicle warning "True" .....	136
Figure 4.40 Scene B, pedestrian warning "True" .....	137
Figure 4.41 Scene C, vehicle warning "True" and vehicle-to-vehicle hazard "True" .....	137
Figure 4.42 Scene D, vehicle warning "True" and vehicle-to-vehicle hazard "True" .....	138
Figure 4.43 Scene E, pedestrian & vehicle warning "True", & vehicle-to-pedestrian hazard "True" .....	138
Figure 4.44 Scene F, vehicle-to-pedestrian hazard "True" at AOI.....	139
Figure 5.1: Block diagram of DARA .....	143

Figure 5.2: Block diagram of Image risk tagging and mapping .....	144
Figure 5.3: Scene segmentation of a scene into matrix .....	145
Figure 5.4 Block diagram within Risk Tagging and Mapping in DARA .....	148
Figure 5.5: Control Tagging of the AV .....	151
Figure 5.6 Flowchart for the Occurrence of <i>PRN</i> visualisation .....	158
Figure 5.7 Location map of AV test site.....	159
Figure 5.8 Scenario 1: Straight path without zebra crossing .....	160
Figure 5.9 Scenario 2: T-junction without traffic lights for AV .....	161
Figure 5.10 Scenario 3: Cornering, detection of pedestrians after AV turns....	161
Figure 5.11 Scene segmentation process .....	162
Figure 5.12 Scenario 1, scene one without pedestrians .....	163
Figure 5.13 Scenario 1, scene two, with pedestrians detected on pavement ..	164
Figure 5.14 Scenario 1, scene two without vehicle .....	165
Figure 5.15 Scenario 2, scene two with vehicle detected .....	166
Figure 5.16 Scenario 3, scene one without object detected. ....	167
Figure 5.17 Scenario 3, scene 2 with a pedestrian and vehicle detected .....	168
Figure 5.18 Regional <i>PRN</i> of first loop test route .....	176
Figure 5.19 Black box regional <i>PRN</i> scene for first loop .....	176
Figure 5.20 <i>PRN</i> for the first loop .....	177
Figure 5.21 <i>C_RT</i> for the first loop.....	178
Figure 5.22 <i>Ctrl</i> for the first loop.....	179
Figure 5.23 Non-zero <i>PRN</i> distribution for the first loop .....	181
Figure 5.24 Non-zero <i>PRN</i> distribution for the second loop.....	182
Figure 5.25 Non-zero <i>PRN</i> distribution for the third loop .....	182
Figure 5.26 Scenario A's <i>PRN</i> , <i>C_RT</i> , <i>Ctrl</i> and parametric data .....	184
Figure 5.27 Scenario E's <i>PRN</i> , <i>C_RT</i> , <i>Ctrl</i> and parametric data .....	191
Figure 5.28 Scenario F's <i>PRN</i> , <i>C_RT</i> , <i>Ctrl</i> and parametric data .....	194
Figure 5.29 Scenario G, <i>PRN</i> , <i>C_RT</i> and <i>Ctrl</i> .....	196
Figure 5.30 Scenario H's <i>PRN</i> , <i>C_RT</i> , <i>Ctrl</i> and parametric data.....	198
Figure 5.31 Scenario I's <i>PRN</i> , <i>C_RT</i> , <i>Ctrl</i> and parametric data.....	201

## List of Publication and Research Grants

1. **Grant 1:** W. M. D. Chia et al, "Real-Time Risk Assessment Assistance for Cooperative Mode (ReRAC) Using V2X for Vehicles and Pedestrian in Urban Conditions," S\$1,576,200.00, ed. Singapore: NRF and LTA under its UMGC-L013, 2021-2024..
2. **Grant 2:** W. M. D. C. et al, "Functional Risk for AV using AI Hybrid Deterministic Method," S\$249,000, ed. Singapore: Singapore Institute of Technology, Ministry of Education, 2019.
3. **Journal:** W. M. D. Chia, S. L. Keoh, C. Goh, and C. Johnson, "Risk Assessment Methodologies for Autonomous Driving: A Survey," IEEE Transactions on Intelligent Transportation Systems, pp. 1-17, 2022, doi: 10.1109/TITS.2022.3163747.
4. **Conference:** W. M. D. Chia, S. L. Keoh, A. L. Michala, and C. Goh, "Real-time Recursive Risk Assessment Framework for Autonomous Vehicle Operations," in 2021 IEEE 93rd Vehicular Technology Conference (VTC2021-Spring), 25-28 April 2021 2021, pp. 1-7, doi: 10.1109/VTC2021-Spring51267.2021.9448759.
5. **Journal:** W. M. D. Chia, S. L. Keoh, A. L. Michala, and C. Goh, "Infrastructure-Based Pedestrian Risk Tagging Methodology to Support AV Risk Assessment," IEEE Access, vol. 10, pp. 71462-71480, 2022, doi: 10.1109/ACCESS.2022.3188306.
6. **Journal:** W. M. D. Chia, S. L. Keoh, A. L. Michala, and C. Goh, "Dynamically Acquired Risk Assessment for Real-world Autonomous Vehicle operations (ongoing)," IEEE Transactions on Intelligent Transportation Systems, 2025.



## Definitions/Abbreviations

Below is the list of definitions and abbreviations used in this thesis. Variables presented as formulas are shown in italics throughout the thesis and are not included in this section.

Abbreviations	Definition
AED	Aggressive Exponential Distribution
AI	Artificial Intelligence
AOI	Area of Interest
ASIL	Automotive Safety Integrity Level
AV	Autonomous Vehicle
AV-TTC	Autonomous Vehicle Time To Collision
CED	Conservative Exponential Distribution
C-I2X	Cellular-Infrastructure-to-Everything
CNN	Convolution Neural Network
COCO	Common Object in Context
CT	Control Tag
C-V2X	Cellular-vehicle-to-Everything
DARA	Dynamic Acquired Risk Assessment
DFMEA	Design Failure Mode Effect Analysis
DPM	Deep Predictive Model
DSRC	Dedicated Short Range Communication
FOV	Field Of View
HARA	Hazard Analysis And Risk Assessment
I2V	Infrastructure to Vehicle
I2X	Infrastructure-to-Everything
ICNet	Image Cascade Network

IoU	Intersection over Union
LID	Linear Interval Distribution
mAP	Mean Average Precision
mIoU	Mean Intersection over Union
MPC	Model Predictive Control
PCA	Principal Component Analysis
PSPNet	Pyramid Scene Parsing Network
RAM	Risk Assessment Module
ReRAC	Real-time Risk Assessment for Cooperative
ReRAF	Real-time Risk Assessment Framework
ResNet8	Residual Networks 8
RSU	Road Side Unit
RSU-TTC	Road Side Unit Time To Collide
RT	Risk Tag
SOTIF	Safety Of The Intended Functionality
SSD	Single-Shot Detector
STREET	Spatial-Temporal Risk Estimation Ensemble Technique
UML	Unified Modelling Language
V2V	Vehicle-to-Vehicle
V2X	Vehicle-to-everything
VANET	Vehicular Ad-Hoc Network
YOLO	You Only Look Once

# Chapter 1

## 1 Introduction

The emergence of Autonomous Vehicles (AV) has garnered substantial attention in recent years [1, 2]. Technological progress in processing power, sensors, and artificial intelligence has made the development and deployment of AVs feasible across many global regions [3]. AVs are classified into three distinct levels, as outlined in the SAEJ3016 standard [4]. SAE level 3, known as self-drive under limited conditions, is to be integrated into upcoming luxury vehicle models from leading OEMs, such as Drive Pilot [5]. Conversely, SAE level 4 is primarily designed for public transportation, including Robo-taxis [6] and AV buses [7], with ongoing test trials for AV deployment [8, 9]. However, SAE level 5, which requires the AV to operate safely under all conditions, is the most challenging, with most OEMs and AV developers hesitant to commit to achieving this level of autonomy. As depicted in Table 1.1, levels 4 and 5 are considered more demanding than level 3, as the autonomous driving system is accountable for safety instead of the driver. The recent accidents [10, 11] in AV deployments have further underscored the pressing need for enhanced safety measures, particularly for SAE levels 4 and 5. These safety measures must be able to quantify environmental risk and measure if existing safety actions are sufficiently deployed, and the outcome can assist regulatory organisations in measuring AV safety assessments. As a result, there is an escalating demand for safety enhancement for SAE levels 4 and 5, particularly in establishing matrices to gauge system safety [12]. This necessitates the need for an accurate, quantifiable approach, which is crucial for the widespread

## 1.1 Safety Standards of AV risk assessment

---

adaptation of AV. These quantifiable methods for AV controls or safety measures should be tested in real-world settings to identify potential safety enhancements over time independently and objectively. These real-world settings refer to unregulated traffic scenarios with a higher occurrence of near misses and collisions between AV and pedestrians and/or vehicles. The unregulated traffic scenarios include corners, T-junctions, and straight roads. The quantifiable method makes AV operations progressively safer, thereby averting near misses and accidents and ensuring smoother rides by reducing abrupt braking, wide steering, and sudden acceleration.

Table 1.1 SAE Levels, fallback responsibility and risk assessment

SAE Levels	Features	Dynamic driving task Fallback Responsibility	Dynamic Driving task
3	Self-drive under limited conditions	Driver	Fallback-ready user (driver becomes fallback)
4		Autonomous driving systems	Autonomous driving systems
5	Self-drive under all conditions	Autonomous driving systems	Autonomous driving systems

The current standards for AV risk assessment [13-16] predominantly concentrate on system malfunctions and identifying potential risks during development. These standards rely on past experiences and knowledge to simulate specific scenarios and mitigate risks during development. However, encompassing all aspects of environmental risk, given the actions of AVs in intricate developmental scenarios, presents a significant challenge. Hence, there is an imperative need to enhance the existing risk assessment methodologies for the current deployment of AVs to encompass more than just accident prevention for real-world deployment [17].

### 1.1 Safety Standards of AV risk assessment

Before explaining the motivation of this research, it is important to understand the existing safety standards for AV risk assessment. The existing automotive functional safety standard ISO 26262 [14] contains parts 1 to 11 that address all

vehicles' functional safety, including both driven and autonomous ones. Part 3 of the standard focuses explicitly on the risk assessment from the initial concept to the product development phase for AVs. Within Part 3, there is a requirement for item definitions of identified hazards, followed by the Hazard Analysis and Risk Assessment (HARA) [18], where safety actions are determined to mitigate the hazards during development. In existing risk assessment, item definitions of hazards are primarily intended to identify potential failures due to past design flaws, errors, and lessons learned that resulted in malfunctions. This approach lacks focus on environmental hazard identification, and the defined safety actions for malfunctions tested during development may differ from real-world AV operational needs. This discrepancy between risk assessment during development and real-world AV operations, if left unaddressed, will increase operational risk and potential hazards for real-world AV deployment. This is exceptionally critical for SAE levels 4 and 5 of AV automation, where the dynamic driving task fallback is passed onto the autonomous driving system other than the driver [19]. It is thus crucial to address the gap between risk assessment performed during development and real-world operation for safer AV operations.

## 1.2 Motivation

Existing risk assessments have several gaps, such as a lack of environmental hazard considerations, safety measurement of inherent safety actions, and a quantifiable method for measuring risk or safety during AV operations beyond development. Since they are performed during development, they are referred to as static risk assessments in this research.

The motivation of this research is to resolve these gaps by proposing a real-time risk assessment that measures the AV's inherent control or safety actions when environmental hazards are detected while using a quantifiable methodology to provide numerical ratings and outcomes in real time. Therefore, this real-time risk assessment is essential to evaluate the AV's control or safety actions during AV operations in addition to existing static risk assessment. Furthermore, to address the limitation of detection hazards beyond the AV's detection range limit, establishing an infrastructure for real-time operations beyond the AV can

## 1.2 Motivation

significantly enhance real-time risk assessment by providing advanced remote risk warnings.

Figure 1.1 illustrates the necessity for risk assessment coverage from development to deployment. It illustrates the AV risk assessment gaps transitioning from development to real-time operations. During AV development, the existing static risk assessment converts potential malfunctions into Severity, Control, and Occurrence figures based on expert knowledge and lessons learned, which are subjectively driven. The outcome of this static risk assessment leads to rule-based safety actions for real-time AV operations.

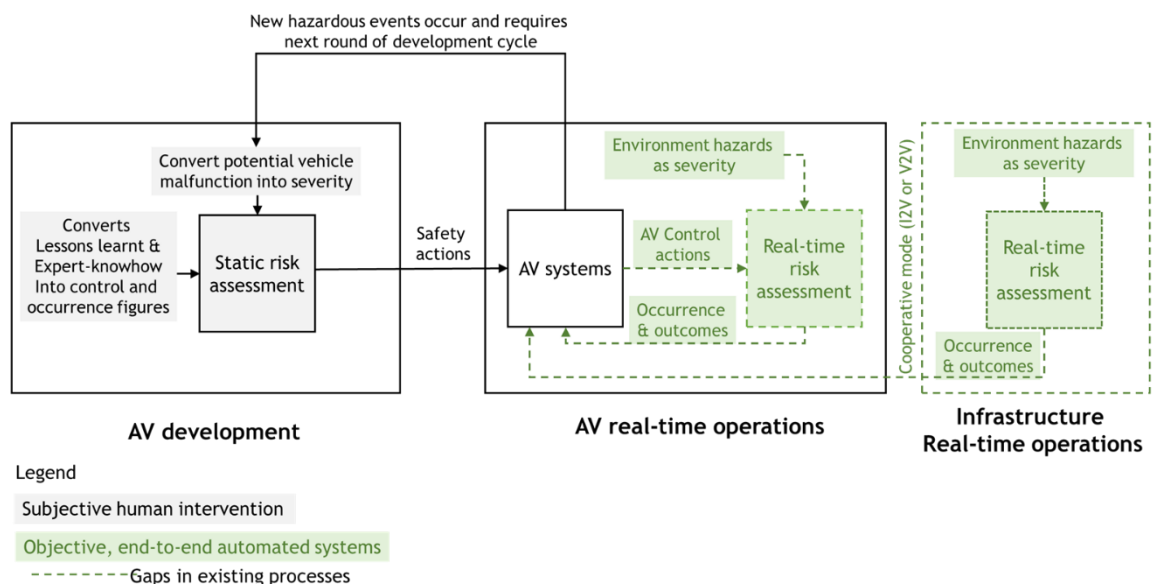


Figure 1.1 Risk assessment coverage from development to deployment

During AV real-time operations, the conceived safety actions derived during development may deviate from the safety actions needed in real-world settings due to differences in environmental settings. Thus, the differences will lead to the effectiveness of the safety actions in managing the detected hazards, which are not measured using existing risk assessment. Moreover, existing risk assessments do not quantitatively measure the real-time effectiveness of safety actions based on environmental risk, making it impossible to identify hotspots for improvement. This leads to the motivation of creating an independent module to perform real-time risk assessment within the AV to evaluate safety actions

(Control) and when environmental hazards (Severity) are detected. By doing so, the AV developer will be able to identify in real time if existing safety actions are sufficient based on the environmental risk and if further enhancement of safety actions is required. The methodology consists of processes that manage image information and the control or safety actions and turn them into quantitative risk numbers for future safety action improvements.

The other challenge of AV operations is the inability to identify hazards or risks beyond the sensors' detection range, which results in sudden safety actions to prevent a collision but creates a higher risk for other motorists and passengers. These real-world scenarios can involve occluding corners or unregulated traffic, where sudden pedestrians or vehicles can reside, and the AV has no advanced information. Thus, real-time infrastructure operations can be used to improve safer AV operations by providing remote advanced risk warnings through infrastructure-to-vehicle (I2V) or vehicle-to-vehicle (V2V) communication. Also known as cooperative mode, these operations can prepare the AV for advanced safety actions before reaching the infrastructure's location where risk is detected.

In summary, several gaps (listed below) exist in static risk assessment coverage for AV operations, which motivate this research on real-time risk assessment.

- 1) Existing static risk assessment does not measure AV's control or safety actions when detecting a hazardous event during AV operations. Existing methods only capture risk based on past lessons learnt, know-how, and experience in formulating safety actions during development. These planned safety actions can also incur risks during AV operations (e.g. sudden braking as a form of safety action).
- 2) Existing static risk assessments cannot fully capture environmental risk within the AV or remotely using infrastructure during operations. As such, scenarios that contain potential accidents with near misses will not be recorded. This granular information is essential for AV to improve its safety operations continuously.

- 3) Existing static risk assessment requires another iteration of the development cycle for safety improvement. Hence, AV safety is compromised if the safety actions are improper and will have to continue using it till the next development release.

### **1.3 Thesis statement**

The thesis statement for this research is known as the real-time recursive risk assessment for AV. Therefore, the research in this thesis consists of the following:

- 1) Research, propose, and develop a novel recursive real-time risk assessment framework used within the AV to provide quantitative risk based on dynamic and real-time environmental hazards and their corresponding AV controls.
- 2) Research, propose and develop a novel real-time risk assessment cooperative mode at the infrastructure to provide advanced risk and hazardous event warnings for the AV.
- 3) Evaluate and verify the proposed framework and cooperative mode using real-world scenarios. The methodologies of the proposed framework and cooperative mode are tested with real-world unregulated traffic conditions to assess risk, hazards, and near-missed accidents, which are more common in these scenarios.

### **1.4 Contribution**

In the course of this research, four main contributions were made towards improving the safety of AV operations for real-time risk assessments with quantitative measures.

- A novel real-time risk assessment framework was researched for the AV to provide a risk measurement of how the AV's control action responds to a detected hazardous event. The concept was published in [17]. The



framework fulfils the requirements of a risk assessment methodology and resolves the identified gap from existing risk assessment, which will be explained in chapter 3.

- A novel algorithm was developed that automatically detects risks and hazards from the AV's environment and controllability into a quantitative outcome. This framework and its algorithm are developed, evaluated and verified using specific real-world unregulated scenarios and AV operational routes [20], which will be explained in chapter 5. This is unique as existing risk assessment methodologies are only tested during development and not in real time. The framework and the algorithm provide an objective end-to-end AV risk assessment in real time at granular levels. The outcomes are used in [21] and [22].
- An infrastructure-based real-time risk assessment cooperative mode was researched to provide the AV with advanced remote risk and hazard warnings, which will be explained in chapter 3. The concept and algorithm were published in [23].
- A novel algorithm for the cooperative mode automatically converts environmental risks and hazards from the infrastructure into risk tagging and hazardous detection outcomes. The algorithm was developed, evaluated and verified using real-world unregulated scenarios, which will be explained in chapter 4. The cooperative mode algorithm provides a lightweight, objective end-to-end risk tagging and real-time hazardous event detection at granular levels. The outcomes are used in [22].

## **1.5 Thesis structure & scope**

In this thesis, chapter 1 introduces the purpose of the research, the motivation, the thesis statements, and the contribution of this thesis. Chapter 2 consists of a literature review exploring the current state of the art in risk assessment methodologies and techniques. Building on the identified gaps in the literature, chapter 3 proposes a new real-time risk assessment framework for AVs and a

cooperative infrastructure-based remote risk warning system for AVs. Chapter 3 also outlines the proposed methodologies for the algorithm and describes their test scenarios. Chapter 4 delves into the theoretical formulation, development, and real-world verification of the real-time risk assessment in cooperative mode. The cooperative mode provides advanced risk and hazardous event detection remotely to the AV. Chapter 4 also shows risk tagging and hazardous event detection test results. Chapter 5 explains the theoretical formulation, evaluation, and verification of the real-time risk assessment framework, through real-world scenarios and operational routes. The framework used within the AV provides a risk assessment of how the AV mitigates its movement through the detected risk. Finally, Chapter 6 concludes the thesis and outlines potential future work.

## **Chapter 2**

### **2 Critical review of existing AV risk assessment**

This chapter reviews the existing risk assessments for AV and begins by explaining the different types of risk assessment, followed by the evolution of risk assessment for AV over the past decades. Existing works are critiqued based on their categorisation, methodologies, and areas of focus, emphasising their strengths and identifying areas that require further attention. Subsequently, gaps in existing risk assessment are identified as requirements to develop new methodologies that enhance and improve AV risk assessment for operations.

#### **2.1 Category, methodologies and areas of focus for AV risk assessment**

AV risk assessments can be categorised into static or real-time approaches as shown in Figure 2.1. Static risk assessments are performed during AV development, while real-time risk assessments are performed during the AV operation. Static risk assessment is a subjective approach that defines the Severity of hazards, the probability of events, and the controllability of events through human decisions and classifications. On the other hand, real-time risk assessment objectively measures the actions to control the AV in real time when hazards are identified. Real-time risk assessments should be performed in an end-to-end manner without human intervention. In general, risk assessments for AV are formulated through different methodologies such as process-based, model-based, probabilistic-based, probabilistic and model-based, AI-based and Cooperative modes.

## 2.1 Category, methodologies and areas of focus for AV risk assessment

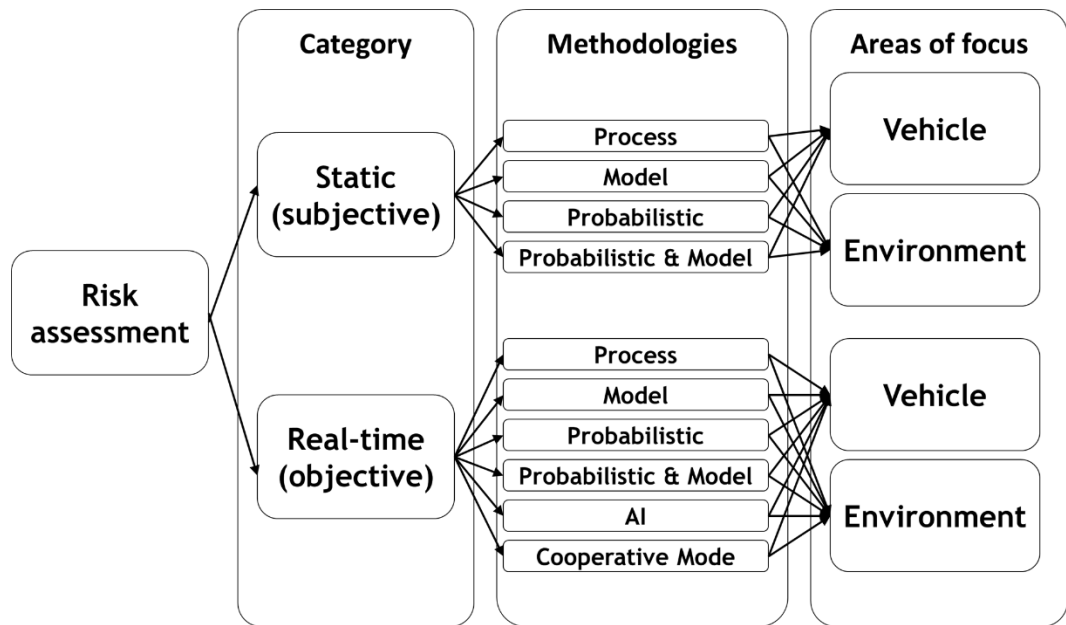


Figure 2.1 AV risk assessment category, methodologies and areas of focus

The process-based methodology involves refining and improving existing processes from the established standards. The model-based methodology aims to quantify hazardous events by converting them into numerical representations. The probabilistic-based methodology systematically evaluates potential hazardous events and provides quantitative measures based on their associated probabilities. The probabilistic and model-based methodology combines the modelling of AV systems with associated probabilities for potentially hazardous events. AI-based methodology employs artificial intelligence, such as artificial neural networks or deep learning, to provide numerical representations of hazardous events. Cooperative modes involve different methodologies that transfer risk-related information between I2V or V2V.

Within these methodologies, existing research focuses on either vehicle and/or environmental levels. Vehicle-level risk assessment considers the malfunctions within the vehicle, whereas environmental-level risk assessment considers the detection of hazardous events from the AV's surroundings. The existing standard for AV risk assessment is classified as a static risk assessment, which uses a process-based methodology focusing on vehicle malfunctions.

## 2.2 Evolution of AV risk assessment

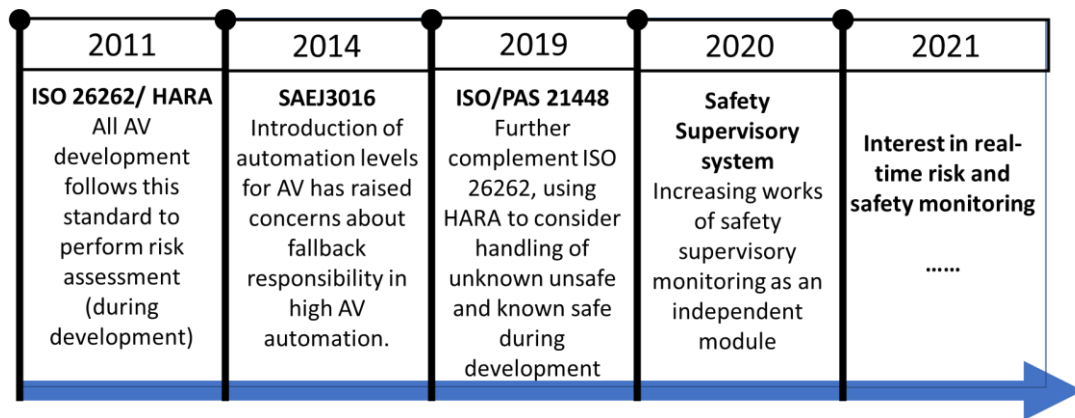


Figure 2.2 Timeline of risk assessment for AV

Figure 2.2 depicts the evolution of AV risk assessment over the years. In 2011, the ISO 26262 standard and the HARA [1] methodology were introduced as a risk assessment and hazard identification standard for AV during development. All AV companies followed this standard to perform their risk assessment during development. As AV technologies advance, a taxonomy for AV automation, SAEJ3016, was published in 2014 [24]. This taxonomy sparked discussions [25] about the inadequacy of the existing ISO 26262 and HARA coverage for AV when it is operating in real-world conditions, especially at automation levels 4 and 5. At these levels of automation, the AV system serves as the default fallback instead of the driver when hazards are identified. One proposed approach is to enhance the HARA process with Safety Of The Intended Functionality (SOTIF) considerations, which was later released as an ISO/PAS 21448 standard in 2019 [26]. These added considerations require the HARA process to define “unknown unsafe” and “known unsafe” conditions as potential hazards and their corresponding defined control actions to reduce their impact. Even with the addition of SOTIF to HARA, these risk assessments with control actions are only conducted and tested during development. However, the environment in which the AV is tested during development may differ in a real-world setting, and the planned control actions might not respond as intended. Instead, these control actions might sometimes have adverse effects and could turn into a risk.

The current challenge lies in the difficulty of understanding and measuring how predefined control actions behave in real-world situations, operating in real time deployment. Since it is impossible to account for all possible scenarios during development, new methods, such as safety supervisors [27] are being proposed to safeguard against unpredicted behaviours and incorporate parametric constraints that reflect the malfunction events. Additionally, employing real-time monitoring as a separate module is proposed in the works of [28]. These led to the interest in real-time monitoring of AV for risk and safety purposes.

## **2.3 Static risk assessment**

Static risk assessment defines the risk assessment performed during the AV's development, where the requirements for risk assessment are defined based on past lessons learnt and know-how. These requirements include the determination of the severity of hazards, the probability of occurrence and the controllability of the event, which are achieved by subjective humanistic conversions of contextual events into rule-based ratings. This section provides a comparative review of the existing static risk assessment methodology, highlighting the strengths, limitations, and areas that require further attention.

### **2.3.1 Process-based risk assessment**

This section shows a list of static risk assessments, as shown in Table 2.1 that use process-based methodology. The ISO 26262 with HARA is listed in the table as a reference focusing on vehicle-level malfunctions, while other existing works [29-32] focus on both vehicle-level malfunctions and environmental-level hazards. The unique approaches for each existing work are indicated in Table 2.1.

## 2.3 Static risk assessment

Table 2.1 Static risk assessment using process-based methodology

Research papers	Static risk assessment (process-based)		
	Vehicle	Vehicle & Environment	Unique approaches
HARA (reference) [33]	Yes	No	No
[29]	Yes	Yes	Iterative refinement
[30]	Yes	Yes	Iterative refinement
[31]	Yes	Yes	Skilled graph
[32]	Yes	Yes	Situational consideration

HARA is defined within part 3.6 of ISO 26262 [18], and it involves the identification of all relevant operational situations and operating modes, known as item definitions, during the vehicle development phase [33]. Hazards are identified based on past lessons learnt and expert know-how. The exposure of these hazards to the AV and its controllability are also assessed. These ratings then determine the Automotive Safety Integrity Level (ASIL) classification outcome, as shown in Table 2.2. For example, during development, if the AV developer defines the HARA's item as "a wrong status of the driving mode occurs, fatal accidents can happen during a parked mode," the severity is rated as S3. The probability of occurrence, known as exposure, is rated at E2, and the safe controllability of the autonomous driving system that responds to this event can be rated as C1. Based on these ratings, the resulting ASIL is determined as "QM", as shown in Table 2.2. "QM" indicates that no further safety action is required (indicated as QM in the green box). However, this process is highly subjective, and a different AV developer may determine that further control actions are necessary (indicated as ASIL A in the red box) based on a different controllability rating, C2. This identification method is subjective and is based on the humanistic rating of Severity, Exposure and Controllability. The risk assessment is therefore performed based on the presumption of the risk severity during development, which may not reflect the real-world situation in actual deployment.

## 2.3 Static risk assessment

Table 2.2 HARA ASIL classification table (QM indicates that no further action is required)

		Probability Class	Controllability class		
			C1	C2	C3
Severity Class	S1	E1	QM	QM	QM
		E2	QM	QM	QM
		E3	QM	QM	A
		E4	QM	A	B
	S2	E1	QM	QM	QM
		E2	QM	QM	A
		E3	QM	A	B
		E4	A	B	C
	S3	E1	QM	QM	A
		E2	QM	A	B
		E3	A	B	C
		E4	B	C	D

In [29], an additional iterative process was added within HARA to identify the dimensions of each hazardous event and refine the functional relationship between the HARA and item definition process within ISO 26262. The strength of this proposed method is that it advocates a broader scope for hazard analysis and considers the entire vehicle's function and environment, thus avoiding overly narrow specifications. The iterative approach is supported by using root cause "trees" to identify hazards' potential causes using generic situations. However, this refinement is constrained by the defined generic situations using a subjective and contextual approach, which will differ in a real-world setting. This proposal aims to improve the HARA process but does not improve the risk assessment coverage for AV operations.

In [30], a secondary iterative loop is introduced to extend the work of [29]. The approach uses item refinement to address malfunctions, hazards, hazardous scenarios, safety goals, ASIL, and safety refinement towards the overall safety concept. Similar to [29], [30] further broadens the scope of hazard analysis through an additional iterative process. However, the outcomes are similar to [29], which provide a subject and contextual approach with an extensive description of the hazardous scenario, its consequences and its rationale. This approach is suitable for static risk assessment but with insufficient risk assessment coverage for AV operations.



## 2.3 Static risk assessment

[31] address the identification of hazardous events using the item definition within ISO26262 and the HARA process. The method proposed by [31] combines a skill graph as a functional model and an overall scene definition to identify potential hazardous events. A skill graph illustrates how different components or skills relate to each other while representing the system's capabilities, interactions and dependencies. Figure 2.3 shows an example of an AV skill graph with its identified components and skills related to AV operations. [31] provides a guided approach compared to [29] and [30] as it links specific skills related to the hazard in an overall scene. The main weakness of [31] is that its primary focus is identifying hazardous events rather than refining the overall risk assessment process.

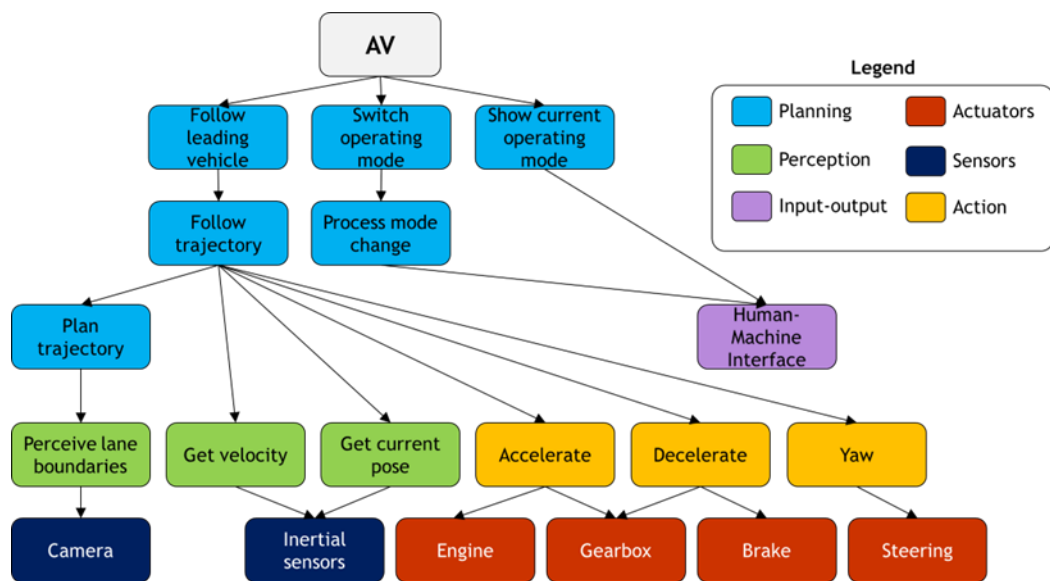


Figure 2.3 Skill graph of an AV categorised into different components or skills

[32] reviews the definitions of scenes, situations and scenarios for AV design and testing that contribute to risk assessment considerations. A scene is defined as a snapshot of the environment, including scenery, dynamic elements, all actors and observers' self-representations and the relationship among those entities. A situation is the entire circumstances to be considered for the selection of appropriate behaviour patterns at a particular time. A scenario describes the temporal development between several scenes in sequence. The outcomes of this

## 2.3 Static risk assessment

---

work assist in the taxonomy in terms of scene, situation and scenarios but do not contribute directly to the technical determination of risk assessment.

### **Summary of existing process-based risk assessment**

[29] and [30] illustrate using an iterative refinement process in HARA to provide more detailed dimensioning and hazardous event descriptions. This provides a more concise safety goal as the mitigation actions for the AV. Other than using iterative loops within HARA, [31] used a skill graph as a functional model and an overall scene definition to represent the relationship of the potential hazardous event. It provides a complete description of the scene in terms of the hazardous relationship instead of using iterative loops. [32] provided alignments in the definition of scene, situation and scenarios, which will assist in the risk assessment approach to identify hazardous events. The work of [29] and [30] combined with [31] could enhance the overall quality of risk assessment during development by expanding the scope for hazard analysis and identifying hazardous events. This is accomplished by incorporating more iterations with deeper consideration of hazardous events and the process of pinpointing their causes. These methods for identifying risk and its control actions are based on subjective human intervention to translate potential malfunctions and hazards, past lessons learned, and know-how into a process-based static risk assessment. Existing process-based methodology relies upon human intervention for static risk assessments. However, this process-based methodology aims to pinpoint clearer safety controls based on a library of past lessons learnt and know-how, which are subjective and might not reflect the situations in real-world AV operations.

### **2.3.2 Model-based risk assessment**

This section explains three existing static risk assessments using model-based methodology, as shown in Table 2.3. The model-based methodology aims to quantify vehicle malfunctions and environmentally hazardous events by converting them into numerical representations.

## 2.3 Static risk assessment

---

Table 2.3 Static risk assessment using model-based methodology

Research papers	Static risk assessment (Model-based)		
	Vehicle	Vehicle & Environment	Unique approaches
[34]	Yes	Partial on environmental roads	Numerical Cost Function
[35]	Yes	Yes	UML
[36]	Yes	Vehicles on road	Discrete Normalized Drive Area

[34] focuses on assessing lane-keeping vehicle risk assessment using a symbolic numerical approach to optimise the trajectory of AV towards the road's path. Therefore, the approach indicates a higher risk if the vehicle is not within the lane. The risk value is determined using a numerical cost function model that mimics the vehicle's movement along an arbitrary track using low-order polynomials. This method's key purpose is to provide a quantitative numerical cost function to represent the error in achieving lane-keeping and collision avoidance. This error figure allows an objective conversion of risk into Severity instead of subjective human intervention. However, it is important to note that the scope of this method is limited to vehicle lane-keeping within environmental roads only. The simulation results did not address unclear lane markings, which would have led to the inability to detect lanes accurately.

[35] presents a framework for systematically documenting and analysing hazardous events and their associated risk causes. This framework leads to a clear Fault Tree Analysis [37]. The Unified Modelling Language (UML) model, as described in [35], utilises fault-type guide-words and a structured set of scenarios to identify relevant risk causes. This is conducted in the context of Hazard Analysis and Risk Assessment (HARA) during the requirements engineering process. The approach further uses object constraint language validation checks to eliminate irrelevant risk causes and map the HARA table to the UML model. The work of [35] is similar to the outcomes of the process-based approach except for table-based mapping with contextual inputs, which is further strengthened with the use of a

## 2.3 Static risk assessment

---

UML model in [35] to trigger mapping for faster and improved software development. This modelling method can be extended to model-based scenarios [38] and model-based safety analysis [39] to further enhance the understanding of hazardous events and their corresponding safety responses. The UML model aims to improve the risk assessment process with a guided approach. However, this approach is limited to known lessons learnt and know-how, where the risk of undefined scenarios is not included within the UML model. Thus, it is not suitable for real-world AV operations.

In [36], a model is developed to determine the drivable area by projecting the vehicular path and considering surrounding vehicles. This model assesses drivable areas and measures time to collision as a method of risk assessment. The findings of [36] aim to provide a quantitative outcome based on the drivable model and time to collision through simulations. These results are intended for use in static risk assessment during the development of autonomous vehicles, as mentioned in [36]. However, [36] does not take into account of pedestrians and other road users, and the model is only demonstrated with simulation. This approach heavily relies on a potential risk field, which will be further explained in the section on real-time risk assessment.

### **Summary of model-based risk assessment**

The model-based static risk assessment approaches listed in Table 2.3 have different focus areas. In [34], a cost function is used for lane-keeping and collision avoidance, while [35] uses the UML approach to identify the root cause of hazards. Additionally, [36] provides a risk indicator for the drivable areas in the vehicles, focusing on areas of highways and regulated traffic intersections. [34] and [36] quantify certain aspects of hazardous events into numerical representations or based on rule-based tables to convert them into numerical ratings. [34] and [36] are demonstrated by simulation, which lacks real-world considerations, and [35] introduces a model that relies on a process-driven approach, which is only suitable during development. Thus, all three works demonstrate static risk assessment and neither work is sufficient to be considered for a real-time risk assessment approach.

### 2.3.3 Probabilistic-based risk assessment

The probabilistic-based methodology for risk assessment systematically evaluates potential hazardous events and provides quantitative measures based on their associated probabilities. Probabilistic-based approaches are divided into two main approaches: Bayesian or Frequentist [40]. These two approaches can also be used as probabilistic methods to perform AV system risk assessments. Probabilistic methods generically provide quantitative measures and are suitable for static and real-time risk assessment. Table 2.4 shows [41] and [42] which use probabilistic risk assessment to detect occlusion within a scene. Occlusion determines the possibility of collision due to objects that are blocked in a normal field of view. A higher probability of occlusions indicates a greater risk of collision.

Table 2.4 Static risk assessment using probabilistic-based methodology

Research papers	Static risk assessment (Probabilistic-based)		
	Vehicle	Vehicle & Environment	Unique approaches
[41]	Yes	Partial for occlusion aware	Cartesian
[42]	Yes	Partial for occlusion aware	Probability of emerging vehicle

[41] identifies object occlusions by considering sensor limitations on unseen areas. For example, a radar might only detect object A if object B is occluded by object A. Therefore, a potential high collision risk can occur when the undetected object B moves towards the radar. This work covers both observed and unobserved regions at urban intersections and can be used for route planning or control to prevent collisions. However, a clear road layout is required to quantify the risk in advance and the limits within the drivable area.

[42] uses a probabilistic collision risk assessment to estimate the risk of a potential collision with a vehicle in an occluded area. This is achieved by identifying the most probable chance of an occluded vehicle entering a mathematically defined occluded region and then estimating the probabilistic collision risk based on the

## 2.3 Static risk assessment

---

speed probability of the emerging vehicle entering the boundary of interest into the sight of the AV. This technique was demonstrated with alleyways, merged lanes and blockage by bulky vehicles and used an assumption that vehicles follow predefined roadways and remain within the lanes. However, in real-world situations, vehicles might not always follow predefined roadways. Moreover, pedestrian occlusion, which is not considered, can also occur within these stated scenarios.

### **Summary of probabilistic-based risk assessment**

Both methods, [41] and [42], require a precise intersection map with accurate road information. They match the current environment to the map data and use a probabilistic approach to identify occlusions. This approach assesses risk at a broader traffic level rather than from a single AV perspective. These methods are designed to enhance static risk assessment using real-world map data. However, within the reported work, only simulations are demonstrated without usage in real-world AV operations or scenarios. Additionally, they have not been compared to real-time occlusion filter techniques, such as the widely used Kalman filter [43] that is commonly implemented in existing AVs. It is important to note that these methods focus specifically on occlusion, which can be a factor for risk assessment considerations. However, they do not address the purpose of risk assessment, making them unsuitable for real-time risk assessment purposes.

### **2.3.4 Probabilistic and model-based risk assessment**

Probabilistic and model-based methodologies for risk assessment present the advantage of having deterministic outcomes with a mixture of quantitative and qualitative results. The deterministic nature is extracted from the model-based methodology. Table 2.5 shows the use of probabilistic and model-based approaches [44-46]. All three approaches are unique and apply to both vehicles and the environment.

## 2.3 Static risk assessment

---

Table 2.5 Static risk assessment using probabilistic and model-based methodology

Research papers	Static risk assessment (probabilistic and model-based)		
	Vehicle	Vehicle & Environment	Unique approaches
[44]	Yes	Yes	Modelling of ADS & Probability of occurrence of the hazardous event
[45]	Yes	Yes	Probability of damage with UML model
[46]	Yes	Yes	Equivalent forced-based theory on the traffic safety field concept

[44] proposes modelling of the autonomous driving system into functional blocks and, through the functional blocks, to identify and quantify hazardous scenarios. The approach attempts to use pre-defined hazardous scenarios to verify and validate AV without relying on mileage-based testing. The paper proposes theoretical modelling of the autonomous driving system into functional blocks and, through the functional blocks, to identify and quantify hazardous scenarios. The approach consists of a probability spread of the potential Severity rating (related to the classified hazardous scenario) and a probability segmentation of the occurrence (based on the hazardous event within scenarios). The final step correlates to the concept of ASIL methodology, where there will be a maximum probability for each rating. This approach proposed improvement to the HARA process by introducing environmental modelling and probability assignment of conditions. Therefore, [44] focuses on pre-defined hazardous situations categorised under static risk assessment since the autonomous driving system modelling aspect requires human intervention to update and refine hazardous situations. Moreover, it is not possible to consider all pre-defined hazardous situations beforehand.

[45] uses the probability of damage to assess the context of risk assessment and uses a model-based UML class diagram to visualise the hierarchical scenario description language for all the descriptive possibilities of scenarios being research. The probability of damage is dependent on the probability of collision. The collision probability is based on the selected scenario while considering the

## 2.3 Static risk assessment

---

specified behaviour of the AV. The highlight of this approach resides in the detailed involvement of adaptive risk analysis, which considers dynamic scenarios in terms of the probability of collision. However, any changes to AV systems, such as the UML modelling in [45], will require human intervention. Thus, this work is classified under static risk assessment.

[46] proposed a model that uses equivalent force based on concepts from the traffic safety field [47]. It assesses traffic risk by analysing the kinetic energy of colliding objects and approximating the risk level based on the actual situation. The kinetic energy is then translated into an equivalent force that describes the traffic risk. The approach also focuses on tracking multiple uncertainties in radar clusters or vision target object occlusion using the Dempster-Shafer theory probabilistic/evidence theory-based detection level, achieved by multi-object perception. [46] uses kinetic energy to differentiate between objects without a clear identification of the object or consideration of where the object resides (road, pavement, etc.). This may cause unwanted risk, and the proposed method was mainly demonstrated for straight roads.

### **Summary of probabilistic and model-based risk assessment**

[44], [45] and [46] provided quantitative measures involving vehicles and environmental considerations with probability theory involved. All three papers focus on the domain of vehicles and the environment throughout the development lifecycle. [45] and [46] emphasise the significance of identifying collision risks as a potential indicator and assessing severity, hazardous events, and their frequency of occurrence. Both [44] and [45] relied on some lessons learnt and domain expertise to pre-defined hazardous scenarios or UML modelling, which limits their real-time applicability. These research also lack realistic examples to illustrate their concepts. [46] is limited by its focus on straight roads, which restricts its use in real-world deployment in real time. Thus, all three approaches only partly fulfil the gap for real-time risk assessments.



## 2.4 Real-time Risk Assessment

Real-time risk assessment involves evaluating the AV's control actions when a hazard is identified during its operations. This control action can be a part of a vehicle's function or movement, and the hazard could stem from vehicle malfunction or environmental events. The detection of these actions and hazards occurs in real time, using either quantitative or qualitative methods. If the control actions or hazardous detection are presented with qualitative outcomes instead of quantitative measures, it indicates that these control actions cannot be effectively employed in real time. Consequently, this approach is not a comprehensive solution and requires further improvements in future development phases. This section examines existing research relevant to real-time risk assessment, highlighting the strengths, limitations, and areas needing more attention.

### 2.4.1 Process-based real-time risk assessment

This section explains three real-time risk assessments using process-based methodology, as shown in Table 2.6. All three approaches have their own unique approaches and apply to both vehicles and the environment.

Table 2.6 Real-time risk assessment coverage using process-based methodology

Research papers	Real-time risk assessment (process-based)		
	Vehicle	Vehicle and Environment	Unique approaches
[48]	Yes	Yes	Dynamic risk assessment
[49]	Yes	Yes	Real-time ASIL
[50]	Yes	Yes	Quantitative Risk Norm

In [48], a dynamic risk assessment is achieved by implementing a concept of safety barriers based on the real-time AV's task planning process. A safety barrier is an obstacle, obstruction, or hindrance that may prevent an action or event from occurring. The task planning process selects possible scenarios, assesses each

scenario's risk, and chooses the optimal scenario with low risk. The advantage of this method is that it provides alternative path planning when a scenario is deemed risky. However, the existing safety barrier concept in a process flow-based configuration may miss out on situations during AV operations. Additionally, the approach in [48] has a heavy contextual approach that is difficult for real-time dynamic use due to the process-based approach. Moreover, the paper did not provide illustrative examples to demonstrate the effectiveness of this concept.

[49] demonstrates another process-based approach using real-time ASIL determination as part of the dynamic tactical decision-making framework. The vehicle and oncoming object velocity are mapped into a Severity rating within the real-time ASIL process. The process will then determine its ASIL rating. Thereafter, the decision and control of the real-time ASIL will provide a control action. The control action process was explained in a descriptive context without simulation or test results to illustrate the process further. One drawback of this work is the lack of explanation of how control and exposure are determined in real time. Thus, the approach recommended a framework slightly modifying the existing ASIL approach using real-time AV elements but only at a framework level.

[50] proposed tailoring of the HARA process for AV with an approach known as quantitative risk norm. The quantitative risk norm measures the frequency of an incident with a consequence class, such as fatalities or severe injuries. The respective quantitative risk norm is then used to map corresponding safety goals. The quantitative risk norm uses an incident classification process to assist in the determination of the quantitative risk norm. The drawback of this approach is that it requires recording of past incidents for quantitative risk norm to support real-time safety goals accurately.

#### **Summary of process-based risk assessment**

[48], [49] and [50] emphasise the importance of measuring real-time performance and mainly provide a descriptive process framework. For example, [48] used a safety barrier process, [49] proposed a real-time ASIL and [50] suggested tailoring HARA with quantitative risk norm process considering the frequency of past

incidents and their consequences. In these works, some attempts suggest partial conversion of qualitative to quantitative data, but they are insufficient to support a real-time end-to-end approach. These works, [48], [49] and [50] also did not substantiate the framework with simulation or realistic use cases.

### 2.4.2 Model-based real-time risk assessment

This section explains two existing works of real-time risk assessments using model-based methodology, as shown in Table 2.7. Both approaches focus mainly on vehicle-to-vehicle interactions.

Table 2.7 Real-time risk assessment coverage using model-based methodology

Research papers	Real-time risk assessment (Model-based)		
	Vehicle	Vehicle and Environment	Unique approaches
[51]	Yes	Partial, for vehicle-to-vehicle	Risk repulsion
[52]	Yes	Partial, for multi-vehicle and weaving area	Risk potential field theory

In [51], a quantitative risk figure for collision prevention (in the case of a vehicle-to-vehicle) is proposed. The concept is based on vehicle risk evaluated using field theory [53]. The paper introduces a unique term, risk repulsion, which is inversely proportional to time to collision. The risk repulsion figures increase exponentially when the difference in speed increases and the distance between the rear and front vehicle becomes smaller. In this approach, the real-time crash prediction is modelled using risk repulsion.

[52] further extended the concept from [51] from vehicle-to-vehicle into multi-vehicle weaving in and out of roads with lane information. The baseline approach of [52] builds on the field theory introduced in [53], similar to [51], but increases the complexity by considering multiple interfaces among multiple vehicles, as opposed to one-to-one communication in [51].

### Summary of model-based risk assessment

Both [51] and [52] have limitations for real-time risk assessment because they only detect vehicle risk and not pedestrians. Moreover, both works focus mainly on highway lane convergence. In addition, implementing field theory would require all vehicles to share their vehicular information with the ego vehicle or backend. However, this approach has drawbacks when there is a mixed fleet of vehicles with and without connectivity, leading to missed risk when unconnected vehicles come close to the ego vehicle. Specifically for [52], a macro view of the traffic situation is needed. Ensuring all vehicles have connectivity to the ego vehicle is challenging, which may be the reason why results are simulated or calculated but lack real-world testing. In summary, both approaches only partially address the gaps identified for real-time risk assessment.

#### 2.4.3 Probabilistic-based real-time risk assessment

This section explains two real-time risk assessments using probabilistic-based methodology, as shown in Table 2.8. This research focuses on using vehicle motion and time to collision to determine probabilistic collision risk.

Table 2.8 Real-time risk assessment coverage using probabilistic-based methodology

Research papers	Real-time risk assessment (probabilistic-based)		
	Vehicle	Vehicle and Environment	Unique approaches
[54]	Yes	Yes	Collision risk vehicle and risk network
[55]	Yes	Yes	Conditional Monte Carlo Dense Occupancy Tracker

In [54], a risk assessment that integrates network-level collision prediction with interaction-aware motion models under a bayesian framework was proposed. The approach uses dynamic bayesian networks, a form of probabilistic graphical model. With this, [54] focuses on the risk of collision at the vehicle and network levels. Network level refers to the safety context of the road segment on which

the AV is travelling, taking into account safe traffic and collision-prone conditions over time. The approach for the network-level collision was supported by basic AI classifiers such as k-Nearest Neighbour or Gaussian processes. Two of the unique approaches of this proposal are the collision risk network-level and collision risk vehicle level. Since a dynamic bayesian network is considered a form of spatial-temporal approach, there is a forward improvement of the current information, which is dependent on the past. Therefore, some basic aspects of learning from the past are applied to this approach.

In [55], the probability of collision risk between the vehicle and the environmental object was used. This was achieved by dividing the scene into cells, and the collision risk occurs when grids overlap in the future prediction of the vehicle movement and the identified object. These cells represent the environment like a grid-based system which is known as a conditional monte carlo dense occupancy tracker [56], which can estimate the probability of collision for each cell in the grid. The mentioned approach in this context also explains the use of time-based propagation, which fits well for real-time usage.

#### **Summary of probabilistic-based risk assessment**

[54] and [55], methods were tested using simulated data and environments. [54] suggested that using a dynamic bayesian network could resolve the challenge of consolidating extensive data from sensors during real-time risk assessment and present the risk of collision with vehicles at the macro level. Moreover, this approach focuses on the risk of collision rather than the control actions of the AV with its surroundings. Thus, for the AV to perform specific improvements from the results of this approach might be challenging. Without specific mention of pedestrians, this approach focuses mainly on highways. On the other hand, [55] utilised a conditional Monte Carlo dense occupancy tracker method that represents the environment as a grid. However, these grids lack further details such as environmental classification (e.g., roads and pavements) to assist in risk assessment. The method focused only on detecting moving objects with the conditional Monte Carlo dense occupancy tracker grid. Both approaches also highlighted the importance of real-time risk assessment and suggested that using

vehicular-to-vehicle data sharing would be overly intensive for data integration in real time. However, both methods have drawbacks, such as not considering pedestrians and missed risk when unconnected vehicles come close to the ego vehicle. Thus, the presented probabilistic-based approaches are insufficient to address the gap identified for real-time risk assessment.

#### **2.4.4 Probabilistic and model-based**

This section identified one example [57] that illustrates the use of probabilistic and model-based real-time risk assessment. [57] considers both vehicle and environment and has its own unique approaches of using Bayesian hierarchical spatial random parameter extreme value model.

[57] introduced a safety assessment based on the bayesian hierarchical spatial random parameter model based on extreme value theory [58]. This approach estimates two real-time safety metrics: the risk of crash and return level, using the time to collision as a conflict indicator. For instance, if the time to collision is zero as the conflict indicator, the risk of crash is almost certain. Return level is measured in terms of safety levels as opposed to risk of crash. Therefore, the risk of a crash is used to measure unsafe conditions, while the return level is used to gauge safe conditions. To determine the risk of crash, the approach utilises the generalised extreme value distribution of the bayesian hierarchical spatial random parameter. This method requires historical data, which is obtained from trajectory data collected from a fleet of AVs that have traversed a particular scenario multiple times.

[57] employs Bayesian probability techniques and time-to-collision model-based methodologies for real-time safety assessment at a macro level, considering a non-AV perspective. It is designed for the macro traffic level rather than the vehicular level. This approach demonstrates the effectiveness of combining a probabilistic approach with modelling to enhance risk indicators based on past data. However, some limitations of the approach include its lack of focus on pedestrians and its difficulty in implementation from the viewpoint of AVs, as local sensors may have limitations in providing a broader macroscopic view. As a result, this approach

may be better suited for real-time risk assessment from a city or macroscopic perspective instead of an AV-focused viewpoint.

#### **2.4.5 AI, Neural Network-based real-time risk assessment**

This section provides an overview of how neural networks are used in AV for risk assessment. Neural networks can be used statically or in real time as part of the AV system or as an end-to-end approach [59]. The use of neural networks in risk assessment depends on the methodology used and whether the inference time is suitable for real-time operations.

Supervised learning is typically preferred when it comes to using machine learning for safety-critical systems. It serves as the foundational technique for object recognition and lane-keeping [60]. Unsupervised learning is utilized to identify patterns and trends with unlabeled data or as a redundancy system [61] to enhance the basic AV system. In recent years, reinforcement learning algorithms have been employed to support path-planning goals with rewards [62].

From another perspective on general AI, an alternative method of classification was described in [63] and [64], where AI is further categorised into physics-based [43, 56], manoeuvre-based [65] and interaction-aware-based models [54, 57, 66]. With the growing trend of utilising cameras in AV, computer vision-based neural networks have also become fundamental within an AV system for risk assessment. This falls into the particular area of manoeuvre-based approaches with the detection of motion patterns. Therefore, before reviewing real-time risk assessment using AI, a background introduction will be explained first on how neural networks for computer vision are used for AV.

**Different types of neural networks for computer vision used within AV**

Table 2.9 neural network for computer vision used within AV

Research papers	Unique approaches
[67]	Object detection
[68, 69]	Semantic segmentation
[70, 71]	Panoptic segmentation
[72]	Instance segmentation

Table 2.9 shows different types of neural networks for computer vision used within the AV [67-72].

Object detection [67] and instance segmentation [72] are used for countable objects, while semantic segmentation [68, 69] aims to identify uncountable objects such as pavements, roads, and offroad regions to identify the scene. On the other hand, Panoptic segmentation [70, 71], identifies both landscapes and object identification. However, increased inferencing time for each image results in low frames per second and renders them unsuitable for real-time [73] purposes. Similarly, for instance segmentation, more inferencing time is needed as it performs object detection first and thereafter, semantic segmentation of the identified object.

Object detection is a widely used technique in AV [67] in recent years. It began with traditional detectors such as histogram of oriented gradients [74], which posed challenges in adjusting the bounding box for different dynamic scenes and rotation by creating blocks within images. Deformable part models [75] recognise objects using a combination of graphical models with root filters, part filters, and spatial modes. While these traditional detectors achieve a high level of accuracy, they have a detection time of less than one frame per second, making them unsuitable for real-time processing [76]. Real-time risk assessment requires a detection rate of at least 10 frames per second to match the data acquisition of an input camera and allows sufficient time for the AV to react.



With the introduction of deep learning, techniques such as convolution neural network based two-stage Detectors like region-based convolutional neural networks [77] use regional proposals to achieve a higher accuracy but with more inferencing time (up to a few seconds per image). Faster region-based convolutional neural networks [78] reduce the inferencing time and can achieve up to 5 frames per second with a mean Average Precision (mAP) of 42.7% and Intersection Over Union (IOU) of 0.5 using Common Objects in Context (COCO) dataset. However, two-Stage detectors have difficulty achieving real-time for typical edge systems deployed in AV. Therefore, the coarse-to-fine processing for the two-stage detector results in missing events between frames from an input camera. One-Stage Detectors like Single-Shot Detector (SSD) [79] and variants of You Only Look Once (YOLO) are considered suitable in object detection to balance frames per second and accuracy. SSD [79] achieved a mAP of 46.5% with IoU of 0.5 with 59 frames per second using COCO dataset to obtain improvements to the multireference and multiresolution technique for small objects. This was considered acceptable for the frame per second, but the mAP is relatively low for real-time usage.

The evolution of YOLOv5 from YOLOv3 (comparable to SSD) surpassed the performance of SSD with VOC07 dataset a mAP = 63.4% (on the large model), with IoU of 0.5 and 45 frames per second. In recent years, YOLO variants such as YOLOv6, YOLOv7 and YOLOv8 have been released, focusing on the accuracies with IoU ranging from 0.5 to 0.95. In Figure 2.4, it is shown that YOLOv6, YOLOv7 and YOLOv8 have mAP improvements as compared to YOLOv5. However, this is at the expense of higher latency. Therefore, models (like tiny (n), small (s), medium (m), large (L) and extra-large (x)) should not be compared among different versions of YOLO without looking at the parameters defined (in millions), as illustrated in Figure 2.4 (the machine used in the graph is based on A100 TensorRT). In real-world applications, machines like A100 TensorRT will not be easily available nor installed in an AV. Thus, there is a trade-off between latency and accuracy. Latency also plays an important role in the product cost and overall system performance.

## 2.4 Real-time Risk Assessment

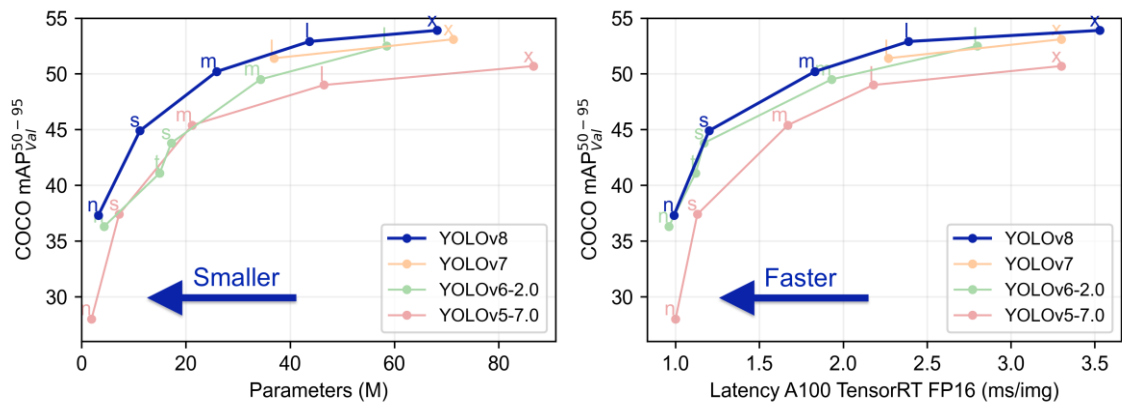


Figure 2.4 Comparison of YOLOv5, v6, v7 and v8 performance

In terms of semantic segmentation, matured methods include Fully Convolution Network [80], DeepLab [81], and Pyramid Scene Parsing Network (PSPNet) [82]. With comparisons in [82], PSPNet achieved the highest mean IoU across classes with 82.6% followed by DeepLab score of 71.6% and Fully Convolution Network with 62.2%. PSPNet inferencing time is better than that of the Fully Convolution Network and DeepLab, as shown in [83]. However, as research progressed, the performance of semantic segmentation improved over recent years with new models such as Image Cascade Network (ICNet) [83], Semantic segmentation Network [84] and Efficient Neural Network [85]. Among the three new models, ICNet has the highest mean IOU with 69.5%, but it is lower than PSPNet (82.6%). ICNet in [83] illustrated a performance of 21 frames per second using a Titan X GPU, whereas in another research, PSPNet in [86] recorded 11 frames per second using a Nvidia GeForce GTX 1070 Ti (which is closer to Jetson than V100). ICNet had a lower mean IoU, which was traded for higher frames per second than PSPNet.

Panoptic segmentation in [73] illustrates that even single-stage panoptic segmentation requires up to 100 ms of inference time, with most models requiring as high as 200-300 ms. A two-stage panoptic segmentation minimally requires 160 ms inferencing time. In the case of instance segmentation [72], performance requires similar inferencing time compared to panoptic segmentation.

This section reviewed the suitability of different neural network computer vision techniques for real-time risk assessment. It is concluded that panoptic

## 2.4 Real-time Risk Assessment

segmentation and instance segmentation are unsuitable for real-time risk assessment, while object detection has the highest capability, followed by semantic segmentation.

Table 2.10 Real-time risk assessment coverage using neural network-based methodology

Research papers	Real-time risk assessment (neural network-based)		
	Vehicle	Vehicle & Environment	Unique approaches
[87]	Yes	Yes	Risk metric
[88]	Yes	For vehicle	Deep Predictive Model (Bayesian ConvLSTM)
[89]	Yes	Yes	Uncertainty measurement
[90]	Yes	Yes	Failure detection of Semantic Segmentation
[91]	Yes	Weather	Using YOLO to detect Sandy Weather environments

Table 2.10 shows a list of different neural network-based real-time risk assessments.

In [87], Convolution Neural Network (CNN) captures the AV's front image and divides it into three sections: normal, caution and warning. The author intends to reduce the operational process needs of CNN to provide an end-to-end paradigm to provide risk directly from the camera input. The image is then fed to a risk metric calculator tool [92] to obtain a risk figure. The risk metric calculator divides the scene into grid boxes and measures the number of unoccupied boxes. The higher the number of unoccupied boxes, the risk is lower as it measures between the autonomous vehicle and its surroundings. [87] demonstrated the use of deep learning neural networks as a form of risk assessment through unoccupied grid boxes that represent risk.

In [88], Bayesian convolution long short-term memory is used as a form of deep predictive model (DPM) as an elevated approach from CNN [87]. The approach is similar in getting the risk related to the time of collision using vision-based deep

learning techniques. This predictive approach incorporates temporal information during decision-making, multi-modal information (i.e. camera and vehicle command) about the environment, and information about the uncertainty of DPM inherent in the prediction. The main objective is to improve vehicle safety by predicting future vehicle collisions in time to activate driver warning systems to recognize and anticipate dynamic catastrophic events beyond the immediate time horizon.

[89] used residual networks 8 (ResNet8) [93] to pre-process the Lidar images to detect small vehicles that occupy small grid cells, followed by Faster Region-based convolutional neural network pipeline to generate the bird's eye view 3D region proposals, followed by the use of deep neural network as the intermediate layers to extract uncertainties. Furthermore, entropy and mutual information techniques are used to classify uncertainty into epistemic or aleatoric. As compared to the generic approach, where neural networks are used to train and detect an object, uncertainties are typically not considered. The interesting result demonstrates that epistemic uncertainty is related to vehicle detection accuracy while the vehicle distance and occlusion influence aleatoric. This research outcome demonstrated an improvement of 1% to 5% in terms of detection.

[90] designed a deep neural network to predict the mean Intersection Over Union (mIoU) of the segmentation map without ground truth and introduce a new loss function for training imbalance data. The objective is to predict the mIoU and also detect the failure cases using the predicted mIoU. The approach uses the Efficient Spatial Pyramid of Dilated Convolutions for Semantic Segmentation network [94] to extract the features from the images. The failure cases are then detected by the fully convolution network for mIoU prediction. [90] is a good approach if the AV system depends highly on semantic segmentation but has an impact to the inferencing time and results in loss of image frames. This is verified by a minimum run time of at least 0.5 seconds for a frame, which is needed for a fully convolution layer to provide good failure detection.

[91] uses object detection such as YOLO with augmentation to identify sandy environments in addition to foggy, snowy and rainy environments. This study

## 2.4 Real-time Risk Assessment

---

perform tests with different YOLO models in an empirical approach with different activation functions and added augmentation with detection in adverse weather dataset.

### Summary of AI, Neural network-based risk assessment

With all the AI, Neural network-based real-time risk assessments, [87] illustrated using CARLA simulation with real-time intentions. However, no latency figures were given and with low accuracy based on the CNN model. [88] looked into a method for near-collision prediction using camera and AV information to trigger a collision avoidance system. This particular approach mainly focused on assessing risks at the vehicle level. It did not consider creating a risk assessment framework for pedestrians or accounting for the surrounding landscape. [89] presented a method for measuring uncertainty in deep learning models, aiming to improve the detection accuracy of 3D lidar using a high-quality training dataset in the Resnet architecture. However, this method was not designed to compute risk. Additionally, there was a focus on improving the accuracy of mIOU prediction [90] and using object detection, such as YOLO with augmentation, to identify sandy environments for AV in real time [91]. However, neither of these methods demonstrated the ability to perform risk assessment coverage by mapping results to a risk assessment framework like HARA, making it challenging to quantify risk.

In summary, existing AI, Neural network-based risk assessment in Table 2.10 showed that either 1) models not suitable for real-time performance with insufficient frames per second or 2) insufficient coverage for the AV vehicle and environmental detection that are not mapped to risk assessment outcomes. Thus, an end-to-end approach from the input to a determined risk assessment in real time is needed to fulfil real-time risk assessment coverage.

### **2.4.6 Cooperative mode**

Cooperative mode is evolved from existing VANET that originated in the early 2000s. Initially, VANET was a mobile ad-hoc network connecting vehicles using the IEEE 802.11p standard. With the advent of Dedicated Short Range Communication

(DSRC)/V2V, it transitioned to a new name Vehicle-to-everything (V2X) [95]. As cellular 5G has become more prevalent in recent years, V2X has evolved into using 5G infrastructure and is now known as Cellular-Vehicle-to-Everything (C-V2X or 5G sidelink) [96]. The advancement of 5G has led to reduced access times and increased bandwidth, heightening VANET's focus on safety-critical concerns such as risk factors. Initially, VANET was primarily for entertainment features, vehicle internet connectivity, and telematics functions.

Consequently, due to the limitations of AV sensors, AVs face challenges in anticipating obstacles beyond the sensors' limit. Therefore, infrastructure-based systems like Infrastructure-to-Everything (I2X) or Cellular-Infrastructure-to-Everything (C-I2X) can assist AVs in planning, particularly at high levels of automation, where the efficiency and safety of AV systems heavily depend on timely information and low latency. The need for dynamic driving task fallback for SAE Levels 4 and 5 further emphasizes this demand.

The general concept of cooperative mode for AVs encompasses various communication modalities such as V2V, V2I, I2V, and I2X, while the communication itself can be either DSRC or Cellular.

#### **Existing cooperative methodology used for AV real-time risk assessment**

Table 2.11 shows the list of cooperative mode methodologies to support real-time risk assessments for AV.

[97] illustrates a model-based methodology, while [98-100] uses a probabilistic and model-based methodology, and [101] and [102] use neural network and AI-fuzzy logic, respectively. [98, 100, 101] and [102] are suitable for V2X, where [97] and [99] focus on V2V only.

## 2.4 Real-time Risk Assessment

Table 2.11 Real-time risk assessment coverage cooperative mode methodology

Research papers	Real-time risk assessment (cooperative mode)		
	Vehicle	Vehicle & Environment	Methodology & Unique approaches
[97]	Yes	V2V	Model-based Model Predictive Control
[98]	No	V2X	Probabilistic and model-based Contextual risk-based approach
[99]	Yes	V2V	Probabilistic and model-based Human-Centric active safety (co-driver),
[100]	No	V2X	Probabilistic and model-based Global collision risk
[101]	No	V2X	Neural Network PCA-BP
[102]	No	V2X	AI-based Fuzzy risk-based approach

[97] used Model Predictive Control (MPC), which involves the optimization of a performance index concerning future control sequences and the use of predicted output signals based on a process model [103]. In this architecture, all the information from V2V is fused with sensors and radars, providing location and motion estimation. These results are passed to the rule-based multi-traffic prediction block. This block uses MPCs to make predictions for both latitudinal and longitudinal aspects. The outcome can be computed as a collision risk assessment, resulting in a probability figure.

[98] proposed a unique use of a contextual risk-based decision approach. The approach consists of a simple probability distribution known as risk values of all the detected parameters collected from V2V, such as lane information, road conditions, traffic congestions, weather, speed and time. Thereafter, the risk of a particular vehicle is determined by the likelihood and impact based on the information collected. The strength of this approach provided some aspects of model conversion of environment information into potential risk factors. However, this approach did not explain the formulation of the tables with indexes and whether they were determined in real time or only during development. This could limit real-time risk assessment determination during AV operations.

[99] used human modelling and probability to mimic the human-centric active safety control that focuses on the “intervention moment” based on prior research findings from [104]. This “intervention moment” occurs when an intervention point is crossed, representing the probability of vehicle collision. This “intervention moment” is the best trade-off between maximum collision risk and predicted human reaction time and acts as a baseline of safety in the AV that mimics human intervention in terms of 1) active safety and 2) reaction time of safety actions.

[100] translated every vehicle into its risk estimation based on two distinct components: collision probability and severity of the collision. For example, Lidar sensor data shows a risk of detected obstacles or collision with the front vehicle that applies sudden braking; both can be analysed using the methodology mentioned above. When multiple sensors are used, a further global collision risk can also be determined at the AV level. The global collision risk figure takes the maximum risk figure among each of these measured sensor sources. At the macro level, if all the AV share their perceived risk values, the identified scenario for the entire driving context can create an average risk estimator known as augmented collision risk - which is the average of all individual local vehicles to establish this risk figure. This average risk value is similar to the approach used in [105]. The latter demonstrates that using V2V relays and passing information sharing risk values from one vehicle to another allows the eventual host vehicle to have additional warning time by notifying of risk while moving towards a hazardous event. However, the approach did not include environmental considerations affecting AV safety other than the information received from other connected vehicles. The approach focuses mainly on safety improvements of using V2V but not on determining the risk assessment of AV operations.

[101] demonstrated the use of neural networks in cooperative mode risk assessment methodology using VANET, stating the specific use of Principal Component Analysis (PCA) to decorrelate the features in the infrastructure traffic data set and recombine them into a set of linearly independent features. Thereafter, a back-propagation neural network is used to train the predictive



model. In order to predict the driving risk of a vehicle using the data collected via VANET, their results are compared with the typical support vector machine approach [106]. The comparison showed a 3% to 8% improvement across the different testing records. The inclusion of PCA also contributes 1% to 2% to the improvement mentioned. However, the approach in [101] is at a macro level on driving risk instead of AV-centric. Thus, the AV control actions are not measured for risk and therefore, it is challenging to recommend safer AV operational improvements.

[102] demonstrates using an AI fuzzy risk-based decision method for cooperative risk assessment methodology. The proposed concept uses vehicle context parameters such as lane, weather, time, traffic, road and speed, and driver's attributes such as age and experience to determine risk. This risk is based on different weights used for the vehicle context and driver attributes multiplied by the impact. The extension includes further classifying the traffic and speed into low, medium, and high risk, improving mapping function formation, and determination of the weights of vehicle contextual parameters, threats, and drivers' attributes.

In summary, the works presented in Table 2.11 had theoretical, simulated or emulated scenarios tested, which might not represent real-world AV deployment. [97] and [99] was simulated using Matlab, Simulink and Carsim. [100] used SiVIC-RTMaps and VEINS with emulated scenarios, while [102] used VEINS with the recommendation of a framework, and [98] was presented as a theoretical framework. Both [98] and [102] lack a demonstration of how contextual information can be converted from images into text or numbers to fit into the framework for usability. Thus lacking an end-to-end approach. [101] analyses past accident data to gain accident risk prediction but depended too heavily on cumulative past accident data without considering near-miss or risky scenarios. All works in Table 2.11 were AV-centric except [101], which used a data analytical approach. [97] and [99] demonstrated V2V focus using the location and proximity between the host and the remote AV without considering pedestrians or scenarios with traffic lights and intersections. [100] explained the use of V2X to pass

## 2.5 Identified gaps in existing works and selection of topics for research approaches

---

information from one vehicle to another to improve safety, but without considering the increased latency that it will incur in real-world scenarios. All scenarios focus heavily on AV to AV (V2X) or AV to infrastructure (V2X). There is a missing gap in the infrastructure to provide AVs with advanced risk identification or even I2I sharing of risk information before sending it to the vehicle. A lack of end-to-end solution explaining a specific method was also evident.

### **2.5 Identified gaps in existing works and selection of topics for research approaches**

This section presents a synopsis of the gaps between current methodologies and the need for real-time risk assessment. Each of the reviewed methodologies is compared against the need to enhance the safety of AV operations further. The existing risk assessment has limitations, as stated in the motivation of this research, which are: 1) inability to perform risk assessment of the AV's control actions based on the detected hazards during AV operations in a real-world environment, 2) inability to provide granular environmental risk information that can represent even near misses, 3) inability to improve subsequent AV safety actions based on current operations without a new development cycle.

- Static process-based methodology: These approaches primarily rely on subjective humanistic qualitative decisions based on past lessons learned and know-how. As such, the outcome assists in determining a set of pre-defined safety actions for the AV based on past lessons learnt and know-how in a subjective approach that defines the hazards. Thus, this methodology confirmed the limitations of the existing approach.
- Static model-based methodology: These approaches aim to quantify hazardous events through numerical representations. Some works also incorporate rule-based tables, which convert contextual inputs into numerical ratings. This shows progress towards objective risk assessment, but the methodology is still unable to fulfil the identified limitations.

## 2.5 Identified gaps in existing works and selection of topics for research approaches

---

- Static probabilistic-based methodology: Existing works demonstrate their utility in occlusion detection, which could be added as a component to be considered an improvement for risk assessment at the AV level. However, they lack the representation of a complete risk assessment process.
- Static probabilistic and model-based methodology: This methodology provides a quantitative approach using vehicle-to-vehicle environmental information. However, it is still confined to assessing collision risks between vehicles, where time-to-collision figures between vehicles do not entirely cover the risk. Moreover, these approaches do not account for pedestrians, unregulated traffic scenarios, and risk measurement during AV operations.
- Real-time process-based methodology: In these works, rule-based tables are demonstrated to perform partial conversion of qualitative to quantitative outcomes. However, end-to-end approaches with explained frameworks, concrete algorithms, or any form of test results with deployment are lacking that could demonstrate the use of these approaches for AV operations.
- Real-time model-based methodology: This methodology focuses on vehicle-to-vehicle aspects without considering pedestrian risk. Calculations and simulations were conducted without illustrating an end-to-end approach required for real-world AV operations use.
- Real-time probabilistic-based methodology: Existing works require scene and vehicle information to be used in their methodology without considering pedestrian risk. In some works, the importance of environmental detection was included, but no specific classes of environmental identification were achieved. Only simulated data was used for these works, without real-time testing. The outcome of these approaches was unable to measure the AV's control actions and assist the AV in subsequent safety action improvements.

## 2.5 Identified gaps in existing works and selection of topics for research approaches

---

- Real-time probabilistic and model-based methodology: These works focus on safety assessment at a macro level from a non-AV point of view. It is suitable for AV fleet management, traffic accidents, and safety predictions but is unsuitable for risk assessment from an AV point of view.
- Real-time AI, neural network-based methodology: It is recognised that in terms of computer vision for real-time detection, object detection, and segmentation are suitable for use. Due to performance and inference time issues, the existing models may not be suitable for real-time implementation. Within these proposed approaches, specific domains of perception are explained as a component for safer AV, but they lack an end-to-end approach that can accurately represent the real-time risk assessment for AV operations.
- Real-time cooperative mode methodology: These works prioritise vehicle aspects without adequately addressing environmental factors such as unregulated scenarios and pedestrians. The focus remains largely on V2V without considering the impact of accumulated latency. There is a lack of work on infrastructure to support risk identification from a non-AV perspective and supply remote risk warnings to the AV prior to reaching the infrastructure location.

The above summary provides an overall critical review of existing work in AV risk assessment. From the review, the progression from process-based to other methodologies illustrates the importance of moving its approach from subjective to objective based risk assessment. This requires the conversion from qualitative to quantitative risk assessment outcomes. Existing works provided mostly partial work of risk assessment considerations, often lacking a framework for risk assessment. Those with a clear framework focus on the process's improvements and lack real-world technical illustrations and examples of deployment. On the other hand, those with a clear methodology presented simulated results, without any real-time trials, pilot or deployment. Thus, an overall real-time risk assessment framework is needed, encompassing an objective end-to-end approach

that covers key aspects of vehicles and pedestrians risk within unregulated traffic in real time. In addition, an infrastructure-based remote risk warning should be available to identify hazardous events before the AV arrives. This assists the AV in identifying risk without the implication of complex real-time processing and bandwidth requirements that will affect AV operations.

## **2.6 Summary**

The existing static risk assessment is deemed insufficient to perform a risk assessment for AV operations. Thus, there is a need for real-time risk assessment. This is because the control/safety actions from risk assessment accomplished during the development phase are insufficient to identify and resolve all situations considered during the development phase. Some control/safety actions might even bring adverse effects to passengers within the AV. Thus, a real-time risk assessment is needed to monitor the control actions of the AV with the identified risk or hazardous event. With this identified gap, existing works are reviewed based on static and real-time risk assessment to determine if these works could provide coverage for the identified gap based on different methodologies. Through this review, existing works have yet to propose a real-time framework for risk assessment, mapping sufficient vehicle and environmental situations, and illustrating the methodology with an end-to-end approach. Existing works for cooperative mode were also reviewed for remote support of hazardous detections. The review showed that there is a lack of risk assessment for AV to be supported by infrastructure, while a significant focus remains on V2V. The cooperative mode's existing approach presents a challenge regarding data integration and latency for sharing information between AVs. Therefore, the proposed solution to mitigate the identified gaps in existing systems and works should consider seven key aspects. 1) The solution should consist of an end-to-end methodology. 2) The approach should be objective without any humanistic involvement. 3) The solution should provide granular levels of risk assessment that would measure the risk performance of the AV. 4) The approach must be capable in real time processing that matches the input information of a camera. 5) The outcome should be lightweight instead of creating large amounts of data that require computationally intensive AV processing. 6) The solution should focus on areas of unregulated

## 2.6 Summary

---

traffic with high risk. 7) The solution should support V2V or I2V operations. These aspects are considered as requirements towards the proposed framework and its cooperative mode, which are discussed in chapter 3.

## Chapter 3

### 3 Real-time risk assessment framework and cooperative mode

In chapter 2, the gaps between static risk assessment and real-time risk assessment for AV operations are identified. The existing approach, which revolves around static risk assessment focusing on component-level failures or malfunctions as hazards during development, falls short of ensuring safer AV operations. Consequently, to mitigate the gaps, this thesis proposes a Real-time Risk Assessment Framework (ReRAF) within the AV and an infrastructure-based Real-time Risk Assessment Cooperative mode (ReRAC) as an additional system to bolster the safety of existing AV systems and provide advanced risk identification and timely warnings remotely in real time. ReRAF is intended for use within the AV to measure how well the AV mitigates its detected environmental risk, while ReRAC assists the AV by identifying risk and hazardous events beyond its sensory limits in the vehicle to enhance safe AV operations. ReRAF and ReRAC are developed using key requirements for risk assessment, adapted from ISO26262 and HARA, while simultaneously addressing the identified gaps. Furthermore, ReRAF and ReRAC focus on unregulated traffic scenarios that have not been research in previous studies. These scenarios pose greater risks to AVs and road users, thus requiring further assistance. The recursive data obtained from ReRAF are used to dynamically adjust the AV's safety goals and enhance path planning in real time.

### 3.1 Adaptation of key requirements

The key requirements for risk assessment reference from ISO 26262 and HARA include the following:

- **Severity:** represents the extent of harm that may be caused to the driver, AV system, and other occupants when a hazard occurs.
- **Controllability:** represents the extent to which the driver or AV system can control the vehicle in a hazardous scenario.
- **Occurrence:** represents the possibility of a system failing or being in a hazardous scenario.

The current risk assessment process is static, as it is conducted during the development phase by completing a risk assessment document filled with descriptive content. Static risk assessment defines a fixed severity/risk with a control action based on a particular scenario decided by a specific developer, and the risk associated with it does not change. Moreover, the severity of a hazard and the controllability of the system are determined based on the knowledge of the developers, which can vary between individuals and organisations. For example, the severity of detecting a pedestrian on the pavement can have different interpretations of risk from different developers. As a result, the static risk assessment is considered subjective and qualitative.

On the other hand, real-time risk assessments measure dynamic severity/risk with control actions in real time. The severity of the environment is assessed by assigning a risk value in accordance with the dynamic situation, as well as the AV's corresponding control and safety actions. Thus, a framework and cooperative approach is proposed to enhance the static risk assessment to achieve a real-time risk assessment. This enhancement is achieved by incorporating quantitative measurements instead of a qualitative approach. Different safety action improvements are planned through quantitative measures compared to fundamental collision avoidance. These different safety actions assist the AV in being safer for passengers and road users surrounding the AV. For example, the



### 3.1 Adaptation of key requirements

---

severity of detecting a pedestrian on the pavement is strictly based on a uniform quantitative risk measurement of objects detected within different landscapes (pavement or roads). Through these measures, the AV can deploy different safety actions to avoid sudden braking or steering according to the real-time exposed risk. This approach objectively evaluates severity, control, and occurrence, regardless of the developers involved or the organisation, allowing for a standardised measurement in real-time and real-world contexts. Therefore, the key components for real-time risk assessment are adapted as follows:

- **Severity:** a quantitative figure representing the risk of the detected hazard resulting in a potential collision with the AV.
- **Control:** a quantitative figure representing the autonomous driving system response to the detected hazard.
- **Occurrence:** a quantitative figure representing the average of past risk assessment outcomes at the AV level or the probability of occurrence for remote warnings at specific locations and time durations.

In addition to the adapted key requirements from ISO 26262 and HARA, seven requirements are summarised from the identified gaps in section 2.5, forming the added requirements for the novel creation of ReRAF and ReRAC. These are listed below.

1. The solution should be an end-to-end methodology.
2. The approach should provide an objective outcome instead of a subjective translation of severity and/or control through human intervention.
3. The solution should provide a more granular level of risk assessment in place of a simple rule-based table to illustrate different risk levels.
4. The proposed approach must be capable of real-time processing in terms of frame per second.
5. The outcome should be lightweight, thus reducing complexity in data integration.

### 3.2 Overview of Real-time Risk Assessment Framework (ReRAF) and Real-time Risk Assessment Cooperative mode (ReRAC)

---

6. Testing should take place in areas of unregulated traffic where high-risk indications can help to avoid accidents
7. The solution should support V2V or I2V operations.

### **3.2 Overview of Real-time Risk Assessment Framework (ReRAF) and Real-time Risk Assessment Cooperative mode (ReRAC)**

The objective of ReRAF is to provide a real-time risk assessment of the AV's control actions based on the detected environmental hazards within the AV, which existing static risk assessments do not measure in real time. ReRAC, on the other hand, provides the AV with remote real-time risk and hazard warnings based on the nearest infrastructure setup. This section provides an overview of the two approaches, their design concepts, and their respective methodology.

Figure 3.1 shows an overview of ReRAF and ReRAC. ReRAF resides within a Risk Assessment Module (RAM), an independent system that assesses the AV's risk while operating in real time. RAM contains a database that stores the risk assessment outcomes with the given timestamp in the spatial and temporal domains. Existing camera systems within the AV provide the environmental scene to the ReRAF. These environmental scenes are converted into a risk figure known as Severity. Severity is defined as a risk figure representing a potential collision between the AV and the detected object residing on roads or pavement. With environmental risk, the AV's response to these severities is known as Control. Control is determined by parametric inputs, which include steering, speed, brake, and throttle. ReRAF then determines the real-time risk assessment based on Severity and Control. These risk assessment outcomes are stored in the AV database. Occurrence is determined from the accumulated risk assessment results in the database, and potential hotspots at different locations over different iterations of AV operations are identified. The 5G connectivity is for receiving remote risk and hazard warnings from ReRAC and data synchronisation with the backend database. Lastly, the localisation provides temporal and spatial information as timestamps.

### 3.3 Real-time Risk Assessment Framework (ReRAF)

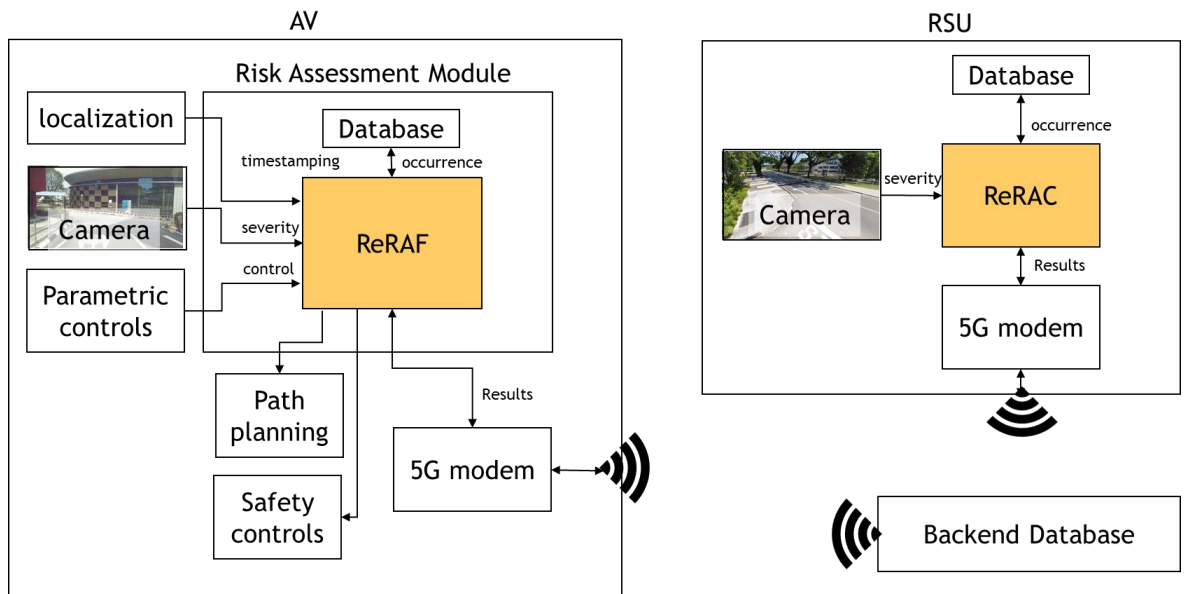


Figure 3.1 Overview of ReRAF and ReRAC

ReRAC resides within a Road Side Unit (RSU) and provides the severity of the hazardous event detected from the environmental scene through an RSU camera mounted at an elevated height for more extensive environmental coverage. The Occurrence is represented by past ReRAC data from the accumulated information in the RSU's database. Since ReRAC is infrastructure-based with fixed geolocation, ReRAC only considers Severity and Occurrence. The ReRAC outcomes are sent to the backend database via 5G. The AVs receive the remote risk and hazard warnings via the backend database (I2V) through its 5G modem based on their proximity to the RSU using the AV's current location and path routing as a reference. With multiple RSUs installed and ReRAC deployed, the outcomes of each RSU are consolidated at the backend. The AV only pulls the data from the RSU nearest to the location of the AV.

### 3.3 Real-time Risk Assessment Framework (ReRAF)

This section explains the design concept of ReRAF, its methodologies and algorithm, tested scenarios, and datatype illustration. The design concept is formulated based on the requirements identified in section 3.1. Various methodologies are employed to meet these requirements, culminating in the development of ReRAF's algorithm. These methodologies are then tested in

### 3.3 Real-time Risk Assessment Framework (ReRAF)

selected unregulated traffic scenarios, and examples of ReRAF data and their datatypes are illustrated.

#### 3.3.1 AV ReRAF design concept

This section explains the design concept of ReRAF. Specifically, it describes the conversion of adapted Severity and Control into quantitative outcomes. These outcomes are Risk Tag (RT) figures, Control Tag (CT) figures, Predicted Risk Number (PRN), AV's Time To Collision (AV-TTC), and Occurrence used for real-time risk assessment.

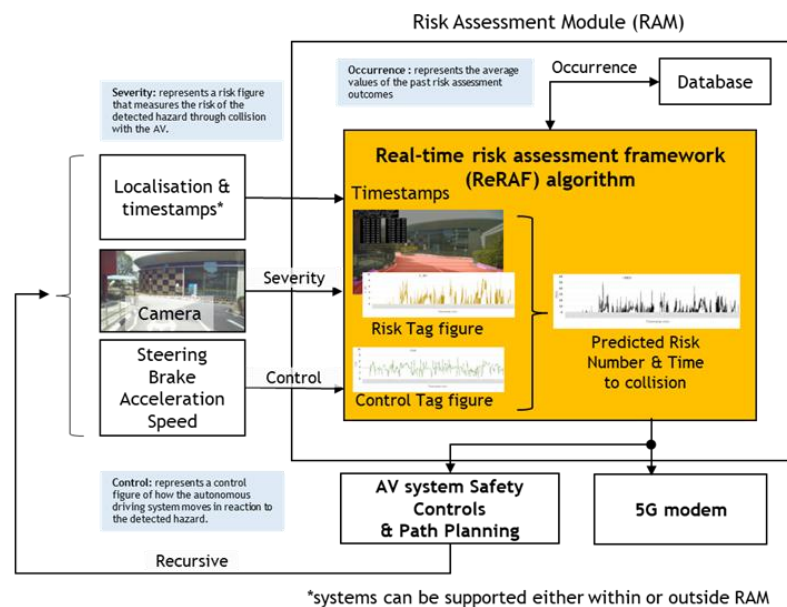


Figure 3.2 Overview of ReRAF

Figure 3.2 shows the overview of ReRAF. ReRAF obtains its location and timestamps from existing information within the AV. These timestamps and locations serve as references for ReRAF to capture input images from the camera and vehicle controls from the AV. Vehicle controls include braking, throttle, speed for longitudinal movements, and steering for lateral movements. The camera images are analysed to detect hazardous events, which are then converted into a real-time RT figure. The RT figure indicates the severity of the hazardous event detected, and it varies according to the distance to the AV, the classes and the

location of objects. The braking, throttle, speed, and steering information form a normalised CT figure. The RT and CT figures are used to determine the *PRN* and AV-TTC. The *PRN* represents how effectively the AV responds to the detected hazardous object from the camera. The range of detection will be limited by the elevation of the camera within the AV. The AV-TTC provides a reference for object collision with the AV. The *PRN* is then sent to AV control and path planning for safer operations and is archived in both RAM's database and via a 5G modem to the backend database. By using recursive AV operations, the *PRN* and Occurrence optimise future operations for a safer path without requiring additional development cycles. For example, the optimisation could involve actions such as reducing the operating speed of the AV if a high *PRN* and Occurrence is consistently observed in certain geographic regions or increasing the operating speed if no *PRN* and Occurrence are observed.

### 3.3.2 ReRAF methodologies and its algorithm

With the stated design concept for ReRAF, different methodologies are identified to achieve the seven requirements in addition to Severity, Control, and Occurrence, as highlighted in section 3.1. This section explains the detailed methodologies used to create the ReRAF's algorithm, providing the respective outcomes.

Figure 3.3 shows how the inputs are linked to ReRAF's methodologies and algorithm, which provides outcomes to other modules within the AV and backend databases. ReRAF's methodologies and algorithm generate RT figures and AV-TTC from object detection, scene segmentation, and probabilistic modelling. At the same time, the CT figure is derived from normalised parametric control inputs. The RT, CT figure and AV-TTC are timestamped with localisation information from the AV. The RT and CT figures determine the *PRN*, while Occurrence is calculated from recursive *PRN* data over time. The selected methodologies objectively generate detailed, recursive outcomes in real time. Converting image and parametric data into a quantitative number makes the data lightweight and efficient for transfer to the backend database over 5G connectivity.

### 3.3 Real-time Risk Assessment Framework (ReRAF)

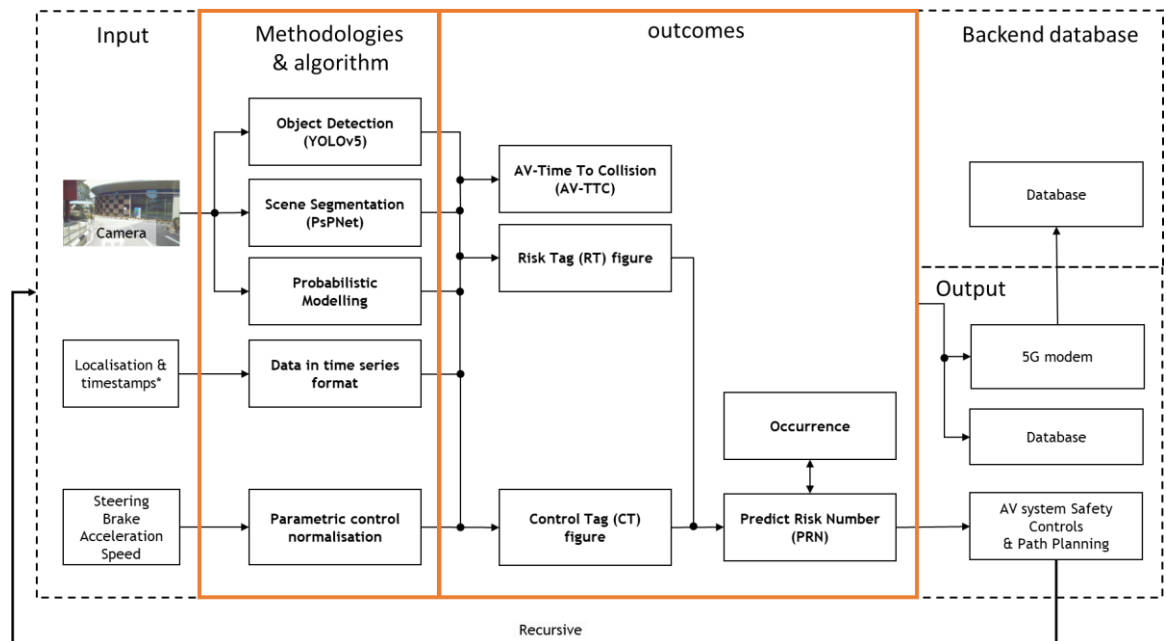


Figure 3.3 ReRAF's methodologies and algorithm that links to the corresponding outcomes

#### Risk Tag (RT) figure

The RT figure represents the severity of potential collisions between the AV and the objects detected on roads or pavement. This RT figure is obtained by capturing the environmental risk observed by the AV camera at specific landscapes. This process happens in real time and provides a quantitative figure representing the risk of encountering pedestrians and vehicles on roads or pavements, which are essential for the AV to identify to prevent collisions. This quantitative figure must be granular, considering factors such as types of objects, landscape, and the distance to the AV. Therefore, it is identified that achieving this outcome requires three different methodologies to create the ReRAF's algorithm: 1) object detection, 2) scene segmentation, and 3) risk probabilistic modelling.

- 1) **Object Detection** is used to identify pedestrians and vehicles from the scene in real time with outcomes that relate to the frame per second. Based on the literature review for object detection, One-stage detector provides results suitable for real-time inferencing. Thus, in this research, YOLOv5 small model is selected, configured with approximately 7.2 million parameters with a mAP of 38% based on IoU of 0.5-0.95. As the research progresses, YOLOv8 is also available, and using it with similar parameters

achieves an estimated 3-5% improvement for mAP. The popularity of YOLOv5 became widespread for many applications [107-110] and forms the basis of many recent research journals in the area of transport. Examples include vehicle and pedestrian detection with precision values between 83.2% to 97.3% and recall values from 72.8% to 95.3%. The dependencies of these results are highly dependent to the amount of datasets being trained and tested. The outcomes of YOLO variants provide the object's classification and localisation in the scene with bounding boxes. More details on the use of YOLOv5 application performance for ReRAF will be discussed in chapter 5.

- 2) **Scene segmentation** is used to identify landscape scenes, for example, like roads, pavements, or other elements. Semantic segmentation [69] is the most suitable for uncountable landscapes, and to process the outcomes in real time, they are given in frames per second. Based on the literature review in section 2.4.5, PSPNet is identified as having the best mean IoU. PSPNet is used in conjunction with YOLOv5 to provide an overall balance model with speed in object detection and a high pixel accuracy for landscape scene detection. For example, YOLOv5 provides frames per second ranging between 25-30, while PSPNet provides landscape detection at 10 frames per second using an Nvidia AGX Jetson. In this process, the PSPNet identifies roads and pavements, and a novel step was taken to add rows to the results of the PSPNet, which enabled the mapping of a scene into a matrix. Further examples are illustrated in chapter 5.
- 3) **Probabilistic modelling** provides a novel way to quantitatively represent the likelihood of collision between the detected object and the AV while considering the landscape scene. This probabilistic model is based on the probability of collision, where the detected object in the front row represents a definite collision as it is nearest to the AV. As the object moves further away from the AV, the probability of collision reduces. The size of the matrix from scene segmentation is used and populated with the probabilistic model. Besides considering the probability of collision with the

### 3.3 Real-time Risk Assessment Framework (ReRAF)

AV in terms of distance, the risk levels between road and pavement are also differentiated by assigning different weights for road and pavement. Therefore, when the corresponding object is detected, RT figures are obtained from a matrix determined within a process known as Risk Tagging and Mapping.

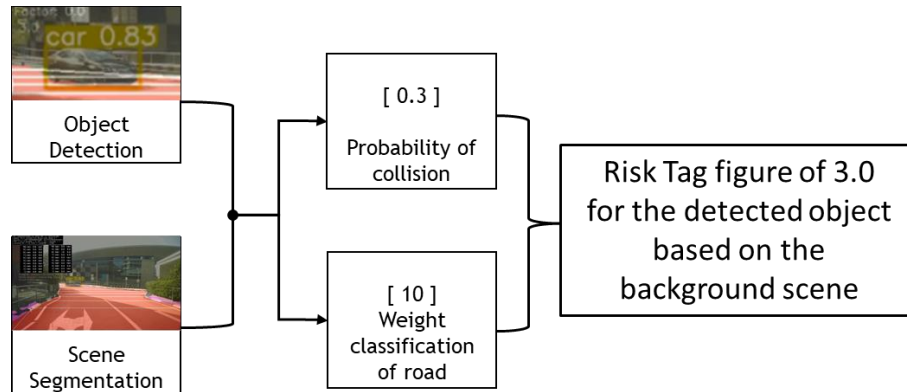


Figure 3.4 Example of probabilistic modelling for risk tagging and mapping

Figure 3.4 shows an example of how an RT figure is determined based on probabilistic modelling. This includes considering the probability of collision between the detected vehicle and the AV and the road's weight classification.

The outcome is an RT figure of a scene that considers the landscape classification, the type of object detected, and their AV collision probability. The RT figure of a scene is represented as equation 3.1.

$$RT_{SUM} = \sum_{rz} RTM_{rz} \circ \omega_{rz} \circ RD_{pm} \quad (3.1)$$

where,

$RT_{SUM}$  : Sum of all RT figures within the scene

$RTM_{rz}$  : Scene segmentation into matrix

$RD_{pm}$  : Risk detection probabilistic modelling

$\omega_{rz}$  : 2D weight classification for road and pavements



**Control Tag (CT) figure**

The CT figure represents the measurement of the AV's parametric control or safety actions. This CT figure is determined using AV parametric controls such as speed, throttle, steering, and braking. These parametric controls are chosen based on studies in [111] that identify changes in hazard perception based on driver behaviour. They are used as a reference for AV that represents the AV's longitudinal and latitudinal movements. The parametric controls are obtained from the drive-by-wire system, and information is connected to the ReRAF using a ROS system. The raw inputs are converted from analogue to digital value, followed by a normalisation process. Each parametric input is attached with an individual weight if further emphasis is required. The normalised inputs with their weights are used to determine a single CT figure, similar to the tagging process in [112] for real-world scenarios used to assess the performance of AV operations. The combined single CT figure represents the AV's controllability during risky and hazardous events. The CT figure is represented as equation 3.2.

$$Ctrl = \frac{1}{3}(B_n W_B + Th_n W_{Th} + St_n W_{St} + Sp_n W_{Sp}) \quad (3.2)$$

where,

$Ctrl$  : CT figure

$B_n$  : Normalised brake values

$W_B$  : Weight of brake values ranging from 1 to 10 (default set at 10)

$Th_n$  : Normalised throttle values

$W_{Th}$  : Weight of throttle values ranging from 1 to 10 (default set at 10)

$St_n$  : Normalised steering values

$W_{St}$  : Weight of steering values ranging from 1 to 10 (default set at 10)

$Sp_n$  : Normalised speed values

$W_{Sp}$  : Weight of speed values ranging from 1 to 10 (default set at 10)

### **Predicted Risk Number (*PRN*)**

*PRN* is derived using RT and CT figures, which resemble the risk priority number used in FMEA [113]. Each scene captured by the image represents a descriptive scenario with a dataset of quantitative figures. RT figures are obtained from different object classes, i.e. vehicles and pedestrians. Each object class will have its own normalised RT figures, and a combined RT figure is obtained by averaging the normalised RT figures across classes. The combined RT figure is used with the CT figure to determine *PRN*. *PRN* can be used as a reference to trigger for safer operations, for example, to reduce sudden steering, braking or throttle. However, the intent is not to replace existing active ADAS to prevent accidents. After several rounds of operation within the designated route, the accumulative *PRN* values, RT figure, and CT figure provide further comparative analysis between each route using Descriptive Statistics [114] to highlight risky scenarios and indicate the overall safety level of each route.

The outcome of *PRN* is a quantitative figure that represents how the AV mitigates and detects hazardous objects in terms of AV movements. *PRN* is obtained in real time with data that corresponds to frames per second and in a lightweight format.

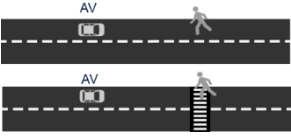
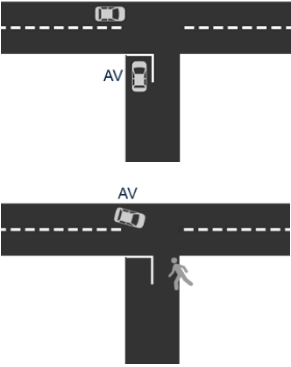
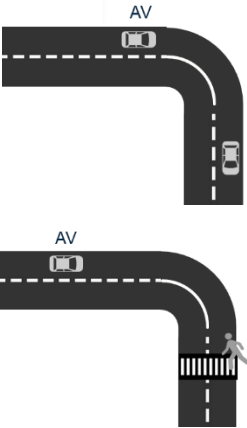
### **Occurrence**

Occurrence in ReRAF is represented in both macro and micro approaches. The macro approach consists of averaging the PRN within a region. Each region has its own latitudinal and longitudinal grid limits. The PRNs with geolocation that fall within the same region are averaged. The geolocation of the AV is represented as latitudinal and longitudinal coordinates obtained via positioning systems such as the global navigation satellite system. These “regions” provide a PRN visualisation for the overall route. The micro approach considers the average *PRN* over “X” number of trips along the same route to identify hotspots. These visualisations using *PRN* highlight the Occurrence of high risk areas. Therefore, these visualisations assist the AV for future path planning based on the average *PRN* and identified hotspots of a particular area and time.

### 3.3.3 Scenarios for ReRAF

Existing work for risk assessment test scenarios are categorised mainly in lane keeping or collision prevention [34, 51, 54, 98], lane overtaking [97], highways [115-117], and regulated junctions with traffic lights [118]. One of the identified gaps is to focus on unregulated traffic in urban areas with no traffic lights to govern the right of way. ReRAF is tested on scenarios representing unregulated urban traffic with unknown hazards or near-misses.

Table 3.1 ReRAF scenarios to be tested

Scenarios	Area of focus
<p data-bbox="339 831 679 898">Straight paths with or without zebra crossings</p> 	<p data-bbox="1007 853 1185 887"><b>Pedestrians</b></p> <p data-bbox="727 904 1453 972">The AV is approaching crossing pedestrians on the road with or without zebra crossing.</p>
<p data-bbox="363 1077 655 1144">T-junctions without traffic lights</p> 	<p data-bbox="1038 1111 1153 1144"><b>Vehicle</b></p> <p data-bbox="727 1167 1465 1267">AV makes a right turn out of the pocket at the T-junction, where another vehicle is driving straight. The T-junction may have a yellow box.</p> <p data-bbox="1015 1346 1177 1379"><b>Pedestrian</b></p> <p data-bbox="727 1402 1437 1503">AV makes a right turn from the main road of a T-junction into a minor road where a pedestrian is crossing. The T-junction may have a yellow box.</p>
<p data-bbox="435 1547 584 1581"><b>Cornering</b></p> 	<p data-bbox="1038 1603 1153 1637"><b>Vehicle</b></p> <p data-bbox="727 1659 1430 1727">AV either stops or overtakes a stationary vehicle observed after the bend.</p> <p data-bbox="1015 1850 1177 1883"><b>Pedestrian</b></p> <p data-bbox="727 1906 1445 2007">AV stops after the bend when it sees a pedestrian crossing. The pedestrian crosses the road either with or without a zebra crossing.</p>

### 3.3 Real-time Risk Assessment Framework (ReRAF)

Table 3.1 provides a descriptive explanation of the scenarios. ReRAF focuses on performing an objective quantitative real-time risk assessment from the AV's perspective in those scenarios by measuring the parametric controls from the detected hazards.

#### 3.3.4 ReRAF database and datatype information

The data generated from ReRAF outcomes are archived in RAM's database as well as the backend database. Table 3.2 illustrates ReRAF's outcome collected over different timestamps within a route. Besides the timestamp in UTC, this data consists of geolocations, RT figures, CT figures, Speed, Throttle, Brake, Steering, and *PRN*. This data is archived in real time with frames per second. Since the data are all in numerical figures instead of images or video, the requirement of being lightweight is fulfilled.

Table 3.2 Sample of database information from ReRAF

Timestamped	1660208498743	1660208506174	1660209408931	16602097218903
Latitude / Longitude	1.3327739848895932 103.77396689657913	13326502615048932 103.77415563192062	13317647997644944 103.77347463552277	1332502014753533 103.77642532359344
Speed	20.96	5.55	15.2	12.44
Throttle	0.12	0.79	0.68	0
Brake	0	0	0	0.95
Steering	0.05	0.95	0.05	0.21
Pedestrians	0	1	4	0
Pedestrians RT figure	0	9	22	0
Vehicles detect	1	12	0	0
Vehicles RT figure	2	2	0	0
CT figure	2.292	6.261	3.69	4.89
<i>PRN</i>	2.292	46.959	10.149	0

### 3.4 Real-time risk assessment with cooperative mode (ReRAC)

Table 3.3 shows the parameters and datatypes within the datasets. A sequence ID generator is used as the primary ID for the backend database. Each parameter provides a description of the scene using quantitative figures without any human interpretation. This information can also be formed as meta-data embedded into the scene for future reference. For example, detected pedestrians and vehicles are defined as integers, while RT and CT figures are non-negative float numbers.

Table 3.3 Parameters and its datatype for ReRAF

Parameters	Datatypes	Parameters	Datatypes
Timestamps	UTC format	Pedestrians	Integer
Latitude / Longitude	Double (degrees)	Pedestrians RT figure	Float (non-negative, max to 100)
Speed	Float type (km/h)	Vehicles detect	Integer
Throttle	Normalised Float (non-negative)	Vehicles RT figures	Float (non-negative, max to 100)
Brake	Normalised Float (non-negative)	CT figures	Float (non-negative, max to 10)
Steering	Normalised Float (non-negative)	<i>PRN</i>	Float (non-negative, max to 100)

### 3.4 Real-time risk assessment with cooperative mode (ReRAC)

This section provides an overview of the design concept of ReRAC, along with its methodologies, algorithms, tested scenarios, and database ensemble. ReRAC functions as a remote warning system for AVs by retrieving data from the backend database in real time. The backend database consolidates the ReRAC data from all the RSUs. The AV only retrieves ReRAC data from the nearest RSU in its path of travel. Since ReRAC is part of an infrastructure with a fixed location, only Severity and Occurrence are relevant in addressing the identified gaps for real-time risk assessment. Developing ReRAC's algorithm required various methodologies, which were then tested in unregulated traffic scenarios. This section also includes examples of ReRAC's data ensemble.

### 3.4.1 AV ReRAC design concept

The ReRAF design concept converts camera images into real-time figures representing severity. Additionally, ReRAC provides RSU Time To Collide (RSU-TTC), Occurrence, and hazard identifications and warnings, which address the requirements for real-time risk assessment.

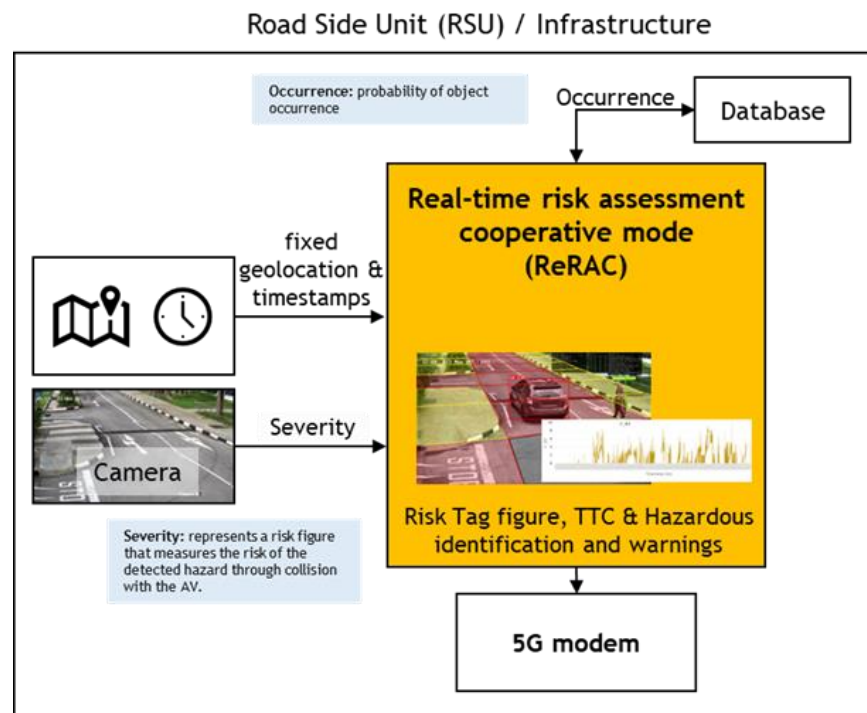


Figure 3.5 ReRAC design concept

Figure 3.5 shows that ReRAC operates within the RSU with camera(s), local database, fixed geolocation with timestamps, and a 5G modem to connect to the backend server. The fixed geolocation with timestamps provides the essential reference for the data created from ReRAC. The camera input scenes are converted into RT figures that represent Severity. The process of deriving RT figures for ReRAC is slightly different from that of ReRAF since the scene is static within the infrastructure. Besides RT figures, ReRAC also provides outcomes such as RSU-TTC and hazard identifications and warnings. RSU-TTC is the time a collision may occur between the detected object and a reference location "X" in the camera's scene. The overall time to collision between the AV and the detected object requires adding the calculated time for the AV to arrive at the reference

### 3.4 Real-time risk assessment with cooperative mode (ReRAC)

location “X” and the RSU-TTC. Hazard identification and warnings are advanced alerts for the AVs, especially in situations where pedestrians or vehicles may be obscured, or where there are traffic jams or accidents before the AV arrives to the RSU’s location. These alerts are triggered when pedestrians or vehicles reside at the intersection or when there are vehicle-to-vehicle, or vehicle-to-pedestrian proximity within the road section or intersection of a T-junction. These ReRAC outcomes are sent to the backend database via 5G connectivity, while the AV retrieves this information when they are in proximity to the infrastructure location.

#### 3.4.2 ReRAC methodologies and its algorithm

This section explains how the ReRAC methodologies and algorithm provide the required outcomes based on the input camera in the RSU. The ReRAC outcomes consist of RT figure, RSU-TTC, hazard identifications and warnings, and occurrence.

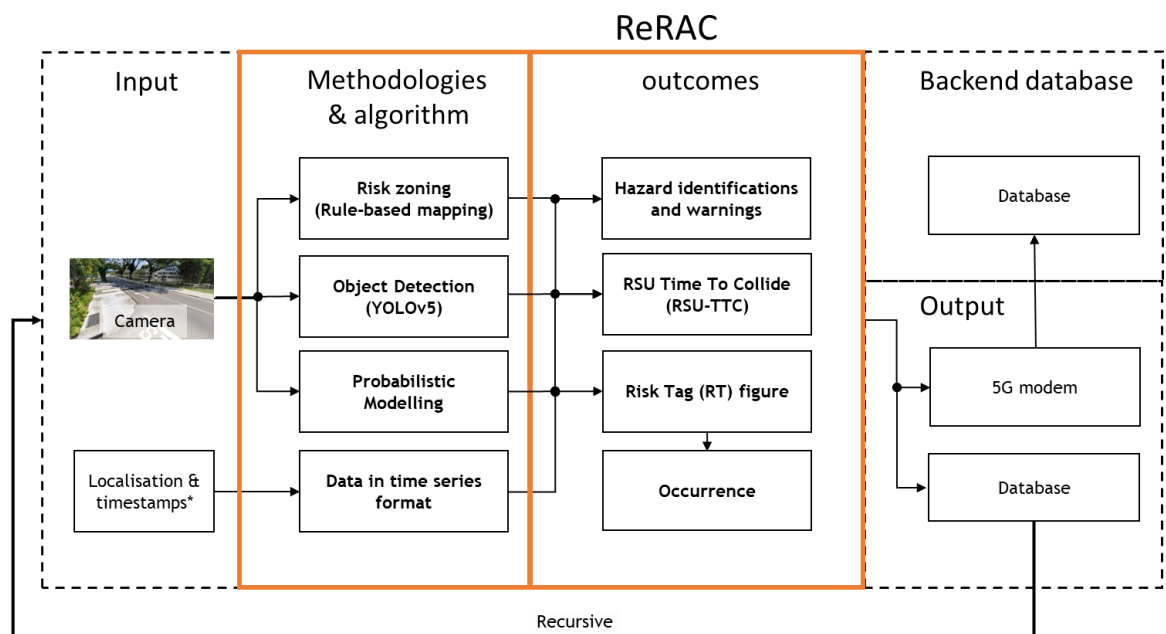


Figure 3.6 ReRAC’s methodologies and algorithm that links to the corresponding outcomes

Figure 3.6 illustrates how ReRAC methodologies and algorithm utilise camera input to produce the desired results. The methodologies and algorithm consist of risk zoning, object detection, and probabilistic modelling presented in a time series

### 3.4 Real-time risk assessment with cooperative mode (ReRAC)

---

format. The outcomes of these methodologies and algorithm include hazard identifications and warnings, RSU-TTC, RT figure, and occurrence. These outcomes are continuously processed in real time. Similar to ReRAF, the data in ReRAC is quantitative rather than qualitative, making it efficient and easily transferable over 5G connectivity when operating in cooperative mode.

#### Risk Tag (RT) figure with RSU field of view

The RT figure represents the severity of potential collision between the reference location “X” and the object detected on roads or pavement. This RT figure used in ReRAC is achieved through qualitative to quantitative conversion of images to risk figures. The aim is to identify pedestrians/vehicles in the image captured by the RSU camera within a selected field of view and thereafter provide a numerical risk presentation using probabilistic modelling. Since the objective is to provide a risk representation of the environmental view using the RSU, the camera is mounted at a height of 3 to 5 m above ground level. At this height, the efficiency of object detection is higher, thus minimising occlusion. The object detection used for risk tagging is similar to ReRAF where YOLOv5 is used. Compared to RT figure for AV in ReRAF, the scene is considered static in ReRAC with a fixed field of view and location. The methodologies used to achieve RT figures for ReRAC include 1) risk zoning, 2) probabilistic modelling and 3) object detection (similar to ReRAF).

- 1) **Risk zoning** is an important initial step in the ReRAC methodology. It helps to define areas of interest within the scene, such as roads, pavements, and off-road areas. In other fields, risk zoning is used to identify potential hazards, such as landslides [119], typhoons [120], and snow disasters [121], by quantifying hazardous areas and assigning a probability to different regions. In this context, risk zoning involves labelling different risk ratings in specific areas within the camera's field of view. This process converts contextual landscape road, pavement or offroad into a quantitative figure known as weights. During the initial setup, the field of view is divided into rows and columns to create a risk zoning matrix. Therefore, this matrix is used to map the localisation of detected pedestrians and vehicles through probabilistic modelling. The risk zoning process is explained in chapter 4



### 3.4 Real-time risk assessment with cooperative mode (ReRAC)

---

with illustrated examples. It is worth noting that risk zoning methods differ from risk field theory [51], which focuses on vehicle-to-vehicle collision using the force repulsion concept, whereas risk zoning uses a probability-model approach.

- 2) **Probabilistic modelling** is designed specifically for ReRAC to provide the reference location “X” with a varying probability of collision based on the detected object in the scene. Three different probabilistic models have been developed to represent different coverages within the area of interest, which will be further explained in chapter 4.
- 3) **Object detection** in ReRAC uses the YOLOv5 model to detect pedestrians and vehicles, where the outcome provides the localisation of the detected pedestrians and vehicles in the scene. This process is similar to the object detection used for ReRAF.

The eventual RT figure is obtained by mapping the detected pedestrians or vehicles to the different zonal areas of the risk zoning matrix, including probabilistic modelling. The RT figure is represented as equation 3.3.

$$RT_{final} = \sum_{rz} OD_{rz} \circ \omega_{rz} \circ RD_{pm} \quad (3.3)$$

where,

$RT_{final}$ : Sum of RT figures within a scene

$OD_{rz}$ : Object detection matrix

$\omega_{rz}$ : 2D risk zoning matrix

$RD_{pm}$ : Risk detection probability modelling

#### **Hazard identifications and warnings**

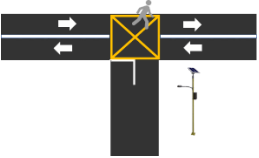
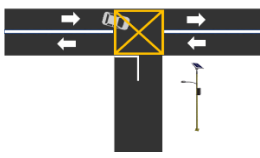
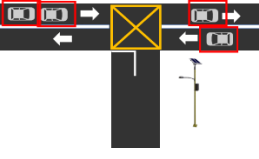
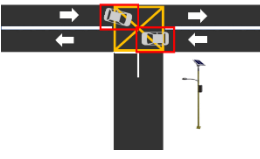
Hazard identifications and warnings aim to provide remote event warnings to the AV at unregulated T-junctions, especially in situations where the scene is obstructed or obscured from the AV's path of travel. These hazard identifications

### 3.4 Real-time risk assessment with cooperative mode (ReRAC)

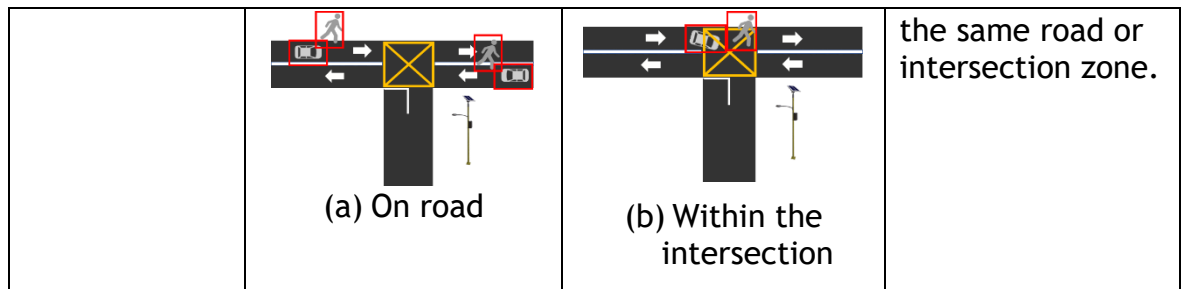
and warnings allow the AV to make better and more informed decisions for their intended path planning before they arrive at the RSU location.

Table 3.4 presents various hazard classifications, including four hazard identifications and two warnings. Hazard warning detection is specifically designed for intersections, providing advanced notice to the AV if certain objects are present in the intersection. Based on this warning, the AV can make decisions to either slow down before reaching the intersection if the warning persists or maintain its current speed if no warning is received. Hazard identifications operate by detecting the proximity of vehicle-to-vehicle or vehicle-to-pedestrian at the road section and intersection. This advanced information assists the AV in upcoming path planning to handle potential congestion or accidents. The path planning may involve slowing down as it approaches the identified hazard or preparing an alternative route, especially if the hazard continues for a period of time.

Table 3.4 Hazard Detection Classification

Hazard Classification	Modality		Description
Hazardous warning	Pedestrians 	Vehicles 	Provide a boolean detection when a pedestrian or vehicle is detected in the intersection zone.
	Vehicle-to-vehicle  (a) On road	Vehicle-to-vehicle  (b) Within the intersection	
Hazard identifications	Vehicle to pedestrian	Vehicle to pedestrian	Provide a boolean detection when a pedestrian and vehicle are detected within

### 3.4 Real-time risk assessment with cooperative mode (ReRAC)



The outcomes of hazard identifications and warnings are presented in boolean statuses, aiding the AV in minimizing sensor integration and processing time for advanced planning in response to detected hazardous events.

#### RSU Time To Collide (RSU-TTC)

RSU-TTC is a countdown in sub-seconds that reflects the time to collide from the detected pedestrian/vehicle to the reference location "X" within the risk zone. The AV uses this countdown to determine its overall time to collision from the AV to the detected objects from the RSU.

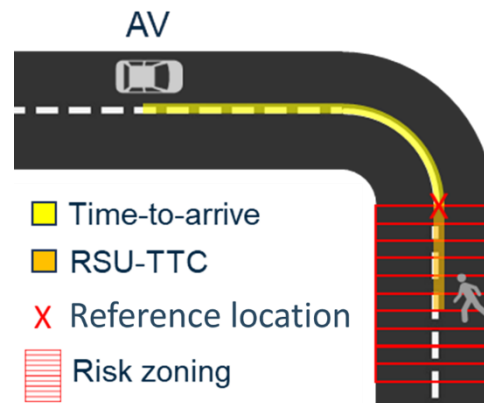


Figure 3.7 Time to collision parameters

Figure 3.7 illustrates an example of a pedestrian who is detected after a bend. ReRAC provides an estimated RSU-TTC based on the detected pedestrian, assuming the AV is at the reference location "X". This information is sent to the AV. By adding the Time-to-arrive determined by the AV, the overall collision time from the AV to the detected pedestrian is determined. The Time-to-arrive is determined based on the distance between the current AV location and the

### 3.4 Real-time risk assessment with cooperative mode (ReRAC)

---

reference location “X” over the AV’s operating speed. Since the AV operates in real time, the overall time to collision will be continuously updated with AV and pedestrian movements.

RSU-TTC is determined based on the distance between each row via pixel mapping [122]. Thus, the distance between the detection object (x,y) to the position marked “X” is determined accordingly with the calibrated data on a pixel per distance. The RSU-TTC from the reference location “X” to the detection object can be calculated using the road section’s speed limit as a reference.

The outcome of RSU-TTC assists the AV in obtaining an advance time to collision countdown if an object is detected within the area of interest of the RSU. This assists the AV in making informed safety decisions, knowing if there is a risk of collision in situations with occluded scenes.

#### Occurrence

Occurrence in ReRAC is represented by observing the number of objects detected within each zonal area of the risk matrix. The distribution of object detection within the risk matrix will identify hotspots where the most pedestrians or vehicles appear. This information can be provided to the AV for future path planning.

In summary, ReRAC’s methodologies consist of risk zoning, probabilistic modelling, and object detection, forming ReRAC’s algorithm to provide the required outcomes. The details are further explained in chapter 4.

#### **3.4.3 Scenarios for ReRAC**

ReRAC is tested on specific unregulated traffic scenarios to address gaps in existing risk assessments, which are considered the most risky for pedestrian crossings. These scenarios cover occlusions before cornering, T-junctions and double T-junctions with pedestrian crossings. Additionally, specific scenarios have been selected to test hazard identifications and warnings for its intended design. Table 3.5 illustrates the different scenarios identified from unregulated traffic for

### 3.4 Real-time risk assessment with cooperative mode (ReRAC)

testing RT figures. Each scenario illustrates a single RSU with ReRAC installed at that location. Each RSU can have a single or multiple camera to detect different risk zoning scenarios.

Table 3.5 ReRAC scenarios to be tested for RT figures

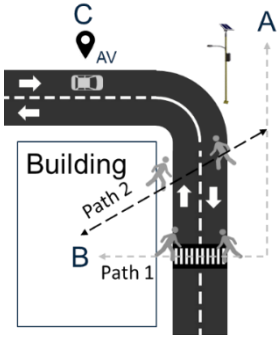
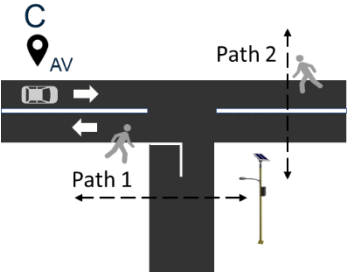
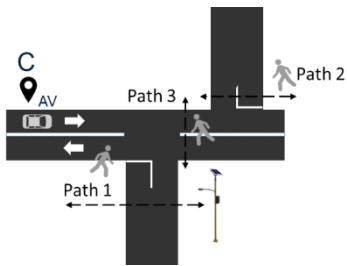
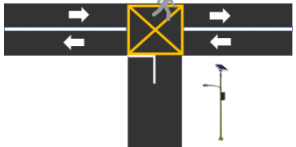
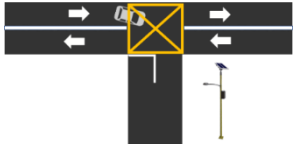
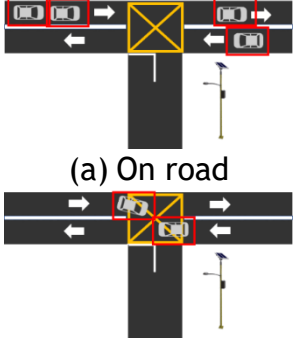
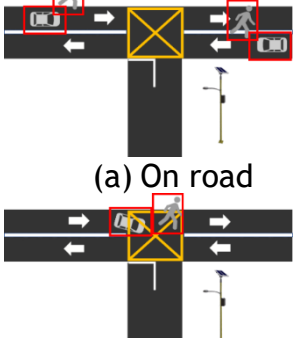
Scenarios	Area of focus
<p data-bbox="443 562 687 595">Cornering/bends</p>  <p data-bbox="480 965 655 999">© 2022 IEEE</p>	<p data-bbox="839 636 1469 925">The AV is moving towards a bend, and with its sensor limitations and occlusion from the building, it cannot detect pedestrians crossing through paths 1 or 2. ReRAC with the RSU provides remote advanced risk information to the AV, representing the scenario.</p>
<p data-bbox="328 1021 804 1055">T-junctions without traffic lights</p>  <p data-bbox="480 1368 655 1402">© 2022 IEEE</p>	<p data-bbox="839 1048 1469 1379">The AV can either travel straight or turn right. As the AV turns right, there is a potential collision with the pedestrian crossing at path 1. If the AV travels straight, the AV will have to react to the dashing pedestrian at path 2. ReRAC with the RSU provides remote advanced risk information to the AV</p>
<p data-bbox="320 1426 812 1496">Double T-junctions without traffic lights</p>  <p data-bbox="480 1789 655 1823">© 2022 IEEE</p>	<p data-bbox="839 1503 1469 1749">There are three possible paths for the AV, with two of them similar to the T-junctions, while the third path refers to the AV turning left into the pedestrian crossing path 2. ReRAC with the RSU provides remote advanced risk information to the AV</p>

Table 3.6 shows the scenarios tested for ReRAC's hazard identifications and warnings. Each scenario illustrates a single RSU with ReRAC installed at that

### 3.4 Real-time risk assessment with cooperative mode (ReRAC)

location. Each RSU can have a single or multiple camera to detect different risk zones within different scenarios.

Table 3.6 ReRAC hazard identifications and warnings to be tested

Scenarios (Note that yellow box demarcation is optional)	Area of focus
<p>Hazard warning (Pedestrian)</p> 	<p>Hazard warning occurs when a pedestrian is crossing within a T-junction's intersection.</p>
<p>Hazard warning (vehicle)</p> 	<p>Hazard warning occurs when a vehicle drives within the T-junction's intersection.</p>
<p>Hazard identifications (vehicle-to-vehicle)</p>  <p>(a) On road</p> <p>(b) Within an intersection</p>	<p>In (a), hazard identification happens on the road when two or more vehicles are close to one another.</p> <p>In (b), hazard identification happens within the intersection when two or more vehicles are detected within the intersection defined at the beginning of the setup.</p>
<p>Hazard identifications (vehicle to pedestrian)</p>  <p>(a) On road</p> <p>(b) Within intersection</p>	<p>In (a), a hazard identification happens on the road when a nearby pedestrian is detected close to a vehicle.</p> <p>In (b), a hazard identification happens within the intersection when a nearby pedestrian is detected close to a vehicle within the intersection defined at the beginning of the setup.</p>

### 3.4 Real-time risk assessment with cooperative mode (ReRAC)

#### 3.4.4 ReRAC database and datatype information

The ReRAC data is archived in the RSUs and backend databases via 5G connectivity. Table 3.7 illustrates ReRAC data and its datatype from the RSU's database. The dataset includes the RT figures, pedestrian detection, vehicle detection, RSU-TTC, and Hazard identifications and warnings. The backend database has a relational model-based schema based on a cluster of RSU within a region of geolocations.

Table 3.7 shows an example of the information stored and its datatype in ReRAC's RSU. Each parameter provides a quantitative figure that represents a descriptive context of the scene without any human interpretation. Table 3.7 provides pedestrian and vehicle RT figures and RS-TTC for both directions (d1, d2). The reference location "X" are different for different directions of travel. Examples with detailed explanations will be given in chapter 4.

Table 3.7 Sample of database information from ReRAC

Data description	Data	Datatype
Timestamped	1701665595.311925	UTC format
Area of Interest (AOI)	1	Char
Pedestrian detection	5	Integer
Pedestrian RT figure [d1,d2]	[19.2, 17.4] (float, non-negative up to 100)	float, non-negative, max up to 100
Pedestrian RSU-TTC [d1,d2]	[1.35, 1.35]	Float
Vehicle detection	3	Integer
Vehicle RT figure [d1,d2]	[18.0, 15.0]	float, non-negative, max up to 100
Vehicle RSU-TTC [d1,d2]	[ 0.9, 1.35]	float
Hazard identifications and warnings	True/False	Boolean

### 3.5 Summary

This chapter explains how ReRAF and ReRAC are developed from requirements into methodologies with the intent to address the identified gaps between static and real-time risk assessment for safer AV operations. The key requirements for static risk assessment are adapted for real-time risk assessment. Furthermore, the identified gaps between static and real-time risk assessment are turned into additional requirements for creating ReRAF and ReRAC. To meet these requirements, various methodologies are identified for developing algorithms to produce the ReRAF and ReRAC outcomes. The purpose of each methodology is detailed, providing explicit reasoning for their implementation. ReRAF is designed for use within AV and provides *PRN* and AV-TTC figures to measure the risk of AV's control actions towards the detected hazardous events through its camera and parametric controls. ReRAC operates within the RSU and sends RT figures with RSU-TTC and hazard identifications and warnings to the AV via a backend server, thus avoiding risks, potential accidents, and road congestion. Together, the outcomes from ReRAF and ReRAC are used to achieve better path planning and to improve AV safety controls. Additionally, this chapter includes descriptive reasoning of different unregulated traffic scenarios used to test ReRAF and ReRAC. Examples of ReRAC and ReRAF data with defined parameters and their datatypes are also illustrated in this chapter.



## Chapter 4

### 4 Real-time risk assessment with cooperative mode

In chapter 3, ReRAC is proposed as an infrastructure-based approach to improve the coverage of static risk assessment. This is achieved by providing remote advanced warnings to the AV from the RSU. Additionally, chapter 3 identifies the requirements and methodologies to develop ReRAC's algorithm. This chapter further details these methodologies, forming the novel ReRAC algorithm, Spatial-Temporal Risk Evaluation Ensemble Technique (STREET). STREET provides various outcomes in real time consist of risk tag (RT) figures, time to collision between reference location "X" and detected object (RSU-TTC), object Occurrences and hazard identifications and warnings. This chapter also introduces and explains three unique probabilistic models that aid in remote risk detection for different coverages within the area of interest. Unregulated traffic scenarios such as cornering is used to test STREET's RT figures with different probabilistic models, while a T-junction is employed to test for hazard identifications and warnings. These results demonstrate STREET's capability to fulfil the intended functionality of ReRAC.

## 4.1 Spatial-Temporal Risk Evaluation Ensemble Technique (STREET) algorithm

This section explains the theoretical formulation of STREET methodology and illustrates the process. By using these methodologies, STREET converts the input images from the RSU's camera into RT figures, Occurrences, RSU-TTC and hazard identifications and warnings. The methodologies used include risk zoning, probabilistic modelling, and object detection techniques, specifically YOLOv5. The primary outcome of STREET, known as the RT figure, is a quantitative figure representing the risk of collision between the detected object and the reference location "X" within the Area Of Interest (AOI). Additionally, RSU-TTC is provided to the AV to determine its overall time to collision based on the RSU's reference location "X". Other information includes Occurrence that represents the probability of pedestrian detection over historical data in the AOI. Lastly, risky events are identified using hazard identifications and warnings for remote event warnings.

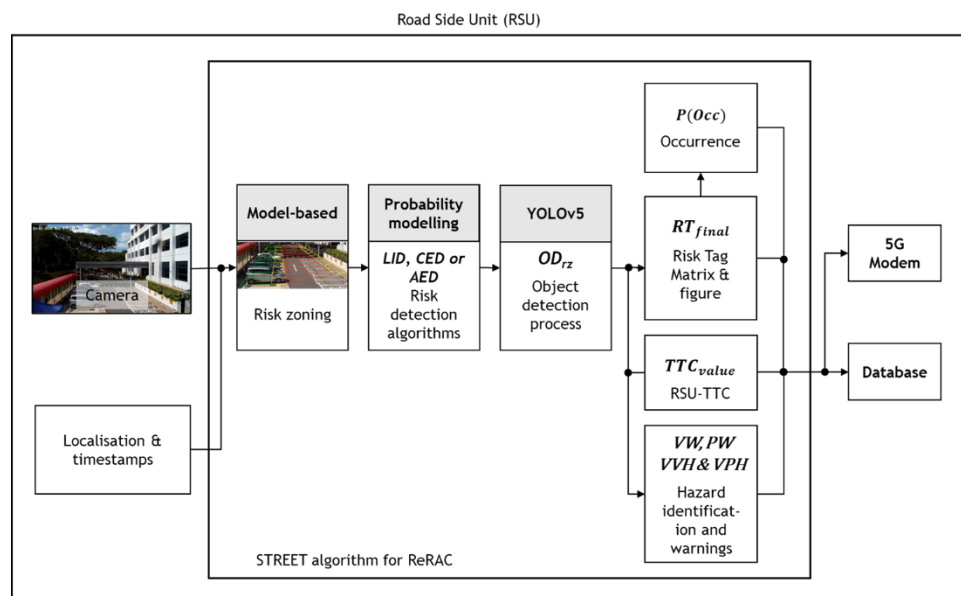


Figure 4.1 Block diagram of STREET algorithm within the RSU

Figure 4.1 shows that the STREET algorithm begins by preparing risk zoning. Risk zoning is an initial setup that annotates the AOI in the scene from RSU's camera, categorising roads, pavements and offroads with rows that convert the scene into a matrix. Different weights are then assigned to the roads, pavement and offroads

since they have different risk of collision. As a result, a 2D risk zoning matrix is formed. The size of the 2D risk zoning matrix is further used by probabilistic modelling. Three unique probabilistic models are developed, Linear Internal Distribution (LID), Aggressive Exponential Distribution (AED), and Conservative Exponential Distribution (CED). LID, CED and AED utilise different probability of collision distributions across the zonal areas, resulting in different AOI coverage. The probability of collision is defined between the zonal area and the reference location “X”. The size of the 2D risk zoning matrix is used in the object detection process to map the detected object’s location into the zonal areas of the matrix, thus forming an object detection matrix. The RT figure ( $RT_{final}$ ), RSU-TTC ( $TTC_{value}$ ) and hazard identifications and warnings are determined by the outcomes of risk zoning, selected probabilistic model, and object detection. The probability of occurrence,  $P(Occ)$ , is determined based on the cumulative object detection matrix over time when determining the RT figure. The following subsections provide detailed derivations and illustrations of each process outcome.

#### 4.1.1 Risk zoning of the environment

This section explains the process of risk zoning. Risk zoning is a rule-based matrix mapping methodology based on the contextual scene. This process is required only for the initial setup, which manually identifies zonal areas for roads, pavements and offroads and converts them into a 2D risk zoning matrix. Risk zoning demarcates the real-time camera image into different zonal areas in a 7-step process as follows:

Step 1: Select road section(s) with the high volume of pedestrians and vehicles using the field of view of the RSU camera.



Step 2: Define the selected AOI based on the field of view.

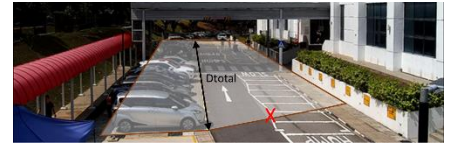


#### 4.1 Spatial-Temporal Risk Evaluation Ensemble Technique (STREET) algorithm

Step 3: From the direction of travel, indicate the reference location “X” using the corresponding geolocation.



Step 4: Measure or determine the total distance ( $D_{total}$ ) of the AOI section either from physical measurements or indications from the source of the available map.



Step 5: Determine the number of rows ( $rows_{int}$ ) within the AOI based on equation 4.1.  $rows_{int}$  is derived from the division of  $D_{total}$  by  $t_{resp}$  which represents the expected driver response in [123],  $V_{max}$  represents the maximum speed limit of the road and  $V_f$  represents the safety speed ratio. The number of rows is inversely proportional to the expected driving responses ( $t_{resp}$ ) and speed limit ( $V_{max}$ ).

$$rows_{int} = \frac{D_{total}}{(t_{resp} \cdot V_{max} \cdot V_f)} \quad (4.1)$$

where,

$rows_{int}$ : maximum number of rows determined

$D_{total}$ : total distance of the AOI section

$t_{resp}$ : time of driver response as a reference

$V_{max}$ : defined speed limit on the selected AOI.

$V_f$ : Safety speed ratio (e.g if the AV driving speed is 70 km/h, and the speed limit is 80 km/h, then  $V_f = 70/80$ )

Step 6: The roads, pavements and offroad are manually demarcated from the AOI into columns. The columns together with the rows defined in step 5, split the AOI into zonal areas. These zonal areas are assigned red for roads, yellow for pavements and green for offroad.



Step 7: The 2D risk zonal matrix ( $\omega_{rz}$ ) is then obtained by mapping the AOI into risk zonal areas with weights in equation 4.2. Table 4.1 illustrates the assignment of weights with colour categorisation for each zonal area referencing methods used for road safety in [124]. The weights represent a look-up table of risk levels correlating to offroad, pavements, and small or main road configurations. Roads represent the highest risk, followed by pavements and offroads. Equation 4.2 converts the scene into a 2D risk zonal matrix with weights that quantify the risk of the landscape.

$$\omega_{rz} = \begin{bmatrix} G_{lrow} & Y_{lrow} & R_{row} & Y_{rrow} & G_{rrow} \\ \cdot & \cdot & \cdot & \cdot & \cdot \\ G_{l2} & Y_{l2} & R_2 & Y_{r2} & G_{r2} \\ G_{l1} & Y_{l1} & R_1 & Y_{r1} & G_{r1} \end{bmatrix} \quad (4.2)$$

where,

$\omega_{rz}$ : 2D risk zonal matrix

$G_{lrow}$ : green left zonal area with row numbers

$Y_{lrow}$ : yellow left zonal area with row numbers

$R_{row}$ : red zonal area with row numbers

$G_{rrow}$ : green right zonal area with row numbers

$Y_{rrow}$ : yellow right zonal area with row numbers

With  $D_{total}$  of the AOI and rows determined in steps 4 and 5, the distance for each row  $D_x$  is illustrated in equation 4.3.

$$D_x = \frac{D_{total}}{rows_{int}} \quad (4.3)$$

where,

$D_{total}$ : total distance of the AOI section

$rows_{int}$ : maximum number of rows determined

$D_x$ : distance of row  $x$

#### 4.1 Spatial-Temporal Risk Evaluation Ensemble Technique (STREET) algorithm

Correspondingly, the time taken for the vehicle to travel in each row is defined as  $t_x$  in equation 4.4 using a linear approach.

$$t_x = \frac{D_x}{V_{max}} \quad (4.4)$$

where,

$D_x$ : distance of row  $x$

$V_{max}$ : speed limit on the selected AOI.

$t_x$ : time taken for the AV to travel each row

Table 4.1 Weight for different risk zonal areas

Zonal areas category	Weights	Scene definition
Red	10	Dual lane main road conditions
Red	9	Dual lane small road conditions
Yellow	8	Dedicated Pavement, shared path or parking lots
Yellow	7	Single lane pedestrian Pavement
Green	6	Accessible pathways away from pavement
Green	5	Thin accessible pathways away from the pavement
Green	4	Green grass patch away from the pavement
Green	3	Tall green grass patch away from the pavement
Green	2	Barricaded pathways
Green	1	Non-accessible paths with short walls
Green	0	Non-accessible paths

The size of the determined 2D risk zonal matrix  $\omega_{rz}$  have rows and columns that match the AOI of the camera's scene. This size of the 2D risk zonal matrix will be used in other parts of the STREET algorithm.

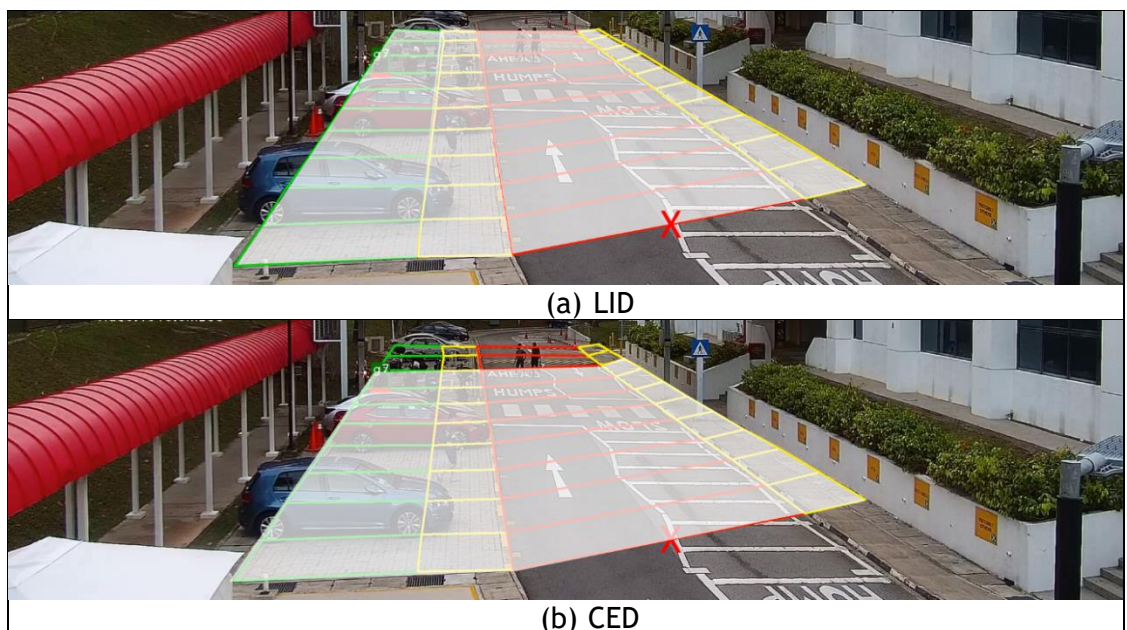
#### 4.1.2 Risk detection matrix with probabilistic models

The risk detection matrix is created based on the size of the 2D risk zoning matrix. The risk detection matrix is decided by a probabilistic model that calculates the probability of a collision between an object in the 2D risk zoning matrix and the reference location "X". Three probabilistic models LID, CED, and AED are designed

#### 4.1 Spatial-Temporal Risk Evaluation Ensemble Technique (STREET) algorithm

to represent different coverages of the AOI. The AV operator first selects the most suitable probabilistic model based on their intended coverage of the AOI and verifies this with the probability of object occurrence (in section 4.1.5) within the AOI. Upon verification, the AV operator will request modification of the probabilistic model at the RSU if changes are required. This cycle repeats itself after a period of time, since the probability of object occurrence might change over time. Thus, the selection of the probabilistic model is a recursive process. However, if the AV operators prefer to have a consistent probabilistic model with the intention of performing real-time analytics, LID will be the default model. This section explains the formulation and different characteristics of the LID, CED and AED probabilistic models and assigns the risk detection matrix values.

Each of the probabilistic models has its own risk detection matrix, populated with different collision probabilities based on each model's characteristics. LID is modelled using a piecewise linear collision probability across the entire AOI. CED is modelled using high collision probability in the front and middle rows of the AOI, while AED is modelled using high collision probability on the front few rows of the AOI.



#### 4.1 Spatial-Temporal Risk Evaluation Ensemble Technique (STREET) algorithm

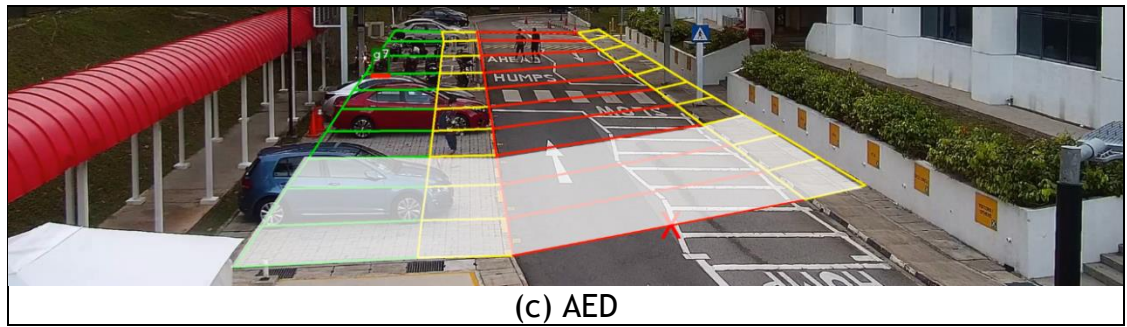


Figure 4.2 LID, CED and AED coverages

Figure 4.2 shows an example of different collision probability coverages within the AOI. With (a) showing LID that covers the whole AOI, (b) showing that CED focuses on the front and middle rows, and (c) AED focusing on the front rows. Besides coverage, each zonal area's collision probability differs for different models.

Figure 4.3 illustrates the definition of zonal and inter-zonal probability distributions used in the risk detection algorithms. The zonal probability distribution refers to the collision probability distribution across different rows. The inter-zonal probability distribution refers to the column-wise probability distribution. The collision probability between the detected object at the first row and the reference location "X" is defined as  $P(C|X) = 1.0$  where a definite collision will take place. The collision probability decreases as the detected object moves further away. All collision probability ranges from 0 to 1.0.

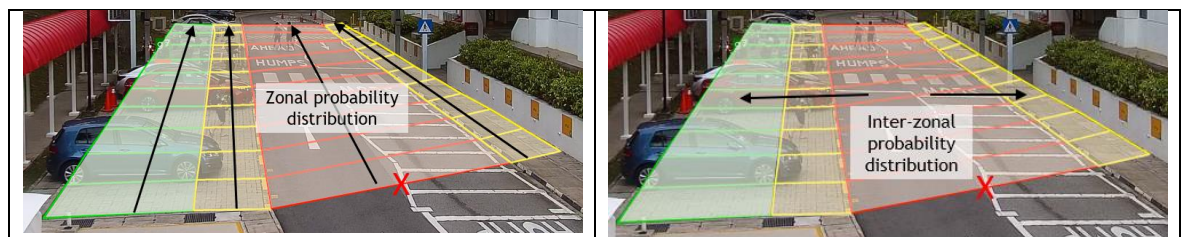


Figure 4.3 Illustration of zonal and inter-zonal probability distribution

In this section, the collision probability (zonal probability distribution) for each model is formulated only for the road region, while a linear inter-zonal probability distribution of collision probability is assumed across the road, pavement and offroad regions.



### Linear Interval Distribution (LID) model

The LID model intends to identify object movement and pedestrians occluded by vehicle, it is best used when there is a long stretch of road. The LID model uses a piecewise linear approach to formulate collision probability across the entire AOI.

The approach starts with determining the likelihood of a collision between an object and an AV, represented as  $P(C|X)$  at  $R_1$  with equation 4.5.

$$R_1 = P(C|X) \quad (4.5)$$

Thereafter, the collision probability for each row ( $R_{row}$ ), shown in equation 4.6, is determined using the relationship between probability interval ( $Z_{\Delta}$ ) and the row number. Equation 4.6 provides a piecewise linear decrease of collision probability as the object moves further away from the reference location “X”. This piecewise linear function forms the zonal probability distribution of the LID model.

$$R_{row} = R_1 - (row - 1)Z_{\Delta}, \quad row \geq 1 \quad (4.6)$$

where,

$R_{row}$ : collision probability at row number

$R_1$ : collision probability at road region “X”

$row$ : row number within the AOI

$Z_{\Delta}$ : probability interval

The probability interval  $Z_{\Delta}$ , defined as the difference in collision probability between each row, is represented by the equation 4.7. The probability interval is formulated using the difference in collision probability between the first and last row divided by the total number of rows. This interval explains how the collision probability decreased in intervals for each row.  $R_{n_a}$  is defined as the probability of collision for the furthest row within the AOI. This value is set between 0 and  $(R_1/rows_{int})$  to achieve a uniform probability interval (as shown in equation 4.7)

#### 4.1 Spatial-Temporal Risk Evaluation Ensemble Technique (STREET) algorithm

---

between rows, while  $R_1$  is set to 1.0 (refer to equation 4.5). A higher value of  $R_{n_a}$  results in a smaller probability interval between rows. It is essential to ensure that the total distance within the AOI accurately represents the actual distance between the reference location “X” and the end of the last row. For instance, if the AOI  $D_{total}$  is 50 meters and detected through a camera mounted at a 6 meters height with a road speed limit of 20 km/h, the calculated  $rows_{int}$  is 10 (equation 4.1). Therefore, the  $R_{n_a}$  is established to range from 0 to 0.1. This limitation assumes that the last row of the AOI road represents the furthest point in the AOI of the scene where an object can be detected.

$$Z_{\Delta} = \frac{R_1 - R_{n_a}}{rows_{int} - 1} \quad (4.7)$$

where,

$Z_{\Delta}$ : probability interval

$R_1$ : collision probability at road region “X”

$rows_{int}$ : maximum number of rows determined

$R_{n_a}$ : user assigned collision probability for the last row

Equation 4.6 applies throughout the entire rows of the risk detection matrix in terms of zonal probability distribution. As for inter-zonal probability distribution, a linear reduction of  $Z_{\Delta}$ , shown in equation 4.7 is applied across columns. This linear reduction of  $Z_{\Delta}$  applies from road to pavement and pavement to offroad regions. Thus, LID is a piecewise linear risk detection that forms the LID risk detection matrix.

#### **Conservative Exponential Distribution (CED) model**

The CED model is meant to detect objects in the front to middle rows of the AOI. The model aims to provide a high collision probability within its coverage of the AOI and to trigger early risk warnings for AV operation. CED’s consistently high collision probability from front to middle rows is designed to prompt the AV for safety actions early, such as slowing down the operating speed and eventually

#### 4.1 Spatial-Temporal Risk Evaluation Ensemble Technique (STREET) algorithm

---

avoiding collisions. This helps the AV take a more cautious approach (thus the name conservative) to prevent collisions as long as the detected object resides between the front and middle rows of the AOI. The risk becomes insignificant if the object is located at the last few rows of the AOI.

The collision probability for the CED model uses a “maximum probability minus decaying exponential” model to achieve the purpose. The collision probability for each row is illustrated in equation 4.8.

$$R_{row} = R_1 - e^{(row - row_{int})}, (row \geq 2) \quad (4.8)$$

where,

$R_{row}$ : collision probability at row number

$R_1$ : collision probability at road region “X”

$row$ : row number

$row_{int}$ : maximum number of rows determined

Equation 4.8 is applied throughout the risk detection matrix in terms of zonal probability distribution. As for inter-zonal probability distribution, a similar approach to LID is applied across columns.

#### **Aggressive Exponential Distribution (AED) model**

AED intends to provide an instantaneous high collision probability when objects are detected at the front rows of the AOI, close to the reference location “X”. When objects move beyond the front rows but within the AOI, the collision probability will reduce drastically. AED is considered an aggressive approach that provides a prompt trigger to the AV for safety actions since the high collision probability only appears as a short surge as an object moves across the front rows.

The formulation of AED uses a decaying exponential model to mimic the high initial collision probability followed by fast decay of values as the object moves away from the first few rows of the AOI, as shown in equation 4.9.

#### 4.1 Spatial-Temporal Risk Evaluation Ensemble Technique (STREET) algorithm

---

$$R_{row} = e^{\left(\frac{-\lambda(row-1)}{row_{int}}\right)}, row \geq 1 \quad (4.9)$$

where,

$R_{row}$ : collision probability at row number

$row$ : row number

$row_{int}$ : maximum number of rows determined

$\lambda$ : rate of decay

This approach allows a faster decay in the collision probability compared to LID and CED. AED has a high collision probability in the first few rows, followed by almost zero collision probability. The AED model's decay rate is determined by  $\lambda$  in equation 4.9. The rate of decay ranges from 1 to 20. The higher the rate of decay, the lower the collision probability starts from the second row onwards. The AV operators can adjust this rate of decay with a typical setting of 6, which indicates that the sensitivity focuses on the first three rows for collision probability.

Equation 4.9 applies to all rows of the risk detection matrix in terms of zonal probability distribution. As for inter-zonal probability distribution, a linear drop of  $Z_{\Delta}$  is applied across columns, similar to LID and CED. Thus, AED is an aggressive risk detection model that forms the AED risk detection matrix.

#### Inter-zonal Probability Distribution

With the concepts of LID, CED, and AED explained, the inter-zonal probability distribution follows a linear decrease of  $Z_{\Delta}$  across zonal areas. This linear decrease in collision probability is applied across inter-zonal areas, as shown in equations 4.10 to 4.13. The amount of linear decrease is defined as the probability interval,  $Z_{\Delta}$ , together with a unity amplifier,  $\alpha$ , which can be used to control the step size.  $\alpha$  controls the percentage of  $Z_{\Delta}$  as a linear decrease across inter-zonal areas (i.e. 1 for 100% and 0.5 for 50%)

#### 4.1 Spatial-Temporal Risk Evaluation Ensemble Technique (STREET) algorithm

---

$$Y_{Ln} = R_n - \alpha Z_{\Delta} \quad (4.10)$$

$$Y_{Rn} = R_n - \alpha Z_{\Delta} \quad (4.11)$$

$$G_{Ln} = Y_{Ln} - \alpha Z_{\Delta} \quad (4.12)$$

$$G_{Rn} = Y_{Ln} - \alpha Z_{\Delta} \quad (4.13)$$

where,

$Z_{\Delta}$ : probability interval

$\alpha$ : unity amplifier to control the step size

$R_n$ : red zonal areas with row n

$Y_{Ln}$ : yellow left zonal areas with row n

$Y_{Rn}$ : yellow right zonal areas with row n

$G_{Ln}$ : green left zonal areas with row n

$G_{Ln}$ : green left zonal areas with row n

In summary, probabilistic models (LID, CED, and AED) can be selected initially based on the intentions of the AV operator for the required risk detection mechanism, as shown in Table 4.2, and thereafter obtained the verification using the probability of object occurrence within the AOI, in a recursive process. The risk detection matrix  $RD_{rzz}$ , contains the collision probability of the selected probabilistic model. As a result, the probabilistic model directly impacts the values of RT figures, which will be further explained in later sections.

## 4.1 Spatial-Temporal Risk Evaluation Ensemble Technique (STREET) algorithm

Table 4.2 Comparison of model and utility

Model	Risk detection mechanism	Event Priority
LID	Focus on the entire AOI. Provides piecewise linear collision probability that vary with distance to the reference location "X". Use primarily for events identified through analytics in real time or post-processing.	Object movements and vehicle occlusion of pedestrians.
CED	Focus on the front and middle rows of the AOI. Provides high collision probability even if the objects are in the middle row, which triggers early risk warnings for AV operation.	Object movements and vehicle occlusion of pedestrians.
AED	Focus on the front few rows of the AOI. Provides high collision probability when objects are detected. Since coverage of AOI is small, any reported high collision probability requires immediate safety actions if the AV is within proximity.	Object movements. Not suitable for occlusion detection.

### 4.1.3 Object detection process

Once the risk zoning and probabilistic model for the risk detection matrix is completed, object detection is done to identify the object within the AOI. The object detection process aims to 1) identify vehicles or pedestrians and 2) map them into an object detection matrix, as shown in Figure 4.4. The object detection matrix is the same size as the 2D risk zoning matrix. Whenever vehicle(s) or pedestrian(s) are detected, an integer value is assigned to each zonal area within the object detection matrix.

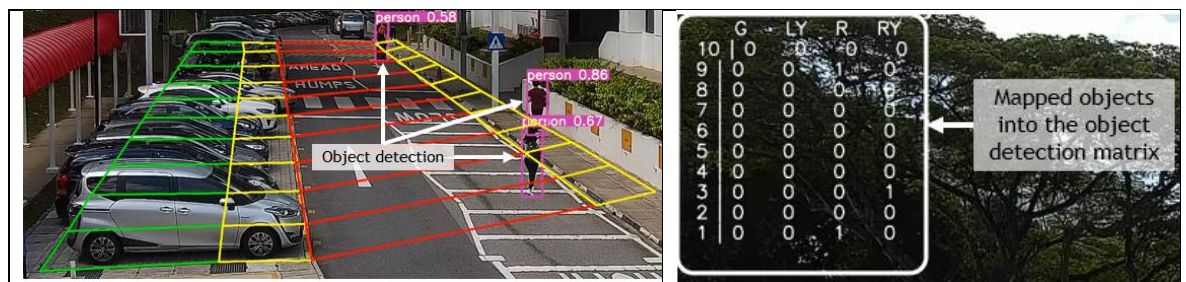


Figure 4.4 Object detection process

### Object identification

Object identification utilises YOLOv5, as described in chapter 3, to obtain bounding boxes of the detected objects. Since there are different YOLO versions, for completeness, the mean average precision (mAP) of YOLOv5 [125] was compared to that of YOLOv6 [126], YOLOv7 [127] and YOLOv8 [128]. Table 4.3 presents the comparison results, showing that YOLOv5 performs better than YOLOv6-N, with an expected 3% to 5% difference between YOLOv5 and YOLOv8 or YOLOv7-Tiny. This aligns with the results reported in [128].

Table 4.3 Comparison of YOLO variants on mAP

Model	No. of parameters (million)	mAP (mIOU 0.5)	mAP (mIOU 0.5 to 0.95)
YOLOv5-S	7.2	0.739	0.576
YOLOv6-N	4.7	0.726	0.568
YOLOv7-Tiny	6.2	0.812	0.622
YOLOv8-S	11.2	0.748	0.606

In addition to comparing mAP results, the Precision, Recall, and F1 scores were compared using their confusion matrix, shown in Table 4.4. The performance of YOLOv5 closely matches that of YOLOv7-Tiny. In another study, YOLOv5 showed a better mAP than YOLOv6, YOLOv7, and YOLOv8 [129]. Therefore, object detection continued with YOLOv5s, considering that newer versions can achieve a slightly higher performance of 3% to 5%. These results were tested using 158,696 images for training and 6,510 images for testing.

Table 4.4 Comparison of YOLO variants on Precision, Recall and F1 score

Model	Precision	Recall	F1 score
YOLOv5-S	0.84	0.65	0.74
YOLOv6-N	0.59	0.66	0.62
YOLOv7-Tiny	0.87	0.66	0.75
YOLOv8-S	0.84	0.62	0.72

### Mapping of object into object detection matrix

The number of detected objects is mapped into each zonal area in real time. The detected object must first be converted from a bounding box into a reference location  $(x, y)$ . The bottom centre of the bounding box is selected since it is the closest to the object's landing point, as shown in Figure 4.5.



Figure 4.5 Reference location for detecting object bounding box

Thereafter, the location  $(x, y)$  of the object is tested with a "point in polygon" [130] for that zonal area. For example, the detected person on the right  $(x_2, y_2)$  in Figure 4.5 is tested if that pixel falls within the second yellow zonal area from the bottom. If the test is positive, which is true in this case, the zonal area will have the integer 1. This approach allows multiple objects to be detected simultaneously within the same scene, even if they belong to different zonal areas. Therefore, the object detection matrix can be separated into different classes (i.e. separate object detection matrix for vehicles and pedestrians)

The outcomes of the object detection process provide an object detection matrix,  $OD_{rz}$ , which indicates the number of detected objects within each zonal area in real time. The size of the object detection matrix is the same as the risk detection matrix and 2D risk zoning matrix.

#### **4.1.4 Risk Tag (RT) Matrix and Risk Tag (RT) figure**

This process determines the RT matrix and its corresponding RT figure. The RT matrix represents the conversion of image information into numerical information (i.e. hazardous detection of objects over a scene into a numerical RT matrix and



#### 4.1 Spatial-Temporal Risk Evaluation Ensemble Technique (STREET) algorithm

figure). The RT matrix is computed based on the 2D risk zoning matrix ( $\omega_{rz}$ ), the risk detection matrix ( $RD_{rz}$ ) used, and the object detection matrix ( $OD_{rz}$ ). An example is illustrated in Figure 4.6.

$\omega_{rz} = \begin{bmatrix} 6 & 8 & 10 & 8 & 6 \\ \cdot & \cdot & \cdot & \cdot & \cdot \\ \cdot & \cdot & \cdot & \cdot & \cdot \\ 6 & 8 & 10 & 8 & 6 \\ 6 & 8 & 10 & 8 & 6 \end{bmatrix}$ <p>2D risk zoning matrix</p>	$RD_{rz} = \begin{bmatrix} 0.0 & 0.0 & 0.1 & 0.0 & 0.0 \\ \cdot & \cdot & \cdot & \cdot & \cdot \\ \cdot & \cdot & \cdot & \cdot & \cdot \\ 0.7 & 0.8 & 0.9 & 0.8 & 0.7 \\ 0.8 & 0.9 & 1.0 & 0.9 & 0.8 \end{bmatrix}$ <p>LID model</p>	$OD_{rz} = \begin{bmatrix} 0 & 0 & 0 & 0 & 0 \\ \cdot & \cdot & \cdot & \cdot & \cdot \\ \cdot & \cdot & \cdot & \cdot & \cdot \\ 0 & 0 & 0 & 0 & 0 \\ 0 & 0 & 1 & 0 & 0 \end{bmatrix}$ <p>1 person was detected at R1.</p>
---	--	---

Figure 4.6 An example of a 2D risk zoning matrix, risk detection matrix and object detection matrix

The process starts with determining the overall object detection matrix ( $OOD_{rz}$ ) by performing the Hadamard product of the 2D risk zoning matrix and object detection matrix shown in equation 4.14.

$$OOD_{rz} = (\omega \circ OD)_{rz} \quad (4.14)$$

where,

$OOD_{rz}$ : overall object detection matrix

$OD_{rz}$ : object detection matrix

$\omega_{rz}$ : 2D risk zoning matrix

Similarly, the RT matrix is derived by performing another element-wise multiplication of the risk detection matrix ( $RD_{rz}$ ) and overall object detection matrix ( $OOD_{rz}$ ). Lastly, the RT figure is obtained by summing all the elements within the risk tag matrix using equation 4.15.

$$RT_{final} = \sum_{rz} (RD \circ OOD)_{rz} \quad (4.15)$$

where,

$RT_{final}$ : RT figure

$RD_{rz}$ : risk detection matrix

$OOD_{rz}$ : overall object detection matrix

$RT_{final}$  ranges from 0 to 100, depending on the number of objects detected in the AOI. The algorithm imposes a maximum limit of 100 since any RT figure higher than 100 requires the same immediate attention. With more objects on the road, the  $RT_{final}$  will be higher than those on the pavement or offroad.  $RT_{final}$  provides the summation of all objects' risks within each scene. Normalisation of  $RT_{final}$  is achieved by dividing it by the number of detected objects. Normalised  $RT_{final}$  ranges from 0 to 10 and provides the average risk of an object within each scene. Further explanation is illustrated using implementation results in section 4.2.

#### 4.1.5 Occurrence

The Occurrence of a hazardous event is obtained as the probability of the detected object based on past accumulated  $OD_{rz}$ . These Occurrence figures are visualised using a heatmap over time. The heatmap refers to the accumulated object occurrence in each zonal area over time of  $OD_{rz}$ . Frame intervals ( $t_{interval}$ ) represent the number of samples for the heatmap. Therefore, the equation for the heatmap is represented as equation 4.16.

$$Heatmap_{rz} = \sum_{N=1}^{t_{interval}} OD_{rzN} \quad (4.16)$$

where,

$Heatmap_{rz}$ : total occurrence of detected objects (maximum number of samples)

$t_{interval}$ : maximum number of samples

$OD_{rzN}$ : object detection matrix of sample N

Using pedestrians as an example, the pedestrian occurrence data and the total number of pedestrians detected, the probability of pedestrian  $P(Occ)$  occurring in each zonal area can be calculated using equation 4.17.

#### 4.1 Spatial-Temporal Risk Evaluation Ensemble Technique (STREET) algorithm

---

$$P(Occ)_{rz} = \frac{Heatmap_{rz}}{\sum_{r=1}^{rows} \sum_{z=1}^{zone} Heatmap_{rz}} \quad (4.17)$$

where,

$P(Occ)_{rz}$ : probability of occurrence

$Heatmap_{rz}$ : total occurrence of detected objects (maximum number of samples)

Since LID, CED, and AED focus on the different AOI coverage, the heatmap can be used to verify the probabilistic models. This is achieved by separating the AOI's collision probability into the front  $P(Fr)$  equation 4.18, middle  $P(Mid)$  equation 4.19 and rear  $P(Re)$  equation 4.20 collision probability. The accumulated  $P(Fr)$ ,  $P(Mid)$ , and  $P(Re)$  provide the probability of occurrence at the front, middle, or rear rows. These  $P(Fr)$ ,  $P(Mid)$ , and  $P(Re)$  assist in verifying the LID, CED, and AED probabilistic models used in the risk detection matrix. For example, if  $P(Fr)$  is high and AED is used, the RT figure should have more instances of high RT figures than LID.

$$P(Fr) = \sum_{r=1}^{front} \sum_{z=1}^{zone} P(Occ)_{rz}, \quad (4.18)$$

where,

$P(Fr)$ : probability for occurrence for front rows

*front*: number of rows considered for front AOI

*zone*: number of columns in the AOI

$P(Occ)_{rz}$ : probability of occurrence

$$P(Mid) = \sum_{r=1}^{middle} \sum_{z=1}^{zone} P(Occ)_{rz} \quad (4.19)$$

#### 4.1 Spatial-Temporal Risk Evaluation Ensemble Technique (STREET) algorithm

---

where,

$P(Mid)$ : probability for occurrence for middle rows

$middle$ : number of rows considered for middle AOI

$zone$ : number of columns in the AOI

$P(Occ)_{rz}$ : probability of occurrence

$$P(Re) = \sum_{r=1}^{rear} \sum_{z=1}^{zone} P(Occ)_{rz} \quad (4.20)$$

where,

$P(Re)$ : probability for occurrence for rear rows

$rear$ : number of rows considered for rear AOI

$zone$ : number of columns in the AOI

$P(Occ)_{rz}$ : probability of occurrence

#### 4.1.6 Road Side Unit Time To Collide (RSU-TTC)

The STREET algorithm provides RSU-TTC from the infrastructure to the AV via cooperative mode. RSU-TTC reflects the estimation of the time taken for the detected object to collide with the reference location “X” from the RSU’s perspective. RSU-TTC is assigned as  $TTC_{value}$  and determined in three steps.

- Step 1. Obtain a normalised object detection matrix known as  $OD_{binary}$  (converting an integer into binary within the matrix, e.g. integer > 1 will be assigned as 1).
- Step 2. Obtain the  $time_{rz}$  matrix by using  $t_{resp}$  (reference from risk zoning equation 4.1 and multiply by each row number. RSU-TTC applies only to red zonal areas (roads).
- Step 3. Calculate  $TTC_{rz}$  by performing a Hadamard product between  $OD_{binary}$  and  $time_{rz}$  matrix shown in equation 4.21 and then determine the

lowest non-zero value where  $TTC_{value} \in TTC_{rz}$  and  $\neq 0$  in equation 4.22.

$$TTC_{rz} = (OD_{binary} \circ time_{rz}) \quad (4.21)$$

$$TTC_{value} = \min(TTC_{rz}) \quad (4.22)$$

### Time to collision from the AV perspective

With the RSU-TTC sent to the AV, the AV obtains the overall time to collision ( $TTC_{overall}$ ) between the detected object and the AV's current location using equation 4.23.

$$TTC_{overall} = t_{RT} + TTC_{value} \quad (4.23)$$

where,

$TTC_{overall}$ : overall time to collision between the AV and the detected object

$TTC_{value}$ : road side unit time to collide (RSU-TTC)

$t_{RT}$ : time from the current AV location to the reference location "X"

The variable  $t_{RT}$  is the time taken from the current AV location to the reference location "X" which is determined from equation 4.24.  $D_{(AV-RT)}$  is the distance from the current AV position to the reference location "X", while  $V_{AV}$  is the speed of the AV.

$$t_{RT} = \frac{D_{(AV-RT)}}{V_{AV}} \quad (4.24)$$

where,

$t_{RT}$ : time from current AV location to reference location "X"

$D_{(AV-RT)}$ : distance between the current AV location to the reference location "X"

$V_{AV}$ : speed of AV

#### 4.1 Spatial-Temporal Risk Evaluation Ensemble Technique (STREET) algorithm

Other than  $TTC_{overall}$ , the overall distance to collision ( $DTC_{overall}$ ) can be obtained by multiplying  $TTC_{overall}$  by the speed of the AV. This allows for another form of representation by distance instead of time between the current AV location and the detected object.

##### 4.1.7 Hazard identifications and warning

STREET's outcome provides the conversion of image information to quantitative RT figures, RSU-TTC, and the probability of object occurrence with data over time. Additionally, STREET also provides hazard identifications and warnings specifically for areas of unregulated traffic (as illustrated in chapter 3). Hazard identifications and warnings are boolean detections of events in areas of road sections and intersections of T-junctions.

Table 4.5 STREET hazard detection features

Category	Hazard Identifications	Hazard warnings
Risk Zone (red zone for road sections)	Yes	No
Intersection Risk zone (black zone for intersections)	Yes	Yes
Datatypes	<ul style="list-style-type: none"> <li>• Vehicle-to-vehicle</li> <li>• Vehicle-to-Pedestrian</li> </ul>	<ul style="list-style-type: none"> <li>• Vehicle Warning</li> <li>• Pedestrian Warning</li> </ul>

Table 4.5 shows two STREET hazard detection features. The first is hazard identifications for any vehicle-to-vehicle and/or vehicle-to-pedestrian in the road sections and intersections. The second is hazard warnings for vehicles and/or pedestrians only at intersections. Detecting these hazards in real time provides an instantaneous identification of scenarios in addition to quantitative RT figures, and they are sent to the AV for necessary safety actions via cooperative mode.

The operations of hazard detection include an additional demarcation of the intersection during risk zoning, such as the black zone. Since there is no quantitative collision probability, the risk detection algorithm is omitted. The

## 4.2 STREET Risk tagging process and results

object detection matrix is used to detect the object's classification and map the object's location (x,y) to the red or black zone using the "point in polygon" test.

Table 4.6 tabulates the conditions for hazard detection. For a "True" vehicle warning within a black zone, a vehicle is detected within the T-junction intersection. For "True" pedestrian warning within a black zone, a pedestrian is detected within the T-junction intersection. Vehicle-to-vehicle hazard identification can happen in red or black zones. Vehicle-to-vehicle hazard identification is "True" when two vehicles are detected within the defined zonal areas for road or T-junction intersection. Similarly, vehicle-to-pedestrian hazard identification is "True" when one vehicle and a pedestrian are detected within the defined zonal areas for road or T-junction intersection.

Table 4.6 Hazard identifications and warnings conditions

Zone(s)	Hazard identifications & warnings	Mechanism (Detected pedestrian = $P_d$ ) (Detected vehicle = $V_d$ )
Black zone ( $B_0$ )	Vehicle warning	"True" if $V_d \subseteq B_0$ else "False"
Black zone ( $B_0$ )	Pedestrian warning	"True" if $P_d \subseteq B_0$ else "False"
Red zone ( $R_i$ ) Black zone ( $B_0$ )	Vehicle-to-vehicle hazard identification	"True" if $[(V_{d1} \subseteq B_0) \cap (V_{d2} \subseteq B_0)]$ or $[(V_{d1} \subseteq R_i) \cap (V_{d2} \subseteq R_i)]$ else "False"
Red zone ( $R_i$ ) Black zone ( $B_0$ )	Vehicle-to-pedestrian hazard identification	"True" if $[(V_d \subseteq B_0) \cap (P_d \subseteq B_0)]$ or $[(V_d \subseteq R_i) \cap (P_d \subseteq R_i)]$ else "False"

## 4.2 STREET Risk tagging process and results

This section illustrates the process and results of the STREET algorithm tested in real-world unregulated traffic scenarios. A cornering scenario, shown in Figure 4.7, was tested for RT figures, RSU-TTC, and Occurrence as outcomes for real-world events. This cornering scenario was also used to compare the performance of different RT figures derived from different probabilistic models.

## 4.2 STREET Risk tagging process and results

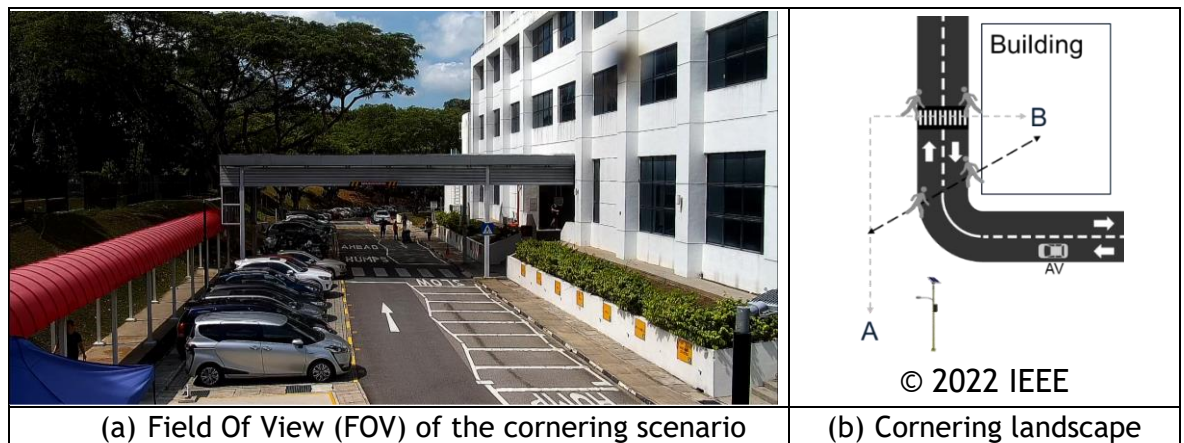


Figure 4.7 STREET testing scenario for cornering

Figure 4.7 (a) shows the FOV of the RSU's camera in the cornering scenario. The RSU's camera was mounted at a height of 5.5 m for a detection range of up to 50 m. Figure 4.7 (b) shows the cornering landscape where the AV, before the corner turn, is unable to detect pedestrians, resulting in the need for sudden and harsh braking immediately after the turn. The pedestrians tend to move in different directions from point A to B and vice versa. In this scenario, the STREET algorithm provides remote advance warnings to the AV with RT figures, RSU-TTC, and Occurrences. RT figures provide a quantitative risk to the AV before the turn, and RSU-TTC assists the AV by determining a time-to-collision towards the detected object. The occurrence was used as post-analytics to verify the effectiveness of the RT figures and identify the locations of hotspots within the AOI.

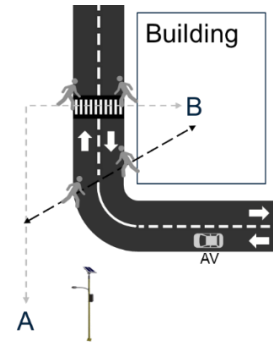
### 4.2.1 Risk zoning matrix

STREET algorithm started by determining the risk zoning matrix of the corner scenario through the risk zoning steps defined in section 4.1.1.



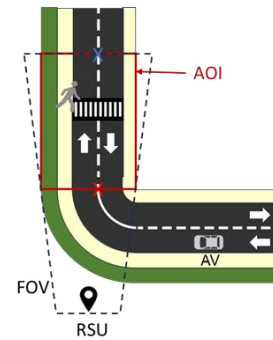
## 4.2 STREET Risk tagging process and results

Step 1: In the cornering scenario, the area with the most traffic happens when pedestrians crossed from location A to B and vice versa.



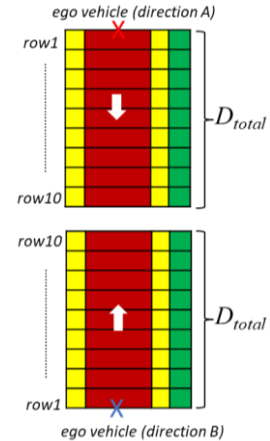
© 2022 IEEE

Step 2: The FOV from the RSU's camera identifies the AOI with the highest traffic occurrence from step 1. The AOI was marked as the hazardous area where pedestrians crossed the road immediately after the cornering of the road.



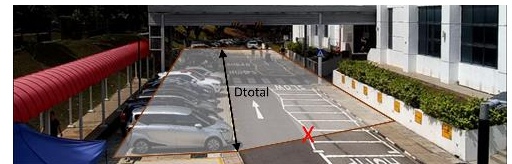
© 2022 IEEE

Step 3: From the selected AOI, indicate the reference location "X" in both directions. The reference location "X" indicates the AV's direction of travel towards the identified hazardous area. The reference location "X" marked in blue indicates the opposite direction.



© 2022 IEEE

Step 4: The  $D_{total}$  was measured at 50 m from the identified AOI.



Step 5: Based on equation 4.1, the number of rows for the AOI was determined with the following variables and values defined.

$$rows_{int} = \frac{D_{total}}{(t_{resp} \cdot V_{max} \cdot V_f)}$$

## 4.2 STREET Risk tagging process and results

where,

$$D_{total} = 50 \text{ m}$$

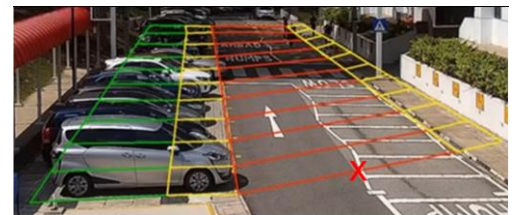
$$t_{resp} = 0.85 \text{ s}$$

$$V_{max} = 20 \text{ (5.55) km/hr (m/s)}$$

$$V_f = 1.0$$

As such,  $rows_{int}$  was determined as 10.

Step 6: Based on the  $rows_{int} = 10$ , the offroad, pavement and roads were demarcated manually into zonal areas.



Step 7: The zonal areas were converted into 2D risk zoning matrix,  $\omega_{rZ}$  (equation 4.2), and assigned with weights defined in Table 4.1. For example, a weight of 6 was assigned for accessible pathways away from pavement, also known as offroad. While a weight of 8 was assigned for dedicated pavements, shared paths or parking lots. The distance for each row ( $D_x$ ) is 5 m (equation 4.3), and the time to travel for each row by the AV ( $t_x$ ) is 0.9s (equation 4.4)

	Left			Right		
D <sub>10</sub>	G <sub>r10</sub>	Y <sub>r10</sub>	R <sub>r10</sub>	Y <sub>r10</sub>	t <sub>10</sub>	
D <sub>9</sub>	G <sub>r9</sub>	Y <sub>r9</sub>	R <sub>r9</sub>	Y <sub>r9</sub>	t <sub>9</sub>	
D <sub>8</sub>	G <sub>r8</sub>	Y <sub>r8</sub>	R <sub>r8</sub>	Y <sub>r8</sub>	t <sub>8</sub>	
D <sub>7</sub>	G <sub>r7</sub>	Y <sub>r7</sub>	R <sub>r7</sub>	Y <sub>r7</sub>	t <sub>7</sub>	
D <sub>6</sub>	G <sub>r6</sub>	Y <sub>r6</sub>	R <sub>r6</sub>	Y <sub>r6</sub>	t <sub>6</sub>	
D <sub>5</sub>	G <sub>r5</sub>	Y <sub>r5</sub>	R <sub>r5</sub>	Y <sub>r5</sub>	t <sub>5</sub>	
D <sub>4</sub>	G <sub>r4</sub>	Y <sub>r4</sub>	R <sub>r4</sub>	Y <sub>r4</sub>	t <sub>4</sub>	
D <sub>3</sub>	G <sub>r3</sub>	Y <sub>r3</sub>	R <sub>r3</sub>	Y <sub>r3</sub>	t <sub>3</sub>	
D <sub>2</sub>	G <sub>r2</sub>	Y <sub>r2</sub>	R <sub>r2</sub>	Y <sub>r2</sub>	t <sub>2</sub>	
D <sub>1</sub>	G <sub>r1</sub>	Y <sub>r1</sub>	R <sub>r1</sub>	Y <sub>r1</sub>	t <sub>1</sub>	

© 2022 IEEE

$$\omega_{rZ} = \begin{bmatrix} 6 & 8 & 10 & 8 \\ 6 & 8 & 10 & 8 \\ 6 & 8 & 10 & 8 \\ 6 & 8 & 10 & 8 \\ 6 & 8 & 10 & 8 \\ 6 & 8 & 10 & 8 \\ 6 & 8 & 10 & 8 \\ 6 & 8 & 10 & 8 \\ 6 & 8 & 10 & 8 \\ 6 & 8 & 10 & 8 \end{bmatrix}$$

© 2022 IEEE

### 4.2.2 Risk detection matrix with probabilistic model

The risk detection matrix determines the collision probability for all the zonal areas within the AOI using the size of 2D risk zoning matrix as a reference. This section shows the three different risk detection matrices based on LID, CED, and AED, respectively. The outcomes were based on the AOI of the cornering scenario as an illustrative example.

#### Linear Interval Distribution (LID)

The LID risk detection matrix was determined using equations 4.5, 4.6 and 4.7. The process of deriving each zonal area within the LID risk detection matrix was accomplished using Table 4.7.

Based on the 2D risk zoning, the matrix size was 4 columns by 10 rows. Table 4.7 shows that the collision probability of the road section was determined first. From equation 4.5,  $R_1$  was determined as 1.0 since the first row is the closest to the reference location “X” and assumes a potential collision with the highest probability. This was followed by finding the collision probability  $Z_{\Delta}$  with the previously obtained input variables and the last row,  $R_{n_a}$  is assigned a collision probability of 0.1. Thereafter, all the zonal area’s collision probability for the road region (from  $R_2$  to  $R_{10}$ ) were determined.

Table 4.7 LID risk detection matrix derivation

Equation	Input variables	Find	Outcome
4.5	NA	$R_1$	1.0
4.7	$R_1 = 1.0$ $R_{n_a} = 0.1$ $rows_{int} = 10$	$Z_{\Delta}$	0.1
4.6	$Z_{\Delta} = 0.1$ $row = 1$ to 10	$R_1, R_2, R_3, R_4, R_5$ $R_6, R_7, R_8, R_9, R_{10}$	1.0, 0.9, 0.8, 0.7, 0.6, 0.5, 0.4, 0.3, 0.2, 0.1

## 4.2 STREET Risk tagging process and results

With the collision probability defined for all the road regions, the pavement (yellow) and offroad (green) collision probability were determined using the linear inter-zonal probability distribution, defined in equations 4.10 to 4.13. Table 4.8 shows an example of how the left pavement, left offroad and right pavement collision probability were determined.

Table 4.8 Inter-zonal probability distribution for LID risk detection matrix

Equation	Input variables	Find	Outcome
4.10	$\alpha=1.0$ $Z_{\Delta} = 0.1$	$Y_{l1}, Y_{l2}, Y_{l3}, Y_{l4}, Y_{l5},$ $Y_{l6}, Y_{l7}, Y_{l8}, Y_{l9}, Y_{l10},$	0.9, 0.8, 0.7, 0.6, 0.5, 0.4, 0.3, 0.2, 0.1, 0.0
4.11	$\alpha=1.0$ $Z_{\Delta} = 0.1$	$Y_{r1}, Y_{r2}, Y_{r3}, Y_{r4}, Y_{r5},$ $Y_{r6}, Y_{r7}, Y_{r8}, Y_{r9}, Y_{r10},$	0.9, 0.8, 0.7, 0.6, 0.5, 0.4, 0.3, 0.2, 0.1, 0.0
4.12	$\alpha=1.0$ $Z_{\Delta} = 0.1$	$G_{l1}, G_{l2}, G_{l3}, G_{l4}, G_{l5},$ $G_{l6}, G_{l7}, G_{l8}, G_{l9}, G_{l10},$	0.8, 0.7, 0.6, 0.5, 0.4, 0.3, 0.2, 0.1, 0.0, 0.0

With all the zonal area's collision probability determined for LID risk detection, the outcome is illustrated as  $RD_{LID}$ .

$$RD_{LID} = \begin{bmatrix} G_{l10} & Y_{l10} & R_{10} & Y_{r10} \\ G_{l9} & Y_{l9} & R_9 & Y_{r9} \\ G_{l8} & Y_{l8} & R_8 & Y_{r8} \\ G_{l7} & Y_{l7} & R_7 & Y_{r7} \\ G_{l6} & Y_{l6} & R_6 & Y_{r6} \\ G_{l5} & Y_{l5} & R_5 & Y_{r5} \\ G_{l4} & Y_{l4} & R_4 & Y_{r4} \\ G_{l3} & Y_{l3} & R_3 & Y_{r3} \\ G_{l2} & Y_{l2} & R_2 & Y_{r2} \\ G_{l1} & Y_{l1} & R_1 & Y_{r1} \end{bmatrix} \Rightarrow RD_{LID} = \begin{bmatrix} 0 & 0 & 0.1 & 0 \\ 0 & 0.1 & 0.2 & 0.1 \\ 0.1 & 0.2 & 0.3 & 0.2 \\ 0.2 & 0.3 & 0.4 & 0.3 \\ 0.3 & 0.4 & 0.5 & 0.4 \\ 0.4 & 0.5 & 0.6 & 0.5 \\ 0.5 & 0.6 & 0.7 & 0.6 \\ 0.6 & 0.7 & 0.8 & 0.7 \\ 0.7 & 0.8 & 0.9 & 0.8 \\ 0.8 & 0.9 & 1.0 & 0.9 \end{bmatrix}$$

### Conservative Exponential Distribution (CED)

The CED risk detection matrix is determined using equation 4.8. This equation was used for calculating the 2<sup>nd</sup> row of the road region ( $R_2$ ) onwards, where  $R_1$  is set

## 4.2 STREET Risk tagging process and results

at 1.0. Similar to LID, the road regions were first determined and the process is shown in Table 4.9.

Table 4.9 CED risk detection matrix derivation

Equation	Input variables	Find	Outcome
4.5	NA	$R_1$	1.0
4.8	$R_1 = 1.0$ $row = 2 \text{ to } 10$ $rows_{int}=10$	$R_2, R_3, R_4,$ $R_5, R_6, R_7,$ $R_8, R_9, R_{10}$	1.00, 1.00, 1.00, 0.99, 0.98, 0.95, 0.86, 0.63, 0.00

Similarly, inter-zonal probability distribution was applied for CED, as defined in equations 4.10 to 4.13. The resulting CED risk detection matrix is shown as  $RD_{CED}$ . The figures were rounded off to 2 decimal places.

$$RD_{CED} = \begin{bmatrix} G_{l10} & Y_{l10} & R_{10} & Y_{r10} \\ G_{l9} & Y_{l9} & R_9 & Y_{r9} \\ G_{l8} & Y_{l8} & R_8 & Y_{r8} \\ G_{l7} & Y_{l7} & R_7 & Y_{r7} \\ G_{l6} & Y_{l6} & R_6 & Y_{r6} \\ G_{l5} & Y_{l5} & R_5 & Y_{r5} \\ G_{l4} & Y_{l4} & R_4 & Y_{r4} \\ G_{l3} & Y_{l3} & R_3 & Y_{r3} \\ G_{l2} & Y_{l2} & R_2 & Y_{r2} \\ G_{l1} & Y_{l1} & R_1 & Y_{r1} \end{bmatrix} \Rightarrow RD_{CED} = \begin{bmatrix} 0 & 0 & 0.0 & 0 \\ 0.43 & 0.53 & 0.63 & 0.53 \\ 0.66 & 0.76 & 0.86 & 0.76 \\ 0.75 & 0.85 & 0.95 & 0.85 \\ 0.78 & 0.88 & 0.98 & 0.88 \\ 0.79 & 0.89 & 0.99 & 0.89 \\ 0.80 & 0.9 & 1.00 & 0.90 \\ 0.80 & 0.9 & 1.00 & 0.90 \\ 0.80 & 0.9 & 1.00 & 0.90 \\ 0.80 & 0.9 & 1.00 & 0.90 \end{bmatrix}$$

### Aggressive Exponential Distribution

Lastly, the AED risk detection matrix was determined using equation 4.9, which determined  $R_1$  and all rows of the road regions. The road regions were determined first, and the outcome is shown in Table 4.10.

Table 4.10 AED risk detection matrix derivation

Equation	Input variables	Find	Outcome
4.9	$\lambda = 6$ $row = 1 \text{ to } 10$ $rows_{int}=10$	$R_1, R_2, R_3, R_4, R_5$ $R_6, R_7, R_8, R_9, R_{10}$	1.00, 0.55, 0.30, 0.17, 0.09, 0.05, 0.03, 0.02, 0.01, 0.00

## 4.2 STREET Risk tagging process and results

Thereafter, inter-zonal probability distribution is similarly applied for AED. The resulting AED risk detection matrix is shown as  $RD_{AED}$ . The figures were rounded off to 2 decimal places.

$$RD_{AED} = \begin{bmatrix} G_{l10} & Y_{l10} & R_{10} & Y_{r10} \\ G_{l9} & Y_{l9} & R_9 & Y_{r9} \\ G_{l8} & Y_{l8} & R_8 & Y_{r8} \\ G_{l7} & Y_{l7} & R_7 & Y_{r7} \\ G_{l6} & Y_{l6} & R_6 & Y_{r6} \\ G_{l5} & Y_{l5} & R_5 & Y_{r5} \\ G_{l4} & Y_{l4} & R_4 & Y_{r4} \\ G_{l3} & Y_{l3} & R_3 & Y_{r3} \\ G_{l2} & Y_{l2} & R_2 & Y_{r2} \\ G_{l1} & Y_{l1} & R_1 & Y_{r1} \end{bmatrix} \Rightarrow RD_{AED} = \begin{bmatrix} 0 & 0 & 0 & 0 \\ 0 & 0 & 0.01 & 0 \\ 0 & 0 & 0.02 & 0 \\ 0 & 0 & 0.03 & 0 \\ 0 & 0 & 0.05 & 0 \\ 0 & 0 & 0.09 & 0 \\ 0 & 0.07 & 0.17 & 0.07 \\ 0.10 & 0.20 & 0.30 & 0.20 \\ 0.35 & 0.45 & 0.55 & 0.45 \\ 0.80 & 0.90 & 1.00 & 0.90 \end{bmatrix}$$

### 4.2.3 Object detection matrix

The object detection matrix was created by obtaining the results of the object detection process and mapping them into the zonal regions within the object detection matrix. Since this research focuses on risk assessment rather than AI performance and optimisation, any object detection algorithm with bounding box results can be integrated into the STREET algorithm. The model used for STREET algorithm is YOLOv5s, and future work can incorporate newer and improved models as they become available. This section explains the summary of testing YOLOv3 and YOLOv5 with the pre-train weight, followed by the outcome of a trained and tested custom model for YOLOv5s and, eventually, the results of YOLOv5s + Mapping performance. The comparison of YOLOv5s with its later variants was already reported in section 4.1.3.

The research started experimenting with the use of YOLOv3 [131] with COCO datasets with pre-trained model for STREET. In recent years, YOLOv5s [125] (section 4.1.3) have been proven to be more effective in performance than YOLOv3. Table 4.11 shows results of YOLOv5 pre-train weights out-performing YOLOv3 by more than 40%.

## 4.2 STREET Risk tagging process and results

Table 4.11 Comparison of YOLOv3 vs YOLOv5s

Model	Sample size	True Positive	True Negative	False Positive	False Negative	Accuracy
YOLOv3	25.60k	17.33%	4.10%	0.97%	77.33%	21.43%
YOLOv5s	74.056k	43.63% (32,307)	23.83% (17,645)	16.93% (12,541)	15.61% (11,563)	67.46%

Table 4.11 shows the results of testing YOLOv3 vs YOLOv5 using pre-trained weight based on the stated sample size using a confusion matrix. With the accuracy 67.46% for the YOLOv5s pre-train model, further training and testing of additional datasets are required to obtain an improved custom model. Therefore, as shown in section 4.1.3, 158,696 images were trained and 6,510 images were tested using YOLOv5s. With the custom model, the mAP 0.5 is 0.739 and mAP 0.5 to 0.95 is 0.576. The confusion matrix of the custom model achieved 84% for Precision, 62% for Recall and 72% for F1 score. The results for the custom trained model were comparable to existing research shown in [108, 109, 127]. Thus the custom YOLOv5s model is sufficient as a baseline for STREET.

The next step was to map the YOLOv5s outcome to the object detection matrix, which was the same size as the 2D risk zoning matrix. This mapping was performed using the “Point in polygon” test (x,y) at the bottom centre of the bounding box to the zonal areas. The object detection matrix will indicate each zonal area for the corresponding objects that have been detected. If no object is detected, the zonal area will be assigned a value of “0”.

Figure 4.8 (a) shows two pedestrians detected at  $R_8$  and one pedestrian at  $G_{L3}$  of the AOI, the detected pedestrians were mapped into  $OD_1$  matrix shown in Figure 4.8 (b).

## 4.2 STREET Risk tagging process and results

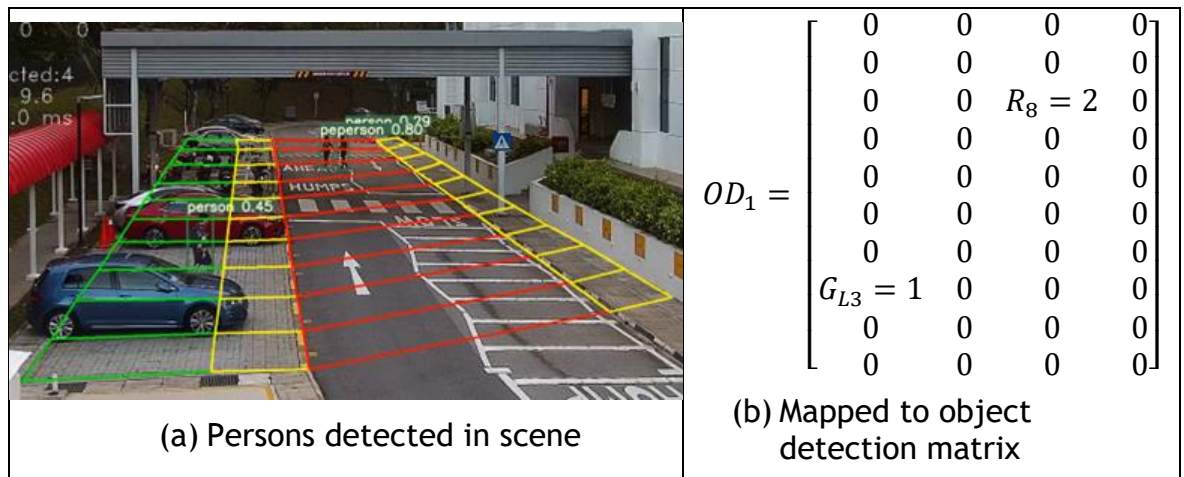


Figure 4.8 Example one: three persons detected and mapped to object detection matrix

In another example, Figure 4.9 (a) shows two pedestrians detected at  $R_8$  and one pedestrian detected at  $R_3$  of the AOI, the detected pedestrians are mapped into  $OD_2$  matrix shown in Figure 4.9 (b). The YOLOv5s performs object detection every 40 ms per image frame. This YOLOv5 + Mapping summarised the function of the object detection matrix.

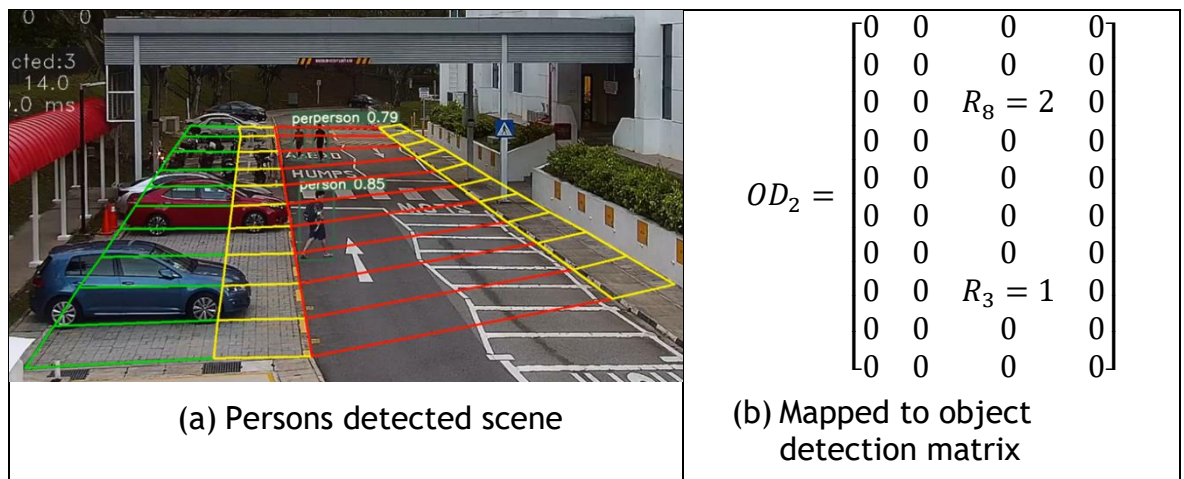


Figure 4.9 Example two: three persons detected and mapped to object detection matrix

With the YOLOv5s + Mapping, additional testing was performed to evaluate the Precision, Recall and F1 score. To achieve this, two specific rules were added for this testing, illustrated in Figure 4.10 and Figure 4.11.



## 4.2 STREET Risk tagging process and results

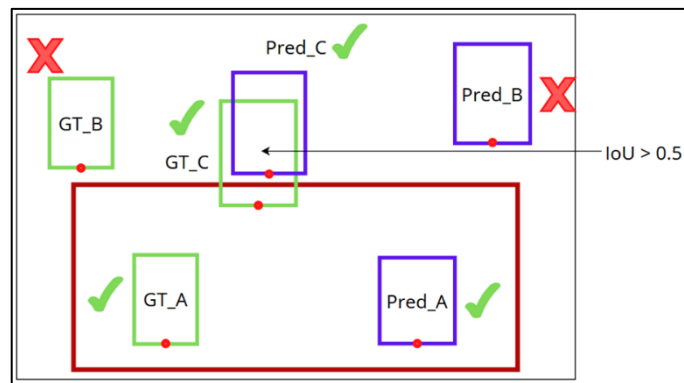


Figure 4.10 Rule 1: YOLOv5 + Mapping

Rule 1: Filtering of objects which are not within the AOI, with examples shown in Figure 4.10. Object detection uses bounding box with Intersection over Union (IoU) greater or equal than 50% with respect to the ground truth as positive prediction. Thus, if ground truth (GT) and predicted object (Pred) falls within the zonal region (red box), they are considered “True Positive”. This includes cases where the Pred\_A has an IoU of less than 50% against the GT\_A. In another case, If GT\_B and Pred\_B are outside the zonal region, they are filtered. However, in another example, if GT\_C is within the zonal region and Pred\_C has an IoU greater than 50% but not within the zonal region, it is still considered as “True Positive”.

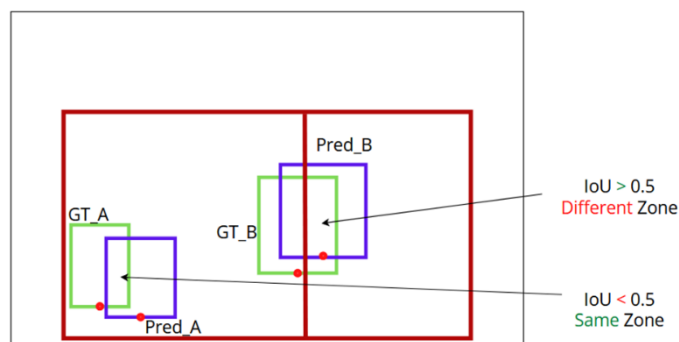


Figure 4.11 Rule 2: YOLOv5 + Mapping

Rule 2: Definition for True Positive. Figure 4.11 is used to explain rule 2. For example, if GT\_A and Pred\_A occurs within the same zonal region but with an IoU of less than 50% between them, their status is changed to “True Positive”. On the contrary, if the GT\_B falls within the zonal region on the left of Figure 4.11 and the Pred\_B has an IoU of more than 50%

## 4.2 STREET Risk tagging process and results

---

between them but it resides at a different zonal region, GT\_B and Pred\_B is converted to “False detection”.

With the two defined rules, testing was done with YOLOv5s + Mapping, with a result of 85% for Precision, 87% for Recall, and 86% for F1 score. These results show that the YOLOv5s + Mapping improved the Recall from 65% to 87%, thus improving the overall F1 score. This improvement gives a benchmark result for all metrics to be above 80% for STREET usage. The variation in the performance of STREET comes from the object detection matrix, since the rest of the methodologies within STREET algorithm are mainly deterministic and probabilistic based.

### 4.2.4 Risk Tag (RT) figure and results

This section provides an overview of the RT figures from the tested corner scenario by converting one hour of real-time images from contextual information into a quantitative risk figure. Different RT figures resulting from different probabilistic models, LID, CED, and AED, were evaluated and compared, using LID as a baseline comparison. This section also explains the use of normalised RT figures. In this test, 97,446 scenes (an hour of camera images) were converted in real time to RT figures. For example, for LID, high RT figures suggest that pedestrians were detected at the first row, while low RT figures suggest that pedestrians were detected at the last row of the AOI towards the reference location “X”. When there are no pedestrians, RT figure will be zero. As a reference for this corner scenario, the distance between each row within the AOI is 5 m. With 10 rows, the total distance is approximately 50 m. The RT figure provides a quantitative risk representation of pedestrian(s) detected within the scenario's AOI. The details of events within the cornering scenarios are further analysed in section 4.2.7.

#### STREET performance represented by RT figures

The primary outcome of the STREET algorithm is the RT figures. RT figures ( $RT_{final}$ ) are obtained using risk zoning matrix ( $\omega_{rz}$ ), risk detection matrix ( $RD_{rz}$ ), and object detection matrix ( $OD_{rz}$ ), from equations 4.14 and 4.15. STREET is a

## 4.2 STREET Risk tagging process and results

---

probabilistic model with AI deep learning and object detection. The main source of variability in STREET's RT figure comes from the object detection matrix ( $OD_{rz}$ ), with a Precision of 85%, Recall of 87% and F1 score of 86%, as stated in section 4.2.3. The risk zoning matrix is deterministic, and the risk detection matrix is a probabilistic model with distributed outcomes. Therefore, the performance of RT figures closely follows the performance of the object detection matrix.

### LID RT figures

LID was used as a baseline for comparing three different probabilistic models. In Figure 4.12 (a), LID RT figures for the cornering scenario are illustrated, with a total of 97,446 RT figures from an hour of real-time images. The RT figure ranges from 0 to a maximum of 39.2, with peaks at different instances and a mean of 3.35. Figure 4.12 (b) shows the LID RT figures with a graph displaying the distribution of RT figures grouped in increments of 5, including the quantity of zero RT figures. The 97,446 scenes within 3,880 seconds of LID RT figures in Figure 4.12 (b) demonstrate that the RT figures appear at different intervals of the RT figure distribution, which is expected when the LID model is used. Further details about the behaviour of LID will be provided in real-world events in section 4.2.7. Figure 4.12 (c) shows that among the LID RT figures, 39,446 (40.48%) have no risk detection, and 58,000 (59.52%) are non-zero RT figures.

## 4.2 STREET Risk tagging process and results

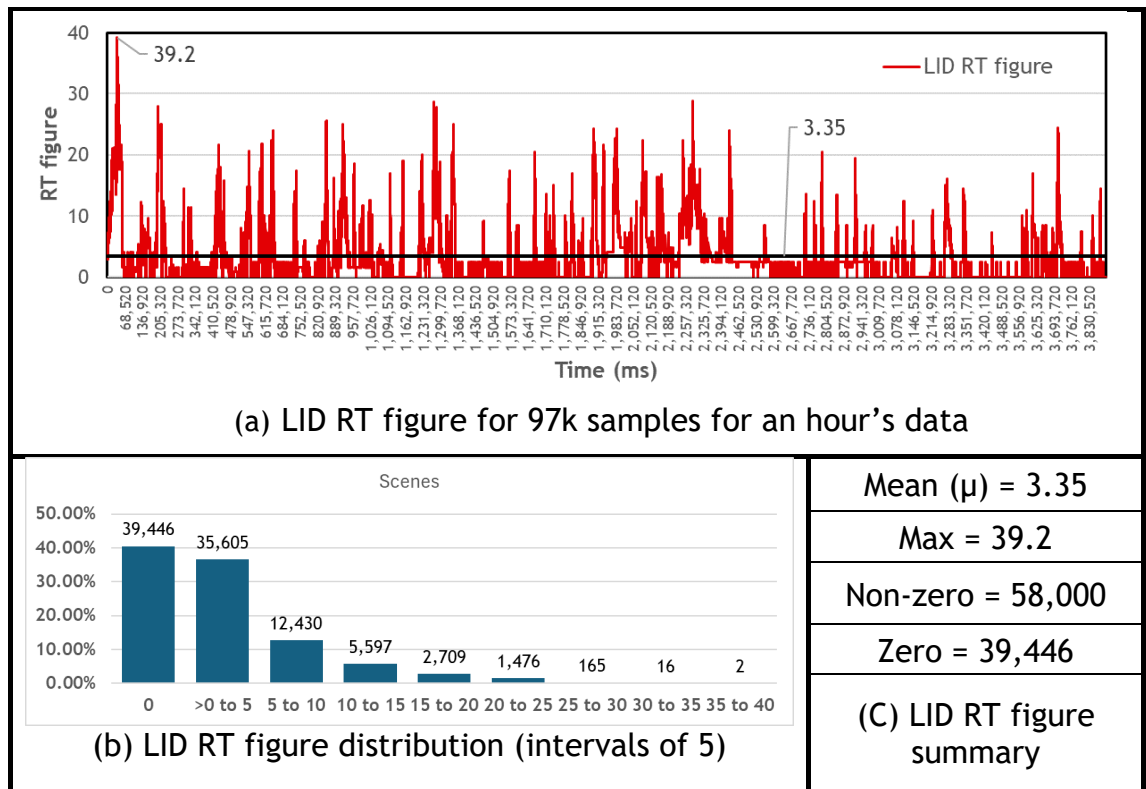


Figure 4.12 LID RT figures illustrations and result

### CED RT figures

The CED RT figures for the cornering scenario are presented in Figure 4.13 using the same image data. In Figure 4.13 (a), the CED RT figures range from 0 to a maximum of 60.27, representing a 16% increase compared to LID. The mean CED RT figure is almost double that of LID, with a mean value of 7.15 compared to LID's 3.35. This difference was due to the CED's different RT figure probability distribution, which focuses on the front and middle rows, as opposed to LID, which focuses on the entire AOI. Figure 4.13 (b) demonstrates that the CED RT figure distribution had fewer counts in the RT figure intervals from ">0 to 5" compared to LID, and these scenes were converted to higher RT figure intervals. This indicates that objects are mostly detected in the middle of the AOI as CED assigned a higher RT figure compared to LID, which is further proven in section 4.2.5. Section 4.2.7 will provide further insights into CED behaviour in real-world events. Despite their differences, CED and LID exhibit similar trends in Figure 4.13 (a) and Figure 4.12 (a). CED and LID also show similar non-zero RT figures (40,089 vs 39,446) and zero RT figures (57,357 vs 58,000). In summary, CED RT figures have

4.2 STREET Risk tagging process and results

a higher mean, higher RT figure and a lower count of RT figures in the range of “>0 to 5” compared to LID. CED assigns a higher RT figure when objects are detected away from the reference location “X”.

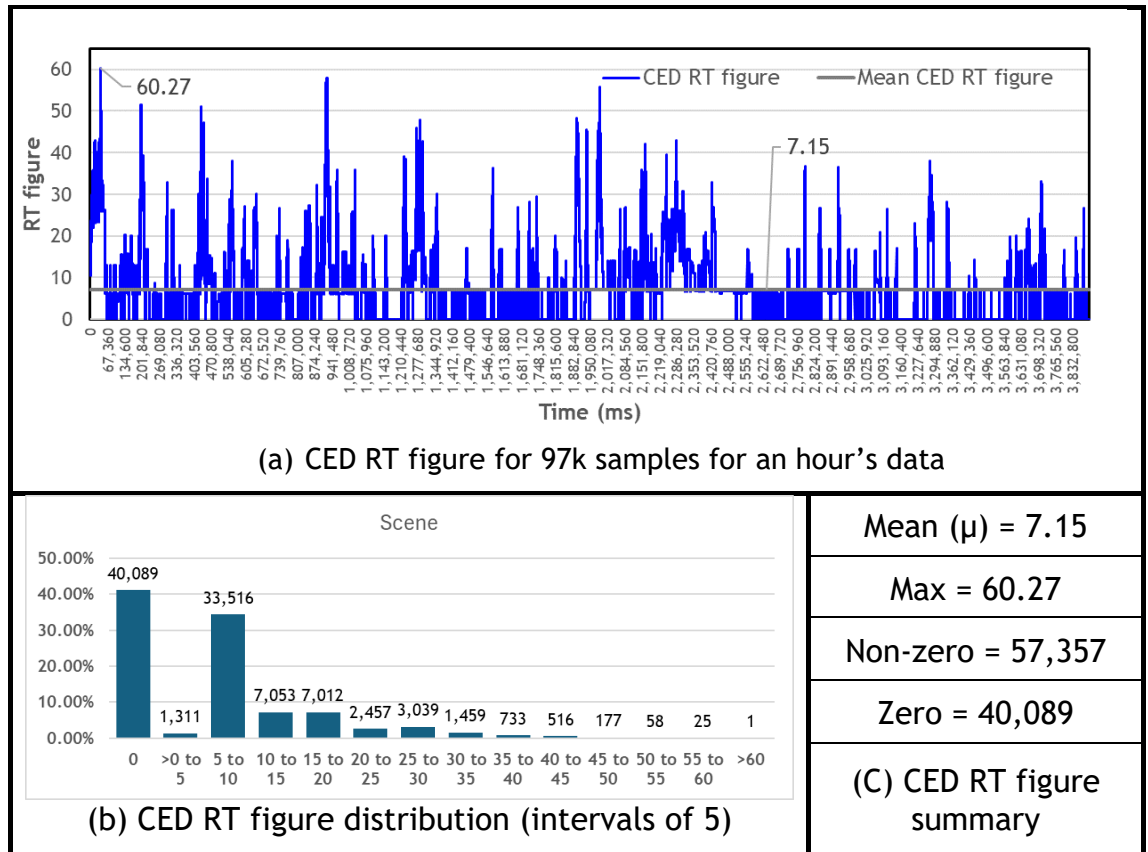


Figure 4.13 CED RT figures illustration and result

**AED RT figures**

Figure 4.14 illustrates the AED RT figures tested in the same scenario. Figure 4.14 (a) shows that AED RT figures vary from 0 to a maximum of 20.08 (48.7% decrease compared to LID). The occurrence of AED RT figures were drastically reduced compared to LID and CED, with a mean of 0.65, the lowest among the three RT figures. The majority of the AED RT figures occur between “>0 to <5”, with 22,862 scenes vs 35,605 scenes from LID. The low mean was the result of high zero RT figures at 70,203 (72.0%) as compared to LID, which is only 39,446 (40.48%). The low mean, lower AED RT figures and lower occurrence of AED RT figures compared to LID, reflected the AED’s intended design. The AED’s AOI coverage had only a high collision probability in the first row, while the 2nd and 3rd rows of the AOI had reduced AED’s collision probability to only 50% or less, which was explained

4.2 STREET Risk tagging process and results

in section 4.2.2. This is further verified by Figure 4.14 (b), where the AED RT figure distribution is only limited to a small number of RT figure intervals as compared to LID and CED.

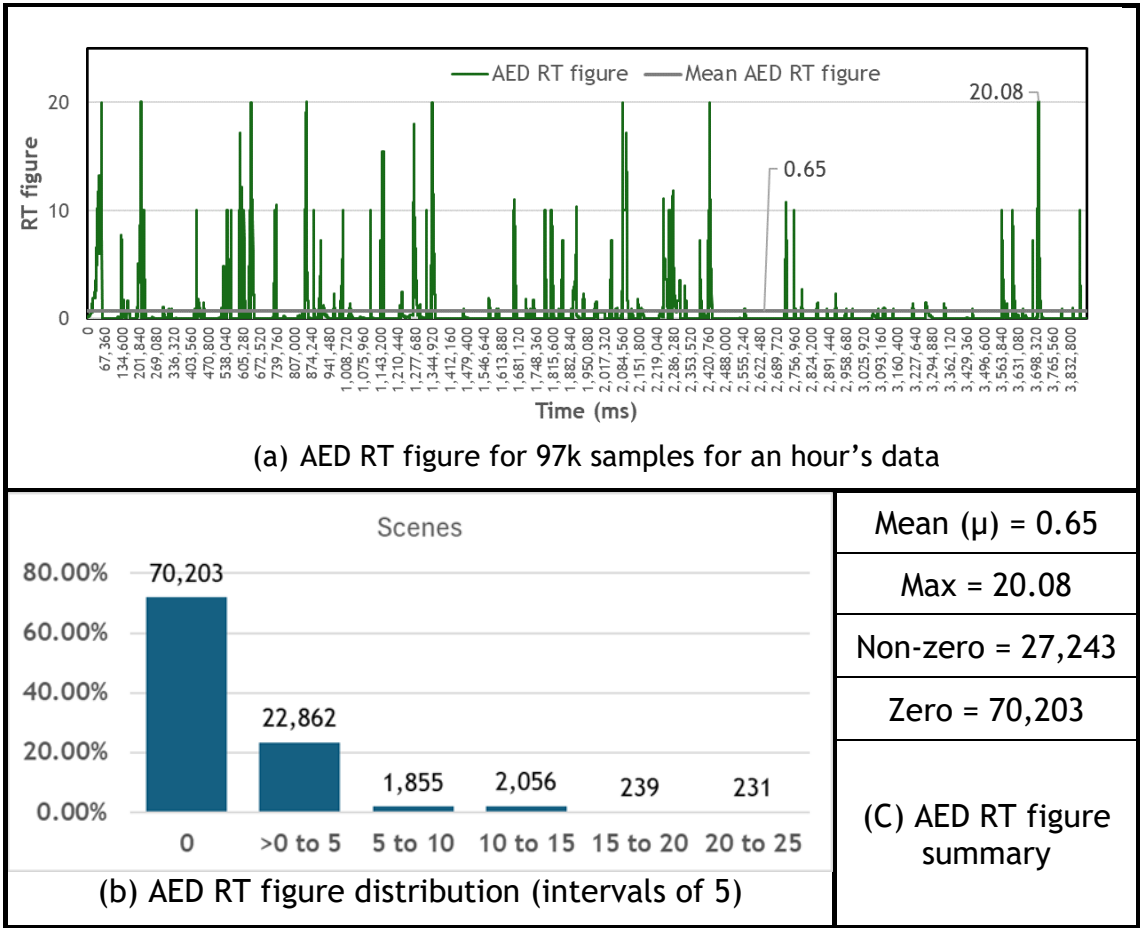


Figure 4.14 AED RT figures illustration and result

### **Limitations of RT figures**

The proposed RT figures have two limitations:

- 1) The LID, CED, and AED RT figures have different maximum values for the same image data, making it challenging to compare and analyse between different scenarios.
- 2) In some scenarios, RT figures might not necessarily represent a high risk. For example, a large group of pedestrians within the last row of the AOI can result in high RT figures. This happens because RT figure sums all the detected pedestrians within the AOI as risk (equation 4.15).

To address the limitations mentioned above, normalised RT figures are calculated by averaging the RT figures across the detected pedestrians in the scene. This allows us to assess the risk per scene within the AOI. A normalised RT figure provides an average RT for the scene on a scale of 0 to 10, making it easy to rate and compare the LID, CED, and AED RT figures. However, the use of normalised RT figures also has its own limitation. For instance, if there are more pedestrians at the rear of the AOI than in the front, the normalised RT figures may underestimate the risk of pedestrians in front of the AOI. Therefore, the optimal approach is to provide the AV with both RT figures and normalised RT figures since RT figures summarise the overall pedestrian risk within the AOI, while normalised RT figures provide an aggregated risk per scene within the AOI.

### **Normalised LID, CED and AED RT figures (Norm RT Figures)**

This section shows all the normalised figures of LID, CED and AED RT figures with illustrations and results. Normalised LID RT figures are compared with normalised CED and AED RT figures. The comparisons focus on the non-zero RT figures instead of zero RT figures.

Figure 4.15 (a) shows the normalised LID RT figures, ranging from 0 to 10, with a mean of 1.86. In Figure 4.15 (b), it is shown that the normalised LID RT figures

4.2 STREET Risk tagging process and results

depict a normal distribution with a mean (zero RT figures are not considered) of 3.12 and a standard deviation of 1.69 in Figure 4.15 (c). The normalised LID RT figures will be used as a baseline comparison for CED and AED.

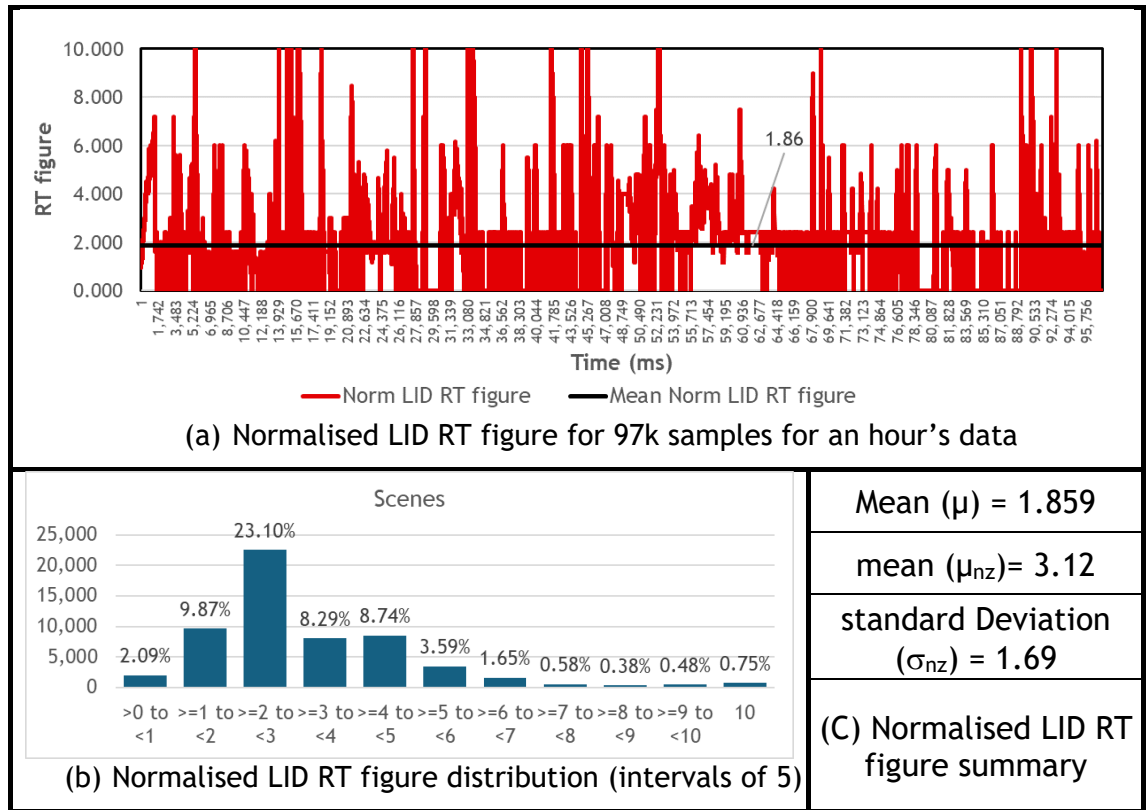


Figure 4.15 Normalised LID RT figures illustration and result

Figure 4.16 (a) displays normalised CED RT figures, with a mean of 4.16, which is more than twice the LID. Figure 4.16 (b) also presents RT figures distribution, with normalised CED RT figures shifted to a higher mean of 7.07 and a standard deviation of 1.38, as shown in Figure 4.16 (c). These results confirmed that CED assigns higher RT figures for the same scenes by comparing CED RT and LID RT figures distribution. Therefore, it is evident that CED provides a relatively high RT figure whenever a pedestrian is detected.



4.2 STREET Risk tagging process and results

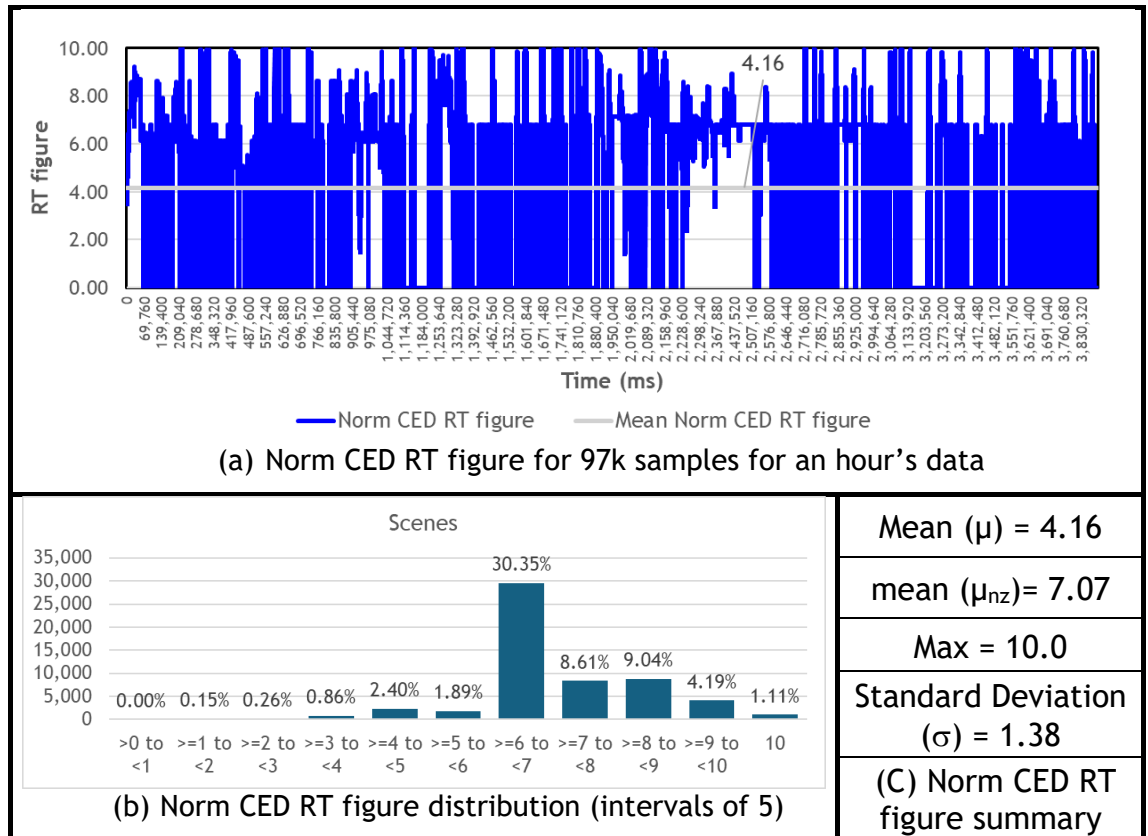


Figure 4.16 Normalised CED RT figures illustration and result

Figure 4.17 (a) shows the normalised AED RT figures with a mean of 0.34. These results show that majority of the pedestrians are detected in the 2nd or 3rd row of the AOI, while the occurrence of pedestrians in the front row is minimal. This was verified by Figure 4.17 (b), which indicates that AED RT figures occur mainly at the RT figure interval of “>0 to <1” with 21.22% and even smaller percentages for the rest of the RT figure intervals. The occurrence of pedestrians in the front row was verified by the low count of normalised AED RT figure = 10, with 0.752% of 97,446 giving 733 occurrences. This occurrence was verified with AED RT figures, with 733 occurrences of 1 pedestrian residing in the front row road region. This normalised RT figure for AED confirmed the intended design and performance of AED.

4.2 STREET Risk tagging process and results

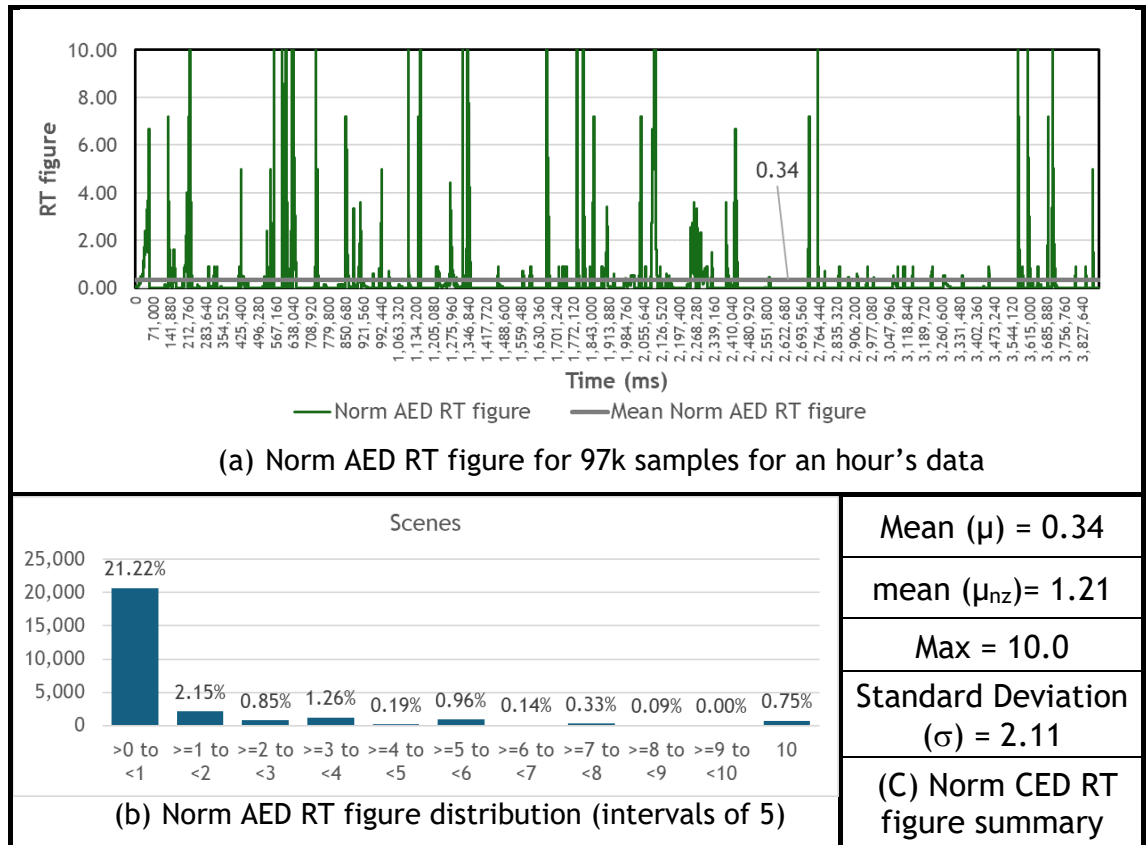


Figure 4.17 Normalised AED RT figures illustration and result

4.2.5 Occurrence data and results visualisation

The occurrence of pedestrians within the AOI, is represented as  $OD_{rz}$  were further transformed into Occurrence visualisation as  $Heatmap_{rz}$  and  $P(Occ)_{rz}$  using equations 4.16 and 4.17, respectively. A total of 99,442 samples were used as data for the  $Heatmap_{rz}$  and  $P(Occ)_{rz}$  illustrated in Figure 4.18 to visualise the pedestrian Occurrence heatmap and the probability of occurrence for each risk zonal area of the AOI. The  $P(Fr)$ ,  $P(Mid)$  and  $P(Re)$ , derived from equations 4.18 to 4.20, were used to verify the RT figures from section 4.2.4. In this application, the front refers to rows 1-3, the middle refers to rows 4-7, and the rear refers to rows 8-10, where  $rows_{int}$  is 10.

## 4.2 STREET Risk tagging process and results

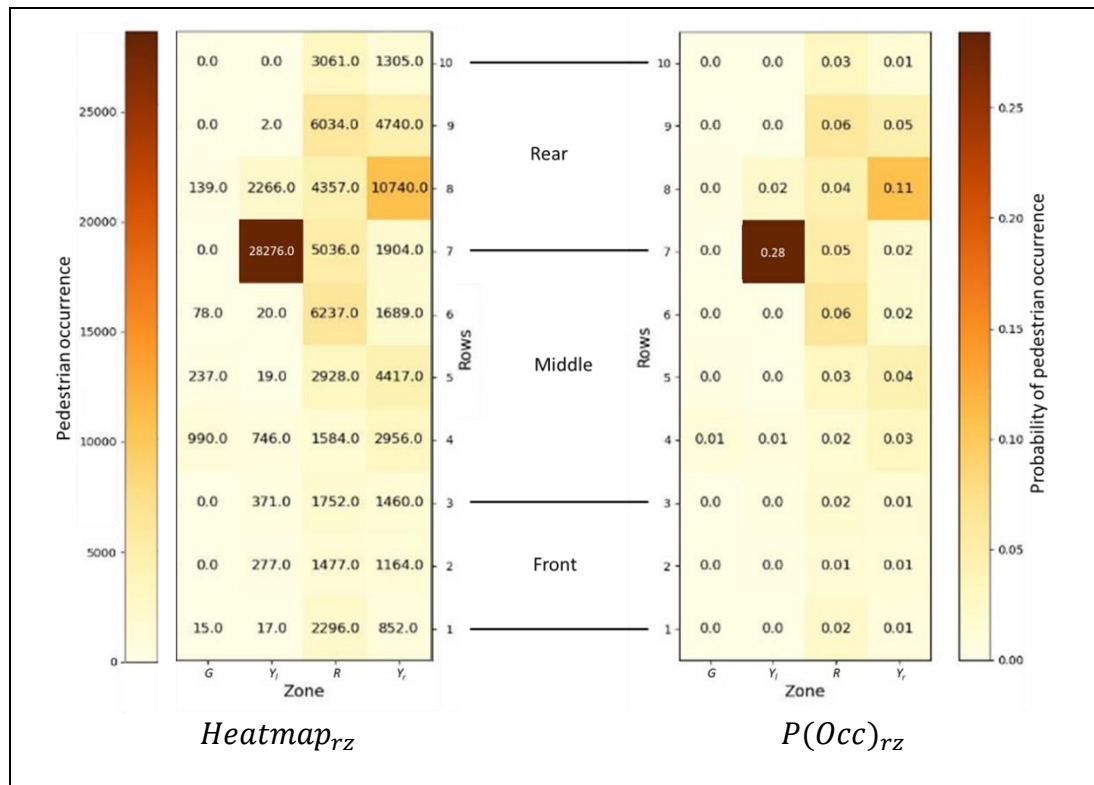


Figure 4.18 Heatmap of overall pedestrian occurrence

Figure 4.18 shows the pedestrian occurrences and the probability of occurrence within the AOI. The results show that the highest number of pedestrians resides in the middle row at  $Y_{l7}$ , (yellow left pavement, row 7 and highlighted in brown) and its surrounding risk zonal areas. The results show that pedestrians do not walk only in a straight line across the designated zebra crossing at row 5/6. Instead, they travel in different directions, congregating around  $Y_{l7}$ . Moreover, this scenario is also concerned with potential pedestrians crossing at the front AOI where the AV does not have visibility before turning into the corner. Therefore, in this scenario, the path planning for AV should start slowing down even before coming close to the zebra crossing. To visualise the pedestrians travelling across the AOI and to verify the suitable probabilistic model, equations 4.18 to 4.20 were used to find  $P(Fr)$ ,  $P(Mid)$  and  $P(Re)$  of the AOI.

## 4.2 STREET Risk tagging process and results

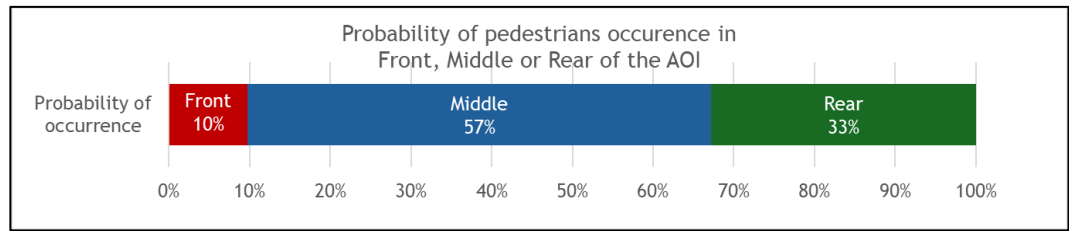


Figure 4.19 Probability of pedestrian occurrence in front, middle and rear rows of the AOI

Figure 4.19 shows that  $P(\text{Mid})$  has the most pedestrian occurrences, followed by  $P(\text{Re})$  and  $P(\text{Fr})$ , which relate to the observations in section 4.2.4. The highest  $P(\text{Mid})$  in Figure 4.19 reflects why CED model has the highest RT figures and the most risk tag instances compared to LID and AED. Similarly,  $P(\text{Fr})$ , having the lowest occurrence in Figure 4.19, reflects the infrequent risk tag instances in the AED model. The probability of pedestrian occurrence is recursively calculated using real-time pedestrian occurrence over a period of time. The results are used to verify the RT figures based on the probabilistic model selected by the AV for its operation. In this illustrated case, 99,442 pedestrian occurrences detected over an hour were used to determine the probability of pedestrian occurrence to verify the RT figures in section 4.2.4. These results verify that either LID or CED would be the best probabilistic models for RT figures in this cornering scenario.

### 4.2.6 Road Side Unit Time to collide matrix and results

RSU-TTC defines the time to collide (in seconds) between the detected pedestrians and the reference location "X" in the AOI. The overall time to the collision of the current AV to the detection of pedestrians is determined by summing the RSU-TTC and time to arrive, as shown in equation 4.23. In STREET, RSU-TTC is sent to the AV via ReRAC. In this section, the results of RSU-TTC was represented as  $TTC_{value}$ . The  $TTC_{value}$  was determined at intervals of 40 ms per frame using equations 4.21 and 4.22. Equation 4.22 further identifies the time to collision between the nearest detected object and the reference location "X" in the AOI, and assigns that to  $TTC_{value}$ . An illustration of  $TTC_{value}$  for the first 10,000 scenes are seen in Figure 4.20. This data illustrates the importance of proximity of pedestrians towards the reference location "X" in the AOI in addition to the RT figures.

## 4.2 STREET Risk tagging process and results

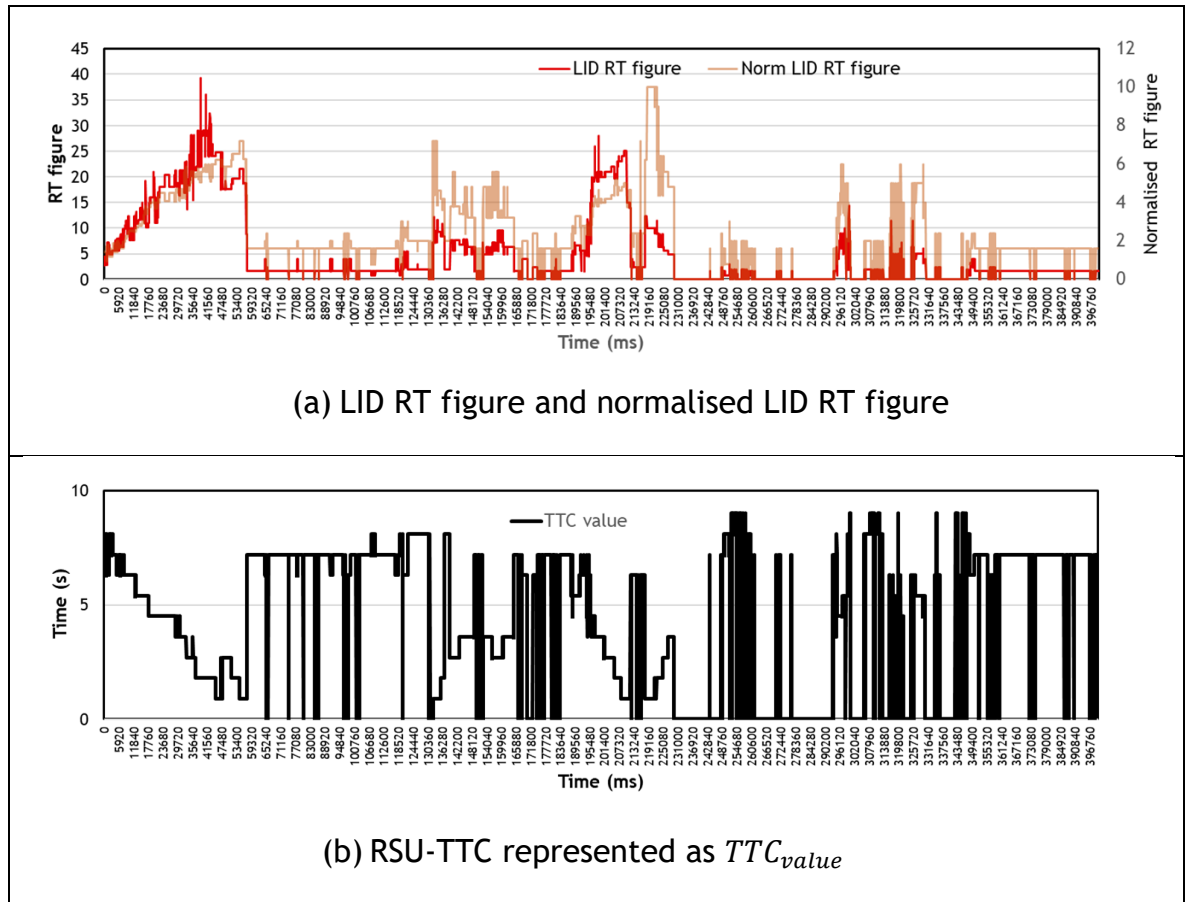


Figure 4.20 Relationship between  $TTC_{value}$ , and normalised LID RT and LID RT figure

Figure 4.20 shows the first 10,000 scenes (400 seconds) of LID RT figures and normalised LID RT figures compared with  $TTC_{value}$ . In Figure 4.20 (a), LID RT figures show the summarised risk value of the scene, while normalised LID RT figures show the average risk per scene. On the other hand, the RSU-TTC represented by  $TTC_{value}$  in Figure 4.20 (b) shows the time to collision between the nearest detected object and the reference location “X” in the AOI. From Figure 4.20 (b), the trend of TTC values is inversely proportional to LID RT figures and normalised LID RT figures. This means that when the LID RT figures were high, the pedestrians were closer to the reference location “X” in the AOI, resulting in low TTC values. Conversely, when LID RT figures were low, it means that the pedestrians were farther away from the reference location “X”, resulting in higher  $TTC_{value}$ . The only exception to this relationship was when the LID RT figure is zero, in which case the TTC values was also zero. Further examples of  $TTC_{value}$  are demonstrated in the next section using events within the corner scenario.

### 4.2.7 Real-world events with RT figures and RSU-TTC

This section identifies real-world events by observing the variation of the RT figures and RSU-TTC over time. The objective is to verify the RT figures and RSU-TTC (represented as  $TTC_{value}$ ) using four different events. Each event is tested with three tasks. The first task was to compare LID RT figures with the ground truth to verify the LID's RT figures. The second task was to compare the performance of LID, CED, and AED RT figures for the same event. The last task was to verify the  $c$  and compare LID RT figures with normalised LID RT figures. Similar to section 4.2.5, the pedestrian class was selected for object detection. Pedestrians detected outside the AOI were not considered for these events analysis. These real-time events analysis shows how RT figures and RSU-TTC vary according to the risk of pedestrian(s) moving within the AOI as part of the corner scenario. The variations of RT figures were illustrated from a temporal point of view with supporting images for each event. Images for each event were annotated to obtain the LID RT ground truth, assuming that the LID operates perfectly for comparative analysis with LID RT figures.

#### **Event 1: Pedestrians' movement from both sides at the middle rows (layer)**

In event 1, pedestrians' crossing occurs from both sides of the road, as shown in Figure 4.21 (a) to (d) at various time points in sequence. The objective is to observe if LID RT figures respond in accordance with the LID RT ground truth. Thereafter, the performance of LID, CED and AED RT figures were compared. Lastly, the figures of  $TTC_{value}$  were verified for the event, and LID RT figures were compared with normalised LID RT figures. Figure 4.21 shows the image sequence of the event with 1) risk zoning of the environment, 2) pedestrian detection for both inside and outside the AOI, 3) the LID RT figures as reference and 4) the video time stamp. The real-time LID RT figures and video time stamp are shown at the top right of Figure 4.21. The same details are provided for the remaining events.

## 4.2 STREET Risk tagging process and results

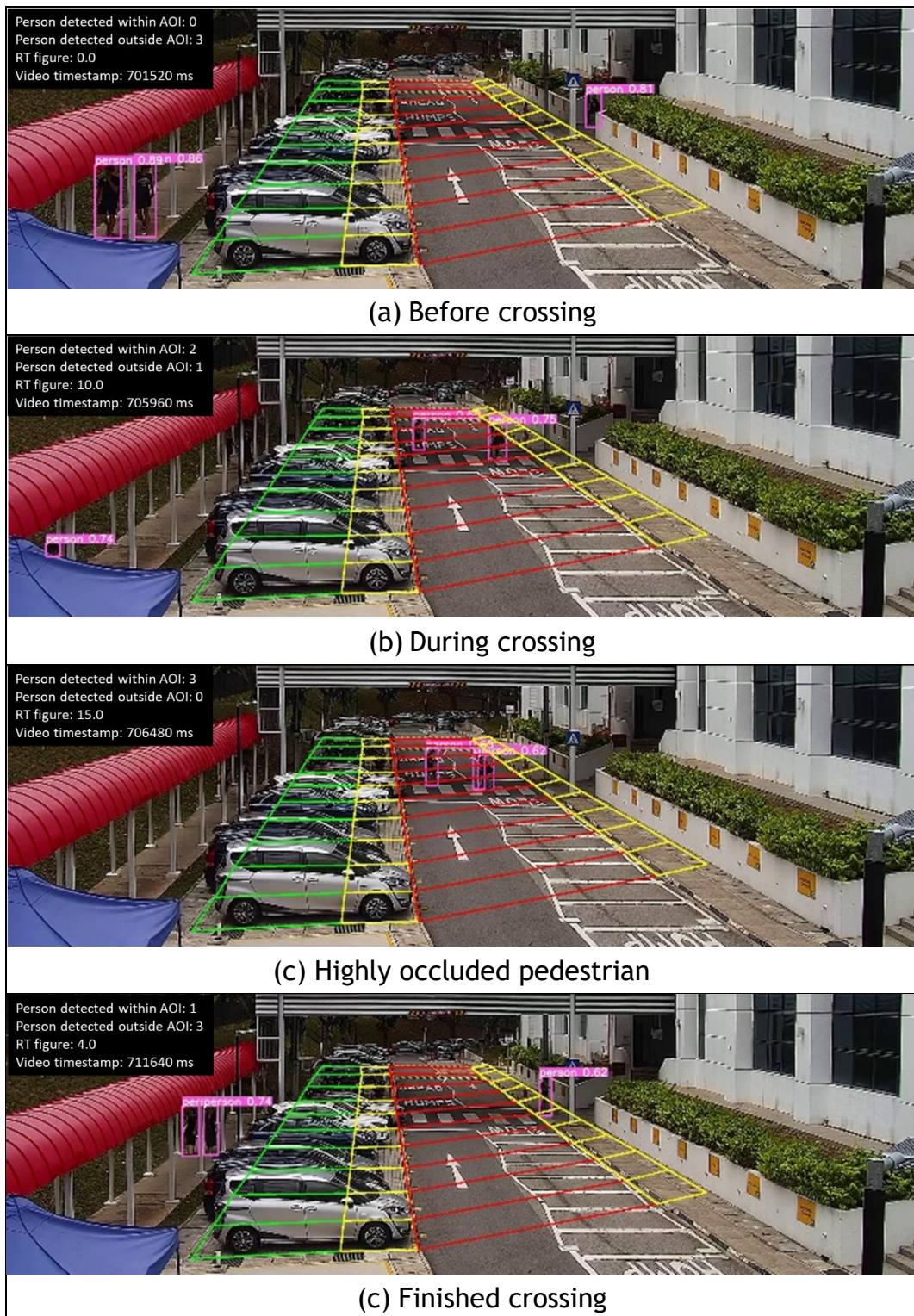


Figure 4.21 Images of pedestrians crossing from both sides for event 1

## 4.2 STREET Risk tagging process and results

### Event 1, task 1: Comparative analysis between LID RT figures and LID RT ground truth

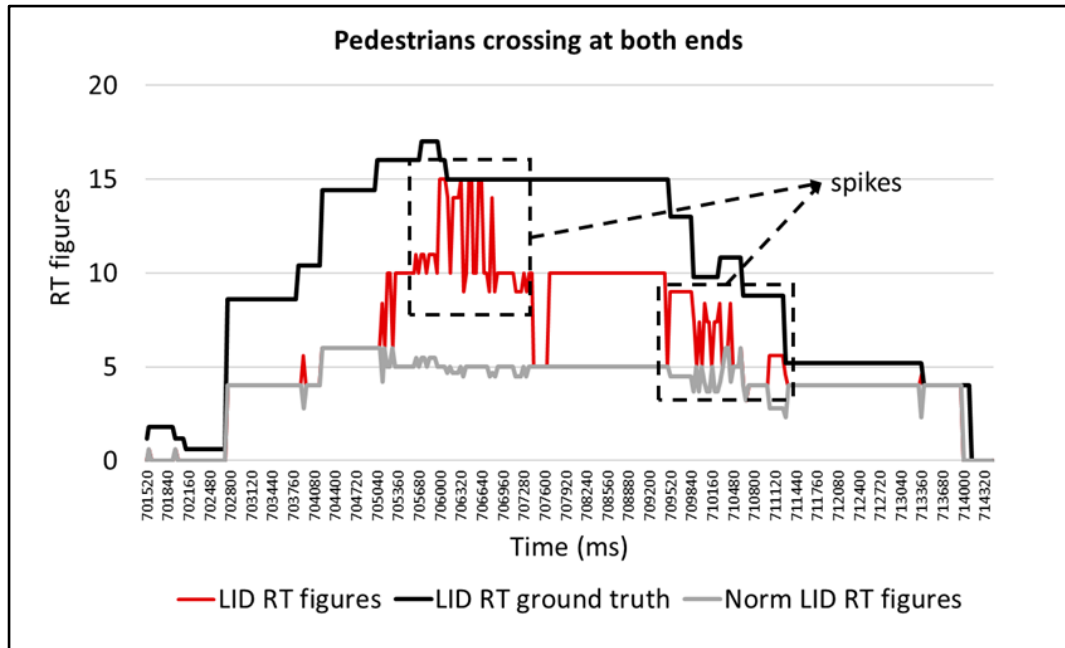


Figure 4.22 LID RT figures vs LID RT ground truth for event 1

Figure 4.22 illustrates the varying LID RT figures compared against the LID RT ground truth. LID RT figures were used instead of normalised LID RT figures since LID RT figures reflect the overall risk of pedestrians within the scene instead of having the average risk of pedestrians. The LID RT ground truth was obtained from manually annotated pedestrians in the scene. The differences between LID RT figures and LID RT ground truth in Figure 4.22 were mainly caused by the highly occluded pedestrian with another pedestrian (i.e., the image in Figure 4.21 (c)). This missed LID RT figure of an additional pedestrian resulted in the differences. Additionally, “spikes” in Figure 4.22 are observed when pedestrians walk behind another pedestrian, and they are either occluded or detected during the process. Overall, the LID RT figure's trend characteristics closely follow the LID RT ground truth.



## 4.2 STREET Risk tagging process and results

### Event 1, task 2: Comparative analysis between LID, CED and AED RT figures

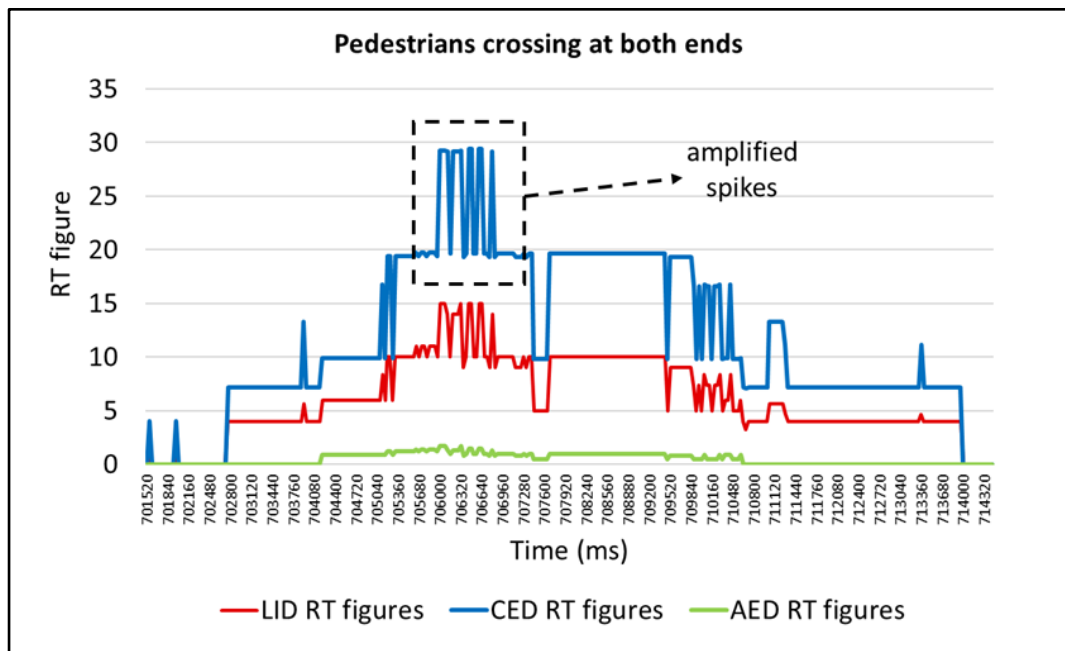


Figure 4.23 Comparison of LID, CED and AED RT figures for event 1

Figure 4.23, illustrates the comparison of LID, CED and AED for event 1. Since the pedestrians occur mainly in the middle rows, AED was not able to detect the details within event 1 since the focus is only on the front rows of the AOI, illustrating an almost flat RT figure. On the other hand, CED RT figures are twice as much as LID RT figures and present similar trend characteristics. CED RT figures also amplify the occlusions, shown as “amplified spikes” in Figure 4.23. This correlates with the findings in section 4.2.4. Therefore, LID and CED are suitable models for event 1. CED provides amplified RT figures when compared to LID. AED has insufficient coverage of the AOI to obtain further information. If CED RT figures are used as remote warnings for the AV, the high RT figures will trigger early safety actions. On the other hand, if AED is used, the AV would miss detecting this event. Lastly, if LID RT figures are used, the variation of the RT figures will be similar to CED but with a lower figure, safety actions will be triggered later (when the RT figure is high) as compared to CED.

## 4.2 STREET Risk tagging process and results

Event 1, task 3: Verify  $TTC_{value}$  and compare LID RT figures to normalised LID RT figures.

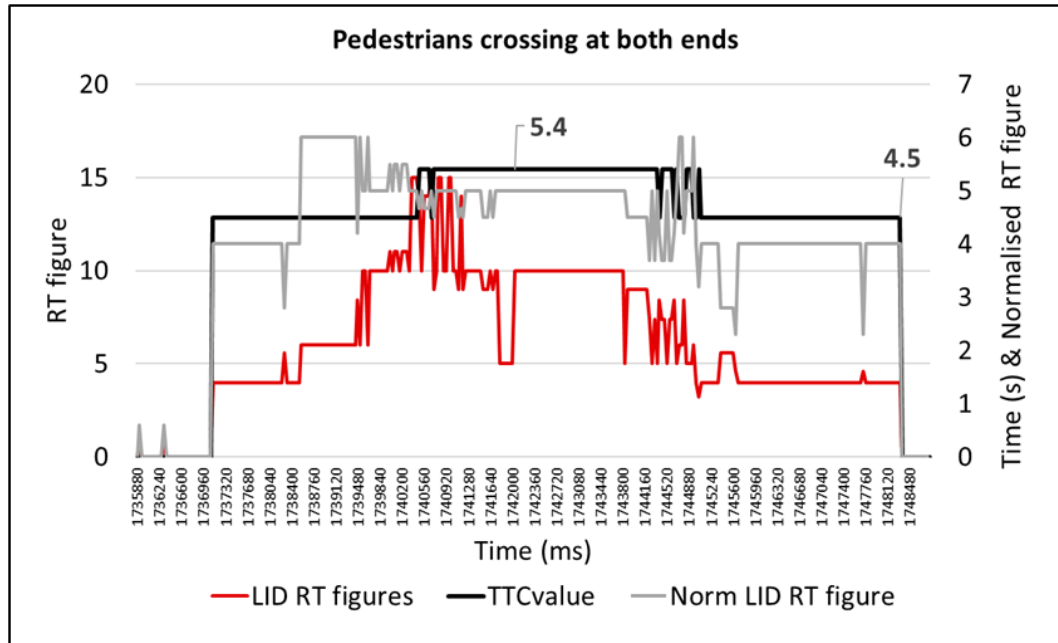


Figure 4.24 Verify  $TTC_{value}$  and compare LID and normalise LID RT figures for event 1

Figure 4.24 compares the LID RT figures to the normalised LID RT figures (secondary axis, range from 0 to 7) and verifies the intent of  $TTC_{value}$  (secondary axis, range from 0 to 7). The normalised LID RT figures show fewer fluctuations than LID RT figures. This is because normalised RT figures are averaged across the detected pedestrians as compared to LID RT figures, which sums up all the risk of pedestrians crossing at both ends of the AOI. Normalised RT figures show high values when most pedestrians are in the road region and drop when most pedestrians leave. Thus, the normalised LID RT figure can provide an average risk per scene, while the LID RT figures reflect pedestrians' movement from pavement to road regions in the middle of the AOI. Separately, the  $TTC_{value}$  remains between 4.5-5.4 seconds since the crossing mainly occurs in the middle rows. The flat  $TTC_{value}$  also indicate that event 1 consists mainly of lateral movement (x-axis), and not much longitudinal movement (y-axis) is detected, which reflect event 1 correctly.

## 4.2 STREET Risk tagging process and results

### Event 2: Pedestrian diagonal movement from middle to front of the AOI

Event 2 represents a situation where the pedestrian crosses diagonally from the AOI's middle right to the front left zonal regions. Figure 4.25 illustrates the pedestrian moving in sequence (a) to (c) from the AOI's rear and middle row to the AOI's front row. The detected pedestrian at the rear remains stationary.

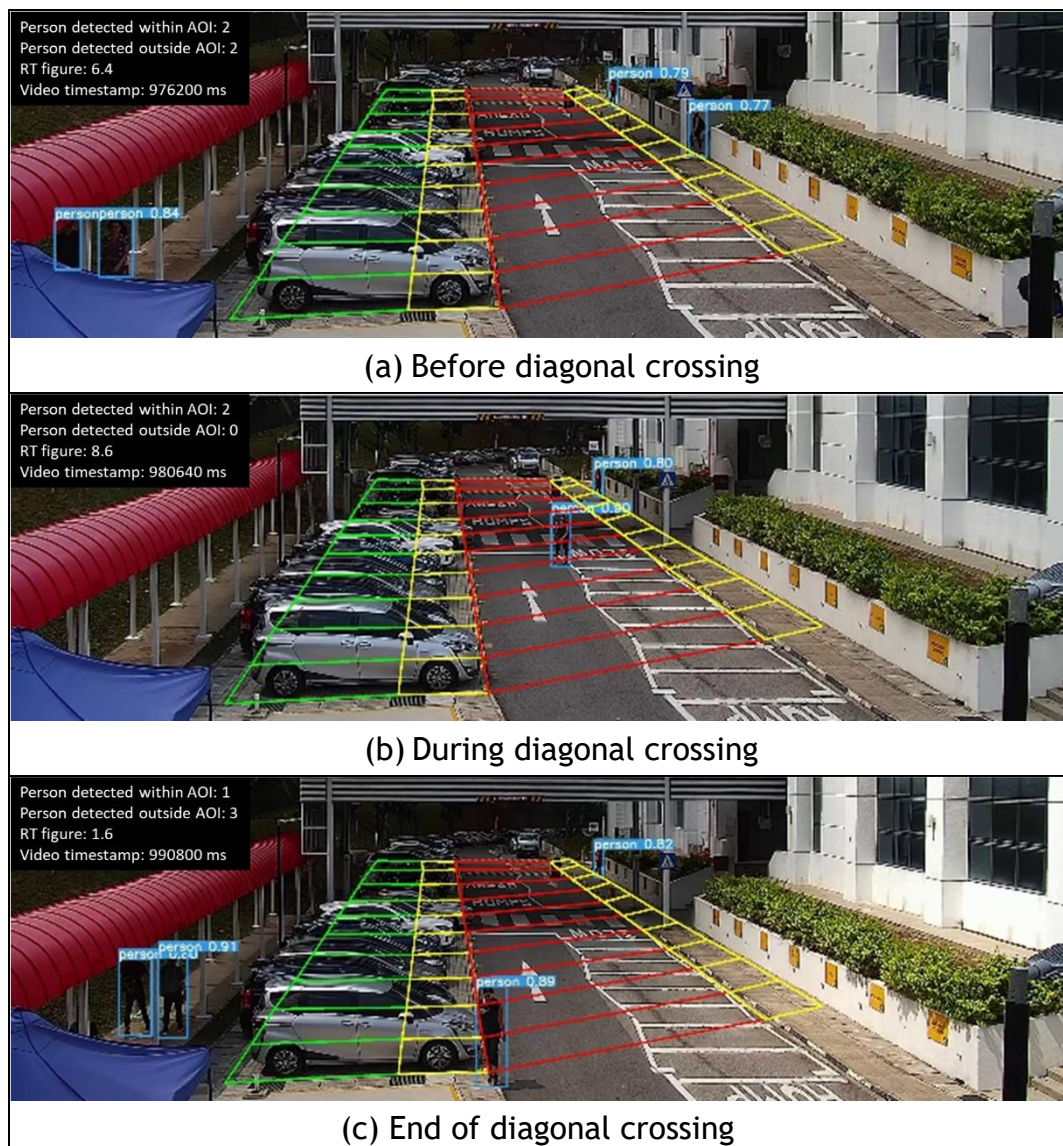


Figure 4.25 Images of pedestrian diagonal crossing for event 2

## 4.2 STREET Risk tagging process and results

### Event 2, task 1: Comparative analysis between LID RT figures with ground truth

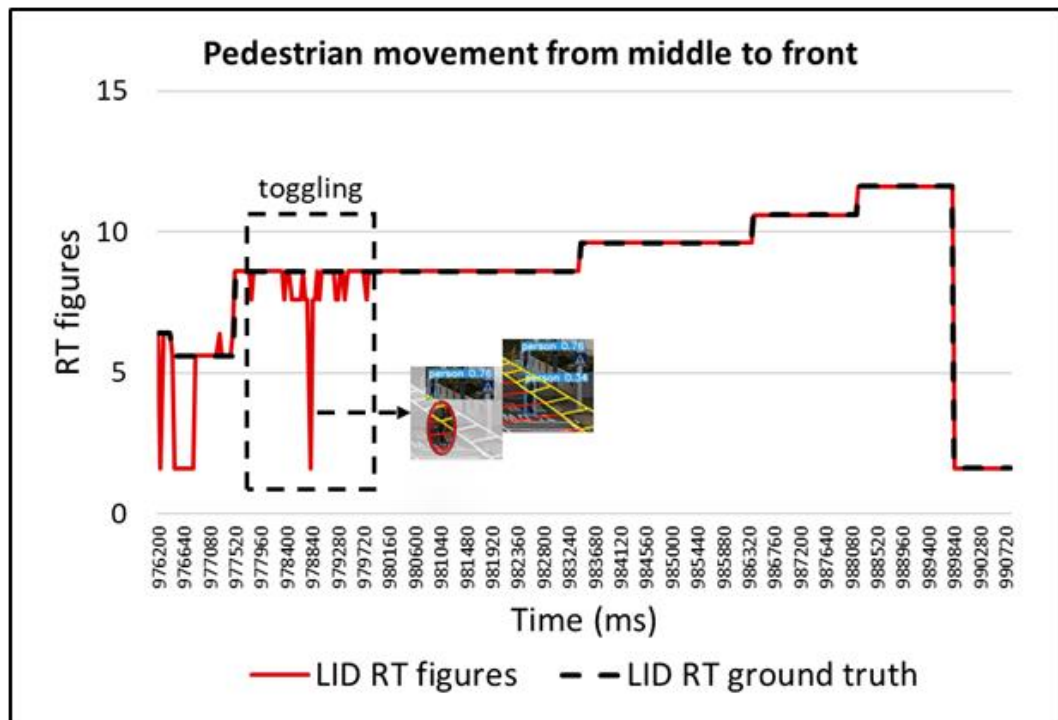


Figure 4.26 LID RT figures vs LID RT ground truth for event 2

Figure 4.26 shows that LID RT figures were similar to the LID RT ground truth, except that one particular pedestrian's detection toggles around the boundary of a zonal area. This phenomenon causes some fluctuations in the LID RT figure. In addition, a single occurrence of "False Negative" pedestrian detection causes a sudden dip to RT figure of 1.6 at 97,880 ms. The "toggling" of pedestrian detection at the boundary of the zonal area is therefore known as a "Boundary condition" for the STREET algorithm. This is known to happen, especially if pedestrians reside close to each zonal region's boundary. Besides the "Boundary condition" and the single-frame false-negative, the LID RT figures perform close to the ground truth.

## 4.2 STREET Risk tagging process and results

### Event 2, task 2: Comparative analysis between LID, CED and AED RT figures

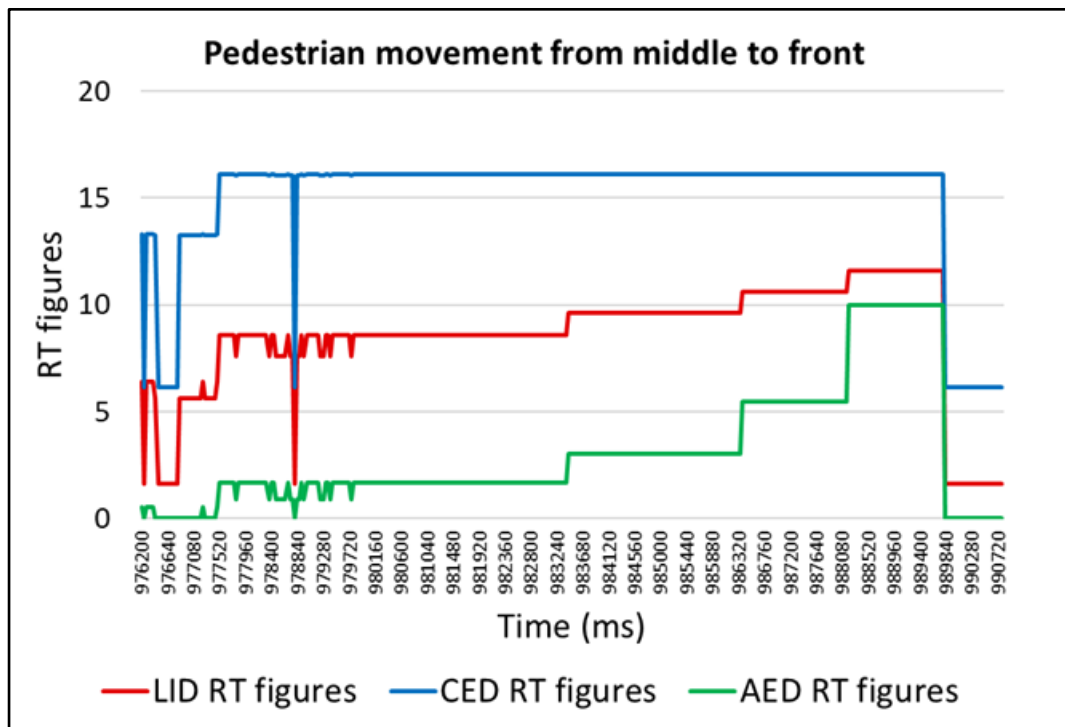


Figure 4.27 Comparison of LID, CED and AED RT figures for event 2

Figure 4.27 compare the performance of CED and AED with LID RT figures. Within the figure, both LID and AED show a gradual increase of RT figures that signify the movement of pedestrians from the middle to the front row. The increase in LID RT figures occurs in a piecewise linear form in tandem with the pedestrian movements. As for the comparison of LID, CED and AED, it is evident that CED was not able to detect the sequence of pedestrian movement since CED have minor differences in collision probability between the front and middle rows. AED is more effective as compared to CED, and its sensitivity increases when the pedestrian moves to the front rows, thus explaining the elevated AED RT figures towards the end. Therefore, LID RT figures provide the most effective detection of pedestrians moving from middle to front rows for event 2.

## 4.2 STREET Risk tagging process and results

Event 2, task 3: Verify  $TTC_{value}$  and compare LID RT figures to normalised LID RT figures.

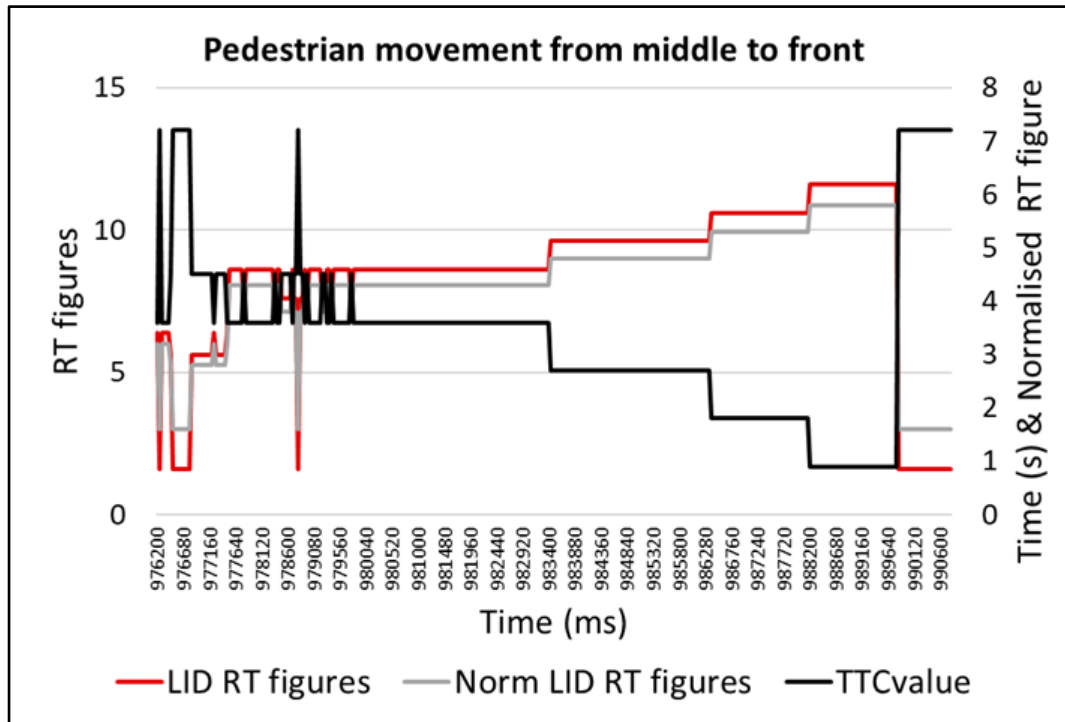


Figure 4.28 Comparing LID RT figure, normalised LID RT figure and  $TTC_{value}$  for event 2

Figure 4.28 compares the LID RT figures to normalised LID RT figures (secondary axis) and verifies the  $TTC_{value}$  (secondary axis). The LID RT figures were similar to the normalised LID RT figures because two pedestrians were detected in the scenes with only one of them moving from the middle to the front of the AOI. As such, the moving trend between the sum of all risks within a scene (RT figure) and the average risk per scene (normalised RT figure) would be the same. Figure 4.28 also illustrates the expected performance of  $TTC_{value}$ , having an inverse figure compared to the LID RT figures.  $TTC_{value}$  shows a higher value when the pedestrian is in the middle row and the  $TTC_{value}$  decreased when the pedestrian moved to the front rows.

## 4.2 STREET Risk tagging process and results

### Event 3: Pedestrians' movement from rear to front

STREET's RT figures and  $TTC_{value}$  were also verified using event 3, which consists of pedestrians' movement from rear to front rows. In this event, the same three tasks were performed and Figure 4.29 illustrates the pedestrians' movement during this event. Five pedestrians were detected, and three of them moved to the front of the AOI, while the other two stayed in the rear and middle rows of the AOI.

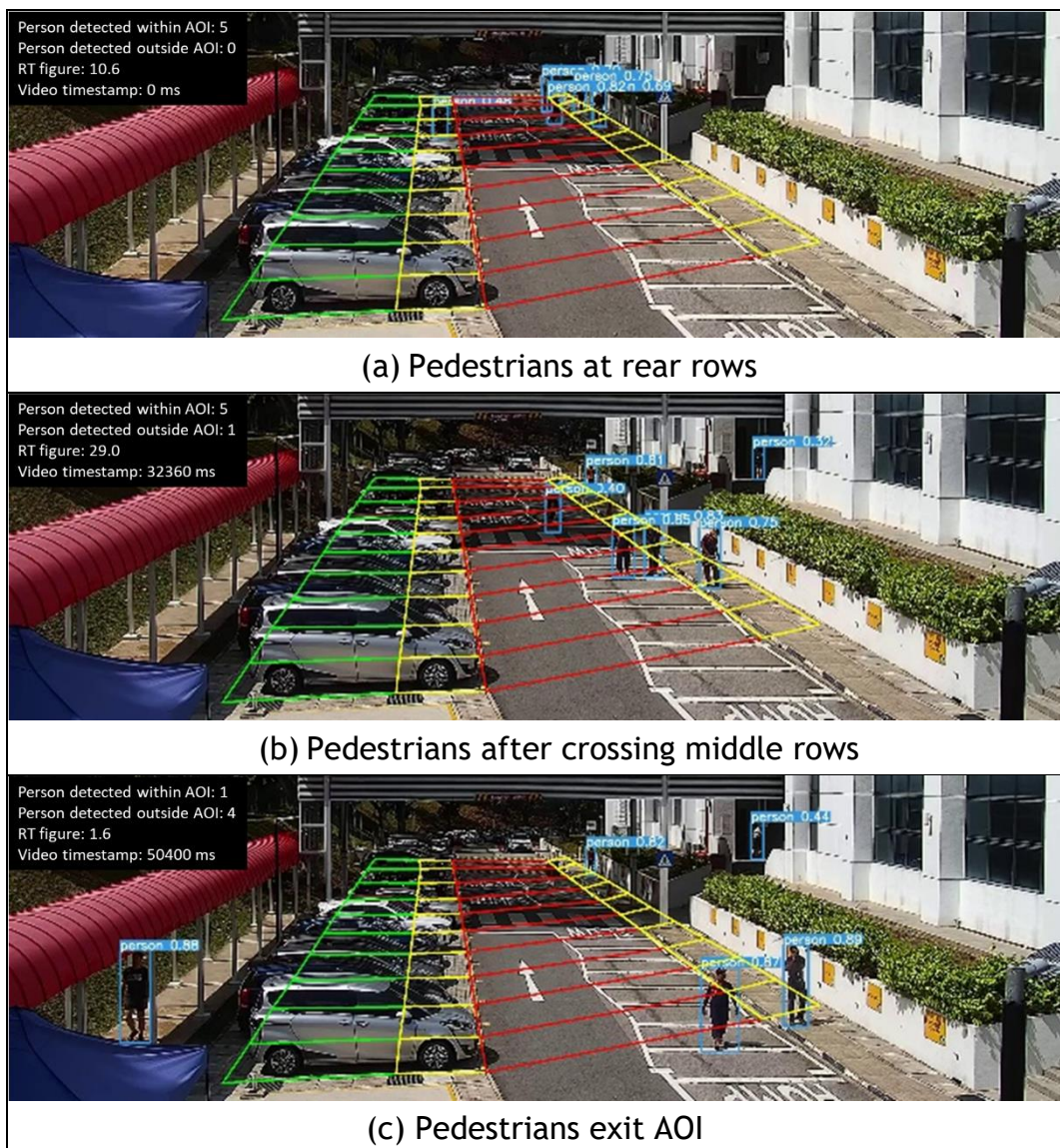


Figure 4.29 Images of pedestrians' movement from rear to front for event 3

## 4.2 STREET Risk tagging process and results

### Event 3, task 1: Comparative analysis between LID RT figures with ground truth

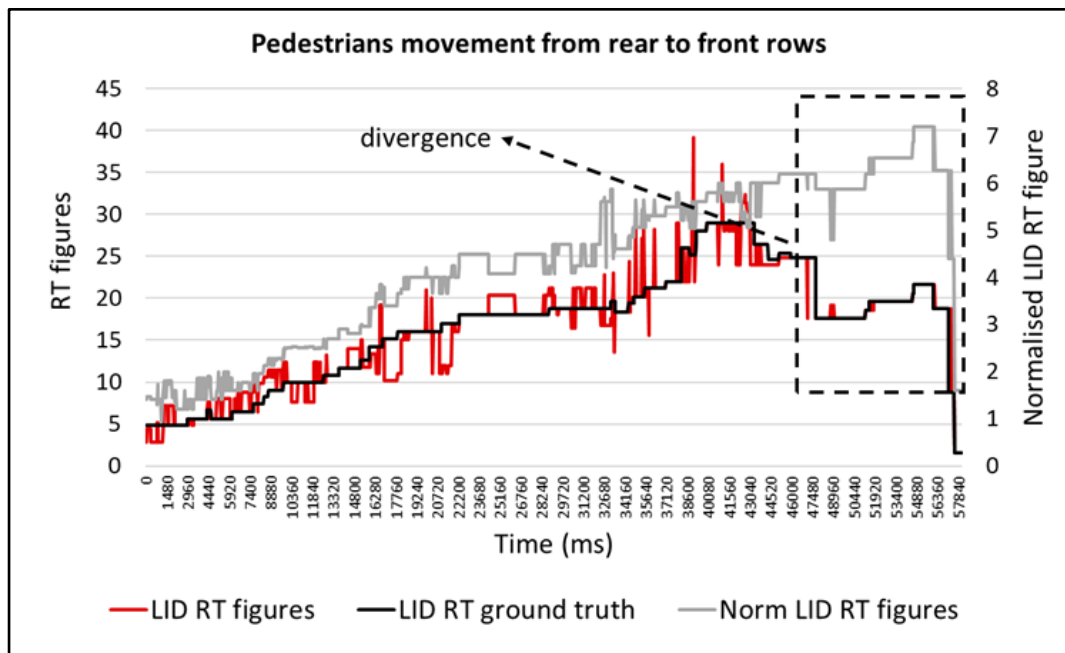


Figure 4.30 LID RT figures, ground truth and normalised RT figure for event 3

Figure 4.30 shows the LID RT figures, LID RT ground truth and the normalised RT figure (on the secondary Y-axis). The LID RT figures track closely to the LID RT ground truth. The LID RT figures had minor spikes caused by pedestrians being occluded and "Boundary conditions" such as pedestrians walking near the boundary between zonal areas. Towards the end of this event, the normalised RT figures showed a "divergence" from the LID RT figure when a pedestrian walked out of the AOI's front rows, reducing the LID RT figure. Since two pedestrians were still in the front row of the AOI, the normalised RT figures did not show a significant drop. Even though there is a slight drop in LID RT figures, both LID RT figures and normalised RT figures are sufficiently high to indicate remote warnings for the AV. Thus representing the remaining pedestrian risk at the front of the AOI. This example illustrated the differences between RT figures and normalised RT figures in a real-world context.



## 4.2 STREET Risk tagging process and results

### Event 3, task 2: Comparative analysis between LID, CED and AED RT figures

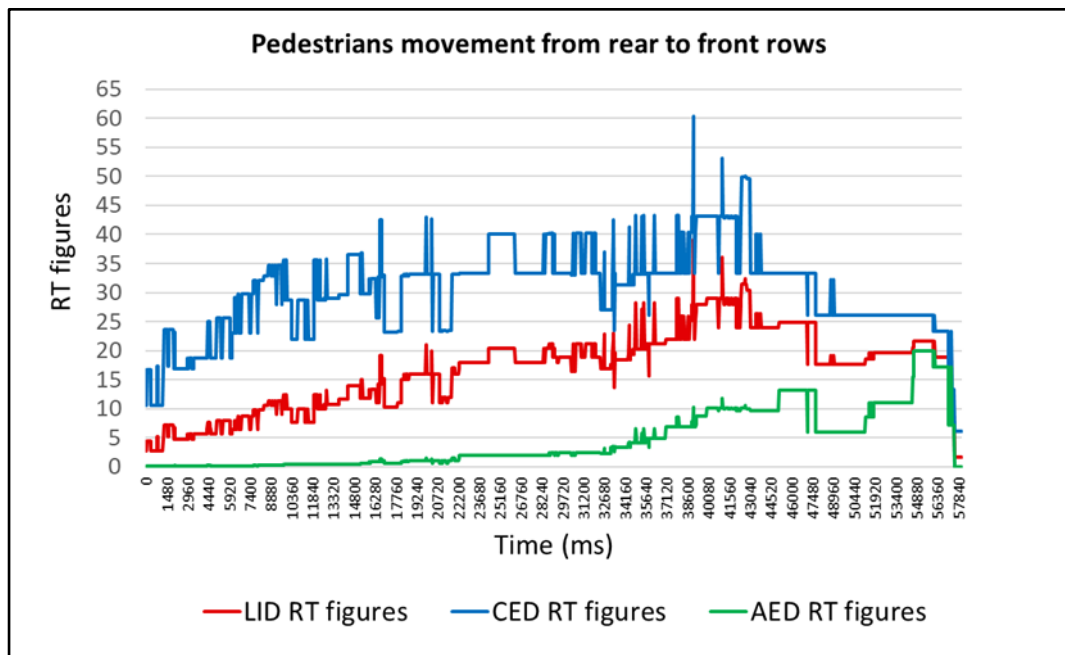


Figure 4.31 Comparison of LID, CED and AED RT figures for event 3

Figure 4.31 shows that LID, CED, and AED are compared in event 3, where pedestrians move from the rear to the front of the AOI. Since AED covers only the front few rows of the AOI, AED RT figures were close to zero until the pedestrian moved closer to the front rows of the AOI. A linear piecewise increase can be observed in the LID RT figures as the pedestrian moves from the rear to the front of the AOI. An exponential increase can be observed in CED RT figures with elevated values. This event verifies the performance intended for the three algorithms.

4.2 STREET Risk tagging process and results

Event 3, task 3: Verify  $TTC_{value}$  and compare LID RT figures to normalised LID RT figures.

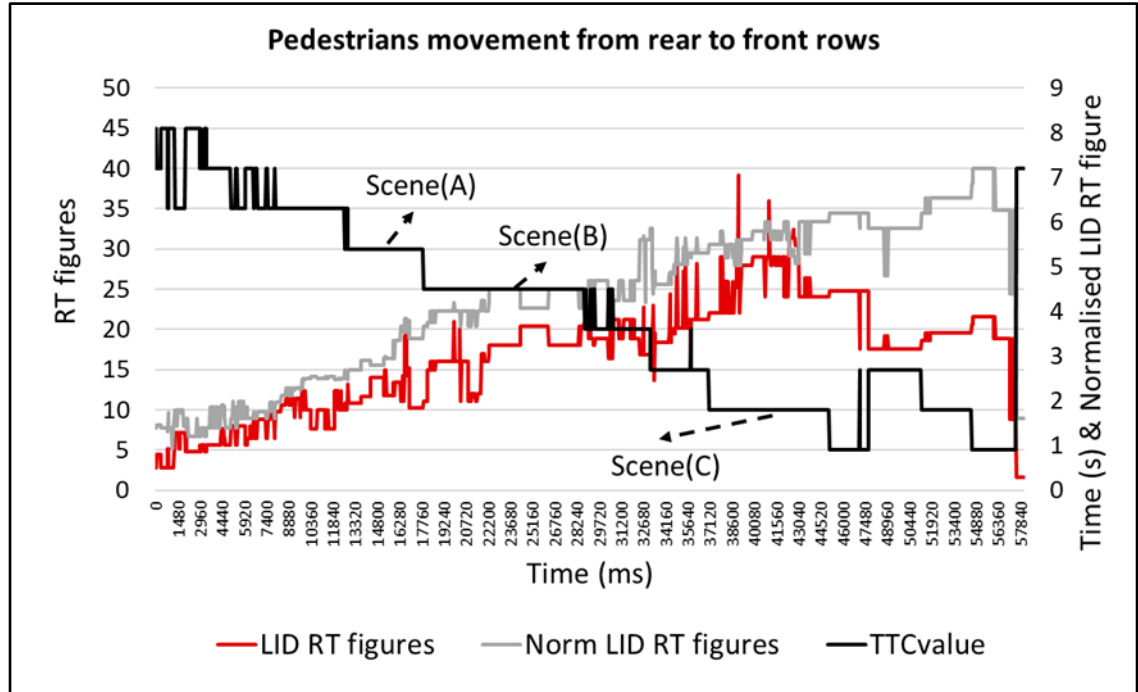


Figure 4.32 Comparing LID RT figure, normalised LID RT figure and  $TTC_{value}$  for event 3

Figure 4.32 shows the linear step-wise decrease of  $TTC_{value}$  inversely proportional to the rising LID RT figures. This verified the performance of  $TTC_{value}$  as it represents the time to collide as the pedestrians move closer to the front rows. Scenes (A), (B) and (C) are illustrated examples for  $TTC_{value}$  in Table 4.12. The difference in performance between LID RT figures and normalised LID RT figures was already commented on in Event 3 task 1.

Table 4.12 Illustrated scenes (A), (B) and (C) for  $TTC_{value}$

Scene (A): 10360 ms $TTC_{value} = 6.3$ s	Scene (B): 19240 ms $TTC_{value} = 4.5$ s	Scene (C): 40080 ms $TTC_{value} = 1.8$ s

## 4.2 STREET Risk tagging process and results

### Event 4: A moving vehicle that occludes pedestrian

Event 4 depicts an occlusion event, as shown in Figure 4.33. The pedestrian on the yellow right second row ( $Y_{r2}$ ) is occluded by the moving truck. When the occlusion disappears, the pedestrian has reached ( $Y_{r3}$ ). The detection of pedestrian occlusion can be observed with the changes to the RT figures.

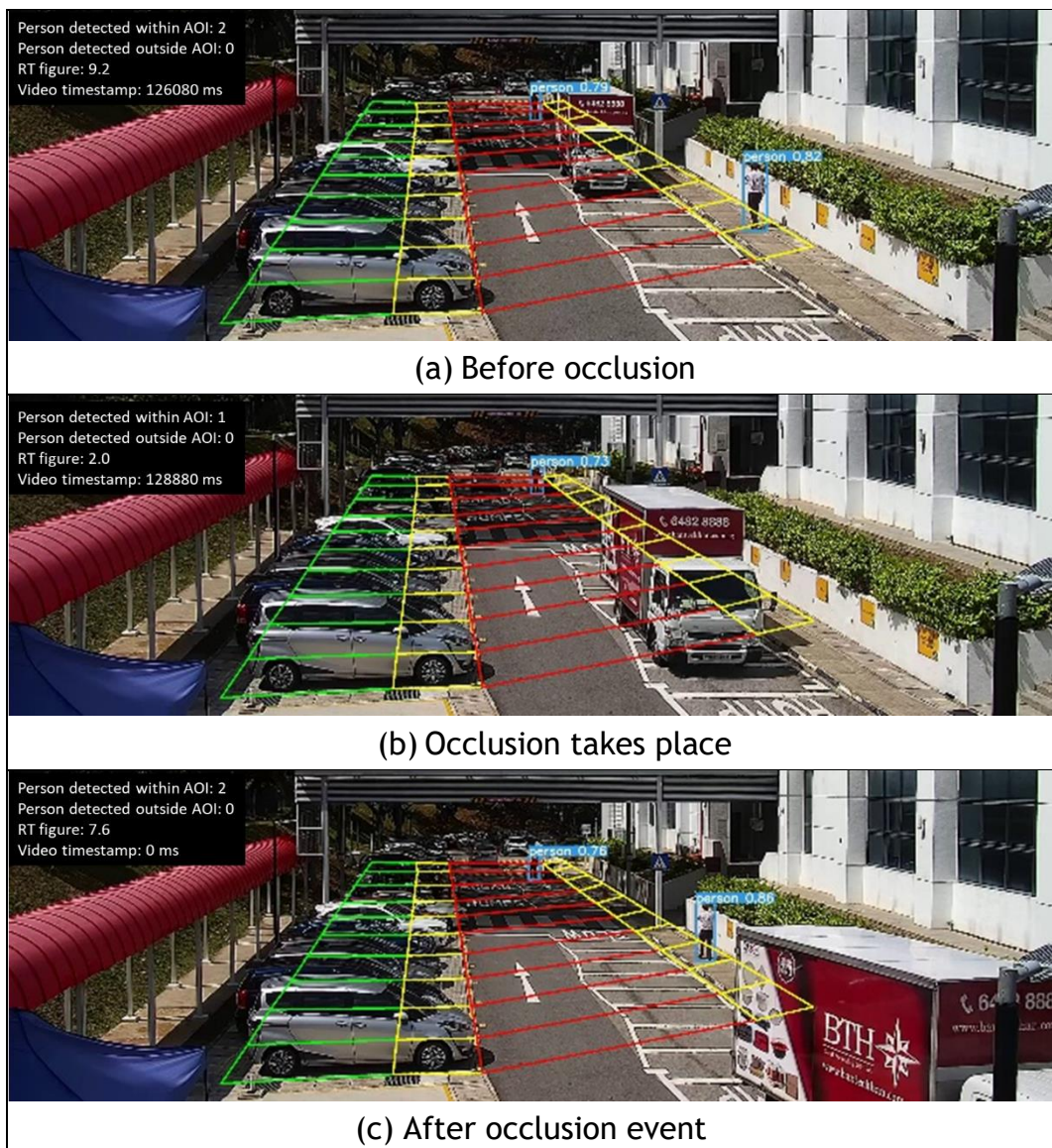


Figure 4.33 Images of pedestrian occluded by moving vehicle for event 4

## 4.2 STREET Risk tagging process and results

### Event 4, task 1: Comparative analysis between LID RT figures with ground truth

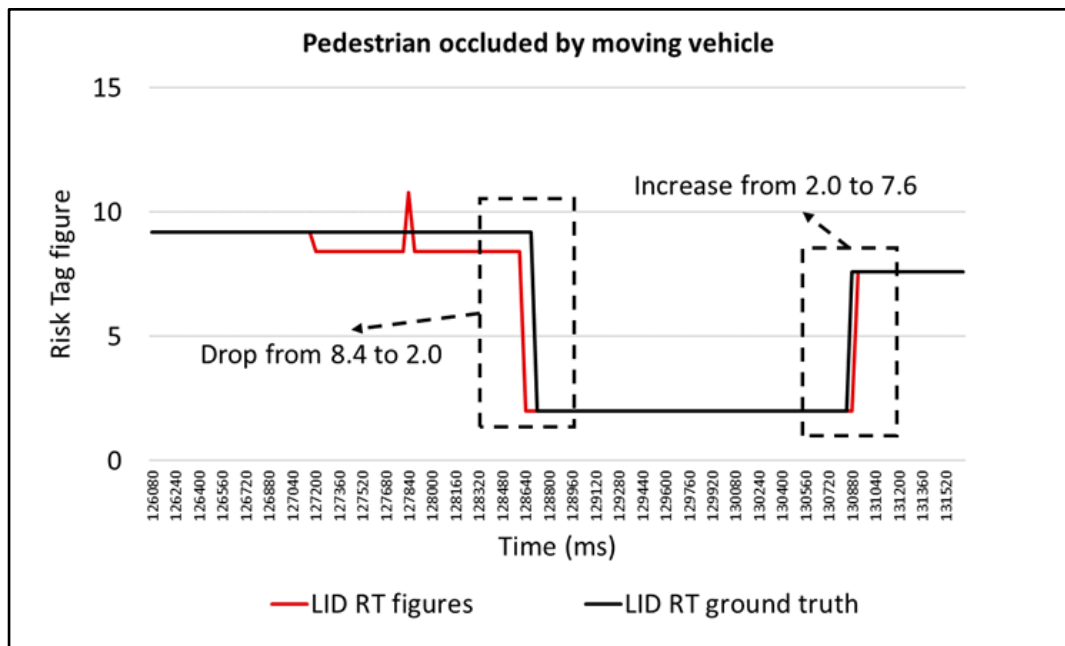


Figure 4.34 LID RT figures vs LID RT ground truth for event 4

Figure 4.34 illustrates the RT figures when a pedestrian is occluded by a moving truck. A sudden drop and increase in LID RT figures over 56 frames occurred in this event, which is equal to 2.24 seconds. The LID RT figure drops instantly from 8.4 to 2.0 and returns to 7.6 (after 56 frames) instead of 8.4, due to the pedestrian's movement from the 2nd to the 3rd row after the occlusion. Event 4 can be detected in real time or post-analytics. However, it is important to note that similar results can also occur when the pedestrian moves away and returns to the front AOI. The key difference lies in the number of frames in which the RT figure stays low. More examples and tests are needed to establish the boundaries for detecting occlusion, which may be very specific to a certain location and field of view (FOV). These boundaries have not been extensively researched but holds potential for future work. The LID RT figures are generally close to the LID ground truth, except for a spike caused by a false positive detection error due to object detection. The LID RT ground truth reflects the actual scene based on the camera input.

## 4.2 STREET Risk tagging process and results

### Event 4, task 2: Comparative analysis between LID, CED and AED RT figures

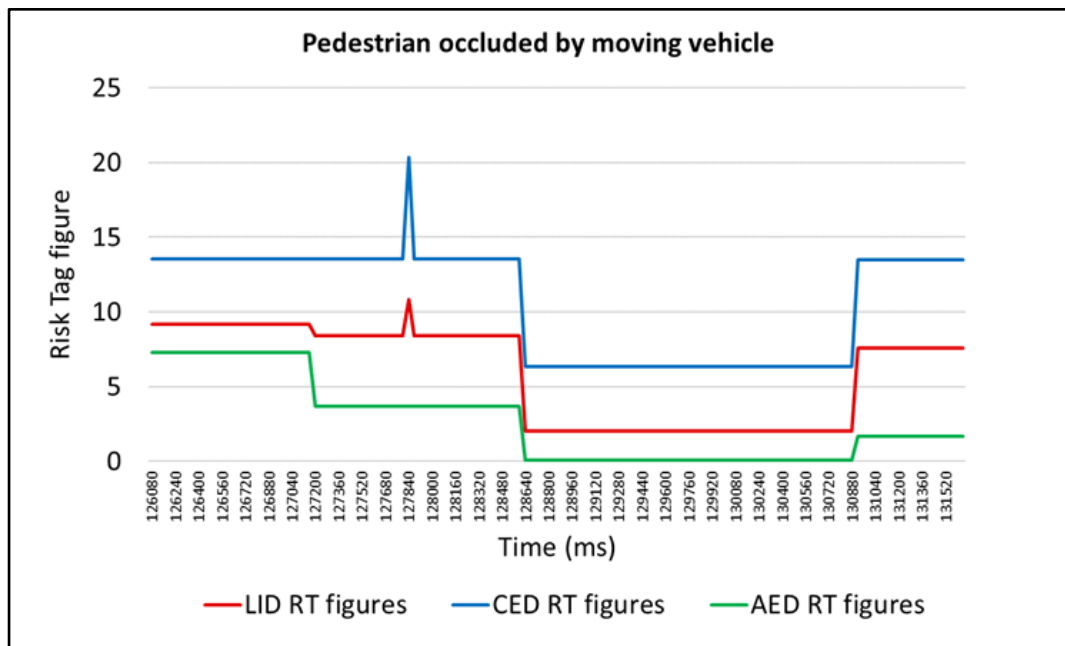


Figure 4.35 Comparison of LID, CED and AED RT figures for event 4

Figure 4.35 compares the performance of LID, AED, or CED mode for occlusion detection. At 128640 ms, LID dropped from 8.4 to 2, while CED dropped from 13.52 to 6.32 and AED dropped from 3.67 to 0.08. At 130880 ms. LID increased from 2 to 7.6, while CED increased from 6.32 to 13.51 and AED increased from 0.08 to 1.69. In terms of absolute decrease, CED dropped the most RT figures, followed by LID. The highest CED RT figure also represents the intended design based on the CED probabilistic model. LID and AED have similar RT figures at the start of the duration because the pedestrian resided in the first row. The gap between LID and AED RT figures increases due to the pedestrian moving to the second row. In this occlusion event, LID and CED perform better for pedestrian moving from the back to the front of the AOI as compared to AED. AED is not suitable for event detection because of the small coverage of the AOI at the front.

## 4.2 STREET Risk tagging process and results

Event 4, task 3: Verify  $TTC_{value}$  and compare LID RT figures to normalised LID RT figures.

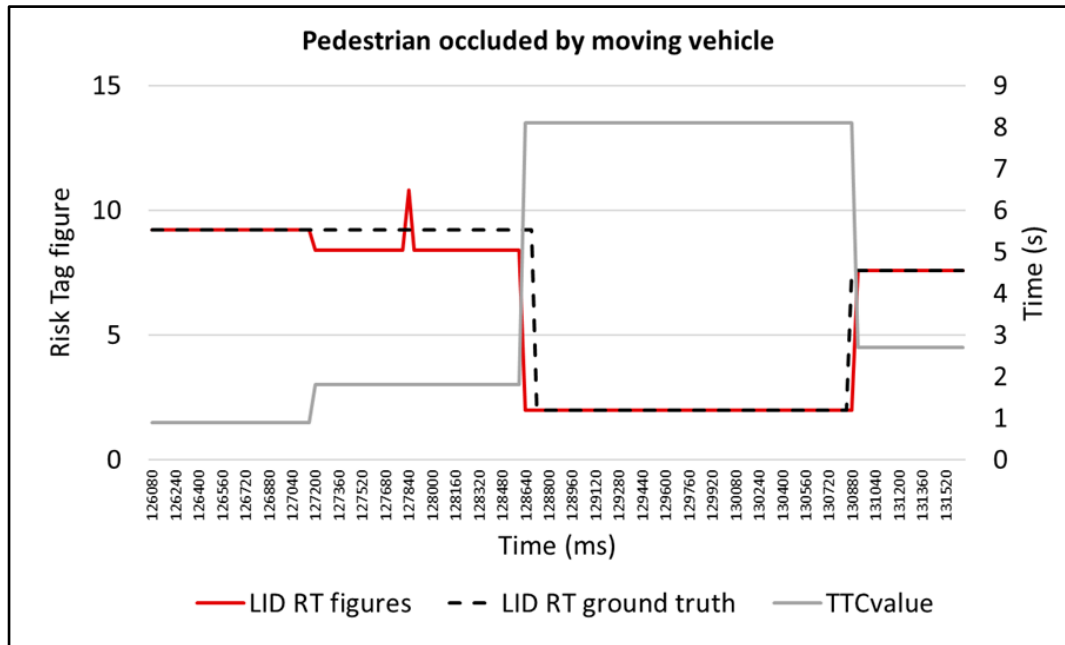


Figure 4.36 Comparing LID RT figure, LID RT ground truth and  $TTC_{value}$  for event 4

Figure 4.36 shows that the  $TTC_{value}$  increases sharply once the pedestrian is occluded. Normally, once the pedestrian is occluded, the  $TTC_{value}$  should be zero. However, a pedestrian residing at the eight row of the road region is detected, thus the  $TTC_{value}$  reflects the time to collision between the detected pedestrian and the reference location “X” in the AOI. Therefore, the  $TTC_{value}$  performs as intended with an inversely proportional relationship with the LID RT figure.

### 4.2.8 Comparison of LID, CED, AED and Time to collision findings

The characteristics of STREET’s three RT figures using the LID, CED, and AED probabilistic model were verified using different events within the corner scenario with the RT ground truth. Time to collide ( $TTC_{value}$ ) were also verified using these events. Table 4.13 summarises the performance of LID, CED and AED with  $TTC_{value}$  for the different events.

## 4.2 STREET Risk tagging process and results

Table 4.13 Summary of LID, CED or AED with  $TTC_{value}$  at corner scenario for different events

Scenario	Events Description	RT figures with probabilistic models and $TTC_{value}$
Corner bend	Event 1: Pedestrians' movement from left to right and vice versa	LID and CED are more effective than AED. If $TTC_{value}$ is flat, the pedestrian crossing is at a similar row.
	Event 2: Pedestrians' diagonal movement from middle to front	LID and AED are more effective than CED, $TTC_{value}$ can be used to verify the same findings with the opposite trend
	Event 3: Pedestrians' movement from rear to front	LID and CED are more effective than AED, $TTC_{value}$ can be used to verify the same findings with the opposite trend
	Event 4: Pedestrian occluded by moving truck	

Additionally, evaluating the scenario based on RT figures and  $TTC_{value}$  provides another perspective, as shown in Table 4.14. For example, if the RT figures are high while having a low  $TTC_{value}$ , it represents a high-risk scenario. If the RT figure is high and the  $TTC_{value}$  is high, it infers that pedestrians are present at the AOI's middle-rear rows (except AED). If the RT figures are low with a high  $TTC_{value}$ , this represents a low-risk scenario (except AED). If RT figures are low with a low  $TTC_{value}$ , this situation does not exist for STREET algorithm. Lastly, for all models, no risk is detected if the RT figures and  $TTC_{value}$  are both zero. High RT figures refer to 7-10 normalised RT figures, while low RT figures refer to 1-3 normalised RT figures. High  $TTC_{value}$  refers to a range of values obtained for the first 3 rows (i.e 0.63s to 9.0 s), while  $TTC_{value}$  refers to a range of values obtained for the last 3 rows (i.e 0.90s to 2.70s).

## 4.2 STREET Risk tagging process and results

Table 4.14 Summary of models with  $TTC_{value}$  to identify high or low risk scenario

Different models		Low $TTC_{value}$	High $TTC_{value}$
LID	High RT figures	High Risk scenario	Pedestrians in the middle to rear rows
	Low RT figures	Not applicable	Low-Risk scenario
CED	High RT figures	High Risk scenario	Pedestrians in the middle to rear rows
	Low RT figures	Not applicable	Low-Risk scenario
AED	High RT figures	High Risk scenario	Not applicable, AED has no high $TTC_{value}$
	Low RT figures	Not applicable	
All models	Zero RT figures	Zero $TTC_{value}$ means no risk detected.	

The STREET algorithm has demonstrated its effectiveness through testing with real-world events. However, some limitations have been identified during this process.

These limitations arise from object detection in a camera system for perception. For instance, issues include occluded pedestrians and varying sizes of object detection boxes that toggle at the edges of the risk zonal areas. Consequently, these limitations lead to some inaccuracies in the RT figures. Object detection performance is measured at 85% for precision, 87% for recall, and 86% for the F1 score. Relative to the industry adoption threshold of 90%, these results suggest that the inaccuracies have a small impact on the overall STREET performance. It is also important to note that STREET and ReRAC are for remote cooperation functions that assist AVs in risk assessment. If the RSU, STREET, or ReRAC camera fail to function, the AV can still measure risk from the AV perspective through ReRAF, while the AV's basic safety functions prevent accidents using its existing sensors and internal algorithm. However, this may result in a higher-risk situation, potentially endangering passengers and surrounding vehicles due to sudden



## 4.2 STREET Risk tagging process and results

braking or abrupt steering manoeuvres, especially in scenarios like cornering without advanced remote warnings.

### 4.2.9 Hazard identifications and warnings results

The ReRAC STREET's hazard identifications and warnings were tested in a real-world T-junction (described in chapter 3), as shown in Figure 4.37. The corner scenario was not used since the hazard identifications and warnings require a T-junction intersection. Figure 4.37 (a) shows the FOV of the RSU's camera and Figure 4.37 (b) shows the T-junction, which includes the road regions (red zone) and intersection (black zone) for STREET algorithm to provide hazardous identification and warning events. The different hazard identifications and warnings provide remote detection of potential accidents and/or congestions so that the AV can prepare alternative paths or exercise caution before reaching the RSU's location. The RSU's camera was mounted at a height of 3.0 m for a detection range of up to 35 m for this specific scene.

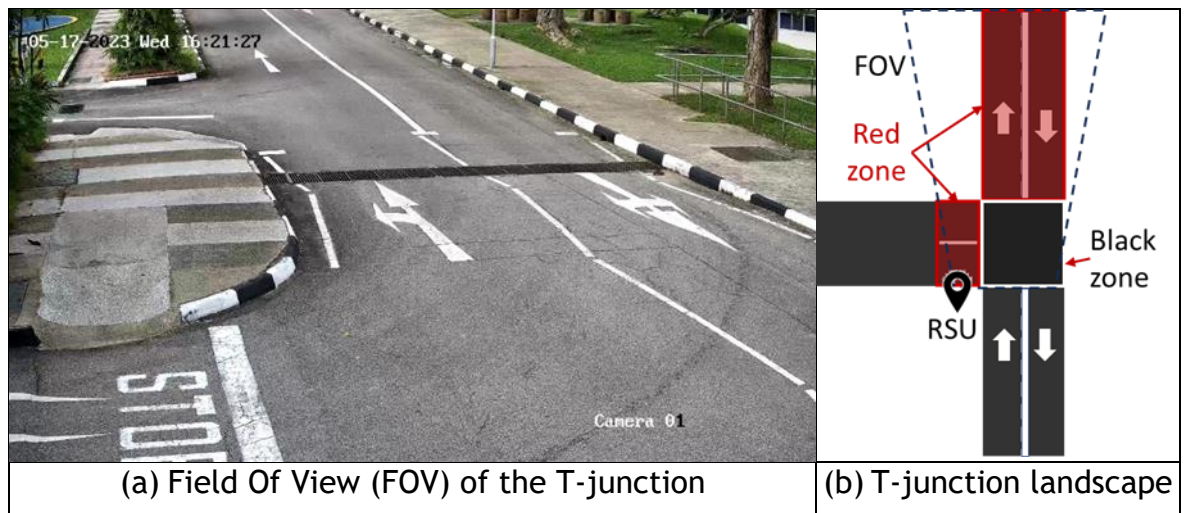


Figure 4.37 Hazard identifications and warnings tested at T-junction

### Hazard identifications and warning zoning

Figure 4.38 shows the risk zoning of a T-junction intersection with red zones for roads, yellow zones for pavement and added an additional step to demarcate the black zone for the intersection.

## 4.2 STREET Risk tagging process and results

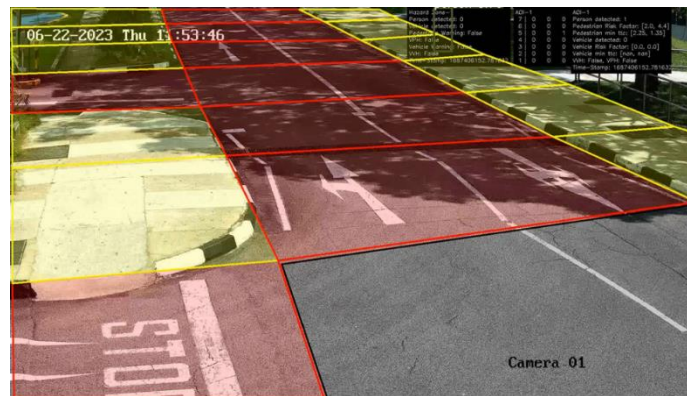


Figure 4.38 Real-world T-junction with zoning

The different hazard identifications and warnings are illustrated with real-world examples using the selected T-junction as an example. As explained in section 4.1.7, using Table 4.5 and Table 4.6, the conditions were implemented in real time to provide boolean hazardous events detection. A total of six scenes (Scene A to G) were identified from this scenario to illustrate the different hazard identifications and warning results. Vehicle and pedestrian warnings were classified as hazard warnings within a T-junction intersection. VVH are vehicle-to-vehicle hazards, and VPH are vehicle-to-pedestrian hazards, which were considered for both road and T-junction intersections. In this scenario, STREET also provides pedestrians and vehicle RT figures and  $TTC_{value}$ .

### SCENE A

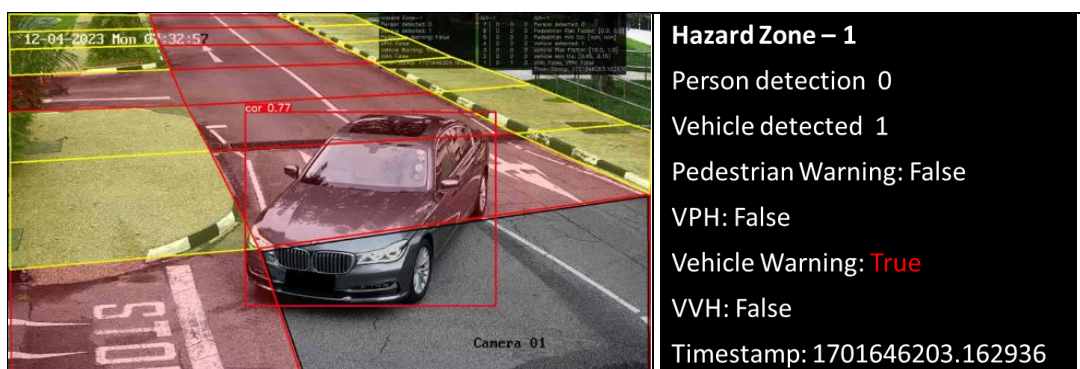


Figure 4.39 Scene A, vehicle warning “True”

Figure 4.39 illustrates scene A, which consists of a vehicle warning. Vehicle warnings occurred when a vehicle is detected within the intersection (black zone).

## 4.2 STREET Risk tagging process and results

This trigger was used to notify the presence of a turning vehicle within the intersection.

### Scene B

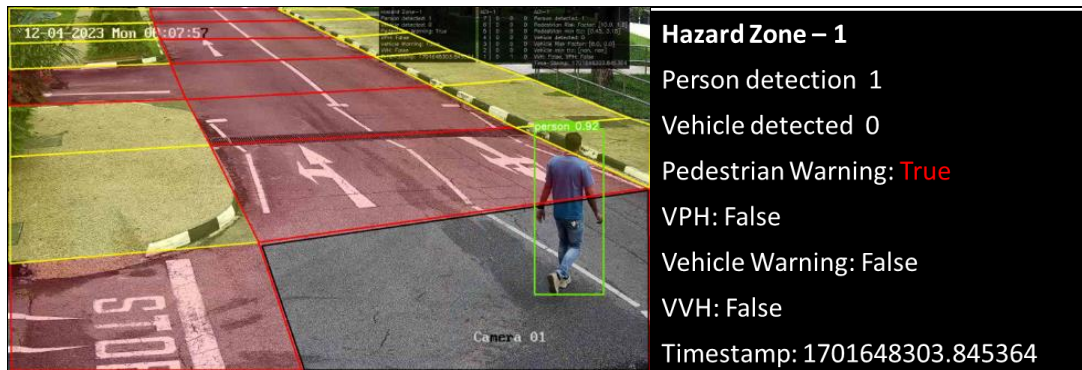


Figure 4.40 Scene B, pedestrian warning “True”

Figure 4.40 illustrates scene B, which consists of a pedestrian warning. The pedestrian warning occurred when a pedestrian was detected within the intersection (black zone). This trigger was used to notify the presence of a pedestrian walking within the intersection and as a warning for AV for any advance plan either in turning or driving straight across that intersection.

### Scene C

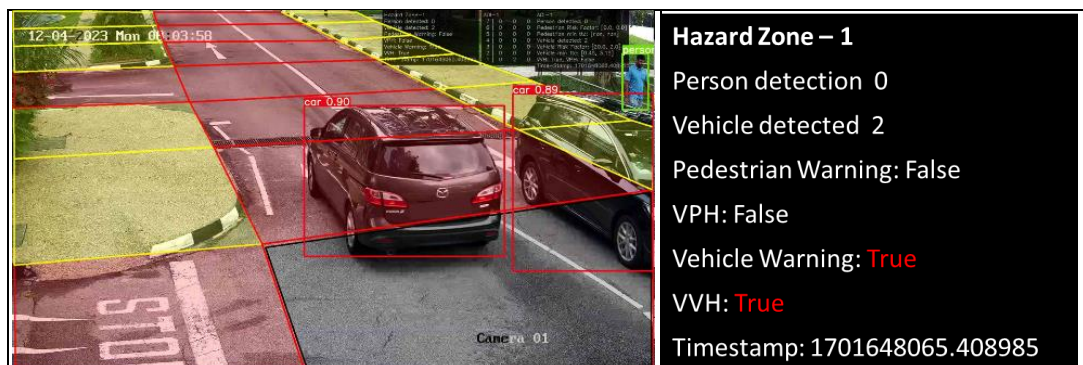


Figure 4.41 Scene C, vehicle warning “True” and vehicle-to-vehicle hazard “True”

Figure 4.41 illustrates scene C, which consists of a vehicle warning and a vehicle-to-vehicle hazard detection within the intersection (black zone). This trigger was to notify the presence of two or more vehicles detected at the intersection and that the intersection was crowded with vehicles.

## 4.2 STREET Risk tagging process and results

### Scene D



Figure 4.42 Scene D, vehicle warning “True” and vehicle-to-vehicle hazard “True”

Figure 4.42 illustrates scene D, which consists of a vehicle warning and a vehicle-to-vehicle hazard detection within the road (red zone). This trigger was to notify the presence of a vehicle in the intersection and a vehicle-to-vehicle in the AOI. If the warning and hazard are triggered for a long duration, it represents roads are congested. The RT figure was used to verify the vehicle-to-vehicle in the AOI further. In this case, the high vehicle RT figure of 27 (normalised RT figure would be 9), with low vehicle  $TTC_{value}$  meant that the vehicle-to-vehicle crowding happens near the RSU (high risk scenario). RT figure and  $TTC_{value}$  have two values. The first number uses the nearest reference location “X” to the RSU, while the other uses the furthest reference location “X”. This is to cater for vehicles moving in different directions.

### Scene E

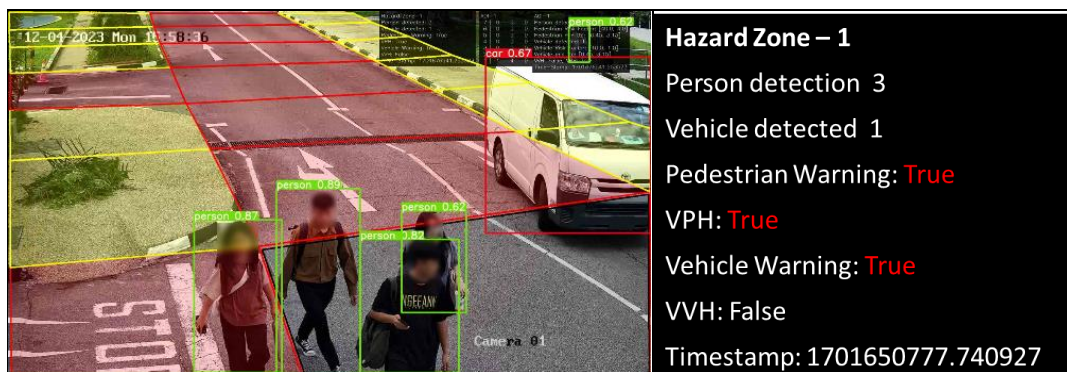


Figure 4.43 Scene E, pedestrian & vehicle warning “True”, & vehicle-to-pedestrian hazard “True”

Figure 4.43 illustrates scene E, which consists of a pedestrian and vehicle warning and a vehicle-to-pedestrian hazard warning at the intersection (black zone). This

## 4.3 Summary

trigger was to notify the presence of vehicle(s) and pedestrian(s) within the intersection. All three warnings indicate that vehicles and pedestrians were within the intersection. Prolong duration of the detected event represents congestion or accidents.

### Scene F

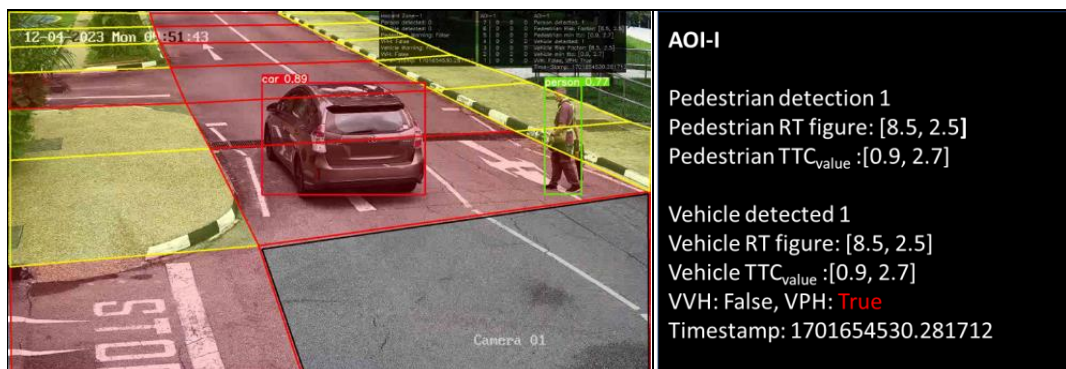


Figure 4.44 Scene F, vehicle-to-pedestrian hazard “True” at AOI

Figure 4.44 illustrates scene F, which consists of a vehicle-to-pedestrian hazard within the red zone. This trigger is to notify the presence of vehicle proximity with pedestrian detection within the red zone. The RT figure further verifies if the hazard is close to the RSU. In this case, the vehicle and pedestrian RT figure is 8.5, which implies that it is close to the RSU with a low pedestrian  $TTC_{value}$ . For comparative purposes, if the same vehicle and pedestrian are detected in the last row, the RT figure will be 2.5.

Any prolonged duration of detected warning or hazards represents congestion or accidents in the AOI or intersection. Situations with long durations of vehicle-to-pedestrian hazards represent an occurrence of accidents or roadworks at that AOI or intersection. This information from the RSU allows the AV to seek alternative path planning to avoid these situations.

## 4.3 Summary

This chapter provides a comprehensive overview of the developed novel STREET algorithm within ReRAC. ReRAC is deployed in an RSU to deliver remote warnings as an infrastructure to AV for measuring environmental risk, time to collision with

### 4.3 Summary

---

the detected object, and hazard identifications and warnings. The STREET algorithm uses risk zoning, probabilistic modelling, and object detection methodologies. The theoretical formulation of STREET is thoroughly explained, accompanied by illustrations for each of the methodologies employed. The risk zoning process was outlined with detailed steps for creating a risk zoning matrix for the chosen FOV. Additionally, three probabilistic models (LID, CED, and AED) were developed to represent different coverages and collision probabilities for the AOI. Object detection methodologies were trained and evaluated using a custom YOLOv5s model, achieving a Precision of 84%, Recall of 65%, and F1 score of 74%. The object detection results were then integrated into a unique mapping process, resulting in an improved performance of 85% for Precision, 87% for Recall, and 86% for F1 score. This mapping process notably boosted the Recall performance by over 20%. The outcomes generated by STREET include RT figures, RSU-TTC, probability of pedestrian occurrence, and hazard identifications and warnings. Notably, STREET operates as an end-to-end process, providing real-time quantitative information directly from the RSU's camera imagery without human interpretation. In addition, this chapter evaluates the STREET algorithm in a real-world setting, specifically in a corner scenario with unregulated traffic. The algorithm processes data at a granular level, providing information at 25 frames per second with a frequency of 40 ms. RT figures and RSU-TTC outcomes were being tested and validated across 97,446 scenes. Additionally, the normalisation of RT figures was developed to quantify the risk per scene, allowing for a comparison of total pedestrian risk (RT figure) across scenes. The RT figures for LID, CED, and AED were compared, and the accuracy of LID RT figures was verified against ground truth. The RT figures performed as designed, with limitations in occlusion and varying object detection box sizes, which have been discussed in this chapter. Pedestrian occurrences and heatmaps were utilised to validate the RT figure outcomes based on pedestrian locations. The performance of different RT figures with LID, CED, and AED probabilistic models was observed and summarised. Furthermore, hazard identifications and warnings are verified using scenes of an unregulated traffic scenario of a T-junction to provide remote event warnings to the AV for route planning and optimisation. The development of STREET's algorithm for ReRAC, together with the outcomes verified in real-world

### 4.3 Summary

---

settings, accomplished the previously identified requirements to increase the coverage of risk assessment for AV operations through I2V approaches.

## Chapter 5

### 5 Real-time risk assessment framework for AV

This chapter presents ReRAF's algorithm, Dynamic Acquired Risk Assessment (DARA). Unlike ReRAC's algorithm, STREET, developed in chapter 4, which achieves real-time risk assessment through a cooperative mode within an RSU, DARA operates within the AV. It provides a safety figure known as the *PRN*, which evaluates the AV's control actions in the presence of detected risk. Additionally, DARA provides the AV Time To Collision (AV-TTC) with the detected object as well as *PRN* Occurrences, which are presented as heatmaps to identify hotspots based on past *PRN* occurrences. These outcomes from DARA allow the AV to improve its safety actions for subsequent operations within the same paths as recursive improvements and risk assessment evaluation. DARA is a novel end-to-end algorithm that does not require human intervention and provides granular quantitative safety figures. The DARA algorithm is processed in real time, ensuring timely and relevant results relative to the camera input frames per second. This chapter presents the theoretical formulation and evaluates DARA through unregulated traffic conditions. DARA is also verified with three iterative loops of AV operations in a real-world environment, highlighting *PRN*'s characteristics and intended functionality. DARA intends to increase the AV overall risk assessment coverage and the controls' safety and path planning through *PRN*, AV-TTC, and Occurrence figures.



## 5.1 Dynamic Acquired Risk Assessment (DARA) algorithm

This section describes DARA's theoretical formulation. As introduced in Chapter 3, DARA's concept was defined using the identified methodologies to fulfil the requirements that address the gap for real-time risk assessment. These methodologies comprise object detection, scene segmentation, probabilistic modelling, and parametric controls. The outcomes of this methodology include RT figures, CT figures, *PRN*, AV-TTC, and Occurrence, which are used to increase the risk assessment coverage for AV operations.

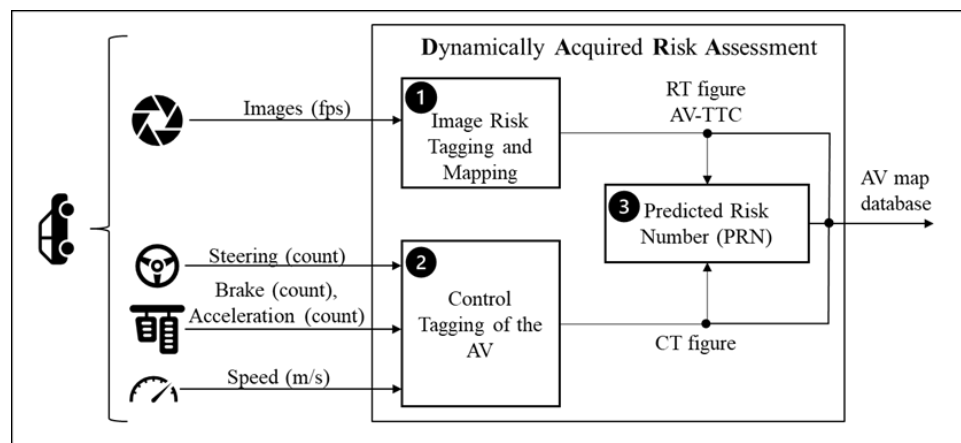


Figure 5.1: Block diagram of DARA

Figure 5.1 shows the block diagram of DARA. Image risk tagging and mapping consists of object detection, scene segmentation, and probabilistic modelling that convert the AV's real-time environmental images into RT figures and AV-TTC. RT figures indicate the severity of environmental hazards. This is achieved by converting images of the detected pedestrians or vehicles on the road or pavements into a single quantitative figure. AV-TTC is an indicator that helps determine the time to collision between the AV and the detected object. The AV's steering, brake, throttle, and speed determine the CT figures. CT figures represent the AV's control actions in response to the detected risk. *PRN* is derived from RT and CT figures, reflects a high value when there is high environmental risk along with harsh braking or wide steering angle, and reflects a low value when the AV control actions are sufficient to manage the exposed risk. The RT, CT, and

*PRN* and AV-TTC figures are stored in the AV map database. The storage of past data aids in determining Occurrence figures related to the *PRN* over time.

### 5.1.1 Image Risk Tagging and Mapping

This section details the risk tagging and mapping process within DARA, as illustrated in Figure 5.2. The input image first goes through object detection and scene segmentation. Object detection identifies the category of the detected object and locates it within the image. Scene segmentation divides the image into road, pavement, and off-road regions and adds rows based on predefined distances. These rows and columns form a matrix outcome. The object detection and scene segmentation outcomes are combined as a dependency for *PRN* calculation within the risk tagging and mapping process. Simultaneously, object detection and scene segmentation results are also used to determine the AV-TTC. The following sub-processes provide more detailed information about each module.

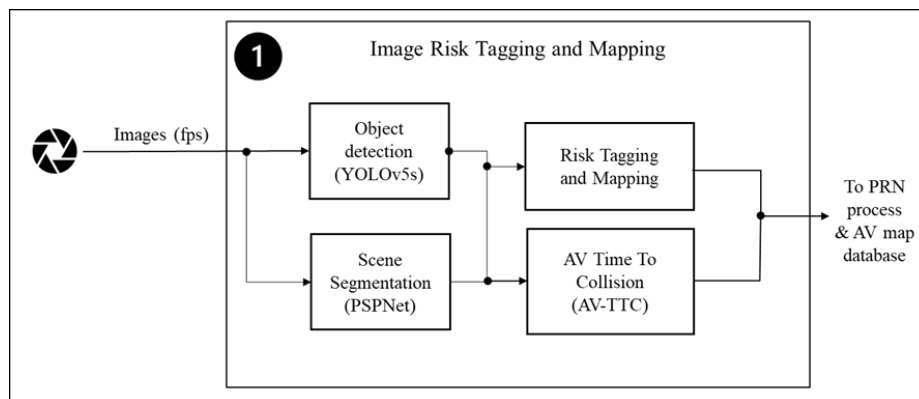


Figure 5.2: Block diagram of Image risk tagging and mapping

#### Object detection

As outlined in chapter 3, YOLOv5s is selected as the reference model for object detection. The detection outcome gives  $(x, y, w, h)$ , where  $x$  and  $y$  are the centre coordinates of the predicted box while  $w$  and  $h$  are the width and height of the box, respectively. Typically, both values  $(x, y)$  are normalised with the resolution of the image.

**Scene segmentation**

Real-time scene segmentation is used to distinguish between roads and pavements, as the risk of collision between the AV and a pedestrian/vehicle on the road should be higher than that of the pavement. Thus, roads and pavements are classified separately, and weights are assigned to roads and pavements, respectively, to differentiate the collision risks. PSPNet [82] was chosen for scene segmentation because it balances accuracy and frame rate well.

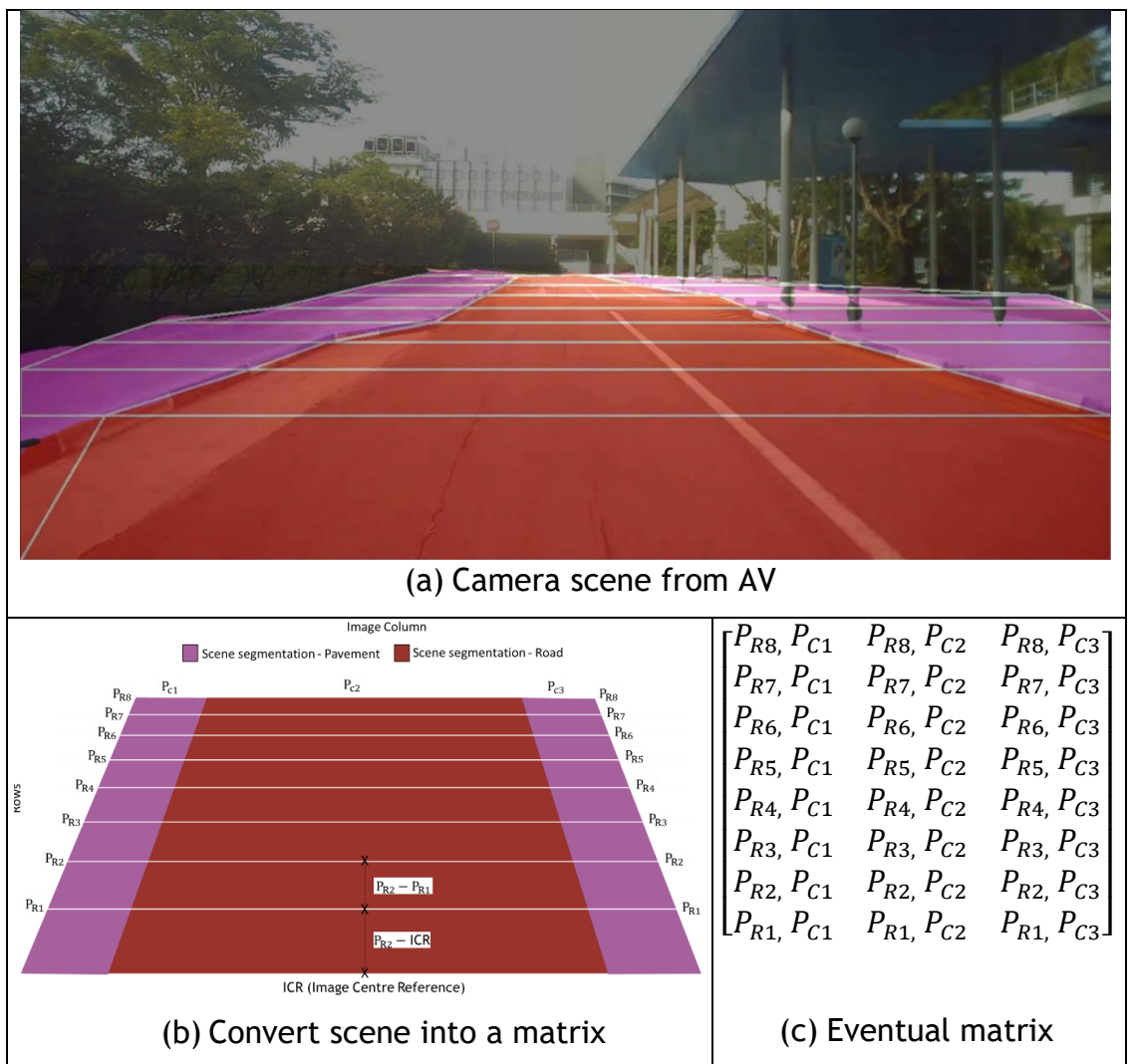


Figure 5.3: Scene segmentation of a scene into matrix

Figure 5.3 illustrates how a scene is converted into left and right pavement and road using PSPNet. Rows are added to the scene segmentation in accordance to a pre-defined distance. The pre-defined distance uses a calibrated distance per pixel relationship [132] that identifies the number of rows to the Image Centre

## 5.1 Dynamic Acquired Risk Assessment (DARA) algorithm

---

Reference (ICR). The number of pixels for each subsequent row is reduced as the distance moves away from ICR. The lines in Figure 5.3 (a) and (b) indicate the rows  $P_{R1}, P_{R2} \dots P_{RN}$  and columns  $P_{C1}, P_{C2} \dots P_{CN}$  of the Risk Tagging Matrix (RTM) as shown in Figure 5.3 (c). The RTM of a scene can be represented as  $S_n$  in equation 5.1 with the suffix rz for a specific risk zone.

$$S_n = RTM_{rz,n} \quad (5.1)$$

where,

$S_n$ : RTM of a scene

$RTM_{rz,n}$ : RTM with risk zone (rows & columns) of an image at nth frame.

$$RTM_{rz,n} = \begin{bmatrix} Y_{l8,n} & R_{8,n} & Y_{r8,n} \\ Y_{l7,n} & R_{7,n} & Y_{r7,n} \\ Y_{l6,n} & R_{6,n} & Y_{r6,n} \\ Y_{l5,n} & R_{5,n} & Y_{r5,n} \\ Y_{l4,n} & R_{4,n} & Y_{r4,n} \\ Y_{l3,n} & R_{3,n} & Y_{r3,n} \\ Y_{l2,n} & R_{2,n} & Y_{r2,n} \\ Y_{l1,n} & R_{1,n} & Y_{r1,n} \end{bmatrix} \quad (5.2)$$

where,

$RTM_{rz,n}$ : RTM with rows R, columns C and specific frame of image nth

$R_{1,n} \dots R_{8,n}$ : Road at rows 1 to 8 at the specific frame of image nth

$Y_{l1,n} \dots Y_{l8,n}$ : Left pavement at rows 1 to 8 at the specific frame of image nth

$Y_{r1,n} \dots Y_{r8,n}$ : Right pavement at rows 1 to 8 at the specific frame of image nth

Equation 5.2 represents the RTM with the defined rows and columns at that particular scene. Variables are assigned for each zonal area in equation 5.2. For example,  $Y_l$  represents the zoning of the scene into pavements on the left,  $Y_r$  represents pavements on the right, and  $R$  represents the road. RTM is used as the baseline matrix for risk tagging and mapping.

### **Performance of combined object detection and scene segmentation**

The combination of object detection and scene segmentation (YOLOv5s + PSPNet) enables real-time dynamic detection of objects and division of the scene into different road and pavement regions. The results are then used in the risk tagging and mapping process. The combined use of both YOLOv5s with PSPNet are seen in works of [133] and [134]. In this research, the methodology of [134] is used as it further enhances YOLOv5s + PSPNet which improves the inference speed of semantic segmentation up to 15 frames per second. This is achieved by adding a receptive field block layer [135] between YOLOv5s and PSPNet processing and adding channel attention [136] after the PSPNet. The receptive field block layer for PSPNet strengthens the deep features learnt with a similar approach to [135]. The channel attention is used after the PSPNet. In [134], only the performance of PSPNet is given with mIOU of 0.73. Thus, a further test was done to verify [134]. A testing data of 444 images from Cityscapes was used to test the pre-trained weights of [134] for YOLOv5s and PSPNet. The test of YOLOv5s resulted in 86% for Precision, 42% for Recall and 57% for F1 score, while the PSPNet had results with pixel accuracy of 0.9437 and mIOU of 0.767. These results showed that it aligned with the mIOU figure reported in [134]. With the object detection mapped into the scene segmentation, a similar YOLOv5s + Mapping test (section 4.2.3) was conducted, which improved Recall from 42% to 57% and F1 score from 57% to 66%, but reduced Precision from 86% to 76%. Since the research focused on the real-time risk assessment framework rather than AI optimisation, it proceeded with YOLOv5s + PSPNet pre-trained weight [134] were used (YOLOv5s can be further adapted with better-performing models in the future).

### **Risk Tagging and Mapping**

This process converts the detected objects, maps them into pavement and roads, and then determines the risk values of the scene represented as RT figures. It utilizes object detection and scene segmentation results by converting the detected object boundary box and mapping them into different regions within the scene's RTM. Once mapped in the different regions, the actual and normalised RT figures for pedestrians and vehicles are determined for *PRN* process.

## 5.1 Dynamic Acquired Risk Assessment (DARA) algorithm

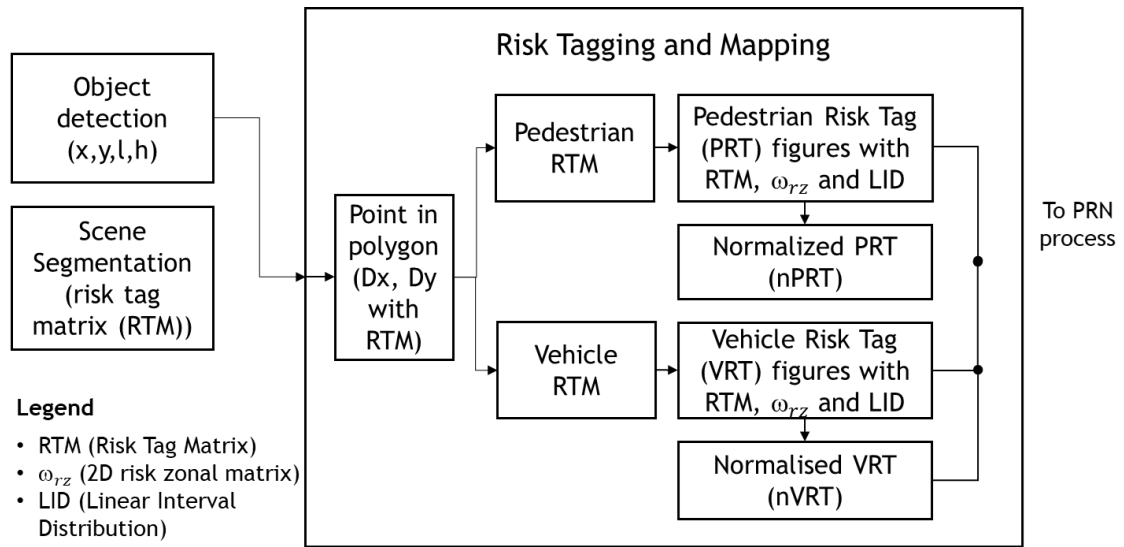


Figure 5.4 Block diagram within Risk Tagging and Mapping in DARA

Figure 5.4 shows the risk tagging and mapping process from the outcome of object detection and scene segmentation. The outcome of object detection provides  $(x, y, w, h)$ , where  $x$  and  $y$  are the centre point, with  $w$  the width and  $h$  the height of the detected object in the image. The variables  $D_x$  and  $D_y$  are defined using equation 5.3 to represent the bottom centre of the detected object by YOLOv5s. Thereafter, the  $D_x$  and  $D_y$  are mapped into the zonal areas of the dynamic scene, RTM. This mapping uses  $(D_x, D_y)$  to test for "point in polygon" [130], and if the test is true, then the objects are accounted for that zonal area within the RTM. This process emulates the same procedure of having an object detection ( $OD_{rz}$ ) matrix as discussed in chapter 4.

$$D_x = x \text{ and } D_y = y - \frac{h}{2} \quad (5.3)$$

where,

$D_x$  : Pixel number of the image width, at the bottom centre of the detected object

$D_y$  : Pixel number of the image height, at the bottom centre of the detected object

$y$  : Pixel number of the image height, at the centre of the detected object

$x$  : Pixel number of the image width, at the centre of the detected object

$h$  : Pixel height of the detected object

## 5.1 Dynamic Acquired Risk Assessment (DARA) algorithm

---

Each RTM has different zonal areas. For example, an 8 rows x 3 columns RTM has 24 zonal areas, as shown in Figure 5.3. Since the detected object can be pedestrians or vehicles, the RTM is split into pedestrians and/or vehicles RTM. The total Pedestrian Risk Tag ( $PRT$ ) figures and Vehicle Risk Tag ( $VRT$ ) figures are represented in equations 5.4 and 5.5, respectively. Equations 5.4 for  $PRT_{sum}$  and 5.5 for  $VRT_{sum}$  are determined first by performing elementwise multiplication between 2D risk zonal matrix ( $\omega_{rz}$ ) and risk detection model of Linear Interval Distribution ( $RD_{LID}$ ), and then the results are elementwise multiplied with RTM. 2D risk zonal matrix ( $\omega_{rz}$ ) is similar in STREET, where the matrix size of the RTM is used and assigned with weights (Table 4.1) that differentiate between the risks on roads and pavements. Linear Interval Distribution ( $RD_{LID}$ ) is the risk detection matrix that uses piecewise linear collision probability between the detected object and the AV. RTM represents detected objects mapped into the zonal areas of scene segmentation. The  $PRT_{sum}$  and  $VRT_{sum}$  sum all the risks of the detected objects based on the road and/or pavement and the probability of collision with the AV.

$$PRT_{SUM} = \sum_{rz} RTM(p)_{rz} \circ \omega_{rz} \circ RD_{LID} \quad (5.4)$$

where,

$PRT_{SUM}$  : Total Pedestrian RT figure

$RTM(p)_{rz}$  : Pedestrian RTM

$RD_{LID}$  : Risk detection matrix based on LID model

$\omega_{rz}$  : 2D risk zonal matrix with weights assigned for road and pavements

$$VRT_{SUM} = \sum_{rz} RTM(v)_{rz} \circ \omega_{rz} \circ RD_{LID} \quad (5.5)$$

where,

$VRT_{SUM}$  : Total Vehicle RT figure for the vehicle RTM

$RTM(v)_{rZ}$  : Vehicle RTM

$RD_{LID}$  : Risk detection matrix based on LID model

$\omega_{rZ}$  : 2D risk zonal matrix with weights assigned for the road and pavements

The  $PRT_{SUM}$  and  $VRT_{SUM}$  for a scene are also normalised to provide  $nPRT$  and  $nVRT$  using equations 5.6 and 5.7, respectively. These normalised RT figures provide the average risk per detected object and can serve as safety ratings on a scale from 0 to 10, making comparing risk levels for different scenarios easier.

$$nPRT = \frac{PRT_{SUM}}{\text{Pedestrians detected}} \quad (5.6)$$

where,

$nPRT$  : Normalised Pedestrian RT figure

$PRT_{SUM}$  : Total Pedestrian RT figure of the scene

*Pedestrians detected* : Total detected pedestrians

$$nVRT = \frac{VRT_{SUM}}{\text{Vehicles detected}} \quad (5.7)$$

where,

$nVRT$  : Normalised Vehicle RT figure

$VRT_{SUM}$  : Total Vehicle RT figure

*Vehicles detected* : Total detected vehicles



### AV Time To Collision (AV-TTC)

This process calculates the time to collision between the AV and the closest detected object. The purpose is to provide a reference for the AV. The result of this process is referred to as AV-TTC. With the rows defined within scene segmentation, the pre-determined distance for each scene and the speed of the moving AV are used to determine the time to collision. The AV-TTC is based on the defined ICR shown in Figure 5.3, and the row closest to the ICR will have the shortest time to collision.

### 5.1.2 Control Tagging of the AV

With the environmental hazards converted to RT figures, the corresponding AV reaction to the environmental hazards needs to be measured. This measurement indicates how well the AV manages the detected risk through movement. The AV's lateral and longitudinal movements are influenced by steering ( $St$ ), braking ( $B$ ), throttle ( $Th$ ), and speed ( $Sp$ ). Harsh braking, wide steering, rapid throttle, and high speed indicate inadequate risk management. Therefore, a single CT figure is calculated to determine the extent of control actions applied by the AV in response to hazards. This section illustrates the conversion of AV's lateral and longitudinal parametric movements into a single CT figure, as shown in Figure 5.5.

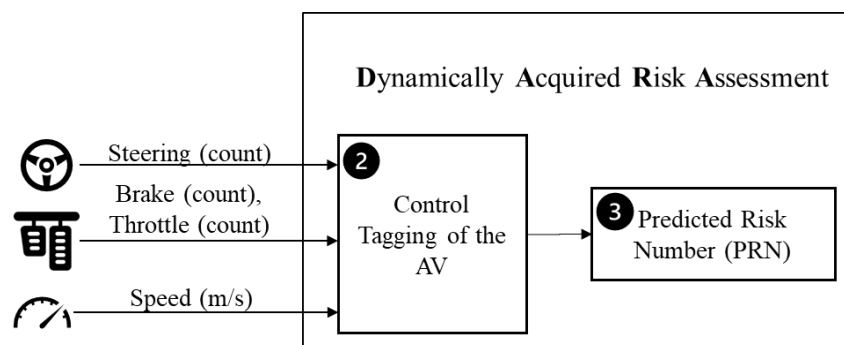


Figure 5.5: Control Tagging of the AV

Normalising the input figure to a range between 0 and 1.0 is necessary for consistency in obtaining values from different parameters. The minimum value is

subtracted from the actual reading during normalisation to remove the offset. This normalisation process is used for brake and throttle using equations 5.8 and 5.9, respectively. Brake and throttle only have positive values since they are non-directional.

$$B_n = \frac{B - B_{min}}{B_{max}} \quad (5.8)$$

where,

$B_n$  : Normalised brake values of the sensor

$B$  : Actual brake values of the sensor

$B_{min}$  : Minimum brake values of the sensor

$B_{max}$  : Maximum brake values of the sensor

$$Th_n = \frac{Th - Th_{min}}{Th_{max}} \quad (5.9)$$

where,

$Th_n$  : Normalised throttle values of the sensor

$Th$  : Actual throttle values of the sensor

$Th_{min}$  : Minimum throttle values of the sensor

$Th_{max}$  : Maximum throttle values of the sensor

Steering provides directional intentions, with inputs in negative and positive values to reflect the directional status. Therefore, the normalised steering shown in equation 5.10 illustrates the use of absolute value to capture the degree of turning and not directional information. Lastly, speed is normalised with the speed

## 5.1 Dynamic Acquired Risk Assessment (DARA) algorithm

---

limit of that section of the road shown in equation 5.11. There are no offsets for steering and speed, as their zero readings are calibrated as their minimum values.

$$St_n = \frac{|St - 0|}{|St_{max}|} \quad (5.10)$$

where,

$St_n$  : Normalised steering values

$St$  : Actual steering values

$St_{max}$  : Maximum steering values

$$Sp_n = \frac{Sp}{Sp_{limit}} \quad (5.11)$$

where,

$Sp_n$  : Normalised speed values

$Sp$  : Actual speed values

$Sp_{limit}$  : Speed limit

The CT figure of the AV, previously known as  $Ctrl$  in equation 3.2, is illustrated for easy reference as equation 5.12.  $Ctrl$  summates all four vehicle parameters with individual weights of  $W_B$ ,  $W_{Th}$ ,  $W_{St}$ , and  $W_{Sp}$ . These weights are used to adjust the individual strength of their components in situations where different emphases are needed for control tagging. For example, if the emphasis on speed needs to be reduced,  $W_{Sp}$  can be assigned to 8 (80%) instead of 10 (100%) without changing the actual conversion of the speed.

$$Ctrl = \frac{1}{3}(B_n W_B + Th_n W_{Th} + St_n W_{St} + Sp_n W_{Sp}) \quad (5.12)$$

where,

$B_n$  : Normalised brake values

$W_B$  : Weight of brake values ranging from 1 to 10 (default set at 10)

$Th_n$  : Normalised throttle values

$W_{Th}$  : Weight of throttle values ranging from 1 to 10 (default set at 10)

$St_n$  : Normalised steering values

$W_{St}$  : Weight of steering values ranging from 1 to 10 (default set at 10)

$Sp_n$  : Normalised speed values

$W_{Sp}$  : Weight of speed values ranging from 1 to 10 (default set at 10)

Through these calculations,  $Ctrl$  represents an average rating of the normalised weights and parameters obtained from the AV. Since brake and throttle do not occur simultaneously (i.e. when the brake is present, the throttle would be zero and vice versa), the averaging is accomplished with three of the four input parameters in equation 5.12. With this definition of  $Ctrl$ , high values of  $Ctrl$ , represent that extreme levels of AV operations are in place (i.e harsh braking, wide steering, rapid throttle and high speed), while low values of  $Ctrl$  represent no extreme levels of controls have taken place. The intention is to map the  $Ctrl$  with the  $PRT/VRT$  for  $PRN$ .

### 5.1.3 Predicted Risk Number ( $PRN$ )

$PRN$  assesses the risk of the AV in real time based on the exposed risk and controllability. The  $PRN$  results represent how the AV manages risk at a specific geolocation, time, and scene. The following section determines the overall risk assessment figure,  $PRN$ , using the converted AV's environment hazards into  $PRT/VRT$  and AV's movement due to the exposed hazards into  $Ctrl$ .  $PRN$  process is the last step of the DARA algorithm. The formulation of  $PRN$  shown in equation 5.13.

$$PRN = Ctrl * C_{RT} \quad (5.13)$$

## 5.1 Dynamic Acquired Risk Assessment (DARA) algorithm

---

where,

$$C_{RT} = \frac{nPRT + nVRT}{\text{Detection classes}}$$

where,

*PRN* : Predicted Risk Number

*Ctrl* : Control Tag figure

*C<sub>RT</sub>* : Combined RT figure

*nPRT*: Normalised Pedestrians RT figure

*nVRT* : Normalised Vehicles RT figure

*Detection classes* : The number of types of detected objects

The *Ctrl* in equation 5.13 represents the CT figure, while *C<sub>RT</sub>* is the combined RT figure of the normalised *PRT* and *VRT*. This is necessary because, in real-world scenarios, the exposed risk consists of different scenes with pedestrians and (or) vehicles. Since *Ctrl* and *C<sub>RT</sub>* range from 0 to 10, the resulting *PRN* varies between 0 to 100. Table 5.1 shows some simulated scenes where *PRN* is derived with environmental risk and parametric controls of the AV. Five categorised scenes are illustrated: extreme risk, high risk, normal risk, low risk, and almost no risk. Thus, from these scenes, a guideline is set, similar to the approach of setting the Risk Priority Number in FMEA [15], such that high *PRN* ratings start from the threshold of 20, while low *PRN* ratings are assigned if they are below 10, and middle *PRN* ratings range between 10 to 20. This guideline is shown in Table 5.2. Another method of determining the threshold of *PRN* ratings can be achieved by using statistical methods (50<sup>th</sup> and 95<sup>th</sup> percentile) of the past *PRN* data, as illustrated in section 5.2.5. More *PRN* evaluations and verifications through DARA will be shown in sections 5.2.4 and 5.3.

## 5.1 Dynamic Acquired Risk Assessment (DARA) algorithm

Table 5.1 Simulated scenes of PRN

Scenes	<i>Ctrl</i> (all weights = 10)	<i>C_RT</i> (detection classes = 2)	PRN & (rating)
Extreme risk	AV drive at a speed limit of 40 km/h. Throttle floored while performing a U-turn. $Sp_n = 1.0, Th_n = 1.0, St_n = 1.0, B_n = 0.0, Ctrl = 10.0$	One Pedestrian and one vehicle are detected right in front of the AV. $nPRT = 10.0, nVRT = 10.0, C_{RT} = 10.0$	100 (high)
High risk (1)	AV driving close to the speed limit at 30 km/h. Throttle at 70% with slight steering to avoid the upcoming pedestrian $Sp_n = 0.75, Th_n = 0.70, St_n = 0.30, B_n = 0.0, Ctrl = 5.83$	One Pedestrian is detected at the 2 <sup>nd</sup> row of the RTM $nPRT = 8.0, nVRT = 0.0, C_{RT} = 4.0$	23.32 (high)
High risk (2)	AV driving perform a sudden braking to avoid collision with a vehicle (near miss accident) 20 km/h. Brake at 100% with no steering $Sp_n = 0.50, Th_n = 0.0, St_n = 0.0, B_n = 1.0, Ctrl = 5.0$	One Vehicle is detected at the 2 <sup>nd</sup> row of the RTM $nPRT = 0.0, nVRT = 8.0, C_{RT} = 4.0$	20.00 (high)
Normal risk (1)	AV stop with a vehicle in front at traffic light $Sp_n = 0.0, Th_n = 0.0, B_n = 1.0, St_n = 0.0, Ctrl = 3.33$	One Vehicle is detected at the second row of the RTM. $nPRT = 0.0, nVRT = 9.0, C_{RT} = 4.5$	14.985 (mid)
Normal risk (2)	AV drive at speed of 20 km/h, limit at 40 km/h. Driving straight with throttle at 50% $Sp_n = 0.5, Th_n = 0.5, B_n = 0.0, St_n = 0.0, Ctrl = 3.33$	One Pedestrian and one vehicle are detected at the middle of the RTM. $nPRT = 5.0, nVRT = 5.0, C_{RT} = 5.0$	16.65 (mid)
Low risk	AV drive at speed of 20 km/h, limit at 40 km/h. Driving straight with throttle at 50% $Sp_n = 0.5, Th_n = 0.5, B_n = 0.0, St_n = 0.0, Ctrl = 3.33$	One Pedestrian/one vehicle is detected at the middle of the RTM. $nPRT = 5.0/0.0, nVRT = 0.0/5.0, C_{RT} = 2.5$ same for either	8.325 (low)
Almost no risk	AV idle $Sp_n = 0.0, Th_n = 0.0, B_n = 1.0, St_n = 0.0, Ctrl = 3.33$	One Pedestrian is detected at the last row of the RTM $nPRT = 1.0, nVRT = 0.0, C_{RT} = 0.5$	1.665 (low)

Table 5.2 PRN rating guideline

PRN rating	Threshold	PRN range
High	20	>20 to 100
Middle	10 to 20	10 to 20
Low	10	0 to <10

*PRNs* are all time-stamped and obtained in sub-seconds to match each camera image frame and vehicle parameter controls. To achieve this, DARA operates as an end-to-end real-time process to provide *PRN*. The outcome of *PRN* is determined objectively without human involvement based on the methodologies described in previous sections. The *PRN* can be used as input related to AV path planning for subsequent or future iterations to improve AV's safety actions. For example, AV can use the *PRN* to recommend a reduction or increase in speed.

#### **5.1.4 Occurrence and visualisation with regional *PRN***

The accumulation of averaged *PRN* over regional geolocation limits indicates potential hotspots for high-risk AV operational scenarios. This accumulation of average *PRN* figures is known as occurrence. Occurrences combine the historical *PRN* data for each area. Without regional *PRN*, the *PRN* calculated for each frame per second and location would appear to be overly complicated through the visualisation of *PRN* on the map. This regional *PRN* provides a quick and objective overview of regions that need more attention to reduce risk. It also aids in AV path planning based on past *PRNs*. Therefore, the regional *PRN* reflects quantitative risk at a specific region and time. This regional *PRN* is illustrated using a flowchart as shown in Figure 5.6.

Figure 5.6 starts with setting the geolocations' grid limits and middle points for different regions. Thereafter, each *PRN* is verified if they are within the geolocation limits of the region. If the latter is true, the geolocation of the *PRN* will be rounded off to the middle point of the region. Otherwise, the *PRN* will be used for the subsequent region with similar checks. Once the geolocation of all *PRN* Occurrences is adjusted, the average *PRN* is determined. The visualisation is accomplished using these average *PRNs* illustrated as colour maps superimposed on the AV operational route.

## 5.2 DARA evaluation process and results

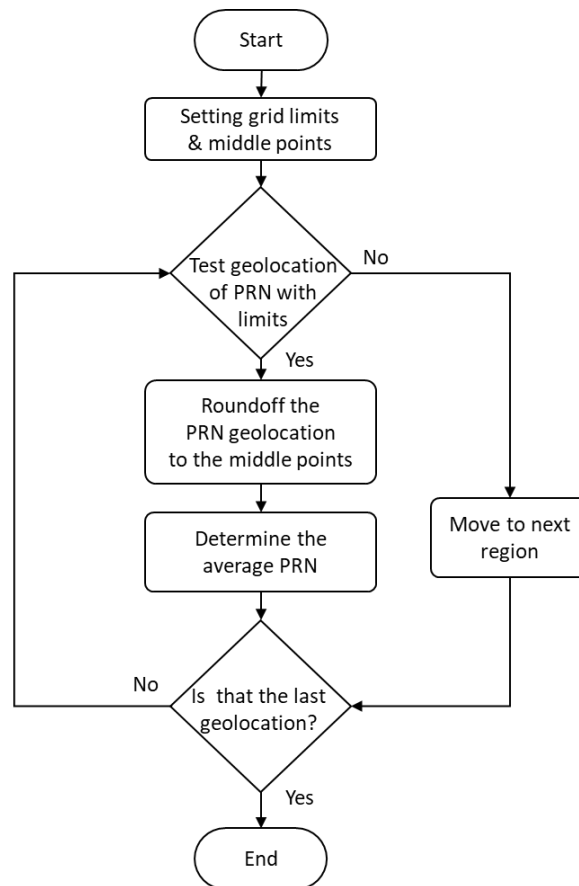


Figure 5.6 Flowchart for the Occurrence of *PRN* visualisation

## 5.2 DARA evaluation process and results

This section expands on the theoretical framework presented in section 5.1 and details the DARA process using three real-world scenarios of AV operations. These scenarios occurred during three iterative loops of AV operations at the test site located at the Ngee Ann Polytechnical campus, as indicated in Figure 5.7. The three scenarios consist of 1) Straight paths with or without zebra crossings, 2) T-junctions without traffic lights, and 3) cornering. The test site was chosen because it presents unregulated traffic within a confined area where pedestrians' and vehicles' movements are similar to public roads. This allows the algorithm to be evaluated and verified in a real-world context with minimum disruption to traffic. This section covers the evaluation process, which involves demonstrating the three scenarios through the DARA process, including image risk tagging and mapping, control tagging of the AV, and determining the *PRN* and post-analytics with



## 5.2 DARA evaluation process and results

Occurrence with regional *PRN*. In section 5.3, DARA will be verified using the entire three iterative loops of AV operations.

Figure 5.7 shows the test route for the AV services, which consists of six stops (A to F). The AV makes a complete loop, passing through all six stops before finally returning to its starting position. Each route contains scenarios 1, 2, and 3, and is repeated three times. The operations took place on a weekday between 3 and 5 pm on a sunny day with fair weather conditions. This section focuses on the evaluation of DARA using the three scenarios.

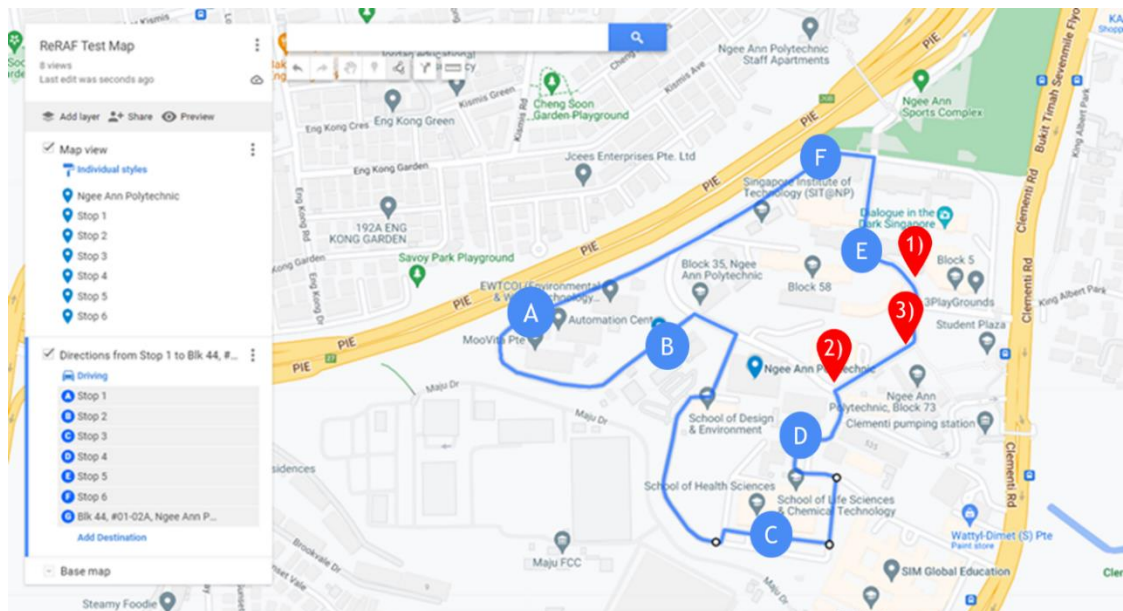


Figure 5.7 Location map of AV test site

The DARA algorithm works by processing data at the edge system using a camera installed on the front screen of the AV at 30 frames per second. The camera had a resolution of 1280 x 720 for the process of tagging and mapping image risks. Through three iterative testing loops, 121,696 instances of scenes were captured using this setup for tagging and mapping risks. The speed, steering, brake, and throttle information were obtained from existing modules within the AV. The information captured was referenced based on timestamps and geolocations with the outcomes and parameters produced by DARA.

## 5.2 DARA evaluation process and results

### 5.2.1 Scenarios for the AV test

This section illustrates the three scenarios used for DARA evaluation. It includes a brief description of each scenario and DARA's performance. The results for different scenes at the same location were compared. For example, a scene where the DARA detects a vehicle can be compared to a scene with no vehicles at a T-junction.

#### Scenario 1: Straight paths without zebra crossing

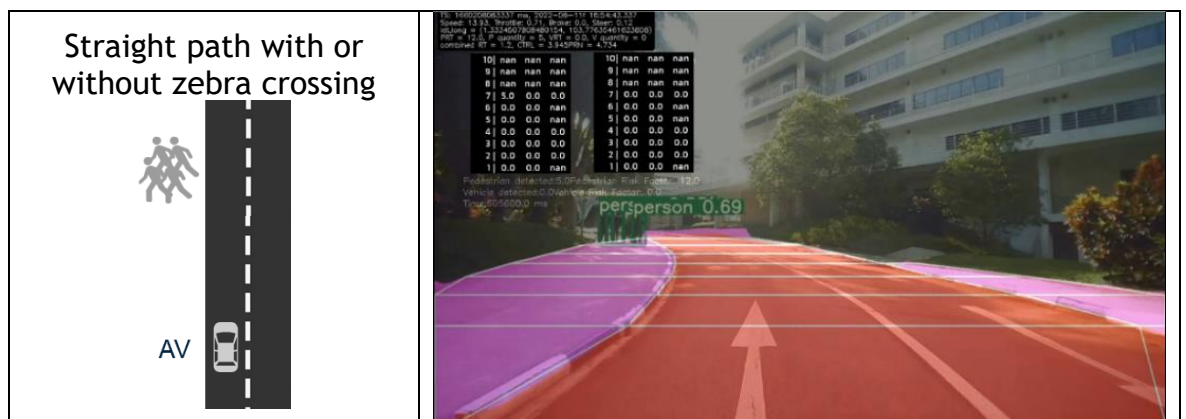


Figure 5.8 Scenario 1: Straight path without zebra crossing

In this scenario, DARA was evaluated on a straight road with a slight left bend. The scenario involves an AV detecting pedestrians on the pavement, as shown in Figure 5.8. DARA aims to measure the AV's risk assessment in handling the potential risk of pedestrians dashing in front of the AV's path. The RT figure increases as the AV moves towards the pedestrian detection area. When a pedestrian is detected, the AV should slow down. The DARA algorithm assesses the AV's response upon detecting pedestrians on the pavement while anticipating potential dashing into the AV's path.

#### Scenario 2: T-junction without traffic lights for AV

In this scenario, the AV attempts to turn right at the unregulated T-junction when an oncoming vehicle is moving straight, as shown in Figure 5.9. The oncoming vehicle is occluded by trees and is detected after it exits. The DARA algorithm

## 5.2 DARA evaluation process and results

assesses the AV's response upon detecting the oncoming vehicle detected at the T-junction.



Figure 5.9 Scenario 2: T-junction without traffic lights for AV

### Scenario 3: Cornering, detection of pedestrians after AV turns

In this scenario, a pedestrian is detected right after the AV turns a left corner, as shown in Figure 5.10. DARA is used to evaluate the response of the AV controls based on the detected immediate crossing pedestrian after the AV turns.

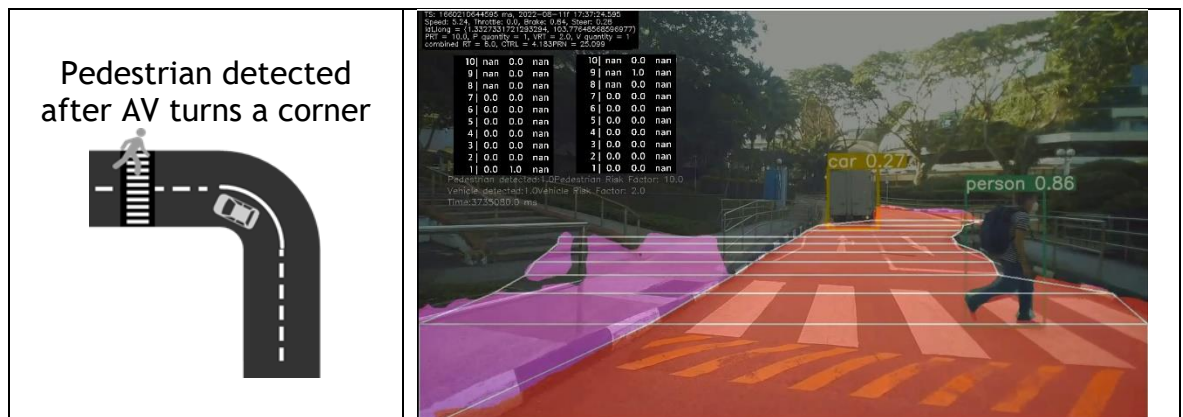


Figure 5.10 Scenario 3: Cornering, detection of pedestrians after AV turns

### 5.2.2 Image risk tagging and mapping

This section illustrates the image risk tagging and mapping process for DARA using the three selected scenarios. The camera was attached to the front of the AV. The image risk tagging and mapping process provides the RT figures of the scene, resulting from the scene segmentation and object detection.

Figure 5.11 illustrates an example of scene segmentation from the AV's POV. The red areas were classified as roads, and the pink areas as pavements. The pre-calibrated distance-to-pixel technique defines the rows (5 m per row) of each RTM as defined in equation 5.2. As illustrated in Figure 5.4, the object detection and the scene segmentation outcomes were further processed by the risk tagging and mapping process to map the detected object onto the RTM based on classes. The RTM with the detected pedestrians and vehicles were divided into  $RTM(p)_{rz}$  and  $RTM(v)_{rz}$  defined in equations 5.4 and 5.5, respectively. The top left image of Figure 5.11 illustrates examples of “nan” within the region of the matrix that represents invalid detection of a region by the scene segmentation. In this case, the regions after the eighth row and the right pavement of rows 1 and 2 within RTM were not detected.

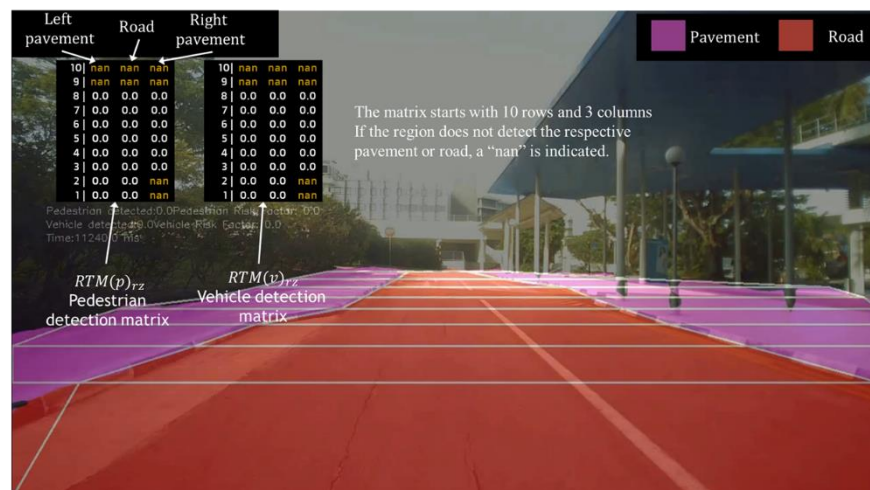


Figure 5.11 Scene segmentation process

### Scenario 1: Straight paths without zebra crossing

In scenario 1, two scenes at the exact location, at different iterations, were used for comparative analysis. Scene one had no objects detected, while scene two consisted of detected pedestrians.

Figure 5.12 shows scenario 1, scene one, which indicates that no pedestrians were present in the scene. The scene segmentation for this scene resulted in 7 rows, each measuring 5 m, thus a total of 35 m. The detection system identified roads and pavements, forming the columns and rows of the RTM. No objects were

## 5.2 DARA evaluation process and results

detected within  $RTM(p)_{r_z}$  and  $RTM(v)_{r_z}$ , resulting in a 0 value for  $PRT_{sum}$  and  $VRT_{sum}$ .



Figure 5.12 Scenario 1, scene one without pedestrians

Figure 5.13 shows scenario 1, scene two, with pedestrians detected on the left pavement, with a value of 5 in row 7 at the leftmost column of  $RTM(p)_{r_z}$ . No vehicles were detected, so  $RTM(v)_{r_z}$  had a zero value in the matrix. In the risk tagging and mapping process, the  $PRT_{sum}$  was determined using equation 5.4 and shown in Table 5.3. To determine  $PRT_{sum}$ ,  $RTM(p)_{r_z}$ ,  $\omega_{r_z}$ , and  $RD_{LID}$ , must be known. With  $RTM(p)_{r_z}$  determined and shown in Figure 5.13,  $\omega_{r_z}$  was defined with a risk weight of 8 for pavement and 10 for roads.  $RD_{LID}$  was defined with the piecewise linear distribution similar to ReRAC. The  $PRT_{sum}$  was determined to be 12 for this scene. The  $nPRT$  of 2.4 was based on equation 5.8 which represents the aggregated pedestrian risk per scene. Both  $PRT_{sum}$  and  $nPRT$  provides an RT figure of the pedestrian presence in this scenario as the AV travels forward.

5.2 DARA evaluation process and results



Figure 5.13 Scenario 1, scene two, with pedestrians detected on pavement

Table 5.3 The determination of  $PRT_{sum}$  based on scenario 1

$PRT_{sum}=12$	$RTM(p)_{rz}$	$\omega_{rz}$	$RD_{LID}$
$\begin{bmatrix} nan & nan & nan \\ nan & nan & nan \\ nan & nan & nan \\ 12.0 & 0.0 & 0.0 \\ 0.0 & 0.0 & nan \\ 0.0 & 0.0 & nan \\ 0.0 & 0.0 & 0.0 \\ 0.0 & 0.0 & 0.0 \\ 0.0 & 0.0 & 0.0 \\ 0.0 & 0.0 & nan \end{bmatrix}$	$\begin{bmatrix} nan & nan & nan \\ nan & nan & nan \\ nan & nan & nan \\ 5.0 & 0.0 & 0.0 \\ 0.0 & 0.0 & nan \\ 0.0 & 0.0 & nan \\ 0.0 & 0.0 & 0.0 \\ 0.0 & 0.0 & 0.0 \\ 0.0 & 0.0 & 0.0 \\ 0.0 & 0.0 & nan \end{bmatrix}$	$\begin{bmatrix} 8 & 10 & 8 \\ 8 & 10 & 8 \\ 8 & 10 & 8 \\ 8 & 10 & 8 \\ 8 & 10 & 8 \\ 8 & 10 & 8 \\ 8 & 10 & 8 \\ 8 & 10 & 8 \\ 8 & 10 & 8 \\ 8 & 10 & 8 \end{bmatrix}$	$\begin{bmatrix} 0 & 0.1 & 0 \\ 0.1 & 0.2 & 0.1 \\ 0.2 & 0.3 & 0.2 \\ 0.3 & 0.4 & 0.3 \\ 0.4 & 0.5 & 0.4 \\ 0.5 & 0.6 & 0.5 \\ 0.6 & 0.7 & 0.6 \\ 0.7 & 0.8 & 0.7 \\ 0.8 & 0.9 & 0.8 \\ 0.9 & 1.0 & 0.9 \end{bmatrix}$

In comparing scenes one and two, the object detection determined 5 pedestrians instead of 4 due to occlusion error in scene 2. There were also three instances of “nan” differences between scene one and two. For example, in scene one, the row 2, right column was “nan”, but in scene two, it is “0.0”. The differences in “nan” are highlighted in yellow within  $RTM(p)_{rz}$  shown in Table 5.3. As a result, the accuracy for object detection over different iterations is 75%, and for scene segmentation, it is 90% (27 out of 30 is common). The  $PRT_{sum}$  of 12 and  $nPRT$  of 2.4 for scene two indicates that although the overall sum of the pedestrian risk is high but the aggregated pedestrian risk per scene is only 2.4, thus the risk is still manageable as the pedestrians are 35 m away and within the pavement area.

### Scenario 2: T-junction without traffic lights for vehicles

Similarly, in scenario 2, a T-junction without traffic lights was evaluated for DARA. Two scenes of the same location were used for comparative analysis. No objects were detected in scene one, while only one vehicle was detected in scene two.

Figure 5.12 shows scenario 2, scene one, which indicates that there were no vehicles present. Since the pavements have metal fences that block pedestrians from crossing, detecting pavements is invalid in most regions within the RTM. The scene segmentation for this scene resulted mainly in the detection of the road, with some areas of the pavement detected. Therefore, all 10 rows are defined within the RTM (50 m). No objects were detected within  $RTM(p)_{rz}$  and  $RTM(v)_{rz}$ , resulting in a 0 value for  $PRT_{sum}$  and  $VRT_{sum}$ .



Figure 5.14 Scenario 1, scene two without vehicle

Figure 5.15 shows scenario 2, scene two, where an occluded vehicle appeared and travelled straight as the AV intended to make a right turn. Since the image had only one vehicle in Figure 5.15,  $RTM(v)_{rz}$  reflects the vehicle at row 9 of the road region at 40 m.  $RTM(p)_{rz}$  reflects no pedestrian detected with zero values. In this scenario, the  $PRT_{sum}$  is 0 and the  $VRT_{sum}$  was determined (Table 5.4) with  $RTM(v)_{rz}$  in Figure 5.15,  $\omega_{rz}$ , and  $RD_{LID}$  using the same values as scenario 1. As such, the  $VRT_{sum}$  has a value of 3.0. Since there is only one vehicle detected,  $nVRT$  is also 3.0.

5.2 DARA evaluation process and results



Figure 5.15 Scenario 2, scene two with vehicle detected

Table 5.4 The determination of  $VRT_{sum}$  based on scenario 2

$VRT_{sum}=3.0$	$RTM(v)_{rz}$	$\omega_{rz}$	$RD_{LID}$
$\begin{bmatrix} nan & 0.0 & nan \\ nan & 0.0 & 0.0 \\ nan & 0.0 & 0.0 \\ nan & 0.0 & 0.0 \\ nan & 0.0 & nan \\ nan & 0.0 & nan \\ nan & 0.0 & nan \\ nan & 0.0 & nan \\ nan & 0.0 & 0.0 \\ nan & 0.0 & nan \\ nan & 0.0 & nan \end{bmatrix}$	$\begin{bmatrix} nan & 0.0 & nan \\ nan & 0.0 & 0.0 \\ nan & 1.0 & 0.0 \\ nan & 0.0 & 0.0 \\ nan & 0.0 & nan \\ nan & 0.0 & nan \\ nan & 0.0 & nan \\ nan & 0.0 & nan \\ nan & 0.0 & 0.0 \\ nan & nan & 0.0 & nan \\ nan & 0.0 & nan \end{bmatrix}$	$\begin{bmatrix} 8 & 10 & 8 \\ 8 & 10 & 8 \\ 8 & 10 & 8 \\ 8 & 10 & 8 \\ 8 & 10 & 8 \\ 8 & 10 & 8 \\ 8 & 10 & 8 \\ 8 & 10 & 8 \\ 8 & 10 & 8 \\ 8 & 10 & 8 \\ 8 & 10 & 8 \end{bmatrix}$	$\begin{bmatrix} 0 & 0.1 & 0 \\ 0.1 & 0.2 & 0.1 \\ 0.2 & 0.3 & 0.2 \\ 0.3 & 0.4 & 0.3 \\ 0.4 & 0.5 & 0.4 \\ 0.5 & 0.6 & 0.5 \\ 0.6 & 0.7 & 0.6 \\ 0.7 & 0.8 & 0.7 \\ 0.8 & 0.9 & 0.8 \\ 0.8 & 0.9 & 0.8 \\ 0.9 & 1.0 & 0.9 \end{bmatrix}$

By comparing scenes one and two for scenario 2, no error for object detection was observed. However, there were three instances of “nan” differences between scene one and two. The differences in “nan” are highlighted in  $RTM(v)_{rz}$  shown in Table 5.4. The accuracy for object detection is 100%, while for scene segmentation is 90% (27 out of 30).  $VRT_{sum}$  and  $nVRT$  illustrate the AV’s RT figure at the T-junction before the AV intends to make a right turn. Given that the vehicle is 40 m away from the AV, the RT figure of 3.0 is logical.



## 5.2 DARA evaluation process and results

### Scenario 3: Cornering, detection of pedestrians after AV turns

Scenario 3 focuses on detecting occluded pedestrians after a turn and measures the AV's response. Similarly, two scenes of the same location are used for comparative analysis. Scene one had no detected object, while in scene two, one pedestrian and one vehicle were detected.

Figure 5.16 shows scenario 3, scene one, where no objects were detected in the scene. All 10 rows of the road were defined within the RTM (50 m). No objects were detected within  $RTM(p)_{rz}$  and  $RTM(v)_{rz}$ , resulting with a 0 value for  $PRT_{sum}$  and  $VRT_{sum}$ .

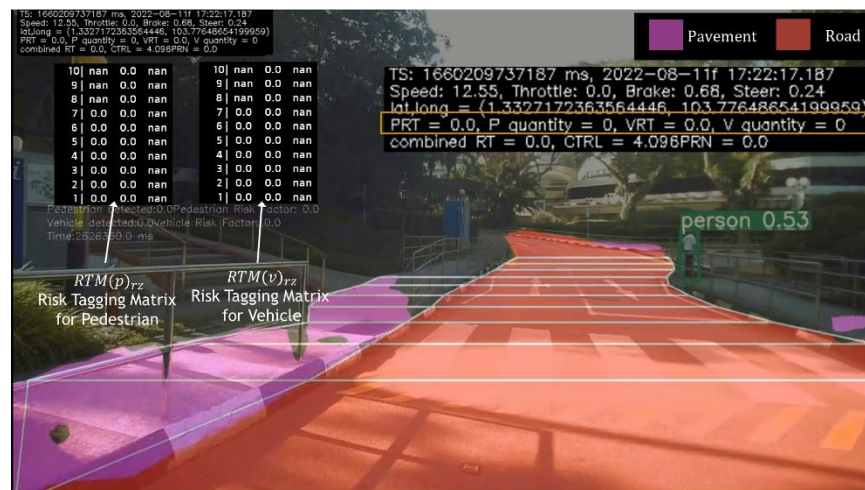


Figure 5.16 Scenario 3, scene one without object detected.

Figure 5.17 shows scenario 3, scene two, where a pedestrian in close proximity and a vehicle at some distance away were detected immediately after turning a left corner. The scenario focuses on detecting occluded pedestrians after a turn and measures the response of the AV. These detections are reflected in the  $RTM(p)_{rz}$  and  $RTM(v)_{rz}$ . The pedestrian detected is at the 1st row of the road region, while a vehicle is detected at the 9th row of the road region, which is a distance away from the AV. The  $RTM(p)_{rz}$  and  $RTM(v)_{rz}$  contains objects that are detected based on the scene in Figure 5.17. The  $PRT_{sum}$  and  $VRT_{sum}$  are determined with illustration shown in Table 5.5 and Table 5.6, respectively. The  $PRT_{sum}$  gives an overall figure of 10.0. The  $nPRT$  is also 10.0 since there is only

5.2 DARA evaluation process and results

one pedestrian. The  $VRT_{sum}$  gives an overall figure of 2.0, and since there is only one vehicle,  $nVRT$  had the same value of 2.0.



Figure 5.17 Scenario 3, scene 2 with a pedestrian and vehicle detected

Table 5.5 The determination of  $PRT_{sum}$  based on scenario 3

$PRT_{sum}=10.0$	$RTM(p)_{rz}$	$\omega_{rz}$	$RD_{LID}$
$\begin{bmatrix} nan & 0.0 & nan \\ nan & 0.0 & nan \\ nan & 0.0 & nan \\ 0.0 & 0.0 & nan \\ 0.0 & 0.0 & nan \\ 0.0 & 0.0 & nan \\ 0.0 & 0.0 & nan \\ 0.0 & 0.0 & nan \\ 0.0 & 0.0 & nan \\ 0.0 & 0.0 & nan \\ 0.0 & 10.0 & nan \end{bmatrix}$	$\begin{bmatrix} nan & 0.0 & nan \\ nan & 0.0 & nan \\ nan & 0.0 & nan \\ 0.0 & 0.0 & nan \\ 0.0 & 0.0 & nan \\ 0.0 & 0.0 & nan \\ 0.0 & 0.0 & nan \\ 0.0 & 0.0 & nan \\ 0.0 & 0.0 & nan \\ 0.0 & 0.0 & nan \\ 0.0 & 1.0 & nan \end{bmatrix}$	$\begin{bmatrix} 8 & 10 & 8 \\ 8 & 10 & 8 \\ 8 & 10 & 8 \\ 8 & 10 & 8 \\ 8 & 10 & 8 \\ 8 & 10 & 8 \\ 8 & 10 & 8 \\ 8 & 10 & 8 \\ 8 & 10 & 8 \\ 8 & 10 & 8 \\ 8 & 10 & 8 \end{bmatrix}$	$\begin{bmatrix} 0 & 0.1 & 0 \\ 0.1 & 0.2 & 0.1 \\ 0.2 & 0.3 & 0.2 \\ 0.3 & 0.4 & 0.3 \\ 0.4 & 0.5 & 0.4 \\ 0.5 & 0.6 & 0.5 \\ 0.6 & 0.7 & 0.6 \\ 0.7 & 0.8 & 0.7 \\ 0.8 & 0.9 & 0.8 \\ 0.9 & 1.0 & 0.9 \end{bmatrix}$

## 5.2 DARA evaluation process and results

Table 5.6 The determination of  $VRT_{sum}$  based on scenario 3

$VRT_{sum}=2.0$	$RTM(v)_{rz}$	$\omega_{rz}$	$RD_{LID}$
$\begin{bmatrix} nan & 0.0 & nan \\ nan & 2.0 & nan \\ nan & 0.0 & nan \\ 0.0 & 0.0 & nan \\ 0.0 & 0.0 & nan \\ 0.0 & 0.0 & nan \\ 0.0 & 0.0 & nan \\ 0.0 & 0.0 & nan \\ 0.0 & 0.0 & nan \\ 0.0 & 0.0 & nan \\ 0.0 & 0.0 & nan \end{bmatrix}$	$\begin{bmatrix} nan & 0.0 & nan \\ nan & 1.0 & nan \\ nan & 0.0 & nan \\ 0.0 & 0.0 & nan \\ 0.0 & 0.0 & nan \\ 0.0 & 0.0 & nan \\ 0.0 & 0.0 & nan \\ 0.0 & 0.0 & nan \\ 0.0 & 0.0 & nan \\ 0.0 & 0.0 & nan \\ 0.0 & 0.0 & nan \end{bmatrix}$	$\begin{bmatrix} 8 & 10 & 8 \\ 8 & 10 & 8 \\ 8 & 10 & 8 \\ 8 & 10 & 8 \\ 8 & 10 & 8 \\ 8 & 10 & 8 \\ 8 & 10 & 8 \\ 8 & 10 & 8 \\ 8 & 10 & 8 \\ 8 & 10 & 8 \\ 8 & 10 & 8 \end{bmatrix}$	$\begin{bmatrix} 0 & 0.1 & 0 \\ 0.1 & 0.2 & 0.1 \\ 0.2 & 0.3 & 0.2 \\ 0.3 & 0.4 & 0.3 \\ 0.4 & 0.5 & 0.4 \\ 0.5 & 0.6 & 0.5 \\ 0.6 & 0.7 & 0.6 \\ 0.7 & 0.8 & 0.7 \\ 0.8 & 0.9 & 0.8 \\ 0.9 & 1.0 & 0.9 \end{bmatrix}$

By comparing scenes one and two for scenario 3, no error was observed in the object detection, and there were no delta “nan” between scenes one and two. The accuracy for object detection and scene segmentation is 100%. The high  $nPRT$  reflects the high risk of a pedestrian crossing right in front of the AV in close proximity. The low  $nVRT$  indicates that the risk of potential collision between the AV and the detected vehicle was low since they were 45 m apart.

### 5.2.3 Control Tagging of the AV

In this section, CT figure known as  $Ctrl$  of the AV is illustrated with the same three scenarios. The AV parameters brake, steering, throttle, and speed information have dynamic range values and require normalisation before they are converted into  $Ctrl$ . These acquired AV parameters based on the three scenarios were first normalised using equations 5.8 to 5.11. The  $Ctrl$  was determined using equation 5.12.

#### Scenario 1: Straight paths without zebra crossing

In scenario 1, scene one, no pedestrians or vehicles were detected. Therefore, the AV had a high throttle of 94%, but still at a safe speed of 16.09 km/h. With that, the  $Ctrl$  was defined at 4.808, as shown in Table 5.7.

## 5.2 DARA evaluation process and results

Table 5.7 Scenario 1, scene one, AV *Ctrl*

Parameters		Normalised values		Overall <i>Ctrl</i> (weights set at 10)
<i>B</i>	0	<i>B<sub>n</sub></i>	0	4.808
<i>Th</i>	3760	<i>Th<sub>n</sub></i>	3760/4000 = 0.94 (94%)	
<i>St</i>	-100	<i>St<sub>n</sub></i>	Abs(-100/1000) =0.10 (12%)	
<i>Sp</i>	16.09 km/h	<i>Sp<sub>n</sub></i>	16.09/40=0.40 (40%)	

```

TS: 1660210677004 ms, 2022-08-11f 17:37:57.004
Speed: 16.09, Throttle: 0.94, Brake: 0.0, Steer: 0.1
lat, long = (1.3334485120424675, 103.77635834714992)
PRT = 0.0, P quantity = 0, VRT = 0.0, V quantity = 0
combined RT = 0.0, CTRL = 4.808 PRN = 0.0

```

In scenario 1, scene two, the AV throttle was measured at 71% with a slight steering of 12% to the left due to the road's curvature. The actual speed was 13.93 km/h with no brakes applied. Table 5.8 shows the normalised AV parameters and the result of *Ctrl*. The *Ctrl* of 3.945 showed no braking event with slight steering and a rapid throttle at 35% of the speed limit.

Table 5.8 Scenario 1, scene two, AV *Ctrl*

Parameters		Normalised values		Overall <i>Ctrl</i> (weights set at 10)
<i>B</i>	0	<i>B<sub>n</sub></i>	0	3.945
<i>Th</i>	2841	<i>Th<sub>n</sub></i>	2841/4000 = 0.71 (71%)	
<i>St</i>	-125	<i>St<sub>n</sub></i>	Abs(-125/1000) =0.12 (12%)	
<i>Sp</i>	13.93 km/h	<i>Sp<sub>n</sub></i>	13.93/40=0.35 (35%)	

```

TS: 1660208083337 ms, 2022-08-11f 16:54:43.337
Speed: 13.93, Throttle: 0.71, Brake: 0.0, Steer: 0.12
lat, long = (1.3334507808480154, 103.77635461623808)
PRT = 12.0, P quantity = 5, VRT = 0.0, V quantity = 0
combined RT = 1.2, CTRL = 3.945 PRN = 4.734

```

By comparing scenes one and two in scenario 1, it was observed that the different *Ctrl* (4.808 for scene one and 3.945 for scene two) reflected the difference in the AV's speed and throttle. In scene two, the AV was more cautious, reducing throttle and speed, resulting in a lower *Ctrl*. Therefore, the *Ctrl* reflects the change in speed and throttle applied.

## 5.2 DARA evaluation process and results

**Scenario 2: T-junction without traffic lights for vehicles**

In scenario 2, scene one, no pedestrians and vehicles were detected at the T-junction without traffic lights. However, the AV braked to stop at the T-junction pocket. Thus, the AV had a high braking of 95%, slowing down from 12.64 km/h. With that, the *Ctrl* was defined at 4.406, as shown in Table 5.9.

Table 5.9 Scenario 2, scene one, AV *Ctrl*

Parameters		Normalised values		Overall <i>Ctrl</i> (weights set at 10)
<i>B</i>	950	<i>B<sub>n</sub></i>	$950/1000=0.95$ (95%)	4.406
<i>Th</i>	0	<i>Th<sub>n</sub></i>	$0/4000 = 0.0$	
<i>St</i>	-60	<i>St<sub>n</sub></i>	$Abs(-60/1000) =0.06$ (6%)	
<i>Sp</i>	12.64 km/h	<i>Sp<sub>n</sub></i>	$12.64/40=0.31$ (31%)	

```
TS: 1660209674854 ms, 2022-08-11f 17:21:14.854
Speed: 12.64, Throttle: 0.0, Brake: 0.95, Steer: 0.06
lat, long = (1.331759566992039, 103.7754653197054)
PRT = 0.0, P quantity = 0, VRT = 0.0, V quantity = 0
combined RT = 0.0, CTRL = 4.406 PRN = 0.0
```

In scenario 2, scene two, the AV braked at 95%, with zero throttle and a slight steering of 12%. The vehicle's speed at the time of braking was 13.77 km/h (34%). Table 5.10 displays the actual values of the normalised AV parameters and the calculation of *Ctrl*. The *Ctrl* of 4.664 is at the middle level due to the harsh braking.

Table 5.10 Scenario 2, scene two, AV *Ctrl*

Parameters		Normalised values		Overall <i>Ctrl</i> (weights set at 10)
<i>B</i>	950	<i>B<sub>n</sub></i>	$950/1000=0.95$ (95%)	4.664
<i>Th</i>	0	<i>Th<sub>n</sub></i>	$0/4000 = 0.0$	
<i>St</i>	-105	<i>St<sub>n</sub></i>	$Abs(-125/1000) =0.12$ (12%)	
<i>Sp</i>	13.77 km/h	<i>Sp<sub>n</sub></i>	$13.77/40=0.34$ (34%)	

```
TS: 1660207974585 ms, 2022-08-11f 16:52:54.585
Speed: 13.77, Throttle: 0.0, Brake: 0.95, Steer: 0.1
lat, long = (1.3317563996978496, 103.77546658465687)
PRT = 0.0, P quantity = 0, VRT = 3.0, V quantity = 1
combined RT = 1.5, CTRL = 4.664 PRN = 6.996
```

## 5.2 DARA evaluation process and results

In comparing scenes one and two in scenario 2, *Ctrl* is comparable between the two figures of 4.406 and 4.664 for scenes one and two, respectively. The minor difference is due to the slightly higher speed for scene 2. This indicates that the AV operations remained consistent regardless of the detected risk.

### Scenario 3: Cornering, detection of pedestrians after AV turns

In scenario 3, scene one, no pedestrians and vehicles were detected within the RTM after turning the corner. The AV was completing its turn (24% steering) with a partial brake of 68% with a remaining speed of 12.55 km/h. With that, the *Ctrl* was defined at 4.096, as shown in Table 5.11 .

Table 5.11 Scenario 3, scene one, AV *Ctrl*

Parameters		Normalised values		Overall <i>Ctrl</i> (weights set at 10)
<i>B</i>	680	<i>B<sub>n</sub></i>	$680/1000=0.68$ (68%)	4.096
<i>Th</i>	0	<i>Th<sub>n</sub></i>	$0/4000 = 0.0$	
<i>St</i>	-240	<i>St<sub>n</sub></i>	$Abs(-240/1000) =0.24$ (24%)	
<i>Sp</i>	12.55 km/h	<i>Sp<sub>n</sub></i>	$12.55/40=0.31$ (31%)	

```
TS: 1660209737187 ms, 2022-08-11f 17:22:17.187
Speed: 12.55, Throttle: 0.0, Brake: 0.68, Steer: 0.24
lat, long = (1.3327172363564446, 103.77648654199959)
PRT = 0.0, P quantity = 0, VRT = 0.0, V quantity = 0
combined RT = 0.0, CTRL = 4.096 PRN = 0.0
```

In scenario 3, scene two, the AV braked at 84% and made a slight steering adjustment of 28% to the left after the turn. Due to a detected pedestrian after turning the corner, the AV was travelling at a speed of 5.24 km/h. As a result, *Ctrl* is 4.183, which is in the middle level because of the slight steering and harsh braking actions with extremely low speed. Table 5.12 summarises the actual values of the normalised AV parameters and the calculation of *Ctrl*.

## 5.2 DARA evaluation process and results

Table 5.12 Scenario 3, scene two, AV *Ctrl*

Parameters		Normalised values		Overall <i>Ctrl</i> (weights set at 10)
$B$	840	$B_n$	$840/1000=0.84$ (84%)	4.183
$Th$	0	$Th_n$	$0/4000 = 0.0$	
$St$	-280	$St_n$	$Abs(-280/1000) =0.28$ (28%)	
$Sp$	5.24 km/h	$Sp_n$	$5.24/40=0.13$ (13%)	

```

TS: 1660210644595 ms, 2022-08-11f 17:37:24.595
Speed: 5.24, Throttle: 0.0, Brake: 0.84, Steer: 0.28
lat, long = (1.3327331721293294, 103.77648568596977)
PRT = 10.0, P quantity = 1, VRT = 2.0, V quantity = 1
combined RT = 6.0, CTRL = 4.183, PRN = 25.099

```

In comparing scenes one and scene two in scenario 3, the *Ctrl* are comparable between the two figures of 4.096 and 4.183 for scenes one and two, respectively. The minor difference in *Ctrl* was due to a harsher brake applied, but it was also compensated with a lower speed in scene two. This implies that the AV has taken some inherent safety actions even without detecting the pedestrian, but the performance of the AV control must be further refined to avoid high risk at this location.

### 5.2.4 Predicted Risk Number (*PRN*)

With the completed *Ctrl*,  $nPRT$  and  $nVRT$ , the *PRN* is determined using the equation 5.13. The derivation of *PRN* in real time is illustrated using scenarios 1 (Figure 5.13), 2 (Figure 5.15) and 3 (Figure 5.17). The *PRN* results and the parameters required are illustrated in Table 5.13.

Table 5.13 Parameters for *PRN* in Scenarios 1, 2 and 3

Parameters	Scenario 1, Figure 5.13	Scenario 2, Figure 5.15	Scenario 3, Figure 5.17
$nPRT$ (/10)	2.4	0.0	10.0
$nVRT$ (/10)	0.0	3.0	2.0
$C_{RT}$ (/10)	1.2	1.5	6.0
<i>Ctrl</i> (/10)	3.945	4.664	4.183
<i>PRN</i> (/100)	4.734	6.996	25.099

## 5.2 DARA evaluation process and results

---

The *Ctrl*, *nPRT* and *nVRT* are normalised to a maximum of 10 and a minimum of 0. *C\_RT* (combined RT) is the average between *nPRT* and *nVRT*, which is also normalised to 10. *PRN* ranges between 0 to 100 since it is the product of *Ctrl* and *C\_RT*, as in equation 5.13. Further details on the *PRN* results are discussed for each scenario.

### **Scenario 1: straight path without zebra crossing**

Scenario 1 in Table 5.13 has a *PRN* value of 4.734, indicating a low-level risk assessment. Firstly, the 5 detected pedestrians in scenario 1 resulted in a low level of *nPRT* and 0 *nVRT* for no vehicles detected. *nPRT* of 2.4 is logical since the detected pedestrians were far from the AV. Secondly, the AV *Ctrl* of 3.945 was determined based on travel speed at 35% (Table 5.8) of its maximum speed limit, with relatively high throttle and low steering. Comparing scenes one and two of scenario 1 demonstrated that the AV triggered inherent safety actions with lower operating speed and throttle in scene two when pedestrians were detected. Therefore, in scene two, the low *PRN* of 4.734 indicates that the AV was operating at low risk, allowing sufficient time for the AV to react when a pedestrian dashes across the road region. Thus, in this case, the AV does not require any further improvements in safety actions, and the *PRN* demonstrated its ability to perform real-time risk assessment of this scenario.

### **Scenario 2: T-junction without traffic lights**

The parameters of Table 5.13 for scenario 2 illustrate a *PRN* of 6.996. Firstly, a vehicle was detected with no pedestrians within the scenario. Thus, only an *nVRT* of 3.0 exists, illustrating that the detected vehicle was far from the AV. Secondly, the *Ctrl* of 4.664 explains that the AV travelling at 34% (Table 5.10) of its maximum speed limit had applied harsh braking with zero throttle. Thus, the overall *PRN* of 6.996 is still considered a low-risk *PRN*. In this scenario, no critical improvements in safety actions are necessary with the low *PRN*. However, minor improvements to existing safety actions for future iterations, such as applying early and gradual braking, will reduce the *PRN* even further for a safer AV operation.



**Scenario 3: Cornering, detection of pedestrians after AV turns**

Scenario 3 results shown in Table 5.13 illustrate the highest *PRN* value of 25.099 among the three scenarios. The high *PRN* occurred after a cornering where the AV applied harsh braking with zero throttle and slight steering at low speed. Firstly, a detected pedestrian that suddenly crosses the road in front of the AV creates an *nPRT* of 10, while a detected vehicle in the 9<sup>th</sup> row provides a low *nVRT* of 2.0. The *nPRT* and *nVRT* resulted in the *C<sub>RT</sub>* of 6.0. Secondly, the *Ctrl* of 4.183 was determined from the harsh braking with slight steering and low speed. The high *C<sub>RT</sub>* with a middle level of *Ctrl* resulted in a high *PRN* because of the risk detected due to a pedestrian's sudden dashing and the AV having harsh braking with zero throttle at low speed. According to the guideline in section 5.1.3, any *PRN* above 20 is considered as high risk for the AV. The recommended improvement to the inherent safety action is to brake early before the corner turn and approach the zebra crossing with low speed and low braking for future iterations. AV can resume at a higher speed after the zebra crossing.

In summary, the three scenarios illustrated *PRN*'s representation of the real-time risk assessment of environmental hazards with AV controllability. These results are demonstrated in real-world scenarios and focused on unregulated traffic areas. The following section shows the Occurrence and visualisation of *PRN* using a regional *PRN* method. More examples of high *PRN* and scenarios will be discussed in section 5.3.

**5.2.5 Occurrence with regional *PRN* visualisation**

The Occurrence of risk assessment is represented by the regional *PRN*, which reflects risk hotspots over regional areas at specific times. The regional *PRN* is determined based on the flowchart in Figure 5.6 for different regions. Figure 5.18 shows an example of the regional *PRN* for the first loop of the test route. The individual *PRNs* determined along the travelled paths are converted into location grids with their *PRN* averaged into regional *PRNs*.

## 5.2 DARA evaluation process and results

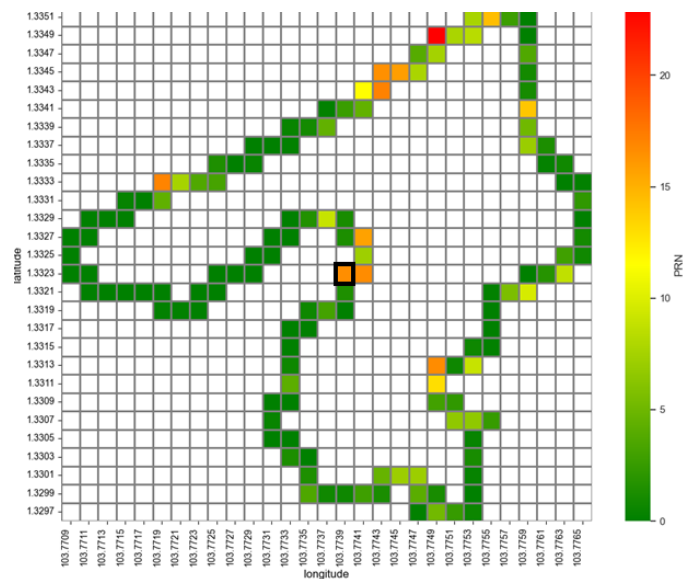


Figure 5.18 Regional *PRN* of first loop test route

Figure 5.18 shows an example that illustrates a regional *PRN*, highlighted as a black box at the centre of Figure 5.18. The centre of this black box has a latitude of  $1.3323^\circ$  and a longitude of  $103.7739^\circ$ , respectively, based on the y-axis and x-axis. The regional *PRN* of this black box is 16, which means that any *PRN* within the latitude and longitude limits are average and presented as a regional *PRN*. The limits (boundary of each geolocation box) in Figure 5.18 are illustrated as grids for each region. This black box location reflects the scenario shown in Figure 5.19 with a pedestrian dashing across the road at a T-junction, within 20 m of the AV right after the AV makes a right turn.



Figure 5.19 Black box regional *PRN* scene for first loop

In the next section, DARA is verified using the iterative test route, and a detailed explanation of scenarios with high *PRN* will be explained.

### 5.3 Verification of DARA with real-world test routes

In this section, DARA is further verified with three iterative test routes. Firstly, an overview of the *PRN*, *C\_RT*, and *Ctrl* across the three iterative test routes with statistical comparisons is presented. These comparisons were made with observations on the *PRN* characteristics to verify the performance of DARA. Secondly, an example of how the *PRN* rating threshold is determined based on past historical data is provided. Lastly, nine scenarios (A to I) were selected to illustrate the different outcomes of *PRN* (three high, three middle and three low) and the simulated recommended actions that would lower the risk and improve the safety performance of the AV, especially for high *PRNs*.

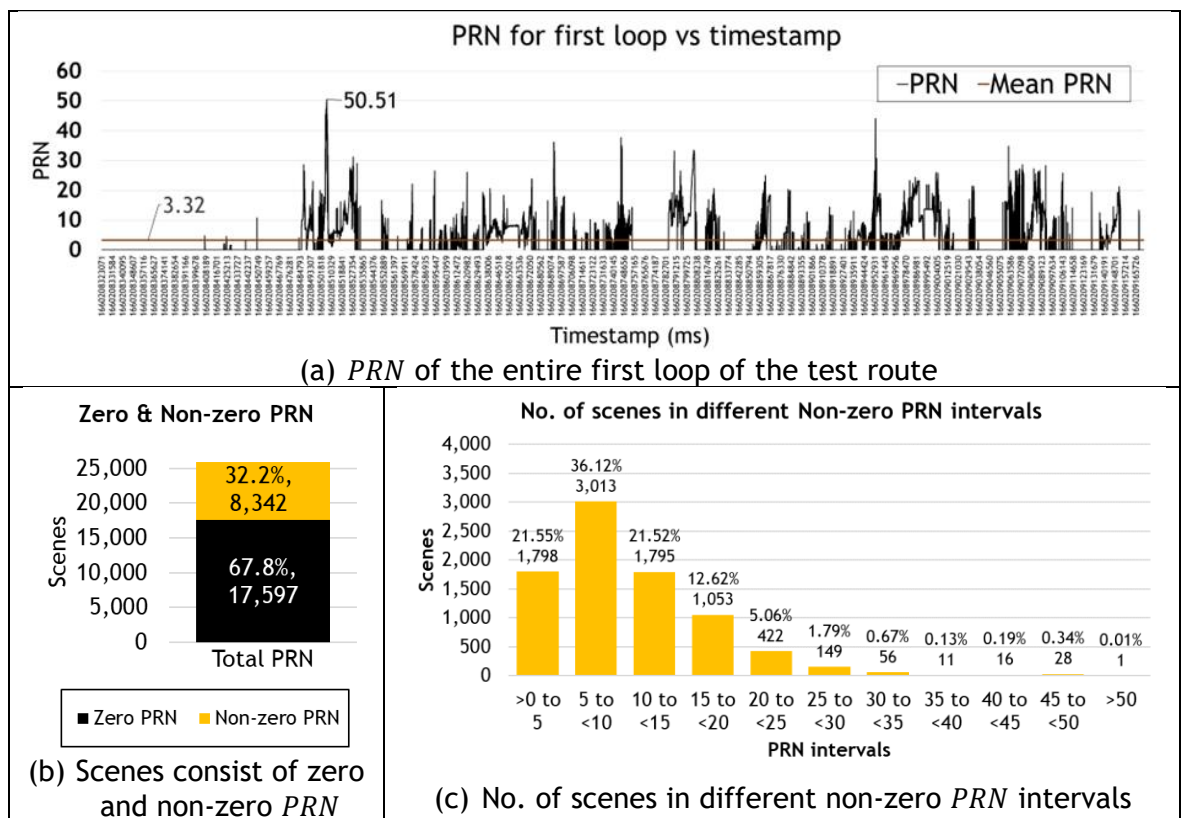


Figure 5.20 *PRN* for the first loop

Figure 5.20 details the *PRN* for the first loop of the test routes. These results illustrate the *PRN*'s characteristics and functionality. Figure 5.20 (a) shows the *PRN* variation over the timestamp of 25,939 samples, with a maximum *PRN* of 50.51 and a mean *PRN* of 3.32. The low mean *PRN* is mainly due to a significant number of zero *PRN* values, which occur when no risks are detected at the scenes.

## 5.3 Verification of DARA with real-world test routes

This is verified by Figure 5.20 (b), which shows 67.8% of the *PRN* values were zero, indicating no identified risks, while 32.2% were non-zero, indicating the detection of risks for vehicles or pedestrians occurred with AV controls. Figure 5.20 (c) further illustrates that 57.67% of the non-zero *PRN* falls within the intervals of  $>0$  to  $<10$ , indicating that the remaining 42.33% of the scenes require safety improvements, as their *PRN* values were 10 or higher (based on the *PRN* default guide in section 5.1.3). High *PRN* occurs when vehicles or pedestrians are close to the AV and when there is a combination of harsh braking, wide steering, or significant speed changes.

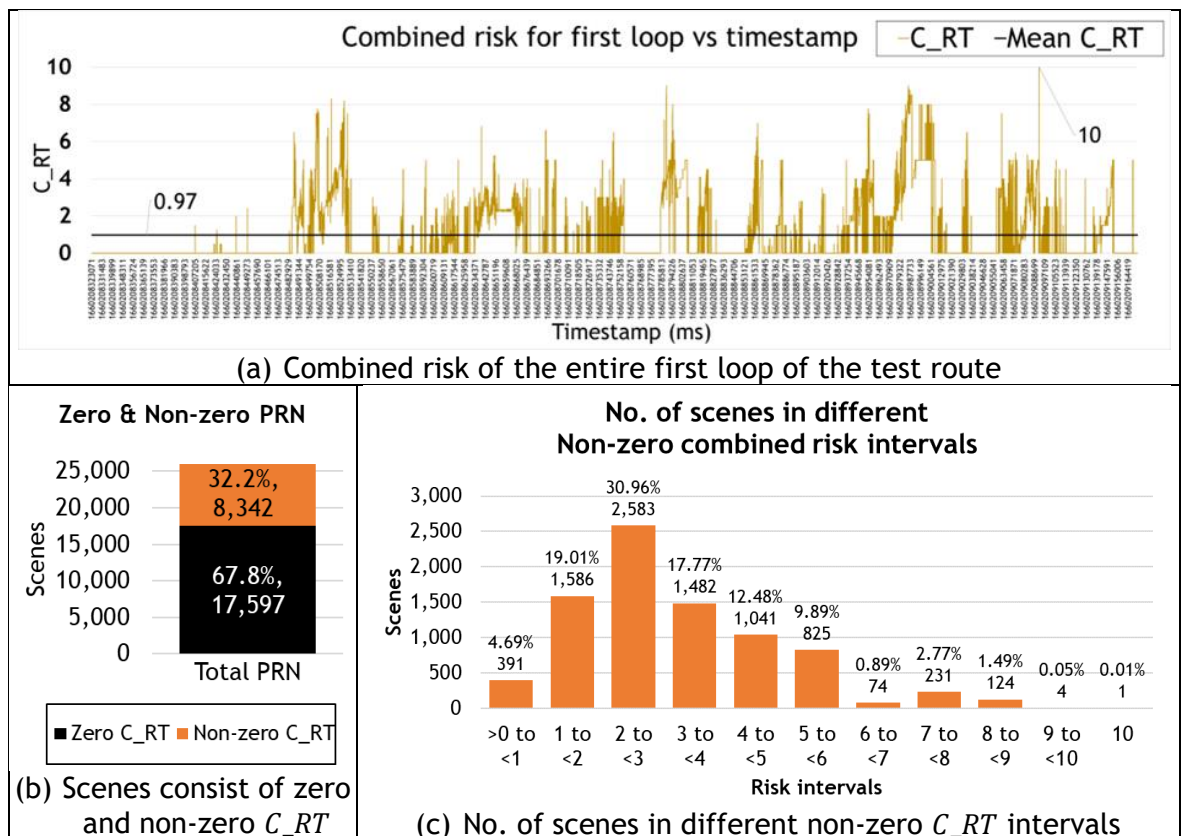
Figure 5.21 *C\_RT* for the first loop

Figure 5.21 details the *C\_RT* results for the entire first loop of the test routes. *C\_RT* represents the average risk per scene, calculated as an average between *nPRT* and *nVRT*. Figure 5.21 (a) shows the *C\_RT* variation over the 25,939 samples, with a maximum *C\_RT* of 10 and a mean *C\_RT* of 0.97. The low *C\_RT* mean is mainly contributed by the significant number of zero *C\_RT* when no risks were detected in the scenes, as shown in Figure 5.21 (b), where 67.8% of *C\_RT* were zero *C\_RT*, and 32.2% were non-zero. These zero and non-zero *C\_RT*

5.3 Verification of DARA with real-world test routes

correspond to the zero and non-zero *PRN*, confirming that *PRN* is only positive when environmental risk is detected (*C\_RT* is non-zero). These results show the relationship between *C\_RT* and *PRN*. Zero *C\_RT* indicates no identified risks, while non-zero *C\_RT* occurrences indicate that risks for vehicle or pedestrian collisions are detected within the RTM. Figure 5.21 (c) further illustrates that 84.91% of the *C\_RT* in this first loop is <5, while 15.09% > 5.

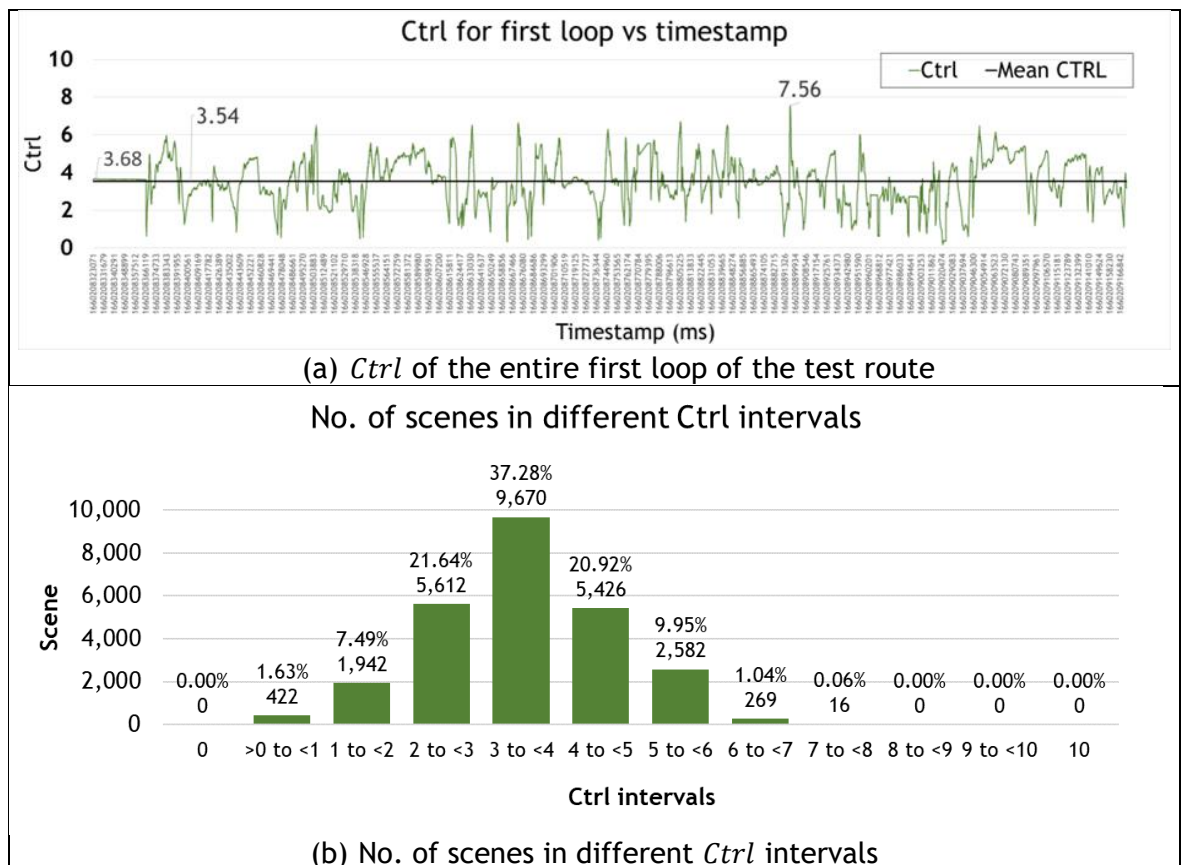


Figure 5.22 Ctrl for the first loop

Figure 5.22 (a) illustrates how *Ctrl* changes based on the AV control movements during the first loop of the test route. *Ctrl* will always be true because there will always be braking or throttle. Thus, when the AV is turned on and remains stationary without movement, the *Ctrl* has a value of 3.68. The *Ctrl* ranges from 0 to 10, with an average of 3.54 for the first loop. Figure 5.22 (b) shows the distribution of *Ctrl* intervals for the first loop, corroborate the mean *Ctrl* value, where the majority of the *Ctrl* is classified within the 3 to <4 interval. This also illustrates that the AV did not have extreme moves within the first loop of operations.

### 5.3 Verification of DARA with real-world test routes

With the quantitative results of DARA using *PRN* with *C\_RT* and *Ctrl*, comparative statistical analysis is conducted across different operating loops to understand the magnitude of exposed risk (*C\_RT*) and AV control movement (*Ctrl*), which results in the AV real-time risk assessment outcome (*PRN*) for each loop. Table 5.14 illustrates these objectives.

Table 5.14 Data statistics for three loops of DARA real-world testing

Variable	Statistics	First loop	Second loop	Third loop
<i>PRN</i>	Max	50.51	43.14	42.62
	Mean	3.22	3.58	4.36
	Zero	17,597	16,734	15,444
	Non-zero	8,342	9,205	10,495
<i>C_RT</i>	Max	10	9.5	10
	Mean	0.97	1.04	1.36
	Zero	17,597	16,734	15,444
	Non-zero	8,342	9,205	10,495
<i>Ctrl</i>	Max	7.56	6.78	7.19
	Mean	3.54	3.40	3.41

Table 5.14 shows that the third loop of AV operation had the highest *PRN*, with a mean of 4.36, and the highest non-zero *PRN* occurrence, 10,495, due to the highest environmental risk (*C\_RT* mean of 1.36). This meant that the AV did not perform sufficient safety actions for the third loop by lowering the *Ctrl* (mean of 3.41) further in order to lower the effects of *C\_RT* for the third loop. Therefore, more safety improvements are needed for the third loop. The outcome of DARA demonstrates the ability to identify safety improvements even at macro levels by comparison across different iterations of AV operations.

The overview results confirm the characteristics of *PRN* as follows: 1) *PRN* is zero when *C\_RT* is zero, and 2) *Ctrl* is always non-zero since the AV is continually operating unless the AV supply is turned off. The DARA outcomes, including *PRN*, *C\_RT*, and *Ctrl*, are used for comparative statistical analysis to identify if more

### 5.3 Verification of DARA with real-world test routes

safety actions are needed for different iterative loops of a fixed AV route. The next section illustrates an alternative method to determine the *PRN* rating for a particular route if the default guideline in Table 5.2 is not preferred.

#### 5.3.1 Determination of *PRN* ratings through statistical methods

This section describes a method for determining *PRN* ratings using statistical methods [137]. The method involves calculating the percentile rank from the results of three test loops. The goal is to map the 50th percentile to the threshold for low *PRN* and the 95th percentile to the threshold for middle *PRN*. *PRN* values beyond the 95th percentile are considered high *PRN*. To identify the thresholds, the zero *PRN* values are first removed from the outcomes, as the focus is on non-zero *PRN*s. The *PRN* values are then sorted in ascending order (x-axis) for each loop, with their frequency of occurrence plotted on the y-axis. Figure 5.23, Figure 5.24 and Figure 5.25 illustrate the ascending order of the non-zero *PRN*s, with the 50th and 95th percentiles indicated.

Figure 5.23, Figure 5.24 and Figure 5.25 display a similar trend in *PRN* numbers across different loops. Based on this, for the iterative loop of a fixed route, the threshold for low *PRN* can be set at the 50th percentile, and the threshold for middle *PRN* can be set at the 95th percentile.

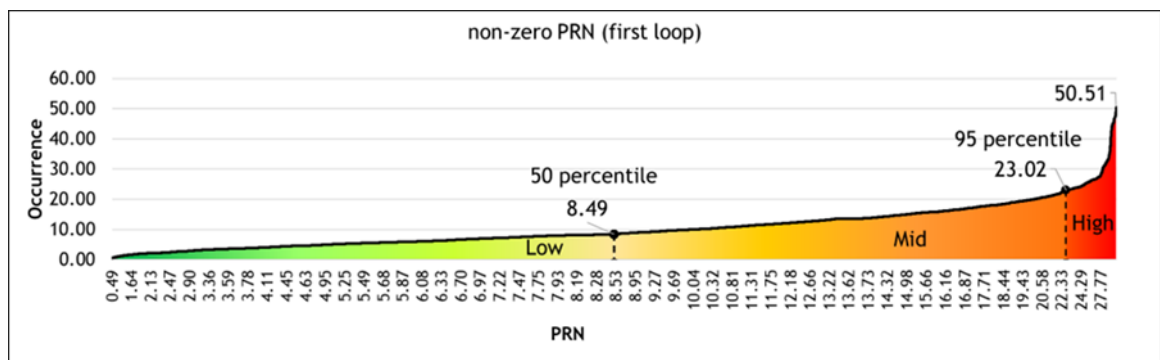


Figure 5.23 Non-zero *PRN* distribution for the first loop

5.3 Verification of DARA with real-world test routes

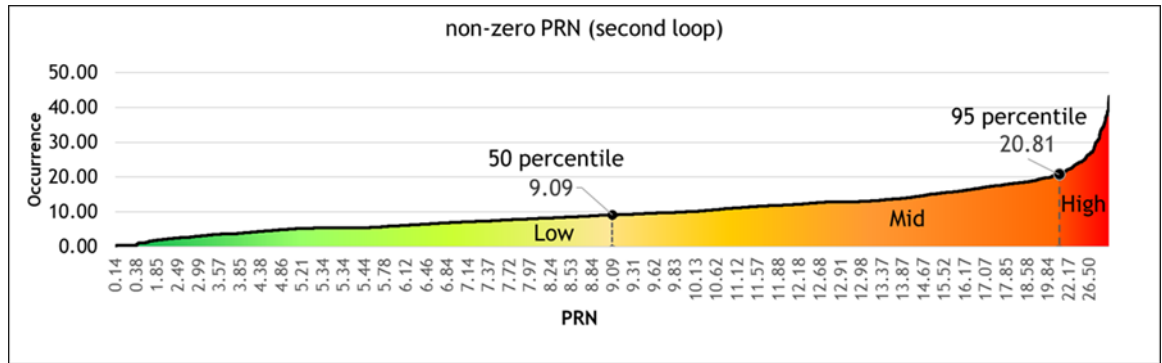


Figure 5.24 Non-zero PRN distribution for the second loop

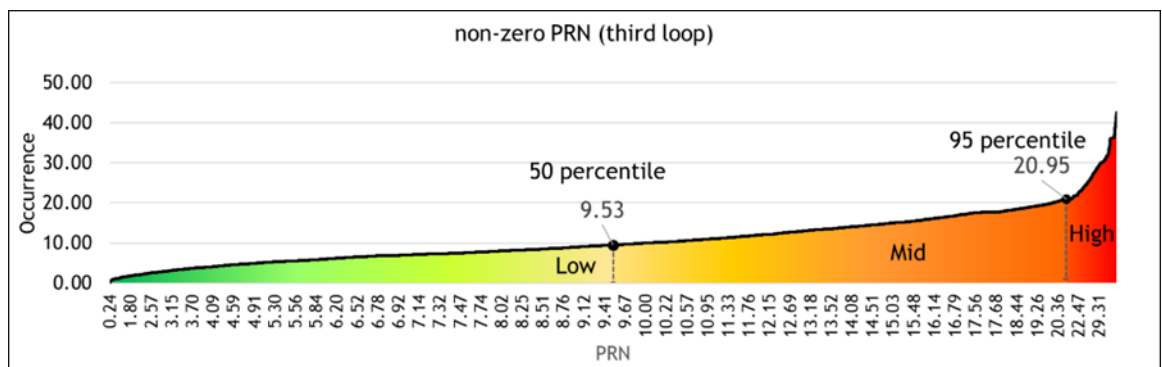


Figure 5.25 Non-zero PRN distribution for the third loop

Table 5.15 summarises all the values from the figures for easier interpretation, with the low PRN threshold set at 9.02 and the middle PRN threshold set at 21.59, after averaging the results. Any PRN above 21.59 is considered high. This statistical determination of the PRN rating threshold aligns with close proximity (less than 10% variation) compared to the guideline provided in Table 5.2. Therefore, this process can be applied to obtain a statistical method for determining the thresholds for low, middle, and high PRN for any AV route with historical data.

Table 5.15 PRN rating thresholds

Statistics	First loop	Second loop	Third loop	Threshold	Guideline
50th percentile	8.48	9.08	9.52	<b>9.02</b>	<b>10.00</b>
95th percentile	23.01	20.81	20.95	<b>21.59</b>	<b>20.00</b>



### 5.3.2 Scenario A, first loop with rated high PRN

This section illustrates different scenarios captured to verify the outcomes of DARA against the ground truth and the measured AV controls in response to the detected risk. To achieve this, each scenario contains the traffic landscape, the DARA application scene, DARA outcomes, and recommended safety actions for subsequent and future iterations to improve *PRN* in a recursive manner.

Scenario A depicts the AV making a right turn from the main road into a smaller road where a pedestrian and vehicles were detected. This scenario was rated as high *PRN*, exceeding the threshold of 20 (guideline from Table 5.2).

Table 5.16 Scenario A first loop with high *PRN* rating

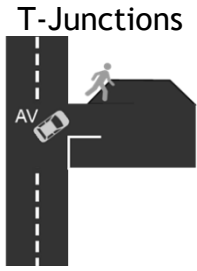

 <p>(a) Scenario with T-junction</p>	 <p>(b) DARA application scene</p>
<p><math>PRT = 9.0, VRT = 13.0</math>  <math>B_n = 0, Th_n = 0.8, St_n = 1.0, Sp_n = 0.16</math>          (weights set at 10)  <math>C_{RT} = 7.75, Ctrl = 6.518,</math>  <math>PRN = 50.513</math></p> <p>(c) DARA outcomes</p>	<p><math>PRT = 9.0, VRT = 6.0</math>  <math>B_n = 0, Th_n = 0.8, St_n = 1.0, Sp_n = 0.16</math>          (weights set at 10)  <math>C_{RT} = 7.50, Ctrl = 6.518,</math>  <math>PRN = 48.885</math></p> <p>(d) DARA ground truth</p>

Table 5.16 (a) shows a T-junction where the AV turned right, and Table 5.16 (b) shows a pedestrian was detected in close proximity to the AV with a moving vehicle some distance away. The AV made a sharp turn with strong steering and high throttle but at low speed. In this scenario, the *PRN* outcome was 50.513, as shown in Table 5.16 (c), while the *PRN* ground truth was 48.885, as shown in Table

## 5.3 Verification of DARA with real-world test routes

5.16 (d). The main difference lies in  $C_{RT}$ , where the inaccuracy is in the object detection and scene segmentation accuracy. The accuracy of the  $C_{RT}$  is 96.6%, which is related to the accuracy of YOLOv5s + mapping. The pedestrian was correctly detected within row 2 of the road region, but the boundaries between the pavement and the road were not clearly defined. The difference between the DARA outcomes and ground truth  $PRN$  was due to the “False positive” detection of parked vehicles onto the row 4 of the road region. Nevertheless, both results for this scenario still incurred a high  $PRN$  rating ( $> 21.59$ ). The  $Ctrl$  for ground truth and DARA were identical since no abnormality was assumed. The wide steering implied that a late turning occurred at a low speed but with a high throttle. The DARA outcomes provided these interpretations into a single  $PRN$ . The  $PRN$  for this scenario was rated as high and act as a trigger for the recommended AV’s safety actions for subsequent loops.

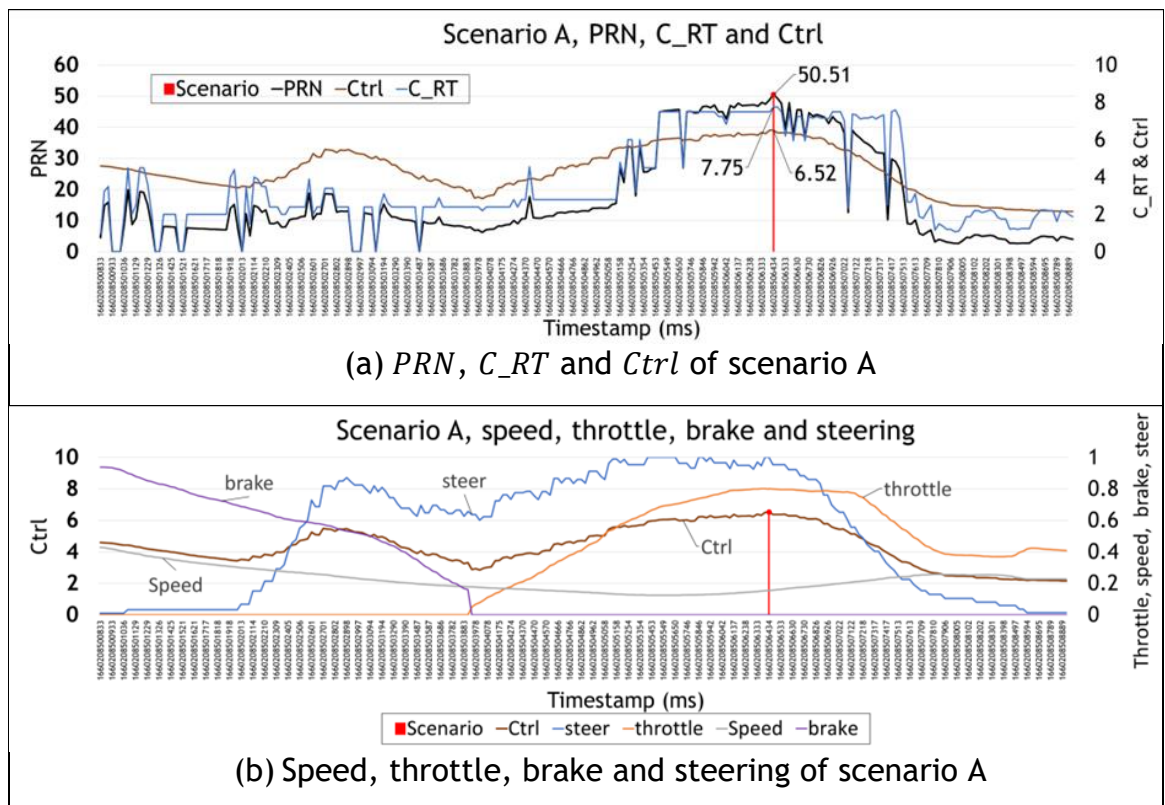


Figure 5.26 Scenario A's  $PRN$ ,  $C_{RT}$ ,  $Ctrl$  and parametric data

Although ReRAF does not provide automated safety recommendations, the DARA outcomes can be used to identify safety actions. For example, Figure 5.26 (a) indicates that the highest  $PRN$  occurred when the AV was closest to the

### 5.3 Verification of DARA with real-world test routes

pedestrian, as marked by the scenario as a red line. The peak *PRN* was a result of the peak *Ctrl* and *C\_RT*. *Ctrl* increased due to the rising throttle and the sharp steering angle of a sudden right turn. The high *PRN* indicated that further improvements could be made to the inherent safety actions for safer AV operations.

#### **Scenario A, recommended safety actions with simulated *PRN***

Therefore, to further enhance AV safety, it is recommended to delay the right turn at the T-junction of the main road for a few seconds while detecting a pedestrian. This delay will allow pedestrians and other vehicles to move away from the AV, reducing the risk of potential collisions. Additionally, during the turn, the throttle should maintain at 0.6 instead of increasing to 0.8, based on Figure 5.26 (b). The steering should also be maintained at 0.7 with a smaller turning angle instead of reaching 1.0 with a large turning angle, as shown in Figure 5.26 (b). Implementing these recommendations will result in improved *PRN* as simulated in Table 5.17. These simulated outcomes represent the improvement in *PRN* for the subsequent loop when a pedestrian is first detected near the T-junction.

Table 5.17 Simulated safety actions for DARA in scenario A

Simulated DARA outcomes	Simulated safety actions
$PRT = 5.0, VRT = 3.0$ $B_n = 0, Th_n = 0.6,$ $St_n = 0.7, Sp_n = 0.16$ (weights set at 10) $C_{RT} = 4.0,$ $Ctrl = 4.386,$ $PRN = 17.546$	<ul style="list-style-type: none"> <li>• Pedestrians moved to the 6<sup>th</sup> row of the RTM.</li> <li>• Vehicle moved to the 8<sup>th</sup> row of the RTM</li> <li>• Throttle stays at 0.6</li> <li>• Steering stays at 0.7 with an earlier turn</li> </ul>

Scenario A verifies that the *PRN* outcome is close to the ground truth, with the main difference being in *C\_RT* due to the precision of YOLOv5's + mapping precision. DARA is used as a trigger for safety actions. If this scenario occurs, there is potential for improved safety measures in the next loop, which can reduce *PRNs*

5.3 Verification of DARA with real-world test routes

to less than 20 in a recursive manner. The *PRN* should decrease over subsequent AV operational loops when safety actions are in place. Therefore, DARA outcomes provide a real-time risk assessment for the AV to use as a tool to trigger safety actions.

**5.3.3 Scenario B, first loop with rated middle *PRN***

Scenario B illustrates a corner scene within the first loop, and the *PRN* had a middle rating since it ranged between 10 and 20. The objective is to use DARA outcomes to measure the AV’s real-time risk assessment as it navigates through the corner.

Table 5.18 Scenario B, first loop with rated middle *PRN*

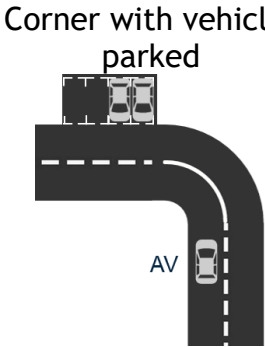

 <p>Corner with vehicles parked</p> <p>AV</p> <p>(a) Scenario with corner</p>	 <p>(b) DARA application scene</p>
<p><math>PRT = 0.0, VRT = 10.0</math>  <math>B_n = 0, Th_n = 0.67, St_n = 0.33, Sp_n = 0.34</math>          (weights set at 10)  <math>C_{RT} = 2.25,</math>  <math>Ctrl = 4.442,</math>  <math>PRN = 11.106</math></p> <p>(c) DARA outcomes</p>	<p><math>PRT = 0.0, VRT = 10.0</math>  <math>B_n = 0, Th_n = 0.67, St_n = 0.33, Sp_n = 0.34</math>          (weights set at 10)  <math>C_{RT} = 2.25,</math>  <math>Ctrl = 4.442,</math>  <math>PRN = 11.106</math></p> <p>(d) DARA ground truth</p>

Table 5.18 (a) shows a corner scenario with the AV moving towards two parked vehicles. The parked vehicles could drive out, leading to sudden AV braking if it disrupts the AV’s path. Table 5.18 (b) shows the DARA application scene from the AV. Table 5.18 (c) illustrates the DARA outcomes having the same results compared to the ground truth with a *PRN* of 11.106 shown in Table 5.18 (d). The

### 5.3 Verification of DARA with real-world test routes

outcome correctly matched the ground truth as it considered the parked area as part of the road region. The *PRN* correctly represented the risky scene and had a middle rating.

#### Scenario B, recommended safety actions with simulated *PRN*

With a middle *PRN* rating, improvements to inherent safety actions are recommended for safer AV operations. For example, in this case, the speed can be reduced to 0.25 (10 km/h), and the throttle can be reduced to 0.6 as the AV navigates the corner. The recommended safety actions lead to an improved *PRN* with the simulated results in Table 5.19. The speed reduction and throttle will improve the safety of the AV when it drives near parked vehicles.

Table 5.19 Simulated safety actions for DARA in scenario B

Simulated DARA outcomes	Simulated safety actions
$PRT = 0.0, VRT = 10.0$ $B_n = 0, Th_n = 0.6, St_n = 0.33, Sp_n = 0.25$ (weights set at 10) $C_{RT} = 2.25, Ctrl = 3.93, PRN = 8.84$	<ul style="list-style-type: none"> <li>• Throttle reduced to 0.6</li> <li>• Speed reduced to 0.25 (10 km/h)</li> </ul>


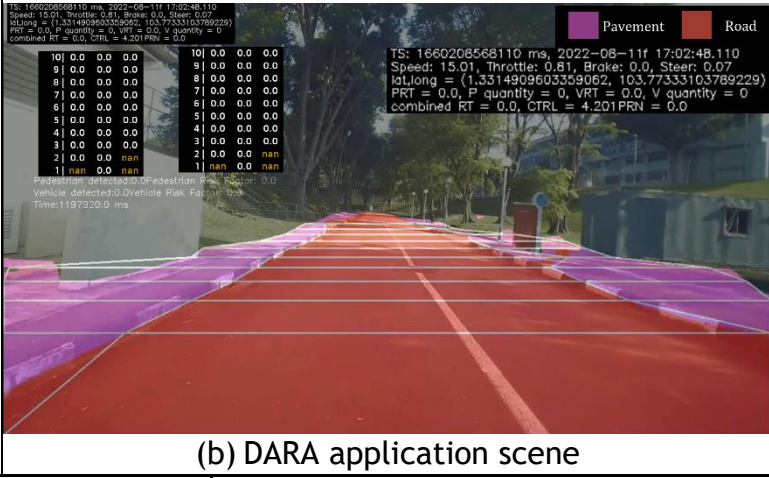
#### 5.3.4 Scenario C, first loop with rated low *PRN*

Scenario C illustrates a straight road scene within the first loop, with zero *PRN*. The outcome of DARA recommends improving efficiency by operating at a higher speed in areas of no risk (no  $C_{RT}$  or zero *PRN*) as opposed to being overly cautious for risk assessment approaches.

Table 5.20 (a) and (b) show the AV was travelling on a straight road without pedestrians or vehicles. Since  $C_{RT}$  was zero, *PRN* would also be zero, as shown in Table 5.20 (c) and (d). Thus, no safety actions were required for this scenario. In this scenario, zero *PRN* suggests the potential to increase the AV's speed to improve efficiency, especially if *PRN* remains zero over several iterations.

5.3 Verification of DARA with real-world test routes

Table 5.20 Scenario C, first loop with rated low PRN

<p style="text-align: center;">Straight road</p>  <p style="text-align: center;">(a) Scenario with corner</p>	 <p style="text-align: center;">(b) DARA application scene</p>
<p style="text-align: center;"><math>PRT = 0.0, VRT = 0.0</math>  <math>B_n = 0, Th_n = 0.81, St_n = 0.07, Sp_n = 0.37</math>                  (weights set at 10)  <math>C_{RT} = 0.0, Ctrl = 4.201, PRN = 0.0</math></p> <p style="text-align: center;">(c) DARA outcomes</p>	<p style="text-align: center;"><math>PRT = 0.0, VRT = 0.0</math>  <math>B_n = 0, Th_n = 0.81, St_n = 0.07, Sp_n = 0.37</math>                  (weights set at 10)  <math>C_{RT} = 0.0, Ctrl = 4.201, PRN = 0.0</math></p> <p style="text-align: center;">(d) DARA ground truth</p>

5.3.5 Scenario D, second loop with rated high PRN

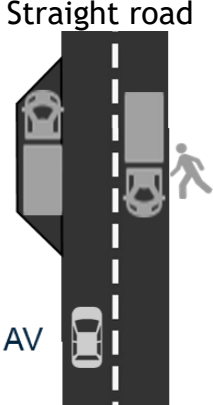

Scenario D depicts a rare event in which the road was not obstructed, but trucks were residing on both sides of the road, one in the bay area and one in the opposite lane. Moreover, a pedestrian was detected on the pavement. The scenario had a high PRN rating of more than 20.

Table 5.21 (a) illustrates scenario with a straight road but with trucks on both sides of the road. The truck on the left was stationary and parked in a bay, while the truck on the right stopped in the opposite lane and blocked the opposing traffic. The DARA application scene is illustrated in Table 5.21 (b). In this scene, the AV would face the risk of driving through a narrow lane and must be able to detect oncoming traffic or pedestrians crossing from the pavement. The PRN was determined as 29.92 in Table 5.21 (c), while the DARA ground truth PRN was 28.82, as shown in Table 5.21 (d). The difference was due to the missed mapping of the truck on the left into the RTM. Thus, causing a difference in  $C_{RT}$ , and the accuracy of  $C_{RT}$  in this scenario was 96.1%. The existing AV operation had a strong throttle and speed, facing risk as it drove into this narrow path. The PRN

5.3 Verification of DARA with real-world test routes

rating for this scenario was high, indicating that an improvement to inherent safety actions is required.

Table 5.21 Scenario D, second loop with rated high PRN

 <p>TS: 1660209826298 ms, 2022-08-11f 17:23:46.298          Speed: 13.91, Throttle: 0.93, Brake: 0.0, Steer: 0.04          lat, long = (1.3339757545092712, 103.77581876489094)          PRT = 5.6, P quantity = 1, VRT = 8.0, V quantity = 1          combined RT = 6.8, CTRL = 4.4PRN = 29.917</p> <p>10] nan nan nan          9] nan nan nan          8] nan nan nan          7] nan 0.0 nan          6] nan 0.0 nan          5] nan 0.0 nan          4] nan 0.0 1.0          3] nan 0.0 0.0          2] nan 0.0 nan          1] nan 0.0 nan</p> <p>AV</p>	 <p>TS: 1660209826298 ms, 2022-08-11f 17:23:46.298          Speed: 13.91, Throttle: 0.93, Brake: 0.0, Steer: 0.04          lat, long = (1.3339757545092712, 103.77581876489094)          PRT = 5.6, P quantity = 1, VRT = 8.0, V quantity = 1          combined RT = 6.8, CTRL = 4.4PRN = 29.917</p> <p>car 0.65          person 0.87</p>
<p>(a) Scenario with a straight road</p> <p><math>PRT = 5.6, VRT = 8.0</math>  <math>B_n = 0, Th_n = 0.93, St_n = 0.04, Sp_n = 0.35</math>          (weights set at 10)  <math>C_{RT} = 6.8,</math>  <math>Ctrl = 4.40,</math>  <math>PRN = 29.92</math></p> <p>(c) DARA outcomes</p>	<p>(b) DARA application scene</p> <p><math>PRT = 5.6, VRT = 15.0</math>  <math>B_n = 0, Th_n = 0.93, St_n = 0.04, Sp_n = 0.35</math>          (weights set at 10)  <math>C_{RT} = 6.55,</math>  <math>Ctrl = 4.40,</math>  <math>PRN = 28.82</math></p> <p>(d) DARA ground truth</p>

Scenario D, recommended safety actions with simulated PRN

The AV should operate at a lower speed and throttle to ensure safe operations. Based on the existing throttle and speed, the recommended speed for the AV can be 0.25 (10 km/h), and the throttle should be set to 0.5. If these safety measures are applied, the simulated PRN is 17.884, as shown in Table 5.22. It is important to note that the speed and throttle should not remain constant, and further reduction is necessary as the AV approaches closer to the truck in case an emergency brake is needed for a pedestrian dashing across the road. It is also important to monitor if the AV can pass through the narrow road lane.

5.3 Verification of DARA with real-world test routes

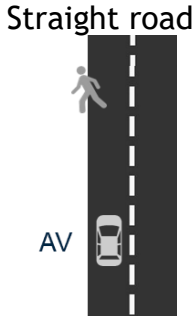

Table 5.22 Simulated safety actions for DARA in scenario D

Simulated DARA outcomes	Simulated safety actions
$PRT = 5.6, VRT = 8.0$ $B_n = 0, Th_n = 0.50, St_n = 0.04, Sp_n = 0.25$ (weights set at 10) $C_{RT} = 6.8, Ctrl = 2.63, PRN = 17.884$	<ul style="list-style-type: none"> <li>Throttle reduced to 0.5</li> <li>Speed reduced to 0.25 (10 km/h)</li> </ul>

5.3.6 Scenario E, second loop with rated middle PRN

Scenario E shows a risk of the AV colliding with a pedestrian in front of the road region. The pedestrian was walking at the side of the road and expected the AV to manoeuvre away from him to avoid collision. This scenario is a good example of using DARA to assess AV's safety action through this exposed risk. The PRN rating of this scenario was considered middle since it exceeded 10 but was less than 20.

Table 5.23 Scenario E, second loop with rated middle PRN

 <p>(a) Scenario with a straight road</p>	 <p>(b) DARA application scene</p>
$PRT = 6.0, VRT = 0.0$ $B_n = 0, Th_n = 0.89, St_n = 0.04, Sp_n = 0.58$ (weights set at 10) $C_{RT} = 3.0, Ctrl = 5.045,$ $PRN = 15.135$ (c) DARA outcomes	$PRT = 6.0, VRT = 15.0$ $B_n = 0, Th_n = 0.89, St_n = 0.04, Sp_n = 0.58$ (weights set at 10) $C_{RT} = 3.0, Ctrl = 5.045,$ $PRN = 15.135$ (d) DARA ground truth



### 5.3 Verification of DARA with real-world test routes

Table 5.23 (a) depicts the scenario of a pedestrian walking on a straight road towards the AV on the road region, as shown in Table 5.23 (b). The scenario was dangerous for the pedestrian, and the AV will have to trigger safety actions to avoid the pedestrian as it came closer. At this moment, shown in Table 5.23 (b), the *PRN* outcome from DARA was 15.135, which matched the ground truth. The operating speed was high at 23.2 km/h with a strong throttle of 0.89. In this scenario, DARA correctly represented the high-risk event with AV approaching a potential collision with a pedestrian on the road without any safety actions yet.

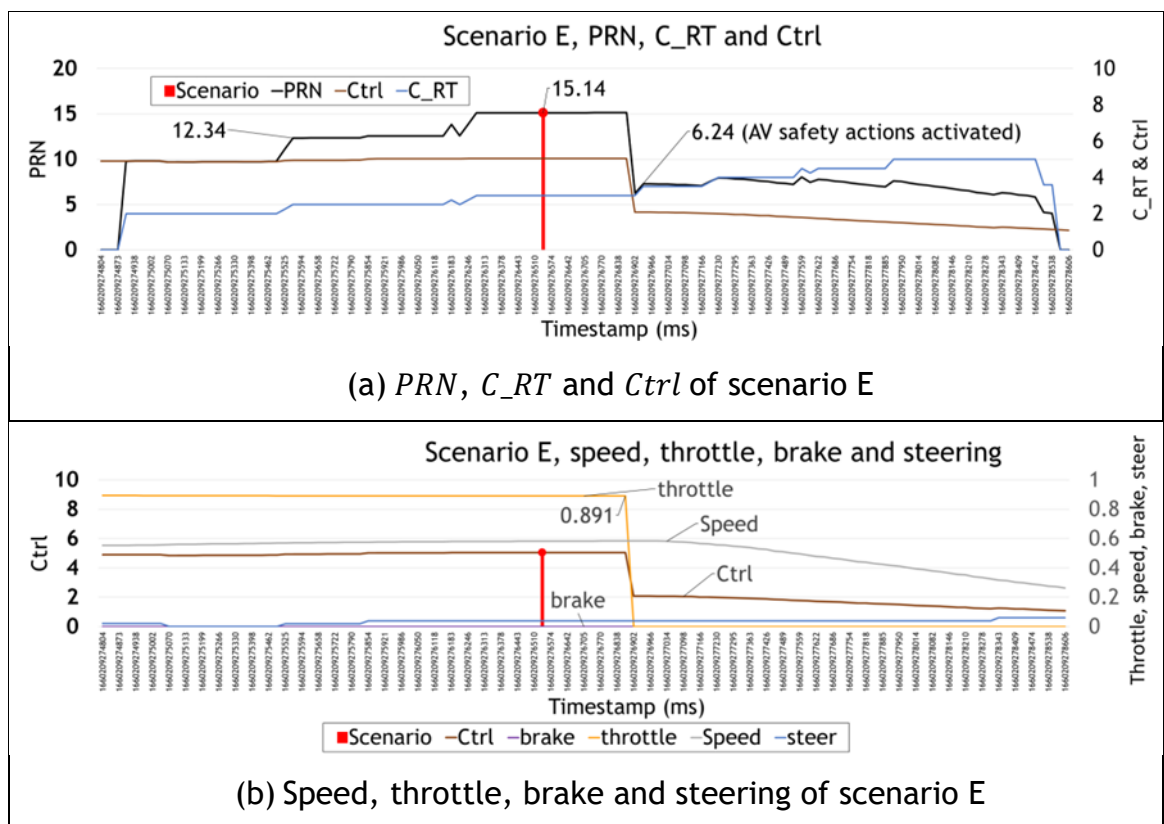


Figure 5.27 Scenario E's *PRN*, *C\_RT*, *Ctrl* and parametric data

This scenario was further evaluated with a couple more scenes to understand the AV's behaviour in mitigating this risk and whether the existing safety actions were sufficient to reduce the *PRN*. Figure 5.27 (a) demonstrated that the AV safety actions did reduce the *PRN*, even though the *C\_RT* was rising (i.e. the AV is moving closer to the pedestrian). The rising *C\_RT* demonstrates the LID behaviour for PRT. The drop in *PRN* resulted in the reduction in *Ctrl*. Figure 5.27 (b) further explains that the reduction in *Ctrl* was achieved by stopping the throttle completely

### 5.3 Verification of DARA with real-world test routes

seconds later from the identified scenario. There was also a slight shift in the steering to avoid the pedestrian.

The DARA outcomes for this scenario show that the inherent AV safety controls had reduced the detected risk from a medium *PRN* rating to a low *PRN* rating. The inherent safety actions were effective in preventing collisions and reducing risk.

#### **Scenario E, recommended safety actions with simulated *PRN***

If further improvements are needed, it is recommended to gradually reduce the throttle starting when *PRN* reaches 10 or 12.34 instead of abruptly cutting the throttle at *PRN* 15.14. This gradual approach will help decrease the *PRN* and *Ctrl*, reducing the risk of collision. No changes are needed for the steering actions. If the recommendations are applied, the simulated *PRN* for this scenario is shown in Table 5.24, where the *PRN* has reduced from a middle to low *PRN* rating. The throttle will have reduced to 0.6, and the speed will have dropped to 14 km/h instead of 23.2 km/h. This scenario demonstrates how DARA can be used for real-time risk assessment of AV operations, and the outcomes can be used to determine future improvements to existing safety measures.

Table 5.24 Simulated safety actions for DARA in scenario E

Simulated DARA outcomes	Simulated safety actions
$PRT = 6.0$ , $VRT = 0.0$ $B_n = 0$ , $Th_n = 0.60$ , $St_n = 0.04$ , $Sp_n = 0.35$ (weights set at 10) $C_{RT} = 3.0$ , $Ctrl = 3.3$ , <b><math>PRN = 9.9</math></b>	<ul style="list-style-type: none"> <li>• Reduce throttle when <math>PRN &gt; 10</math></li> <li>• This results in a reduction in speed</li> </ul>

#### **5.3.7 Scenario F, second loop with rated low *PRN***

Scenario F shows the AV stopped at a T-junction where a vehicle crossed the T-junction in front of the AV. The AV detected the vehicle and continued to brake till the vehicle passed the midpoint of the T-junction. At that point, the AV started moving and made a right turn while keeping a distance from the detected vehicle.

5.3 Verification of DARA with real-world test routes

The *PRN* was rated low since it is below 9.02. This scenario demonstrated how DARA assesses the AV safety controls as it manages its risk when a vehicle travelling in front of it is detected. A detailed analysis using the DARA outcomes was also explained in detail for this scenario.

Table 5.25 (a) shows the scenario where the AV waited for the detected vehicle to drive past the T-junction. Table 5.25 (b) illustrates the DARA application scene where the vehicle passed the “mid-point” of the T-junction. For this scene in Table 5.25 (c) and (d), the DARA outcomes were the same as the ground truth since the detected vehicle was correctly identified and mapped correctly in the RTM. Since the *PRN* was rated low, no safety improvement actions are required for this scenario. Further analysis was conducted to validate the *Ctrl* actions of the AV as the detected vehicle passes the T-junction.

Table 5.25 Scenario F, second loop with rated low *PRN*

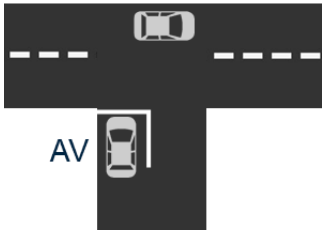

 <p>(a) Scenario with T-junction</p>	 <p>(b) DARA application scene</p>
<p><math>PRT = 0.0</math> , <math>VRT = 7.0</math>  <math>B_n = 0</math> , <math>Th_n = 0.31</math> , <math>St_n = 0.01</math> , <math>Sp_n = 0.0</math>          (weights set at 10)  <math>C_{RT} = 3.5</math> ,  <math>Ctrl = 1.058</math> ,  <b><math>PRN = 3.704</math></b></p> <p>(c) DARA outcomes</p>	<p><math>PRT = 0.0</math> , <math>VRT = 7.0</math>  <math>B_n = 0</math> , <math>Th_n = 0.31</math> , <math>St_n = 0.01</math> , <math>Sp_n = 0.0</math>          (weights set at 10)  <math>C_{RT} = 3.5</math> ,  <math>Ctrl = 1.058</math> ,  <b><math>PRN = 3.704</math></b></p> <p>(d) DARA ground truth</p>

Figure 5.28 (a) shows that the *PRN* stayed around 10 as the *Ctrl* decreases (2.53) with  $C_{RT}$  at 4.00. This decrease in *Ctrl* was due to the high braking, zero throttle

5.3 Verification of DARA with real-world test routes

and almost zero speed, as shown in Figure 5.28 (b). As the detected vehicle passed near the “mid-point” of the T-junction, the AV had a moment of almost zero *PRN* with zero speed, residual steer, zero throttles and zero brakes, as shown in Figure 5.28 (a) and (b). As the detected vehicle passed the AV, the *PRN* increased as the AV started to move and speed up while maintaining a distance from the detected vehicle with a low *PRN* not exceeding 8.

This scenario shows that DARA performs a detailed risk assessment of the AV in real time using *PRN* and its outcomes. In this case, no further improvements in safety actions are required for subsequent similar events. The only minor adjustment is to have gradual braking at point A, as shown in Figure 5.28 (b), instead of harsh braking.

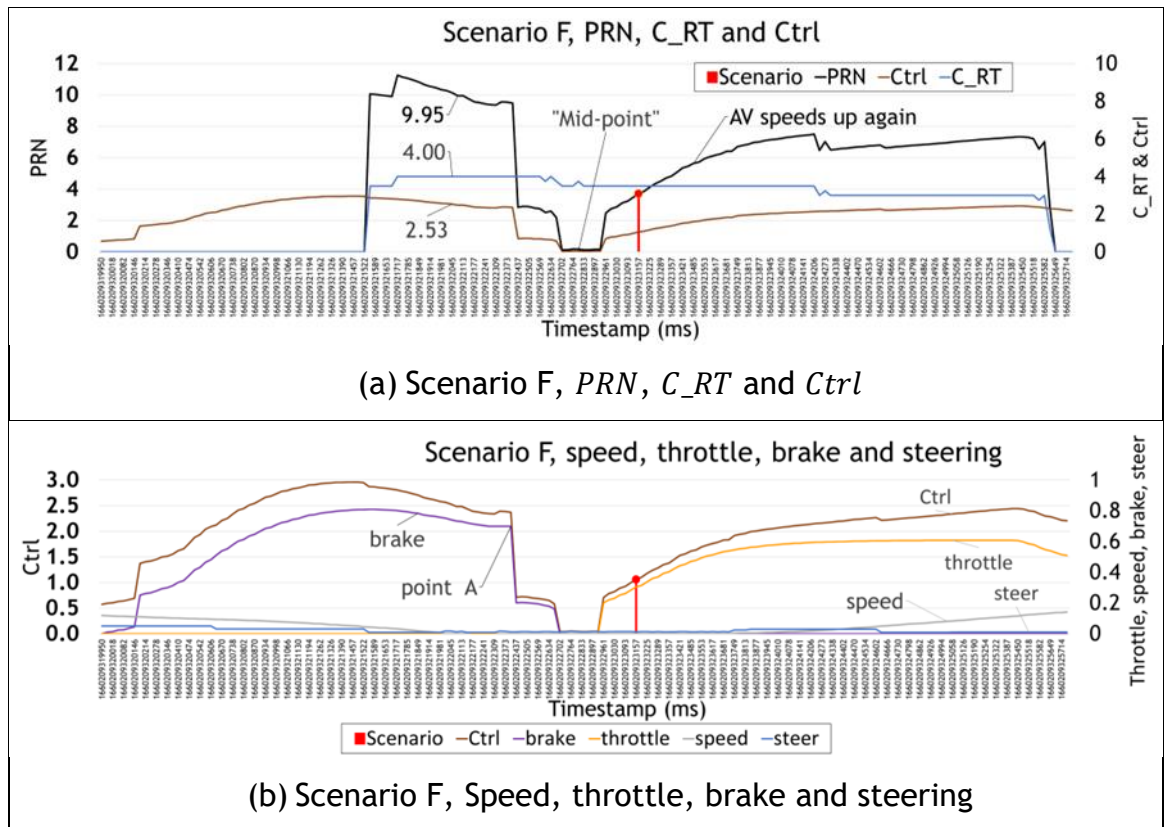


Figure 5.28 Scenario F's *PRN*, *C\_RT*, *Ctrl* and parametric data

5.3.8 Scenario G, third loop with rated high *PRN*

Scenario G describes the AV travelling on a straight road while an oncoming vehicle appeared in the opposite lane. The oncoming vehicle could obstruct the AV's path

5.3 Verification of DARA with real-world test routes

since there is no barrier between the two lanes. This scenario shows that the *PRN* was higher than 20, indicating a high *PRN* rating.

Table 5.26 (a) shows the scenario where the AV came close to the vehicle travelling in the opposite lane. If each vehicle travels within its lane, the risk would be minimal. However, as there is no barrier between the opposing lanes, there could be a potential risk where the vehicle could drive out of its lane, especially when the vehicle comes close to the AV, as shown in Table 5.26 (b). Thus, Table 5.26 (c) and (d) shows that the DARA algorithm indicates a *PRN* of 22.178 that matched the intended ground truth. The high *PRN* was mainly caused by the high *Ctrl*.

Table 5.26 Scenario G, third loop with rated high *PRN*


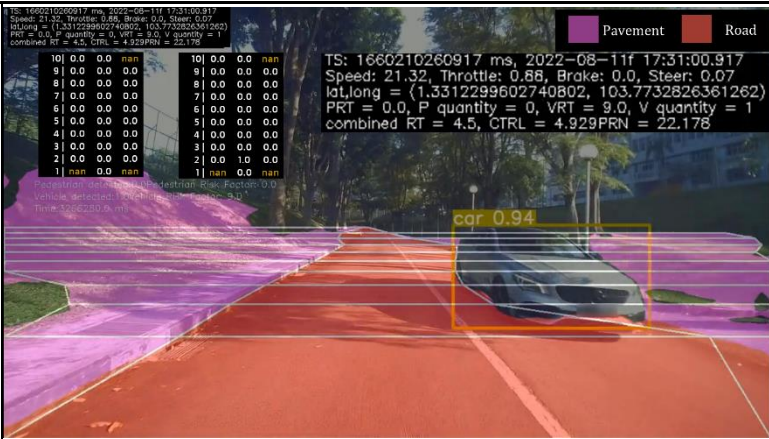
<p style="text-align: center;">Straight road</p>  <p style="text-align: center;">(a) Scenario with straight road</p>	 <p style="text-align: center;">(b) DARA application scene</p>
<p style="text-align: center;"><i>PRT</i> = 0.0 , <i>VRT</i> = 9.0  <i>B<sub>n</sub></i> = 0, <i>Th<sub>n</sub></i> = 0.88, <i>St<sub>n</sub></i> = 0.07, <i>Sp<sub>n</sub></i> = 0.53                      (weights set at 10)  <i>C<sub>RT</sub></i> = 4.5,  <i>Ctrl</i> = 4.929,  <b><i>PRN</i> = 22.178</b></p> <p style="text-align: center;">(c) DARA outcomes</p>	<p style="text-align: center;"><i>PRT</i> = 0.0 , <i>VRT</i> = 9.0  <i>B<sub>n</sub></i> = 0, <i>Th<sub>n</sub></i> = 0.88, <i>St<sub>n</sub></i> = 0.07, <i>Sp<sub>n</sub></i> = 0.53                      (weights set at 10)  <i>C<sub>RT</sub></i> = 4.5,  <i>Ctrl</i> = 4.929,  <b><i>PRN</i> = 22.178</b></p> <p style="text-align: center;">(d) DARA ground truth</p>

Figure 5.29 indicates that the *C<sub>RT</sub>* increased as the detected vehicle approached the AV, while the *Ctrl* remained the same. The *Ctrl* was maintained at a speed of 21.32 km/h and a high throttle of 0.88. The spikes in Figure 5.29 were caused by the precision of YOLOv5s, where object detection is not as accurate when the

5.3 Verification of DARA with real-world test routes

objects are small and far from the AV. Object detection has higher precision as the object comes close to the middle of the scene.

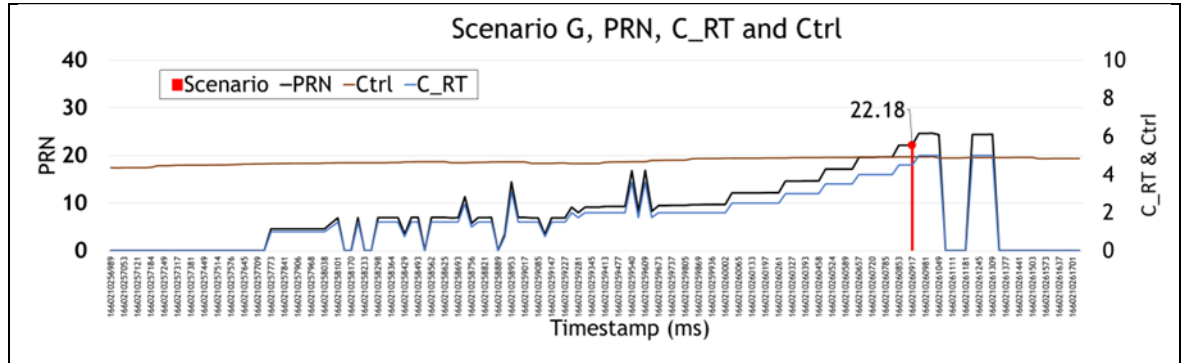


Figure 5.29 Scenario G, PRN, C\_RT and Ctrl

**Scenario G, recommended safety actions with simulated PRN**

In this scenario, the recommendation is to cut the throttle when the PRN reaches 10. Once the vehicle passes the AV without any risk of collision, the AV can resume the throttle and vehicle speed. If the recommendation is applied for the subsequent round, the PRN can be reduced to 9.0, as shown in Table 5.27, from a high to low PRN rating.

Table 5.27 Simulated safety actions for DARA in scenario G

Simulated DARA outcomes	Simulated safety actions
$PRT = 0.0, VRT = 9.0$ $B_n = 0, Th_n = 0.0, St_n = 0.07, Sp_n = 0.53$ (weights set at 10) $C_{RT} = 4.5,$ $Ctrl = 2.0,$ $PRN = 9.0$	<ul style="list-style-type: none"> <li>Cut the throttle when <math>PRN &gt; 10</math></li> </ul>

**5.3.9 Scenario H, third loop with rated middle PRN**

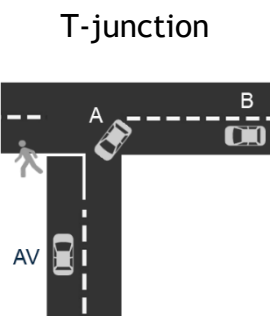

Scenario H illustrates the AV approaching a T-junction and stopping at the pocket with a pedestrian on the left while a vehicle turned from the main road into the AV path. The AV operated safely, as its original intention was to stop at the pocket, which reduced the risk at this T-junction. However, a second vehicle started to turn into the AV path as soon as the first vehicle passed the AV. The

5.3 Verification of DARA with real-world test routes

scenario uses DARA to evaluate the AV's risk assessment. The PRN of the scenario was given a middle rating.

Table 5.28 (a) depicts the AV approaching the T-junction's pocket from the minor road. As the AV moved towards the pocket, a pedestrian started to cross from the road to the pavement, while simultaneously, a vehicle turned from the main road into the minor road, as illustrated in Table 5.28 (b). Both the DARA outcomes and the ground truth aligned in this scene, as indicated in Table 5.28 (c) and (d). The significance of this scenario extends beyond the scene, as shown in Table 5.28 (b). Once the AV reached the pocket, vehicle A passed the AV in the opposite lane into the minor road, and seconds later, vehicle B also turned into the minor road. Therefore, a more comprehensive analysis using DARA outcomes can be used to verify if the AV is implementing appropriate safety actions for this scenario.

Table 5.28 Scenario H, third loop with rated middle PRN

 <p>(a) Scenario with T-junction</p>	 <p>(b) DARA application scene</p>
<p><math>PRT = 7.0</math> , <math>VRT = 8.0</math>  <math>B_n = 0</math> , <math>Th_n = 0.24</math> , <math>St_n = 0.03</math> , <math>Sp_n = 0.21</math>          (weights set at 10)  <math>C_{RT} = 7.5</math> ,  <math>Ctrl = 1.599</math> ,  <b><math>PRN = 11.991</math></b></p> <p>(c) DARA outcomes</p>	<p><math>PRT = 7.0</math> , <math>VRT = 8.0</math>  <math>B_n = 0</math> , <math>Th_n = 0.24</math> , <math>St_n = 0.03</math> , <math>Sp_n = 0.21</math>          (weights set at 10)  <math>C_{RT} = 7.5</math> ,  <math>Ctrl = 1.599</math> ,  <b><math>PRN = 11.991</math></b></p> <p>(d) DARA ground truth</p>

## 5.3 Verification of DARA with real-world test routes

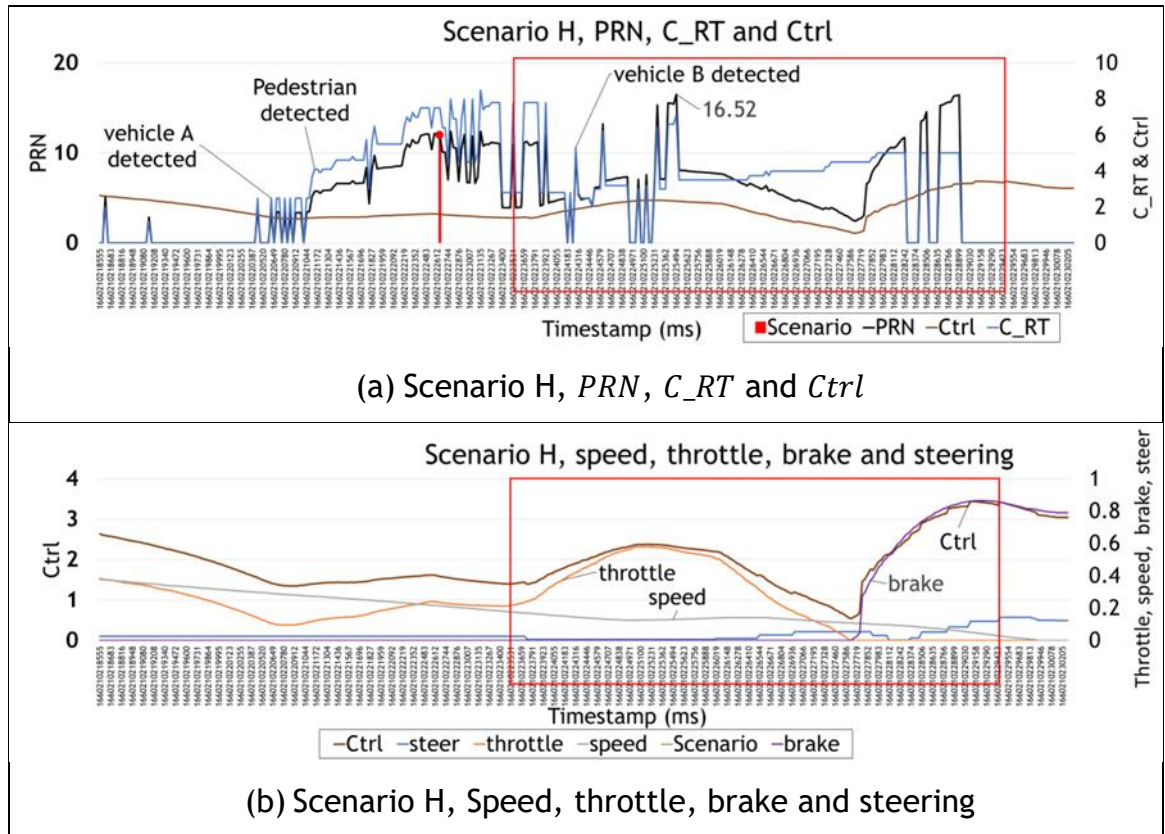
Figure 5.30 Scenario H's *PRN*, *C\_RT*, *Ctrl* and parametric data

Figure 5.30 (a) shows that when vehicle A was detected, the AV deployed inherent safety actions by reducing the throttle. Alternatively, the reduction in throttle could also be due to AV slowing down as it approached the pocket of the T-junction. However, when the pedestrian was detected, the *C\_RT* raised the *PRN* slightly above 10. The increase in *C\_RT* was due to a pedestrian and vehicle A moving closer to the AV. There was also a slight increase in *Ctrl*, which was contributed by the increase in throttle, as shown in Figure 5.30 (b). The "red box" depicts the focus of this scenario, where improvements to inherent safety actions are needed. The "red box" illustrates the scene where *Ctrl* increased when the second vehicle (vehicle B) was detected before turning into the minor road, as shown in Figure 5.30 (a). This increase in *Ctrl* was due to the increased throttle by the AV moving ahead and attempted to turn right. During this event ("red box"), the AV detected the second vehicle (vehicle B) and deployed sudden braking to reduce the speed effect of the throttle. This sudden throttle and braking event between vehicles A and B caused the elevated *PRN* with *Ctrl*. Due to the low speed, the risk was not high and thus *PRN* did not reach a high rating.



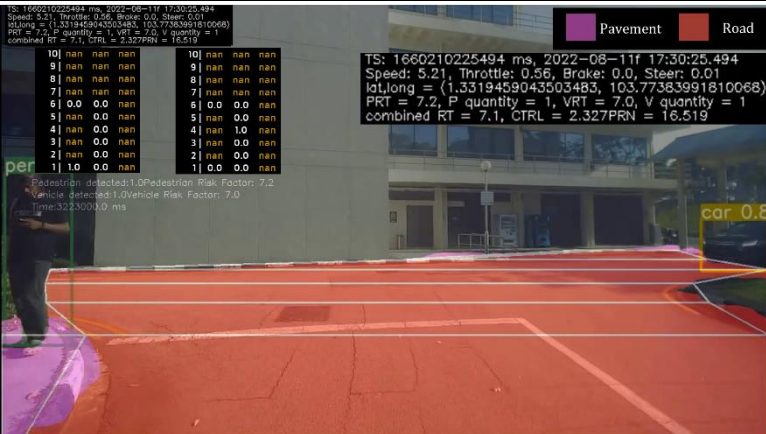
### 5.3 Verification of DARA with real-world test routes

The outcome of DARA for this scenario demonstrated its ability to perform a real-time risk assessment of the AV controls with the detected environmental risk. This is represented by *PRN*, and detailed analyses were further investigated with *C\_RT* and *Ctrl*. The AV safety actions in this scenario were correctly deployed for vehicle A, and the pedestrian was detected, but further improvements to the inherent safety actions are needed when vehicle B is detected.

#### Scenario H, recommended safety actions with simulated *PRN*

Potential improvements are suggested when vehicle B is detected. A peak *PRN* of 16.52 was shown in Figure 5.30 (a). The peak was due to the pedestrian detected on the pavement at the point nearest to the AV, while vehicle B was detected before the turn. Table 5.29 (a) also verified that the *PRN* was high due to the elevated *Ctrl*. Table 5.29 (b) represents the illustrated *PRN* 16.52 scene. Thus, a reduction in throttle when vehicle B is detected, eliminates the need for sudden breaking at a later time.

Table 5.29 “Red box” scene for scenario H

<p> <math>PRT = 7.2</math> , <math>VRT = 7.0</math>  <math>B_n = 0</math> , <math>Th_n = 0.56</math> ,  <math>St_n = 0.01</math> , <math>Sp_n = 0.13</math>            (weights set at 10)  <math>C_{RT} = 7.1</math> ,  <math>Ctrl = 2.327</math> ,  <math>PRN = 16.521</math> </p> <p>(a) DARA outcome at peak <i>PRN</i> when vehicle B is detected</p>	 <p> <small>TS: 1660210225494 ms, 2022-08-11T 17:30:25.494</small>  <small>Speed: 5.21, Throttle: 0.56, Brake: 0.0, Steer: 0.01</small>  <small>lat, long = (1.3319459043503483, 103.77383991810068)</small>  <small>PRT = 7.2, P quantity = 1, VRT = 7.0, V quantity = 1</small>  <small>combined RT = 7.1, CTRL = 2.327, PRN = 16.519</small> </p> <table border="1"> <tbody> <tr><td>10  nan</td><td>nan</td><td>nan</td><td>nan</td><td>10  nan</td><td>nan</td><td>nan</td></tr> <tr><td>9  nan</td><td>nan</td><td>nan</td><td>nan</td><td>9  nan</td><td>nan</td><td>nan</td></tr> <tr><td>8  nan</td><td>nan</td><td>nan</td><td>nan</td><td>8  nan</td><td>nan</td><td>nan</td></tr> <tr><td>7  nan</td><td>nan</td><td>nan</td><td>nan</td><td>7  nan</td><td>nan</td><td>nan</td></tr> <tr><td>6  0.0</td><td>0.0</td><td>nan</td><td>nan</td><td>6  0.0</td><td>0.0</td><td>nan</td></tr> <tr><td>5  nan</td><td>0.0</td><td>nan</td><td>nan</td><td>5  nan</td><td>0.0</td><td>nan</td></tr> <tr><td>4  nan</td><td>0.0</td><td>nan</td><td>nan</td><td>4  nan</td><td>1.0</td><td>nan</td></tr> <tr><td>3  nan</td><td>0.0</td><td>nan</td><td>nan</td><td>3  nan</td><td>0.0</td><td>nan</td></tr> <tr><td>2  nan</td><td>0.0</td><td>nan</td><td>nan</td><td>2  nan</td><td>0.0</td><td>nan</td></tr> <tr><td>1  1.0</td><td>0.0</td><td>nan</td><td>nan</td><td>1  0.0</td><td>0.0</td><td>nan</td></tr> </tbody> </table> <p> <small>Pedestrian detected: 1.0, Pedestrian Risk Factor: 7.2</small>  <small>Vehicle detected: 1.0, Vehicle Risk Factor: 7.0</small>  <small>Time: 32.3000.0 ms</small> </p> <p>(b) DARA application scene</p>	10  nan	nan	nan	nan	10  nan	nan	nan	9  nan	nan	nan	nan	9  nan	nan	nan	8  nan	nan	nan	nan	8  nan	nan	nan	7  nan	nan	nan	nan	7  nan	nan	nan	6  0.0	0.0	nan	nan	6  0.0	0.0	nan	5  nan	0.0	nan	nan	5  nan	0.0	nan	4  nan	0.0	nan	nan	4  nan	1.0	nan	3  nan	0.0	nan	nan	3  nan	0.0	nan	2  nan	0.0	nan	nan	2  nan	0.0	nan	1  1.0	0.0	nan	nan	1  0.0	0.0	nan
10  nan	nan	nan	nan	10  nan	nan	nan																																																																	
9  nan	nan	nan	nan	9  nan	nan	nan																																																																	
8  nan	nan	nan	nan	8  nan	nan	nan																																																																	
7  nan	nan	nan	nan	7  nan	nan	nan																																																																	
6  0.0	0.0	nan	nan	6  0.0	0.0	nan																																																																	
5  nan	0.0	nan	nan	5  nan	0.0	nan																																																																	
4  nan	0.0	nan	nan	4  nan	1.0	nan																																																																	
3  nan	0.0	nan	nan	3  nan	0.0	nan																																																																	
2  nan	0.0	nan	nan	2  nan	0.0	nan																																																																	
1  1.0	0.0	nan	nan	1  0.0	0.0	nan																																																																	

If the suggested safety improvements are made with the throttle reduced to 0.25, the speed will also slow down. Thus, the simulated *PRN* will change from 16.521 to 8.52, as shown in Table 5.30, lowering the corresponding *PRN* rating from middle to low.

5.3 Verification of DARA with real-world test routes



Table 5.30 Simulated safety actions for DARA in “red box” scenario H

Simulated DARA outcomes	Simulated safety actions
$PRT = 7.2$ , $VRT = 7.0$ $B_n = 0$ , $Th_n = 0.25$ , $St_n = 0.01$ , $Sp_n = 0.10$ (weights set at 10) $C_{RT} = 7.1$ , $Ctrl = 1.2$ , $PRN = 8.52$	<ul style="list-style-type: none"> <li>Reduce the throttle to 0.25</li> <li>Speed will also be reduced to 4km/h.</li> </ul>

5.3.10 Scenario I, third loop with rated low PRN

Scenario I illustrates the AV moving on a straight road with a pedestrian walking across the pavement region. This scenario uses DARA to evaluate a typical case where the AV should not be overly conservative in reducing or triggering safety actions as the pedestrian had already walked out of the road region. Thus, the PRN of the scenario was assigned a low rating.

Table 5.31 Scenario H, third loop with rated low PRN

 <p>(e) Scenario with T-junction</p>	 <p>(f) DARA application scene</p>
<p>(g) DARA outcomes</p> $PRT = 5.0$ , $VRT = 0.0$ $B_n = 0$ , $Th_n = 0.7$ , $St_n = 0.06$ , $Sp_n = 0.12$ (weights set at 10) $C_{RT} = 2.5$ , $Ctrl = 2.922$ , $PRN = 7.304$	<p>(h) DARA ground truth</p> $PRT = 5.0$ , $VRT = 0.0$ $B_n = 0$ , $Th_n = 0.7$ , $St_n = 0.06$ , $Sp_n = 0.12$ (weights set at 10) $C_{RT} = 2.5$ , $Ctrl = 2.922$ , $PRN = 7.304$

## 5.3 Verification of DARA with real-world test routes

Table 5.31 (a) and (b) depict the AV on a straight road with pedestrians residing on the 5<sup>th</sup> row of the road region. Therefore, the AV was travelling at a low speed but with high throttle since it was 30 m away from the pedestrians. DARA outcomes and ground truth were matched, as shown in Table 5.31 (c) and (d). Further scenes are analysed using DARA to evaluate the pedestrian movement and if the AV took any safety actions related to this movement.

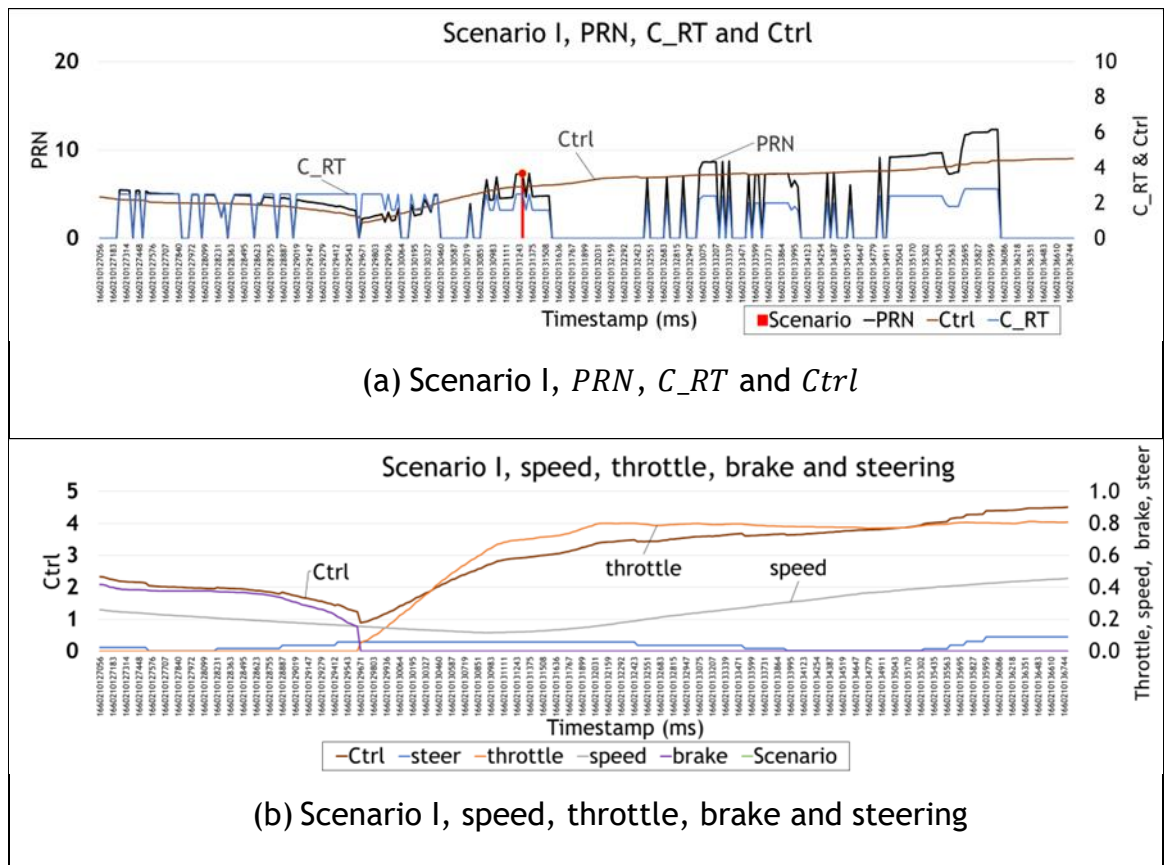


Figure 5.31 Scenario I's PRN, C\_RT, Ctrl and parametric data

Figure 5.31 (a) shows that  $C_{RT}$  remains below 6.0 as the AV travelled straight, thus implying that the pedestrian should be walking away from the AV and moving out of the RTM. Moreover, there were no inherent safety actions triggered, proven by the increase in  $Ctrl$ . The increase in  $Ctrl$  was due to the increased in throttle shown in Figure 5.31 (b). The only minor improvement is to lower the throttle, shown in Figure 5.31 (b), at the tail end of this scenario to prevent the  $PRN$  from exceeding 10 to reduce risk (i.e. if the pedestrian decides to turn around). Other than that, no critical safety actions are required in this scenario.

Similarly, the DARA outcomes for this scenario demonstrated its ability to assess if the AV's safety actions are overly conservative by verifying with the  $C_{RT}$ . If no environmental risks are detected (zero  $C_{RT}$ ), the AV could improve its speed for higher efficiency, but it should be validated with more routes before making the final decision.

### 5.3.11 Verification summary for all scenarios

This section summarises the DARA outcomes for all nine scenarios A to I. Using these nine scenarios, the  $PRN$  vs ground truth, the risk assessment outcomes and the proposed improvements to inherent safety actions with simulated  $PRN$  are summarised in Table 5.32 and Table 5.33.

Table 5.32 shows a summary of the  $PRN$  vs ground truth across the nine scenarios. Two (scenarios A and D) out of the nine scenarios had  $PRN$  differences between the  $PRN$  actual and ground truth with an error range of 3-4%. Similar to STREET, the variance mainly comes from the YOLOv5s object detection and in the case of DARA, the variances were contributed from both YOLOv5s and PSPNet, as indicated in section 5.1.1. These verifications are accomplished based on the scenarios mentioned in chapter 3, which consist of T-junctions, straight roads and corners. Therefore, the results show that DARA can still manage 77.7% of the different scenarios with an accurate  $PRN$ , while the remaining only have a 3-4%  $PRN$  error, despite the challenges on the performance of YOLOv5 and PSPNet.

Table 5.32 Summary of  $PRN$  vs ground truth across the nine scenarios

Scenario	Trip	Scene	$PRN$ rating	$PRN$	Ground truth	Delta
A	First loop	T-junction	High	50.513	48.885	3.33%
B	First loop	Corner	Middle	11.106	11.106	0%
C	First loop	Straight road	Low	0	0	NA
D	Second loop	Straight road	High	29.92	28.82	3.82%
E	Second loop	Straight road	Middle	15.135	15.135	0%
F	Second loop	T-junction	Low	3.704	3.704	0%
G	Third loop	Straight road	High	22.178	22.178	0%
H	Third loop	T-junction	Middle	11.991	11.991	0%
I	Third loop	Straight road	Low	7.304	7.304	0%

### 5.3 Verification of DARA with real-world test routes

Table 5.33 indicates the AV's existing safety actions and proposed improvements in safety actions based on the real-time risk assessment conducted for these scenarios. Four (scenarios A, B, D and G) out of the nine scenarios require improvements to the inherent safety actions, and one of them (scenario H) requires partial improvements, which represents a 50% improvement on the existing safety actions. Table 5.33 also shows that the improvement for each scenario varies from 20% to 65% of the *PRN* to improve safety for AV operations. From these verifications, DARA converts these contextual events and represents them into a *PRN*. Thereafter, the DARA outcomes (*PRN, C\_RT, PRT, VRT, Ctrl*, speed, brake, steer and throttle) are used to analyse for further improvements in AV safety actions. Therefore, in the subsequent route, the AV should reduce their *PRN* if similar scenario is observed using *PRN* as a trigger, thus demonstrating the recursive process in the ReRAF concept.

Table 5.33 AV's risk assessment outcome with improvements to inherent safety actions

Scenario	<i>PRN</i>	Is improvement to inherent safety actions needed? (Yes/No)	Simulated <i>PRN</i> with recommended improvements	<i>PRN</i> reduction
A	50.513	Yes	17.546	65.26%
B	11.106	Yes	8.84	20.40%
C	0	No	NA	NA
D	29.92	Yes	17.884	40.23%
E	15.135	No	Potential minor improvements to 9.9	Potential of 34.58%
F	3.704	No	NA	NA
G	22.178	Yes	9.0	59.42%
H	16.521 (2 <sup>nd</sup> vehicle)	Partial	8.52	48.43%
I	7.304	No	NA	NA

The DARA algorithm has demonstrated its functionality by testing three iterative loops of AV real-world operations. The nine scenarios tested showed that the inaccuracies of the *PRN* results are mainly attributed to the object detection process, which is similar to STREET. The impact of this *PRN* inaccuracy is measured, with a 3-4% error compared to the *PRN* ground truth if it occurs. The error does not impact the decision to make safety improvements, which are evaluated based on *PRN* thresholds, while the safety actions are determined based

on the PRN over time instead of a single instance of PRN. In situations where DARA or ReRAF malfunctions as an independent module for risk assessment, the AV can still rely on ReRAC to receive remote advance warnings, while the inherent AV safety system can still prevent accidents.

## 5.4 Summary

This chapter provides a comprehensive theoretical formulation, evaluation and verification of the novel DARA algorithm within ReRAF. ReRAF is utilised in AVs to conduct an independent end-to-end, real-time risk assessment of the AV by measuring its inherent safety actions based on environmental risk. It converts image information into a quantitative risk measurement without human interpretation. The DARA algorithm employs image risk tagging and mapping in conjunction with control tagging of the AV, to generate a *PRN* representing the AV's risk assessment. Image risk tagging and mapping utilises object detection and scene segmentation, using YOLOv5s and PSPNet to identify contextual risks, such as pedestrians and vehicles, residing at different landscape to form a quantitative risk figure known as *C\_RT*. Control tagging of the AV converts the obtained AV parametric data, such as speed, brake, steer, and throttle, into a single variable known as *Ctrl*. The result of *C\_RT* and *Ctrl* were used to determine *PRN*, which measures the AV's ability to reduce risk through its safety actions when responding to detected risks. Based on the simulated *PRN* scenes, a guideline for *PRN* rating

(low, middle, and high) was provided. Additionally, a visualisation technique known as regional *PRN*, obtained by averaging *PRNs* over a geolocation grid, helps to identify potential hotspots. This chapter evaluates DARA over three unregulated traffic scenarios, such as T-junctions, corners, and straight roads. Furthermore, DARA was verified with three iterative loops of AV operation, consisting of 77,817 scenes. The results illustrate the distribution of risk intervals and statistical comparison at the macro level to identify the specific loop that requires safety action improvements. A statistical method was also illustrated to determine an alternate *PRN* rating, in addition to the defined *PRN* guideline. Lastly, nine scenarios within the three iterative loops of AV operation were used to test the DARA algorithm against its ground truth. The nine scenarios have diverse low,

## 5.4 Summary

---

middle, and high *PRN* ratings at various road scenes. The results show that seven out of nine scenes produced identical results, while only two scenarios showed a 3-4% error. These errors occurred due to the inaccurate object detection process. However, these errors do not impact the decision to make safety improvements, which are evaluated based on the *PRN* thresholds, while the safety actions are determined based on *PRN* over time. DARA uses these nine scenarios to assess AV's safety actions when exposed to these environmental risks. The assessment revealed that for 50% of the scenarios, improvements in the inherent safety action were recommended. When implemented, these resulted in simulated *PRN* improvements ranging from 20% to 65%. The real-world verification results confirm that the DARA algorithm can effectively perform real-time risk assessments for AVs, suggesting potential improvements to their safety actions for future routes. This ability to continuously improve safety actions through real-time risk assessment highlights the advantage of the recursive process within ReRAF.

## Chapter 6

### 6 Conclusion and further work

This section concludes the thesis and discusses future research opportunities based on the findings.

#### 6.1 Conclusion

The current static risk assessment used in the development of AV does not adequately cover all aspects of AV operations. These gaps in coverage include the need to consider real-time evaluation of the AV's safety actions when hazardous risks are detected, insufficient consideration of remote hazardous risks through cooperative mode, and the inability to implement safety improvements for upcoming AV operations without waiting for the next development cycle.

The review of existing risk assessment suggested that environmental considerations, objective measurement of the of hazardous events, and end-to-end solutions are missing. Most notably, a holistic framework for real-time risk assessment and a cooperative mode must be included to address the identified gaps.

This thesis presents a real-time risk assessment framework and a cooperative mode, conceptualised using the baseline of risk assessment standards and



additional requirements from the identified gaps between static and real-time risk assessment. The framework, ReRAF is used within the AV to evaluate the AV's control or safety actions when hazardous risks are detected. The cooperative mode, ReRAC, is used within an infrastructure that assists the AV in providing remote risk measurements and identifying hazardous events and warnings.

The design and development of ReRAC for RSU are explained with illustrations of real-time AV operations. The AV operations focused on detecting hazardous events at unregulated traffic and T-junctions instead of highways and regulated intersections in existing approaches since risk is more prevalent in unregulated traffic and T-junctions. Results of ReRAC demonstrated how the STREET algorithm worked with different probabilistic models (LID, CED, and AED), providing different coverage of the AOI. STREET operates in real time and converts a scene into RT figures, RSU-TTC, Occurrence, hazardous identification, and warnings. The primary focuses of STREET are the RT figures and its normalised RT figures. RT figures provide a summation of the environmental risk within the scene, while normalised RT figures provide the aggregate risk per scene. STREET was tested and proven effective in detecting different pedestrian events in a corner scenario with a total of 97,446 scenes. Furthermore, four real-world events verified the RT figures with the LID model with its ground truth, compared the between LID, CED, and AED, and verified the expected relationship between RSU-TTC, RT figure based on LID, and normalised RT figure based on LID. These quantitative RT figures offer real-time risk values of the scene within the scenario. RSU-TTC offers a time-based countdown to determine the time to collide between the reference location "X" and the detected pedestrian, giving a different perspective on potential collision impact. The formulated hazardous identification and warnings were tested on a T-junction that illustrates its functionality to provide instantaneous event detection of vehicles and pedestrian hazards within the intersection or road section. Additionally, Occurrence is used to verify the selected probability model used for STREET.

The ReRAC outcomes provide different methods of remote warning before the AV arrives at the infrastructure's exact location. These remote warnings aid in

dynamic path planning for the AV. The recursive accumulation of ReRAC outcomes over time can also assist the AV in better path planning. The outcome of STREET, with different probabilistic models, demonstrated how the RT figures with RSU-TTC identify low/high risk scenarios or the presence of pedestrians in the middle of the AOI. The hazard identifications and warnings are also verified, and its functionality is demonstrated in a T-junction. Therefore, the outcome of the RT figure, RSU-TTC and hazard identifications and warnings are provided every 40 ms, proving its end-to-end process at granular levels. With the conversion from camera images into quantitative figures without any human intervention, the STREET process is objective, and the outcome is lightweight with only data and not a series of images. These results conclude the motivation and contributions for ReRAC.

The ReRAF concept design and development in an AV system were explained with illustrations of real-time AV operations. The ReRAF concept uses the DARA algorithm, which combines  $C_{RT}$  and  $Ctrl$  to provide  $PRN$ .  $C_{RT}$  are similar to those RT figures used in ReRAC to detect hazardous events within the scene, except in the ReRAF's case they will dynamically change with the moving landscape.  $Ctrl$  represent the longitudinal and latitudinal control of the AV and the deployed safety actions.  $PRN$  represents the risk measurement of the AV control that corresponds to the detected hazardous events. A guideline for  $PRN$  rating thresholds is provided based on simulated  $PRNs$ . The level of  $PRN$  will determine how safe the AV operates in the presence of hazardous events. As an alternative, a statistical method to determine  $PRN$  rating thresholds was illustrated using past  $PRN$  results, reflecting the proximity between the guideline and the statistical method. The Occurrences of  $PRNs$  were also used to formulate visualisation maps of regional  $PRN$  for the identification of potential hotspots of high  $PRNs$  over iterations of AV operations. ReRAF was tested with three iterative loops of AV operations consisting of 77,817 scenes with the distribution of risk intervals and statistical comparison to identify the loop requiring safety action improvements. The DARA algorithm was analysed by verifying the  $PRN$  outcomes with the ground truth using the scenes within the scenarios identified. The evaluation of AV's control or safety actions were also demonstrated using DARA

algorithm if improvements were needed for subsequent loop within those identified scenarios. Additionally, safety action improvements were provided that illustrate the reduction of *PRN* through simulation. These improvements in safety actions, if deployed for subsequent AV operational loops, will reduce the *PRN*. This continuous improvement of *PRN* over loops illustrates the intention of a recursive process.

The ReRAF with DARA outcomes demonstrated *PRN* risk measurement as an end-to-end process providing granular levels at intervals between 32-50 ms. The *PRN* was determined by the objective process of image conversion into *C\_RT* and AV's parametric control into a single *Ctrl* without any human intervention. The *PRN* with *C\_RT* and *Ctrl* proves that the outcome is lightweight with only quantitative data instead of timestamp images with vehicle data. These results conclude the motivation and contributions of ReRAF.

The results of ReRAC and ReRAF are partially dependent on the object detection process, which can introduce inaccuracies to RT figures and PRN due to occlusion and varying sizes of object detection boxes. These results indicate that the performance is relatively close to industry acceptance, and there is room for further improvement regarding STREET's accuracy. As for the error in DARA accuracy due to the object detection process, this error does not significantly impact the safety actions taken to improve the safety of AV since a period of PRNs is considered instead of a single PRN instance. Furthermore, ReRAC and ReRAF complement each other when one malfunctions. In the extremes, if ReRAC and ReRAF malfunction, the AV with inherent safety systems can still prevent accidents. Without ReRAC and ReRAF deployed, sudden braking or steering events can occur and impact the safety of passengers and other motorists due to abrupt movements.

The combination of ReRAF from the AV perspective and ReRAC from the infrastructure perspective complements each other to derive a "holistic" risk measurement of a given situation. ReRAF uses DARA to provide real-time evaluation of the AV control or safety actions when a hazardous event is detected.

## 6.2 Key benefits

---

Simultaneously, ReRAC uses the STREET algorithm within the RSU to send remote risk and event warnings to the AV before reaching the infrastructure's location. Both ReRAF and ReRAC are objectively processed using an end-to-end approach.

Using the remote risk and event warnings from ReRAC, AV will be able to prevent accidents or potential collisions. On the other hand, ReRAF evaluation served as a trigger for subsequent safety action improvements. As such, the AV operations achieved safety improvements in current and subsequent operations. These cyclic improvements justify the recursive elements of ReRAF and ReRAC over time. The quantitative results from ReRAF and ReRAC can be used to continuously learn and improve the AV's path planning, eliminating the need to wait for the next development cycle. This research concludes the development and verification of ReRAC and ReRAF in real-world scenarios focusing on unregulated traffic that mitigates the existing gaps in static risk assessment for AV operations. Thus, it fulfils the motivation and contribution of this research.

## 6.2 Key benefits

This research presents a novel approach for performing risk assessment in real time AV operations in addition to traditional static risk assessment. The key benefits of having a real-time risk assessment for AV operations are stated below:

- A remote risk measurement with hazard identifications and warnings via ReRAC.

The outcomes of ReRAC provide remote quantitative risk measurement (RT figures) and hazard identification and warnings of the locations beyond the AV path. RSUs installed at certain locations provide ReRAC outcomes to the AV through cooperative mode. This allows AVs to be remotely informed about environmental risks at specific locations and potential events like congestion and accidents. It acts as an extended view for the AV, particularly in areas with limited visibility and the possibility of pedestrians or vehicles being occluded. This remote information enables the AV to react in advance and provide a safer and smoother ride before reaching the RSU location, thereby reducing operational risks.

## 6.2 Key benefits

---

- Evaluation of the AV's inherent safety actions when risks are exposed by ReRAF.

ReRAF outcomes evaluate the inherent safety actions reflected through the AV's control actions when environmental risks are identified. The steering, brake, speed, and throttle responses are measured with the detected risk to provide a *PRN*. *PRN* represents how well the AV reacts to the exposed risk. Furthermore, a *PRN* rating is also devised to prompt AV for improvements in safety action if a middle or high level is determined. This research further suggests improvements in safety action through simulated *PRN* to improve the measured *PRN*. These improvements can be applied for subsequent operations.

- ReRAF and ReRAC improve AV operations recursively.

With ReRAC providing remote risk measurement and hazardous identification and warnings, instantaneous improvements to safer AV operations can be achieved. On the other hand, ReRAF focuses on the subsequent operational route for safety action improvements. Thus, this cyclic process of improvements for existing and subsequent iterations of operational routes illustrates the effects of recursive improvements for safer AV operations.

- ReRAF and ReRAC as a fast and efficient end-to-end solution

ReRAF and ReRAC offer a fast and efficient end-to-end solution. The ReRAC STREET algorithm operates at the RSU and swiftly converts scenes from a camera to quantitative parameters in 30-40ms using an NVIDIA AGX edge system. This quick processing time enables real-time processing at the RSU, with outcomes transmitted to vehicles with minimal communication latency. The latency is under 60ms in a 5G private network environment for providing a remote risk warning and detection of hazardous events.

Meanwhile, the ReRAF DARA algorithm operates as an independent edge system within the AV and takes 60-80ms to convert scenes from a camera to quantitative parameters. The additional time compared to ReRAC is due to the scene

## 6.2 Key benefits

---

segmentation in dynamic landscapes. The outcomes provide *PRN*, *Ctrl* and *C\_RT* that evaluate the control or safety actions of the AV when environmental risks are detected.

- ReRAF acts as a risk measurement device for AV operations that can assist regulatory processes.

ReRAF can be a risk assessment tool for AV operations that provides real-time quantitative measures, focusing on AV operational risk and safety. It enables risk assessment evaluation from a regulatory perspective without companies needing to expose their proprietary algorithms since independent camera(s) and AV's speed, steering, braking and throttle are used to perform this risk assessment.

- ReRAF and ReRAC quantitative outcomes are used to analyse improvements for safety actions.

The ReRAF and ReRAC outcomes enable the AV system to identify and document situations where the AV controls may not be optimal when the *PRNs* are high. In high *PRN* scenarios, the AV's path planning can make minor adjustments using the real-time data of *Ctrl*, brake, speed, steer and throttle to reduce the *PRN* for the next round of operations. These adjustments include and are not limited to: 1) increasing speed or throttle if there have consistently been zero *PRNs* in the past few rounds at a specific time and location, 2) pre-emptively decreasing throttle in regions (hot spots) with consistently high *PRNs* in previous rounds, and 3) utilising ReRAC (RT figure and hazardous events) for early warning in case of persistent events or risks suggesting an alternative route is required.

- The lightweight data of ReRAC allows low latency transmission for V2V

The rapid conversion of scenes to RT figures and parametric data enables low-latency transmission (due to the small data packet) to any vehicle through cooperative mode. The reduction in the overall bandwidth thus offers the potential for the proposed approaches to be deployed on fleets of AVs. The small

data packet also decreases the time needed for sensor data integration and delays in data relay within a V2V context.

### 6.3 Recommendation for future works

It is acknowledged that the research has some limitations and potential improvements to the presented work in the thesis. These are discussed as follows:

- Object detection and Scene segmentation accuracy

The accuracy of ReRAF and ReRAC depends on object detection and semantic segmentation. Both approaches belong to supervised machine learning, where precision and recall increase with more training datasets and better quality in the annotation of the dataset. Industry requirements for such AI-related technology typically demand an F1 score of 90% and above for application products. In this research, ReRAC using object detection has achieved an F1 score of 86% with 150k dataset samples. Therefore, more datasets and improved annotation quality will help it meet the application requirements. As for ReRAF, the default training model has an F1 score of 66%. Hence, training with a larger dataset is required to meet the application requirements. To address existing weaknesses in object detection for smaller-sized objects, new models such as vision transformers need to be investigated, while potential improvements in scene segmentation can be explored with enhanced versions of ICNET or UNET. These advancements will improve the F1 score and pixel accuracy for ReRAF. Additionally, if existing models are used, further exploration of using a filter to remove sudden spikes or dips in the RT figure for one frame can reduce the effect of object detection inaccuracies. Averaging the RT figure across a time period could also nullify the effects of the inaccuracies.

- Use of ReRAC RT figures for risk forecasting for AV and driven vehicles

With ReRAC RT figures, the accumulated time series data can be extended to forecast risk at locations where RSUs are installed. The forecasted traffic risk can be used as advanced pre-emptive safety awareness. This forecasting assists the

### 6.3 Recommendation for future works

---

AV in predicting the traffic at the RSU before they arrive. For example, the traffic situation at an RSU appears uncongested at 6:45 am but becomes congested at 7:00 am. Therefore, the remote information provided by the RSU at 7:00 am to the AV might not be advanced enough to avoid congestion. Thus, ReRAC's risk forecasting can be achieved using real-time training based on recent quantitative data. This means the risk forecasting will provide AV at 6:45 am stating that RSU's location will be congested at 7:00 am. The forecasting will assist the fleet management system to avoid the RSU's location if it knows that upcoming congestion will occur and allows ample time for re-routing. Some initial findings for short-term forecasting using risk tagging data are reported in [138]. This information can be made available to driven vehicles, with tests conducted and reported in the research project [22].

- ReRAF and ReRAC outcomes over a long period of AV operations

This is the next step that can only be completed from the perspective of the AV developer and integration of AV's entire safety actions. It will be interesting to evaluate the eventual impact of ReRAF and ReRAC over periods of AV operations. It is anticipated that with the recursive method, the *PRN* for ReRAF should reduce over time with improved safety actions deployed. It is also possible that further refinement of the weights to ReRAF and ReRAC is necessary to reflect actual operations.



## 7 List of reference

### 7.1 References

- [1] D. Parekh *et al.*, "A Review on Autonomous Vehicles: Progress, Methods and Challenges," *Electronics*, vol. 11, no. 14, p. 2162, 2022. [Online]. Available: <https://www.mdpi.com/2079-9292/11/14/2162>.
- [2] B. Padmaja, C. V. K. N. S. N. Moorthy, N. Venkateswarulu, and M. M. Bala, "Exploration of issues, challenges and latest developments in autonomous cars," *Journal of Big Data*, vol. 10, no. 1, p. 61, 2023/05/06 2023, doi: 10.1186/s40537-023-00701-y.
- [3] Dentons, "Global Guide to Autonomous Vehicles 2023," 2023. [Online]. Available: <https://www.dentons.com/en/insights/guides-reports-and-whitepapers/2023/march/8/global-guide-to-autonomous-vehicles-2023>
- [4] *J3016\_202104 Taxonomy and Definitions for Terms Related to Driving Automation Systems for On-Road Motor Vehicles*, SAE, [https://saemobilus.sae.org/content/j3016\\_202104/](https://saemobilus.sae.org/content/j3016_202104/), 2021. [Online]. Available: [https://saemobilus.sae.org/content/j3016\\_202104/](https://saemobilus.sae.org/content/j3016_202104/)
- [5] S. Schwindt-Drews, K. Storms, S. Peters, and B. Abendroth, "Acceptance and Trust: Drivers' First Contact with Released Automated Vehicles in Naturalistic Traffic," *ArXiv*, vol. abs/2312.08957, 2023.
- [6] M. Liu, J. Wu, C. Zhu, and K. Hu, "A Study on Public Adoption of Robo-Taxis in China," *Journal of Advanced Transportation*, vol. 2020, no. 1, p. 8877499, 2020, doi: <https://doi.org/10.1155/2020/8877499>.
- [7] J. Hatzenbühler, O. Cats, and E. Jenelius, "Transitioning towards the deployment of line-based autonomous buses: Consequences for service frequency and vehicle capacity," *Transportation Research Part A: Policy*

- and Practice*, vol. 138, pp. 491-507, 2020/08/01/ 2020, doi:  
<https://doi.org/10.1016/j.tra.2020.06.019>.
- [8] C. N. Asia, "Driverless bus service begins in Ngee Ann Polytechnic, and it's free," ed, 2023.
- [9] WeRide, "Singapore Launches Autonomous Shuttle Service, WeRide Robobus Becomes a New Attraction at Resorts World Sentosa," ed, 2024.
- [10] T. S. Times, "Driverless taxi accident in China sparks discussions on challenges of autonomous driving tech," in *The Straits Times*, ed, 2024.
- [11] Reuters, "GM's Cruise recalling 950 driverless cars after pedestrian dragged in crash," ed: Reuters, 2023.
- [12] W. E. Forum, "Why autonomous vehicles need a large-systems approach to safety," 18 Jun 2021 2021. [Online]. Available:  
<https://www.weforum.org/agenda/2021/06/autonomous-vehicles-safety-large-systems-approach/>
- [13] *IEC 61508 Functional safety of electrical/electronic/programmable electronic safety-related systems*, IEC, 2010.
- [14] *ISO 26262-1:2018 Road vehicles Functional Safety*, ISO, 2018. [Online]. Available: <https://www.iso.org/standard/68383.html>
- [15] *IEC 60812 Failure modes and effects analysis (FMEA and FMECA)*, IEC, IEC, 2018.
- [16] IEC, "IEC 61882 Hazard and operability studies (HAZOP studies) - Application guide," 2016.
- [17] W. M. D. Chia, S. L. Keoh, A. L. Michala, and C. Goh, "Real-time Recursive Risk Assessment Framework for Autonomous Vehicle Operations," in *2021 IEEE 93rd Vehicular Technology Conference*

- (VTC2021-Spring), 25-28 April 2021, pp. 1-7, doi: 10.1109/VTC2021-Spring51267.2021.9448759.
- [18] *Surface Vehicle Recommended Practice (r) Considerations for ISO 26262 ASIL Hazard Classification*, SAE, 2018.
- [19] N. Merat *et al.*, "The "Out-of-the-Loop" concept in automated driving: proposed definition, measures and implications," *Cognition, Technology & Work*, vol. 21, no. 1, pp. 87-98, 2019/02/01 2019, doi: 10.1007/s10111-018-0525-8.
- [20] W. M. D. Chia, S. L. Keoh, A. L. Michala, and C. Goh, "Dynamically Acquired Risk Assessment for Real-world Autonomous Vehicle operations (ongoing)," *IEEE Transactions on Intelligent Transportation Systems*, 2025.
- [21] W. M. D. C. e. al, "Functional Risk for AV using AI Hybrid Deterministic Method," vol. S\$249,000, ed. Singapore: Singapore Institute of Technology, Ministry of Education, 2019.
- [22] W.M.D. Chia et al, "Real-Time Risk Assessment Assistance for Cooperative Mode (ReRAC) Using V2X for Vehicles and Pedestrian in Urban Conditions," vol. amt S\$1,576,200.00, ed. Singapore: NRF and LTA under its UMGC-L013, 2021-2024.
- [23] W. M. D. Chia, S. L. Keoh, A. L. Michala, and C. Goh, "Infrastructure-Based Pedestrian Risk Tagging Methodology to Support AV Risk Assessment," *IEEE Access*, vol. 10, pp. 71462-71480, 2022, doi: 10.1109/ACCESS.2022.3188306.
- [24] *J3016\_201401 Taxonomy and Definitions for Terms Related to Driving Automation Systems for On-Road Motor Vehicles*, SAE, 2014. [Online]. Available: [https://www.sae.org/standards/content/j3016\\_201401/](https://www.sae.org/standards/content/j3016_201401/)

- [25] S. Khastgir, S. Birrell, G. Dhadyalla, H. Sivencrona, and P. Jennings, "Towards increased reliability by objectification of Hazard Analysis and Risk Assessment (HARA) of automated automotive systems," *Safety Science*, vol. 99, pp. 166-177, 2017/11/01/ 2017, doi: <https://doi.org/10.1016/j.ssci.2017.03.024>.
- [26] *ISO/PAS 21448 Road vehicles - Safety of the intended functionality*, ISO, 2019.
- [27] R. Adler, P. Feth, and D. Schneider, "Safety Engineering for Autonomous Vehicles," in *2016 46th Annual IEEE/IFIP International Conference on Dependable Systems and Networks Workshop (DSN-W)*, 28 June-1 July 2016 2016, pp. 200-205, doi: 10.1109/DSN-W.2016.30.
- [28] C. B. S. T. Molina, J. R. d. Almeida, L. F. Vismari, R. I. R. González, J. K. Naufal, and J. B. Camargo, "Assuring Fully Autonomous Vehicles Safety by Design: The Autonomous Vehicle Control (AVC) Module Strategy," in *2017 47th Annual IEEE/IFIP International Conference on Dependable Systems and Networks Workshops (DSN-W)*, 26-29 June 2017 2017, pp. 16-21, doi: 10.1109/DSN-W.2017.14.
- [29] F. Warg, M. Gassilewski, J. Tryggvesson, V. Izosimov, A. Werneman, and R. Johansson, *Defining Autonomous Functions Using Iterative Hazard Analysis and Requirements Refinement*. 2016, pp. 286-297.
- [30] T. Stolte, G. Bagschik, A. Reschka, and M. Maurer, "Hazard analysis and risk assessment for an automated unmanned protective vehicle," presented at the IEEE Intelligent Vehicles Symposium (IV), Redondo Beach, CA, USA, June 11-14, , 2017.
- [31] G. Bagschik, A. Reschka, T. Stolte, and M. Maurer, "Identification of Potential Hazardous Events for an Unmanned Protective Vehicle," 2018.

- [32] S. Ulbrich, T. Menzel, A. Reschka, F. Schuldt, and M. Maurer, "Defining and Substantiating the Terms Scene, Situation, and Scenario for Automated Driving," in *2015 IEEE 18th International Conference on Intelligent Transportation Systems*, 15-18 Sept. 2015 2015, pp. 982-988, doi: 10.1109/ITSC.2015.164.
- [33] E. Petry, "Hazard Analysis and Risk Assessment According to ISO 26262:2018," Kugler Maag CIE, 2022. [Online]. Available: <https://www.kuglermaag.com/functional-safety/hara/>
- [34] H. M. Fahmy, M. A. A. E. Ghany, and G. Baumann, "Vehicle Risk Assessment and Control for Lane-Keeping and Collision Avoidance at Low-Speed and High-Speed Scenarios," *IEEE Transactions on Vehicular Technology*, vol. 67, no. 6, pp. 4806-4818, 2018, doi: 10.1109/TVT.2018.2807796.
- [35] K. Beckers, M. Heisel, T. Frese, and D. Hatebur, "A structured and model-based hazard analysis and risk assessment method for automotive systems," ed: IEEE, 2013, pp. 238-247.
- [36] X. Wu, X. Xing, J. Chen, Y. Shen, and L. Xiong, "Risk Assessment Method for Driving Scenarios of Autonomous Vehicles Based on Drivable Area," in *2022 IEEE 25th International Conference on Intelligent Transportation Systems (ITSC)*, 8-12 Oct. 2022 2022, pp. 2206-2213, doi: 10.1109/ITSC55140.2022.9922210.
- [37] IEC, "IEC 61025 Fault Tree Analysis," 2006.
- [38] J. Bach, S. Otten, and E. Sax, "Model based scenario specification for development and test of automated driving functions," vol. 2016-, ed: IEEE, 2016, pp. 1149-1155.
- [39] M. Tlig *et al.*, "Autonomous Driving System : Model Based Safety Analysis," in *2018 48th Annual IEEE/IFIP International Conference on Dependable*

- Systems and Networks Workshops (DSN-W)*, 25-28 June 2018 2018, pp. 2-5, doi: 10.1109/DSN-W.2018.00012.
- [40] J. Patterson and A. Gibson, *Deep Learning*, 1 ed. O'Reilly Media, Inc, 2017.
- [41] M. Yu, R. Vasudevan, and M. Johnson-Roberson, "Occlusion-Aware Risk Assessment for Autonomous Driving in Urban Environments," *IEEE Robotics and Automation Letters*, vol. 4, no. 2, pp. 2235-2241, 2019, doi: 10.1109/LRA.2019.2900453.
- [42] M. Lee, M. Sunwoo, and K. Jo, "Collision risk assessment of occluded vehicle based on the motion predictions using the precise road map," *Robotics and Autonomous Systems*, vol. 106, pp. 179-191, 2018/08/01/ 2018, doi: <https://doi.org/10.1016/j.robot.2018.05.005>.
- [43] R. Panahi, I. Gholampour, and M. Jamzad, "Real time occlusion handling using Kalman Filter and mean-shift," in *2013 8th Iranian Conference on Machine Vision and Image Processing (MVIP)*, 10-12 Sept. 2013 2013, pp. 320-323, doi: 10.1109/IranianMVIP.2013.6780003.
- [44] B. Kramer, C. Neurohr, M. Bükér, E. Böde, M. Fränzle, and W. Damm, "Identification and Quantification of Hazardous Scenarios for Automated Driving," in *Model-Based Safety and Assessment*, Cham, M. Zeller and K. Höfig, Eds., 2020// 2020: Springer International Publishing, pp. 163-178.
- [45] D. Wittmann, M. Lienkamp, and C. Wang, "Method for comprehensive and adaptive risk analysis for the development of automated driving," in *2017 IEEE 20th International Conference on Intelligent Transportation Systems (ITSC)*, 16-19 Oct. 2017 2017, pp. 1-7, doi: 10.1109/ITSC.2017.8317791.
- [46] X. Zheng, B. Huang, D. Ni, and Q. Xu, "A novel intelligent vehicle risk assessment method combined with multi-sensor fusion in dense traffic

- environment," *Journal of Intelligent and Connected Vehicles*, vol. 1, no. 2, pp. 41-54, 2018, doi: 10.1108/JICV-02-2018-0004.
- [47] W. Jianqiang, W. Jian, and L. Yang, "The Driving Safety Field Based on Driver-Vehicle-Road Interactions," *IEEE transactions on intelligent transportation systems*, vol. 16, no. 4, pp. 2203-2214, 2015, doi: 10.1109/TITS.2015.2401837.
- [48] A. Wardziński, "Safety Assurance Strategies for Autonomous Vehicles," in *Computer Safety, Reliability, and Security*, Berlin, Heidelberg, M. D. Harrison and M.-A. Sujan, Eds., 2008// 2008: Springer Berlin Heidelberg, pp. 277-290.
- [49] S. Khastgir, H. Sivencrona, G. Dhadyalla, P. Billing, S. Birrell, and P. Jennings, "Introducing ASIL inspired dynamic tactical safety decision framework for automated vehicles," in *2017 IEEE 20th International Conference on Intelligent Transportation Systems (ITSC)*, 16-19 Oct. 2017 2017, pp. 1-6, doi: 10.1109/ITSC.2017.8317868.
- [50] F. Warg *et al.*, "The Quantitative Risk Norm - A Proposed Tailoring of HARA for ADS," in *2020 50th Annual IEEE/IFIP International Conference on Dependable Systems and Networks Workshops (DSN-W)*, 29 June-2 July 2020 2020, pp. 86-93, doi: 10.1109/DSN-W50199.2020.00026.
- [51] B. Wu, Y. Yan, D. Ni, and L. Li, "A longitudinal car-following risk assessment model based on risk field theory for autonomous vehicles," *International Journal of Transportation Science and Technology*, 2020/06/08/ 2020, doi: <https://doi.org/10.1016/j.ijst.2020.05.005>.
- [52] Y. Ma, F. Dong, B. Yin, and Y. Lou, "Real-time risk assessment model for multi-vehicle interaction of connected and autonomous vehicles in weaving area based on risk potential field," *Physica A: Statistical Mechanics and its Applications*, vol. 620, p. 128725, 2023/06/15/ 2023, doi: <https://doi.org/10.1016/j.physa.2023.128725>.

- [53] D. Ni, "A Unified Perspective on Traffic Flow Theory, Part I: The Field Theory," ed, 2011, pp. 4227-4243.
- [54] C. Katrakazas, M. Quddus, and W.-H. Chen, "A new integrated collision risk assessment methodology for autonomous vehicles," *Accident; analysis and prevention*, vol. 127, pp. 61-79, 2019, doi: 10.1016/j.aap.2019.01.029.
- [55] P. Ledent, A. Paigwar, A. Renzaglia, R. Mateescu, and C. Laugier, "Formal Validation of Probabilistic Collision Risk Estimation for Autonomous Driving," in *2019 IEEE International Conference on Cybernetics and Intelligent Systems (CIS) and IEEE Conference on Robotics, Automation and Mechatronics (RAM)*, 18-20 Nov. 2019 2019, pp. 433-438, doi: 10.1109/CIS-RAM47153.2019.9095806.
- [56] L. Rummelhard, A. Nègre, and C. Laugier, "Conditional Monte Carlo Dense Occupancy Tracker," in *2015 IEEE 18th International Conference on Intelligent Transportation Systems*, 15-18 Sept. 2015 2015, pp. 2485-2490, doi: 10.1109/ITSC.2015.400.
- [57] A. Kamel, T. Sayed, and M. Kamel, "Real-time combined safety-mobility assessment using self-driving vehicles collected data," *Accident Analysis & Prevention*, vol. 199, p. 107513, 2024/05/01/ 2024, doi: <https://doi.org/10.1016/j.aap.2024.107513>.
- [58] L. de Haan and A. Ferreira, *Extreme Value Theory: An Introduction*. Springer New York, 2007.
- [59] S. Grigorescu, B. Trasnea, T. Cocias, and G. Macesanu, "A Survey of Deep Learning Techniques for Autonomous Driving," 2019, doi: 10.1002/rob.21918.
- [60] H. Gajjar, S. Sanyal, and M. Shah, "A comprehensive study on lane detecting autonomous car using computer vision," *Expert Systems with*



- Applications*, vol. 233, p. 120929, 2023/12/15/ 2023, doi:  
<https://doi.org/10.1016/j.eswa.2023.120929>.
- [61] B. W. Abegaz, "A Parallelized Self-Driving Vehicle Controller Using Unsupervised Machine Learning," *IEEE Transactions on Industry Applications*, vol. 58, no. 4, pp. 5148-5156, 2022, doi: 10.1109/TIA.2022.3164861.
- [62] A. Tammewar *et al.*, "Improving the Performance of Autonomous Driving through Deep Reinforcement Learning," *Sustainability*, vol. 15, no. 18, p. 13799, 2023. [Online]. Available: <https://www.mdpi.com/2071-1050/15/18/13799>.
- [63] S. Lefèvre, D. Vasquez, and C. Laugier, "A survey on motion prediction and risk assessment for intelligent vehicles," *ROBOMECH journal*, vol. 1, no. 1, pp. 1-14, 2014, doi: 10.1186/s40648-014-0001-z.
- [64] J. Wang, L. Zhang, Y. Huang, and J. Zhao, "Safety of Autonomous Vehicles," *Journal of Advanced Transportation*, vol. 2020, p. 8867757, 2020/10/06 2020, doi: 10.1155/2020/8867757.
- [65] A. Zyner, S. Worrall, and E. Nebot, "A Recurrent Neural Network Solution for Predicting Driver Intention at Unsignalized Intersections," *IEEE Robotics and Automation Letters*, vol. 3, no. 3, pp. 1759-1764, 2018, doi: 10.1109/LRA.2018.2805314.
- [66] S. Lefevre, "Risk estimation at road intersections for connected vehicle safety applications," 2012.
- [67] R. A. Bratulescu, R. I. Vatasoiu, G. Sucic, S. A. Mitroi, M. C. Vochin, and M. A. Sachian, "Object Detection in Autonomous Vehicles," in *2022 25th International Symposium on Wireless Personal Multimedia Communications (WPMC)*, 30 Oct.-2 Nov. 2022 2022, pp. 375-380, doi: 10.1109/WPMC55625.2022.10014804.

- [68] J. Yang, S. Guo, M. J. Bocus, Q. Chen, and R. Fan, "Semantic Segmentation for Autonomous Driving," in *Autonomous Driving Perception: Fundamentals and Applications*, R. Fan, S. Guo, and M. J. Bocus Eds. Singapore: Springer Nature Singapore, 2023, pp. 101-137.
- [69] S. Hao, Y. Zhou, and Y. Guo, "A Brief Survey on Semantic Segmentation with Deep Learning," *Neurocomputing*, vol. 406, pp. 302-321, 2020/09/17/ 2020, doi: <https://doi.org/10.1016/j.neucom.2019.11.118>.
- [70] O. Zendel, M. Schörghuber, B. Rainer, M. Murschitz, and C. Beleznai, "Unifying Panoptic Segmentation for Autonomous Driving," in *2022 IEEE/CVF Conference on Computer Vision and Pattern Recognition (CVPR)*, 18-24 June 2022 2022, pp. 21319-21328, doi: 10.1109/CVPR52688.2022.02066.
- [71] A. Kirillov, K. He, R. Girshick, C. Rother, and P. Dollár, "Panoptic Segmentation," in *2019 IEEE/CVF Conference on Computer Vision and Pattern Recognition (CVPR)*, 15-20 June 2019 2019, pp. 9396-9405, doi: 10.1109/CVPR.2019.00963.
- [72] R. Sharma, M. Saqib, C. T. Lin, and M. Blumenstein, "A Survey on Object Instance Segmentation," *SN Computer Science*, vol. 3, no. 6, p. 499, 2022/09/29 2022, doi: 10.1007/s42979-022-01407-3.
- [73] R. Hou *et al.*, "Real-Time Panoptic Segmentation From Dense Detections," in *2020 IEEE/CVF Conference on Computer Vision and Pattern Recognition (CVPR)*, 13-19 June 2020 2020, pp. 8520-8529, doi: 10.1109/CVPR42600.2020.00855.
- [74] N. Dalal and B. Triggs, "Histograms of oriented gradients for human detection," in *2005 IEEE Computer Society Conference on Computer Vision and Pattern Recognition (CVPR'05)*, 20-25 June 2005 2005, vol. 1, pp. 886-893 vol. 1, doi: 10.1109/CVPR.2005.177.

- [75] P. Felzenszwalb, D. McAllester, and D. Ramanan, "A discriminatively trained, multiscale, deformable part model," in *2008 IEEE Conference on Computer Vision and Pattern Recognition*, 23-28 June 2008 2008, pp. 1-8, doi: 10.1109/CVPR.2008.4587597.
- [76] B. Wang, "Research on Pedestrian Detection Algorithm Based on Image," *Journal of Physics: Conference Series*, vol. 1345, no. 6, p. 062023, 2019/11/01 2019, doi: 10.1088/1742-6596/1345/6/062023.
- [77] R. Girshick, J. Donahue, T. Darrell, and J. Malik, "Region-Based Convolutional Networks for Accurate Object Detection and Segmentation," *IEEE Transactions on Pattern Analysis and Machine Intelligence*, vol. 38, no. 1, pp. 142-158, 2016, doi: 10.1109/TPAMI.2015.2437384.
- [78] S. Ren, K. He, R. Girshick, and J. Sun, "Faster R-CNN: Towards Real-Time Object Detection with Region Proposal Networks," *IEEE Transactions on Pattern Analysis and Machine Intelligence*, vol. 39, no. 6, pp. 1137-1149, 2017, doi: 10.1109/TPAMI.2016.2577031.
- [79] W. Liu *et al.*, "SSD: Single Shot MultiBox Detector," in *Computer Vision - ECCV 2016*, Cham, B. Leibe, J. Matas, N. Sebe, and M. Welling, Eds., 2016// 2016: Springer International Publishing, pp. 21-37.
- [80] J. Long, E. Shelhamer, and T. Darrell, "Fully convolutional networks for semantic segmentation," in *2015 IEEE Conference on Computer Vision and Pattern Recognition (CVPR)*, 7-12 June 2015 2015, pp. 3431-3440, doi: 10.1109/CVPR.2015.7298965. [Online]. Available: <http://doi.ieeecomputersociety.org/10.1109/CVPR.2015.7298965>
- [81] L. C. Chen, G. Papandreou, I. Kokkinos, K. Murphy, and A. L. Yuille, "DeepLab: Semantic Image Segmentation with Deep Convolutional Nets, Atrous Convolution, and Fully Connected CRFs," *IEEE Transactions on Pattern Analysis and Machine Intelligence*, vol. 40, no. 4, pp. 834-848, 2018, doi: 10.1109/TPAMI.2017.2699184.

- [82] H. Zhao, J. Shi, X. Qi, X. Wang, and J. Jia, "Pyramid Scene Parsing Network," in *2017 IEEE Conference on Computer Vision and Pattern Recognition (CVPR)*, 21-26 July 2017 2017, pp. 6230-6239, doi: 10.1109/CVPR.2017.660.
- [83] H. Zhao, X. Qi, X. Shen, J. Shi, and J. Jia, "ICNet for Real-Time Semantic Segmentation on High-Resolution Images," in *European Conference on Computer Vision*, 2017.
- [84] V. Badrinarayanan, A. Kendall, and R. Cipolla, "SegNet: A Deep Convolutional Encoder-Decoder Architecture for Image Segmentation," *IEEE Transactions on Pattern Analysis and Machine Intelligence*, vol. 39, no. 12, pp. 2481-2495, 2017, doi: 10.1109/TPAMI.2016.2644615.
- [85] A. Paszke, A. Chaurasia, S. Kim, and E. Culurciello, "ENet: A Deep Neural Network Architecture for Real-Time Semantic Segmentation," *ArXiv*, vol. abs/1606.02147, 2016.
- [86] M. Krestenitis, G. Orfanidis, K. Ioannidis, K. Avgerinakis, S. Vrochidis, and I. Kompatsiaris, "Oil Spill Identification from Satellite Images Using Deep Neural Networks," *Remote Sensing*, vol. 11, no. 15, doi: 10.3390/rs11151762.
- [87] P. Feth, M. N. Akram, R. Schuster, and O. Wasenmüller, "Dynamic Risk Assessment for Vehicles of Higher Automation Levels by Deep Learning," ed. Cham: Springer International Publishing, 2018, pp. 535-547.
- [88] M. Strickland, G. Fainekos, and H. B. Amor, "Deep Predictive Models for Collision Risk Assessment in Autonomous Driving," 2017.
- [89] D. Feng, L. Rosenbaum, and K. Dietmayer, "Towards Safe Autonomous Driving: Capture Uncertainty in the Deep Neural Network For Lidar 3D Vehicle Detection," 2018.

- [90] J. Song, W. Ahn, S. Park, and M. Lim, "Failure Detection for Semantic Segmentation on Road Scenes Using Deep Learning," *Applied Sciences*, vol. 11, no. 4, p. 1870, 2021. [Online]. Available: <https://www.mdpi.com/2076-3417/11/4/1870>.
- [91] N. Aloufi, A. Alnori, V. Thayananthan, and A. Basuhail, "Object Detection Performance Evaluation for Autonomous Vehicles in Sandy Weather Environments," *Applied Sciences*, vol. 13, no. 18, p. 10249, 2023. [Online]. Available: <https://www.mdpi.com/2076-3417/13/18/10249>.
- [92] P. Feth, "A Tool for the Development and Comparison of Approaches for the Dynamic Risk Assessment of Active Safety Systems," Wiesbaden, 2018: Springer Fachmedien Wiesbaden, in *Commercial Vehicle Technology 2018*, pp. 387-399.
- [93] S. Li, J. Jiao, Y. Han, and T. Weissman, "Demystifying ResNet," *arXiv*, 2016, doi: 10.48550/ARXIV.1611.01186.
- [94] S. Mehta, M. Rastegari, A. Caspi, L. Shapiro, and H. Hajishirzi, "ESPNNet: Efficient Spatial Pyramid of Dilated Convolutions for Semantic Segmentation," in *Computer Vision - ECCV 2018*, Cham, V. Ferrari, M. Hebert, C. Sminchisescu, and Y. Weiss, Eds., 2018// 2018: Springer International Publishing, pp. 561-580.
- [95] S. U. Bhoover, A. Tugashetti, and P. Rashinkar, "V2X communication protocol in VANET for co-operative intelligent transportation system," in *2017 International Conference on Innovative Mechanisms for Industry Applications (ICIMIA)*, 21-23 Feb. 2017 2017, pp. 602-607, doi: 10.1109/ICIMIA.2017.7975531.
- [96] 5GAA, "Timeline for deployment of C-V2X (V2V/V2I)," 22 Jan 2019. [Online]. Available: [https://5gaa.org/wp-content/uploads/2019/01/5GAA\\_White-Paper-CV2X-Roadmap.pdf](https://5gaa.org/wp-content/uploads/2019/01/5GAA_White-Paper-CV2X-Roadmap.pdf)

- [97] D. Shin, B. Kim, J. Seo, and K. Yi, "Effects of Wireless Communication on Integrated Risk Management Based Automated Vehicle," in *2015 IEEE 18th International Conference on Intelligent Transportation Systems*, 15-18 Sept. 2015 2015, pp. 1767-1772, doi: 10.1109/ITSC.2015.287.
- [98] V. Thayananthan and R. Shaikh, "Contextual Risk-based Decision Modeling for Vehicular Networks," *International Journal of Computer Network and Information Security*, vol. 8, pp. 1-9, 2016.
- [99] D. Shin, B. Kim, K. Yi, A. Carvalho, and F. Borrelli, "Human-Centered Risk Assessment of an Automated Vehicle Using Vehicular Wireless Communication," *IEEE transactions on intelligent transportation systems*, vol. 20, no. 2, pp. 667-681, 2019, doi: 10.1109/TITS.2018.2823744.
- [100] S. Demmel *et al.*, "Global risk assessment in an autonomous driving context: Impact on both the car and the driver," *IFAC-PapersOnLine*, vol. 51, no. 34, pp. 390-395, 2019/01/01/ 2019, doi: <https://doi.org/10.1016/j.ifacol.2019.01.009>.
- [101] H. Zhao, T. Mao, H. Yu, M. Zhang, and H. Zhu, "A Driving Risk Prediction Algorithm Based on PCA -BP Neural Network in Vehicular Communication," vol. 2, ed: IEEE, 2018, pp. 164-169.
- [102] R. A. Shaikh and V. Thayananthan, "Risk-Based Decision Methods for Vehicular Networks," *Electronics (Basel)*, vol. 8, no. 6, p. 627, 2019, doi: 10.3390/electronics8060627.
- [103] P. E. Orukpe, "MODEL PREDICTIVE CONTROL FUNDAMENTALS," *Nigerian Journal of Technology (NIJOTECH)*, vol. Vol. 31, No. 2, July, 2012, pp. 139-148, 2012. [Online]. Available: <https://www.ajol.info/index.php/njt/article/viewFile/123569/113097>.
- [104] D. Shin, K. Park, and M. Park, "Effects of Vehicular Communication on Risk Assessment in Automated Driving Vehicles," 2018.

- [105] E. Fitzgerald and B. Landfeldt, "A system for coupled road traffic utility maximisation and risk management using VANET," ed: IEEE, 2012, pp. 1880-1887.
- [106] D. Delen, R. Sharda, and M. Bessonov, "Identifying significant predictors of injury severity in traffic accidents using a series of artificial neural networks," (in eng), *Accid Anal Prev*, vol. 38, no. 3, pp. 434-44, May 2006, doi: 10.1016/j.aap.2005.06.024.
- [107] N. L. A. A. Shukhair, H. Mansor, T. S. Gunawan, and K. A. Kadir, "Enhancing Public Transportation Detection using YOLOv5," 2023: IEEE, pp. 89-94, doi: 10.1109/ICSIMA59853.2023.10373549.
- [108] Z. Ren, H. Zhang, and Z. Li, "Improved YOLOv5 Network for Real-Time Object Detection in Vehicle-Mounted Camera Capture Scenarios," (in eng), *Sensors (Basel)*, vol. 23, no. 10, May 9 2023, doi: 10.3390/s23104589.
- [109] Y. Zhang, Y. Gong, and X. Chen, "Research on YOLOv5 Vehicle Detection and Positioning System Based on Binocular Vision," *World Electric Vehicle Journal*, vol. 15, no. 2, p. 62, 2024. [Online]. Available: <https://www.mdpi.com/2032-6653/15/2/62>.
- [110] M. A. Malbog, R. J. Marasigan, J. Mindoro, Y. C. Mortos, and L. F. Ilustre, "PED-AI: Pedestrian Detection for Autonomous Vehicles using YOLOv5," *E3S Web of Conf.*, vol. 488, p. 03013, 2024. [Online]. Available: <https://doi.org/10.1051/e3sconf/202448803013>.
- [111] T. Wei, T. Zhu, C. Li, and H. Liu, "Analysis of hazard perception characteristics based on driving behavior considering overt and covert hazard scenarios," (in eng), *PLoS One*, vol. 17, no. 4, p. e0266126, 2022, doi: 10.1371/journal.pone.0266126.

- [112] E. de Gelder and O. O. den Camp, "Tagging Real-World Scenarios for the Assessment of Autonomous Vehicles," *arXiv [cs.RO]*, 2020 2020. [Online]. Available: <http://arxiv.org/abs/2012.01081>.
- [113] N. Belu, L. M. Ionescu, and N. Rachieru, "Risk-cost model for FMEA approach through Genetic algorithms - A case study in automotive industry," *IOP Conference Series: Materials Science and Engineering*, vol. 564, p. 012102, 2019/10/30 2019, doi: 10.1088/1757-899x/564/1/012102.
- [114] G. Marshall and L. Jonker, "An introduction to descriptive statistics: A review and practical guide," *Radiography*, vol. 16, no. 4, pp. e1-e7, 2010/11/01/ 2010, doi: <https://doi.org/10.1016/j.radi.2010.01.001>.
- [115] C. Oh, J. Oh, and J. Min, "Real-Time Detection of Hazardous Traffic Events on Freeways: Methodology and Prototypical Implementation," *Transportation research record*, vol. 2129, no. 1, pp. 35-44, 2009, doi: 10.3141/2129-05.
- [116] M. Aeberhard *et al.*, "Experience, Results and Lessons Learned from Automated Driving on Germany's Highways," *IEEE Intelligent Transportation Systems Magazine*, vol. 7, no. 1, pp. 42-57, 2015, doi: 10.1109/MITS.2014.2360306.
- [117] J. Zhu, Y. Ma, and Y. Lou, "Multi-vehicle interaction safety of connected automated vehicles in merging area: A real-time risk assessment approach," *Accident Analysis & Prevention*, vol. 166, p. 106546, 2022/03/01/ 2022, doi: <https://doi.org/10.1016/j.aap.2021.106546>.
- [118] W. Yu, Y. Qian, J. Xu, H. Sun, and J. Wang, "Driving Decisions for Autonomous Vehicles in Intersection Environments: Deep Reinforcement Learning Approaches with Risk Assessment," *World Electric Vehicle Journal*, vol. 14, no. 4, doi: 10.3390/wevj14040079.



- [119] R. Fell, J. Corominas, C. Bonnard, L. Cascini, E. Leroi, and W. Z. Savage, "Guidelines for landslide susceptibility, hazard and risk zoning for land use planning," *Engineering Geology*, vol. 102, no. 3, pp. 85-98, 2008/12/01/2008, doi: <https://doi.org/10.1016/j.enggeo.2008.03.022>.
- [120] Y. Lu, F. Ren, and W. Zhu, "Risk zoning of typhoon disasters in Zhejiang Province, China," *Nat. Hazards Earth Syst. Sci.*, vol. 18, no. 11, pp. 2921-2932, 2018, doi: 10.5194/nhess-18-2921-2018.
- [121] H. Li, W. Xi, L. Zhang, and S. Zang, "Snow-Disaster Risk Zoning and Assessment in Heilongjiang Province," *Sustainability*, vol. 13, no. 24, p. 14010, 2021. [Online]. Available: <https://www.mdpi.com/2071-1050/13/24/14010>.
- [122] A. Rahman, A. Salam, M. Islam, and P. Sarker, "An Image Based Approach to Compute Object Distance," *Int. J. Comput. Intell. Syst.*, vol. 1, pp. 304-312, 2008.
- [123] P. Drożdziel, S. Tarkowski, I. Rybicka, and R. Wrona, "Drivers' reaction time research in the conditions in the real traffic," *Open Engineering*, vol. 10, no. 1, pp. 35-47, 2020, doi: doi:10.1515/eng-2020-0004.
- [124] *Infrastructure Risk Rating Manual for Australian Roads*, Austroads, 2019.
- [125] YOLOv5 by Ultralytics. (2020). <https://github.com/ultralytics/yolov5>. [Online]. Available: <https://github.com/ultralytics/yolov5>
- [126] C. Li *et al.*, "YOLOv6: A Single-Stage Object Detection Framework for Industrial Applications," *ArXiv*, vol. abs/2209.02976, 2022.
- [127] C.-Y. Wang, A. Bochkovskiy, and H.-Y. M. Liao, "YOLOv7: Trainable Bag-of-Freebies Sets New State-of-the-Art for Real-Time Object Detectors," *2023 IEEE/CVF Conference on Computer Vision and Pattern Recognition (CVPR)*, pp. 7464-7475, 2022.

- [128] *Ultralytics YOLOv8*. (2023). GitHub. [Online]. Available: <https://github.com/ultralytics/ultralytics>
- [129] B. Gašparović, G. Mauša, J. Rukavina, and J. Lerga, "Evaluating YOLOV5, YOLOV6, YOLOV7, and YOLOV8 in Underwater Environment: Is There Real Improvement?," in *2023 8th International Conference on Smart and Sustainable Technologies (SpliTech)*, 20-23 June 2023 2023, pp. 1-4, doi: 10.23919/SpliTech58164.2023.10193505.
- [130] K. Hormann and A. Agathos, "The point in polygon problem for arbitrary polygons," *Computational Geometry*, vol. 20, no. 3, pp. 131-144, 2001/11/01/ 2001, doi: [https://doi.org/10.1016/S0925-7721\(01\)00012-8](https://doi.org/10.1016/S0925-7721(01)00012-8).
- [131] J. Redmon, S. Divvala, R. Girshick, and A. Farhadi, "You Only Look Once: Unified, Real-Time Object Detection," in *2016 IEEE Conference on Computer Vision and Pattern Recognition (CVPR)*, 27-30 June 2016 2016, pp. 779-788, doi: 10.1109/CVPR.2016.91.
- [132] J. Jeong and A. Kim, "Adaptive Inverse Perspective Mapping for lane map generation with SLAM," in *2016 13th International Conference on Ubiquitous Robots and Ambient Intelligence (URAI)*, 19-22 Aug. 2016 2016, pp. 38-41, doi: 10.1109/URAI.2016.7734016.
- [133] X. Chen, P. Shi, and Y. Hu, "A Precise Semantic Segmentation Model for Seabed Sediment Detection Using YOLO-C," *Journal of Marine Science and Engineering*, vol. 11, no. 7, p. 1475, 2023. [Online]. Available: <https://www.mdpi.com/2077-1312/11/7/1475>.
- [134] *Multi YOLO V5 - Detection and Semantic Segmentation*. (2021). [Online]. Available: <https://github.com/TomMao23/multiyolov5?tab=readme-ov-file>

- [135] S. Liu, D. Huang, and Y. Wang, "Receptive Field Block Net for Accurate and Fast Object Detection," Cham, 2018: Springer International Publishing, in *Computer Vision - ECCV 2018*, pp. 404-419.
- [136] X. Qin, Z. Wang, Y. Bai, X. Xie, and H. Jia, "FFA-Net: Feature Fusion Attention Network for Single Image Dehazing," *ArXiv*, vol. abs/1911.07559, 2019.
- [137] A. Shokri and A. Kythreotis, "Enhancing portfolio risk management: a comparative study of parametric, non-parametric, and Monte Carlo methods, with VaR and percentile ranking," *International Journal of Business and Emerging Markets*, vol. 16, no. 3, pp. 411-428, 2024, doi: 10.1504/ijbem.2024.139472.
- [138] Z. M. Lee, L. X. Tan, C. T. Choo, and W. M. D. Chia, "Real-Time Risk Tag Forecasting for Safer Intelligent Transportation," in *2024 IEEE 99th Vehicular Technology Conference (VTC2024-Spring)*, 24-27 June 2024 2024, pp. 1-7, doi: 10.1109/VTC2024-Spring62846.2024.10683525.